Development of Ultrafast Laser Sources using Multi-Pass Cells

Dissertation zur Erlangung des Doktorgrades
an der Fakultät für Mathematik, Informatik und
Naturwissenschaften
Fachbereich Physik
der Universität Hamburg

Vorgelegt von
Arthur Schönberg

Hamburg
2026

Gutachter/innen der Dissertation:	Prof. Dr. Franz X. Kärtner Dr. Christoph M. Heyl
Zusammensetzung der Prüfungskommission:	Prof. Dr. Arwen Pearson Prof. Dr. Nina Rohringer Dr. Cord L. Arnold Prof. Dr. Franz X. Kärtner Dr. Christoph M. Heyl
Vorsitzende/r der Prüfungskommission:	Prof. Dr. Arwen Pearson
Datum der Disputation:	11.09.2026
Vorsitzender des Fach-Promotionsausschusses PHYSIK:	Prof. Dr. Johannes Haller
Leiter des Fachbereichs PHYSIK:	Prof. Dr. Markus Drescher
Dekan der Fakultät MIN:	Prof. Dr.-Ing. Norbert Ritter

Contents

List of Publications relevant for this work **III**

List of Figures **IV**

List of Tables **VI**

List of Abbreviations **VII**

Abstract **IX**

Zusammenfassung **X**

1 Introduction **1**

2 Energy Scaling of MPC-based Post-Compression **7**
2.1 Introduction . . . 7
2.2 Self-phase modulation in gas-filled MPCs . . . 7
2.3 MPCs for post-compression and MPC size scaling . . . 9
2.4 Non-geometric approaches for energy-scaling . . . 11
2.5 Geometric approaches for energy-scaling of MPCs . . . 12
2.6 Summary and Outlook . . . 23

3 Post-Compression of Nanosecond Pulses in Multi-Pass Cells **26**
3.1 Introduction . . . 26
3.2 Concept . . . 27
3.3 Challenges of post-compression of nanosecond pulses . . . 30
3.3.1 Temporal quality of post-compressed Q-switched pulses . . . 30
3.3.2 Longitudinal mode-beating in Q-switched lasers . . . 31
3.3.3 Stimulated Brillouin scattering . . . 32
3.3.4 Stimulated Raman Scattering . . . 34
3.3.5 Quasi-phase-matched four-wave-mixing . . . 35
3.4 Experiment . . . 37
3.5 Conclusion and Outlook . . . 39

4 Second-Harmonic Generation in Multi-Pass Cells **40**
4.1 Introduction . . . 40
4.2 Concept . . . 41
4.3 Theory . . . 45
4.3.1 General equations for second-order nonlinear conversion . . . 46
4.3.2 Fourier expansions of the fields . . . 47
4.3.3 Coupled wave equations for second-harmonic generation . . . 48
4.3.4 Equation for SHG in MPCs in the non-depleting pump approximation . . . 49
4.3.5 Linearization of the phase-terms . . . 52
4.3.6 Analytic SHG-MPC equation . . . 53
4.3.7 Comparison of the analytical model to experimental data . . . 55
4.3.8 Expansion of the relative phase up to second order . . . 58
4.3.9 Gouy phase contribution . . . 59
4.3.10 Numerical model (3+1)D . . . 60
4.3.11 ABCD-formalism-based (1+1)D model . . . 61
4.4 Experiment and Simulation: Second-Harmonic in MPCs . . . 62

4.5 Discussion . . . 68
4.5.1 Overview of previous SHG works . . . 68
4.5.2 Pulse energy-scaling of the SHG-MPC . . . 69
4.5.3 Pulse duration down-scaling and GDD compensation . . . 70
4.5.4 Geometry considerations for uniaxial crystals . . . 71
4.5.5 Mode-matching of the second-harmonic . . . 71
4.6 Conclusion . . . 72

5 Conclusion **74**

Literatur **76**

A Appendix: Compact, Folded Multi-Pass Cells for Energy Scaling of Post-Compression **92**

B Appendix: Post-Compression of a Q-Switched Laser in a Glass-Rod Multi-Pass Cell **104**

C Appendix: Efficient Broadband Second-Harmonic Generation in a Multi-Pass Cell **122**

List of Publications Included in this Cumulative Thesis

Main publications

1. **A. Schönberg**, S. Rajhans, E. Escoto, N. Khodakovskiy, V. Hariton, B. Farace, K. Pøder, A.-K. Raab, S. Westerberg, M. Merdanov, A.-L. Viotti, C. L. Arnold, W. P. Leemans, I. Hartl, and C. M. Heyl, "*Compact, folded multi-pass cells for energy scaling of post-compression,*" **Photonics Research 13, 761–771** (2025). DOI: 10.1364/PRJ.540977

   Contributions: Initial planning, mathematical modeling and simulations, design, experiments, data analysis and writing the manuscript.

2. P. Biesterfeld, **A. Schönberg**, M. Seitz, N. Jimenez, T. Lang, M. Seidel, P. Balla, L. Winkelmann, J. K. Sunny, S. Fröhlich, P. Mosel, I. Hartl, F. Calegari, U. Morgner, M. Kovacev, C. M. Heyl, and A. Trabattoni, "*Post-compression of a Q-switched laser in a glass-rod multi-pass cell,*" **Journal of Physics: Photonics 8, 015013** (2026). DOI: 10.1088/2515-7647/ae1fc4

   Contributions: Initial planning, mathematical modeling and simulations, design, experiments, data analysis and writing substantial parts the manuscript.

3. **A. Schönberg**, N. Rupp, A. O. e Silva, L. Pratolli, Y. Jiang, V. Wanie, T. Mullins, F. Calegari, and C. M. Heyl, *"Efficient broadband second-harmonic generation in a multi-pass cell,"* arXiv:2607.03192 (2026). DOI: 10.48550/arXiv.2607.03192.

   Current status: Submitted for publication. Preprint submitted in arXiv (arxiv.org). The attached document in Appendix C is the arXiv preprint version.

   Contributions: Initial planning, mathematical modeling and simulations, design, experiments, data analysis and writing the manuscript.

Secondary publications

1. C. M. Heyl, M. Seidel, E. Escoto, **A. Schönberg**, S. Carlström, G. Arisholm, T. Lang, and I. Hartl, "*High-energy bow tie multi-pass cells for nonlinear spectral broadening applications,*" **Journal of Physics: Photonics 4, 014002** (2022). DOI: 10.1088/2515-7647/ac483a

2. V. Hariton, Y. Jiang, **A. Schönberg**, M. Seidel, M. Wieland, M. J. Prandolini, I. Hartl, M. Drescher, and C. M. Heyl, "*UV 30 fs laser pulse generation using a multi-pass cell,*" **Optics Letters 49, 3769** (2024). DOI: 10.1364/OL.527988

3. S. Rajhans, N. Rupp, E. Escoto, **A. Schönberg**, D. Laumer, M. Sumfleth, I. Abdallah, B. Manschwetus, C. Juliano, N. Javid, C. L. Arnold, T. Gorkhover, M. Drescher, R. Riedel, I. Hartl, C. M. Heyl, and T. Lang, "*Optical parametric multi-pass cell amplifier,*" **Optica** (2026). DOI: 10.1364/OPTICA.597010

List of Figures

1 Typical MPC-based post-compression scheme. 2
2 Overview of eight key parameters driving current MPC research. 3
3 Detailed overview map of scaling parameters and current MPC topics in MPC development. 5
4 Simple size-scaling of an MPC. 10
5 Laguerre-Gauss (LG) mode structure for four different $LG_{0,l}$ beams with azimuthal numbers $l = 0, 1, 2, 3$. 12
6 Stability diagram and different MPC geometries. 13
7 Convex-concave MPC and a folded convex-concave MPC. 15
8 Bow-Tie MPC geometry in comparison to a standard MPC. 17
9 Comparison of a standard MPC and a CMPC. 18
10 Energy scaling characteristics of a CMPC compared to a standard MPC 19
11 Setup of the CMPC experiment 20
12 Experimental results of the CMPC experiment in air 21
13 Results of the STC mesurements. 22
14 Estimated energy scaling potential of different MPC-based post-compression techniques. 24
15 Post-compression methods covering the parameter space from nanoseconds to femtoseconds 28
16 Simulated post-compression using the nMPC concept 29
17 Simulated nMPC post-compression using a parabolic temporal pulse shape 30
18 Simulation results visualizing the influence of a secondary longitudinal mode on the compressibility of the MPC output 32
19 SBS threshold in an nMPC 33
20 Impact of SRS in an nMPC for various Stokes losses 35
21 Impact of QPM-FWM in an nMPC 36
22 Sketch of the experimental setup used in the nMPC experiments. 37
23 Results of the nMPC experiment 38
24 Illustration of the SHG-MPC in comparison to SHG in thick and thin crystals . . . 42
25 Index ellipsoids of a negative uniaxial crystal for type I phase-matching 43
26 Illustration of the SHG-MPC in consecutive order and the actual configuration. . . 44
27 Simulated idealized spectrograms of the SH pulse for two different crystal angles . 45
28 Schematical representation of the evolution of the non-depleting fundamental field $E_1(\omega)$ 50
29 Schematic of the solution to the evolution equation (94) of the second-harmonic electric field in the non-depleting pump approximation 52
30 The function $|\Phi^N(\Delta\varphi)|^2$ appearing in Eq. 118 plotted as a function of the relative phase $\Delta\varphi$ between fundamental and SH per pass for different numbers of passes N. 54
31 Figure illustrating the origin of the features of the pressure spectrograms similar to the experiments 55
32 Mirror data for the mirrors used in the experiments and simulations, as provided by the manufacturer LAYERTEC GmbH. Reprinted and modified with permission from [6] 56
33 Comparison between the analytical model and the measurements in the experiment for Krypton as the ambient gas medium in the SHG-MPC 57
34 Comparison between the analytical model and the measurements in the experiment for air as the ambient gas medium in the SHG-MPC 58

35 Experimental setup for both the long pulse and the short pulse experiment 63
36 Measurement results of the long pulse experiment 64
37 Experimental and simulated spectrograms for experiment A using Krypton as the ambient gas 65
38 Experimental and simulated spectrograms for experiment A using air as the ambient gas 65
39 Measurement results of the short pulse experiment 66
40 Experimental (left) and simulated (right) spectrograms for experiment B using air as the ambient gas for 15.4 fs, 20 µm input fundamental pulses 67
41 Simulated SHG-MPC spectrograms and efficiencies including a θ variation of about $\pm 0.4°$, emulating the realistic experimental conditions. 67
42 Overview of various works on second-harmonic generation 68
43 Simulations of energy-scaled SHG-MPCs 69
44 Simulated spectrogram traces and efficiencies for a 7 fs Gaussian pulse input using a 100 µm BBO crystal and air as the ambient ga 70
45 Optimized MPC geometry for an SHG-MPC with a uniaxial crystal 71
46 Simulated $1/e^2$ beam radii of the fundamental and second-harmonic beam 72

List of Tables

1 BBO relative phase coefficients 56
2 Relative phase-mismatch coefficients for krypton and air 57
3 Table showing the relative phase and group-delay introduced by the SHG-MPC mirrors 57

List of Abbreviations

ABCD	ray transfer matrix formalism
AC	autocorrelation
AR	anti-reflective
as	attosecond
BBO	beta-barium borate
BT-MPC	Bow-Tie Multi-Pass Cell
c.c.	complex conjugate
CCD	charge-coupled device (camera)
CER	chirped ellipse rotation
CPA	chirped-pulse amplification
CVBG	chirped volume Bragg grating
CMPC	compact, folded Multi-Pass Cell
cx-cv MPC	convex-concave Multi-Pass Cell
DCM	double-chirped mirror
DFG	difference-frequency generation
EFC	enhanced frequency chirping
FM	focusing mirror
FROG	frequency-resolved optical gating
fs	femtosecond
FS	fused silica
FTL	Fourier-transform limit
FWHM	full width at half maximum
FWM	four-wave mixing
GD	group delay
GDD	group-delay dispersion
GW	gigawatt
HHG	high-harmonic generation
HR	high reflectivity
HS	harmonic separator
I/O	input/output
k-vector	wavevector
LG	Laguerre-Gaussian
LiDAR	light detection and ranging
LIDT	laser-induced damage threshold
LPA	laser-plasma accelerator
LM	longitudinal mode
MIR	mid-infrared
MM	mode-matching
MPC	(Herriott-type) multi-pass cell
MW	megawatt
N_2	nitrogen
nMPC	nanosecond multi-pass cell
NIR	near-infrared
ns	nanosecond
O_2	oxygen
OPA	optical parametric amplification
OPMPC	optical parametric multi-pass cell amplifier

OR	optical rectification
POM	pick-off mirror
PM	planar mirror
PPLN	periodically poled lithium niobate
ps	picosecond
QPM	quasi-phase matching
QPM-FWM	quasi-phase-matched four-wave mixing
Q-switched	quality-switched
ROC	radius of curvature
RK4	Runge-Kutta 4
SH	second harmonic
SHG	second-harmonic generation
SHG-MPC	second-harmonic generation multi-pass cell
SFG	sum-frequency generation
SBS	stimulated Brillouin scattering
SPF	short-pass filter
SPM	self-phase modulation
SRS	stimulated Raman scattering
SSH	spatio-spectral homogeneity
STC	spatio-temporal coupling
SVEA	slowly varying envelope approximation
THG	third-harmonic generation
THz	terahertz
Ti:Sa	titanium-sapphire
TW	terawatt
UV	ultraviolet
UV-MPC	ultraviolet Multi-Pass Cell
UPPE	unidirectional pulse propagation equation
VIS	visible
XUV	extreme-ultraviolet
YAG	yttrium aluminum garnet
Yb	ytterbium

Abstract

Ultrafast laser technology has developed into a central pillar of modern photonics, driven by the continuing demand for shorter pulses, higher peak powers, and greater control over light–matter interaction. In parallel, nonlinear optics has become indispensable for extending laser performance beyond the limits of available gain media, enabling frequency conversion, spectral broadening, and access to new wavelength regimes. Among the nonlinear tools that have emerged in this context, Herriott-type multi-pass cells (MPCs) have proven particularly powerful. By combining long effective nonlinear interaction lengths with compact geometries, high transmission, and excellent beam-quality preservation, MPCs have become a versatile platform for post-compression and, increasingly, for a broader range of nonlinear optical processes.

This thesis investigates the evolving role of MPCs in ultrafast science and laser development. The central theme is the use of MPCs not only as pulse post-compressors, but as a tool for scalable and adaptable systems for generating and controlling ultrafast light across a wide parameter space.

A major part of the thesis focuses on the energy scaling of MPC-based post-compression systems. Here, the fundamental limitations imposed by mirror damage, nonlinear propagation, and ionization are considered, and different strategies for overcoming these constraints are reviewed and compared. These include straightforward size scaling, non-geometric approaches that alter the spatial or temporal structure of the input pulse, and geometric approaches that modify the MPC layout itself. In this context, the compact folded MPC (CMPC) is developed and examined in detail as a compact and highly scalable geometry that illustrates how pulse-energy scaling can be achieved without sacrificing the practical advantages of MPC-based systems.

A second focus of this thesis is the extension of multipass-cell concepts beyond the ultrafast regime. While MPCs have traditionally been employed for the compression of femtosecond and picosecond pulses from mode-locked lasers, we demonstrate their applicability to substantially longer pulses with much lower peak powers, including nanosecond pulses from Q-switched laser systems. This significantly expands the operational range of MPC technology and establishes a new approach for nonlinear pulse manipulation at millijoule pulse energies, bridging the gap between mode-locked and Q-switched laser platforms.

Finally, the thesis explores how MPCs can be used beyond traditional post-compression. By tailoring the propagation conditions and the nonlinear interaction over each pass, MPCs can serve as a platform for efficient frequency conversion. In particular, second-harmonic generation in MPCs is investigated as a route toward efficient broadband wavelength conversion. The results demonstrate that MPC-based frequency conversion, in particular the second-harmonic generation, can reach substantially higher efficiencies and broader bandwidths than conventional single-pass approaches, highlighting the potential of MPCs as a general platform for nonlinear photonics.

In summary, this work presents MPCs as a highly versatile technology that bridges established ultrafast laser architectures and emerging nonlinear optical applications. The results and concepts discussed in this thesis contribute to the broader effort of making ultrafast laser systems more compact, more scalable, and more versatile, thereby expanding their usefulness across fundamental research, applied photonics and industrial applications.

Zusammenfassung

Die Ultrakurzpulslasertechnologie hat sich zu einer zentralen Säule der modernen Photonik entwickelt, angetrieben durch die kontinuierliche Nachfrage nach kürzeren Pulsen, höheren Spitzenleistungen und einer verbesserten Kontrolle der Licht–Materie-Wechselwirkung. Parallel dazu ist die nichtlineare Optik unverzichtbar geworden, um die Leistungsfähigkeit von Lasersystemen über die Grenzen verfügbarer Verstärkermedien hinaus zu erweitern und Frequenzkonversion, spektrale Verbreiterung sowie den Zugang zu neuen Wellenlängenbereichen zu ermöglichen. Unter den nichtlinearen optischen Technologien, die sich in diesem Zusammenhang etabliert haben, haben sich Herriott-artige Multipasszellen (MPCs) als besonders leistungsfähig erwiesen. Durch die Kombination großer effektiver nichtlinearer Wechselwirkungslängen mit kompakten Geometrien, hoher Transmission und ausgezeichneter Erhaltung der Strahlqualität haben sich MPCs zu einer vielseitigen Plattform für die Nachkompression und zunehmend auch für ein breiteres Spektrum nichtlinearer optischer Prozesse entwickelt.

Diese Dissertation untersucht die sich wandelnde Rolle von MPCs in der Ultrakurzpulslaserwissenschaft und Laserentwicklung. Das zentrale Thema ist die Nutzung von MPCs nicht nur als Systeme zur Pulsnachkompression, sondern als skalierbare und anpassungsfähige Systeme zur Erzeugung und Kontrolle ultrakurzer Lichtpulse über einen weiten Parameterbereich.

Ein wesentlicher Teil der Dissertation konzentriert sich auf die Skalierung MPC-basierter Nachkompressionssysteme. Dabei werden die grundlegenden Einschränkungen betrachtet, die durch Spiegelschädigung, nichtlineare Ausbreitung und Ionisation vorgegeben werden, und verschiedene Strategien zu deren Überwindung werden untersucht und verglichen. Dazu gehören die direkte Größenskalierung, nicht-geometrische Ansätze, welche die räumliche oder zeitliche Struktur des Eingangspulses verändern, sowie geometrische Ansätze, die das Layout der MPC selbst modifizieren. In diesem Zusammenhang wird die kompakte gefaltete Multipasszelle (Compact, Folded Multi-Pass Cell, CMPC) entwickelt und detailliert untersucht, da sie eine kompakte und hochskalierbare Geometrie darstellt, die veranschaulicht, wie eine Skalierung der Pulsenergie erreicht werden kann, ohne die praktischen Vorteile MPC-basierter Systeme aufzugeben.

Ein weiterer Schwerpunkt dieser Dissertation ist die Erweiterung von Multipasszellenkonzepten über den Ultrakurzpulsbereich hinaus. Während MPCs traditionell für die Kompression von Femtosekunden- und Pikosekundenpulsen aus modeengekoppelten Lasern eingesetzt wurden, demonstrieren wir ihre Anwendbarkeit auf deutlich längere Pulse mit wesentlich geringeren Spitzenleistungen, einschließlich Nanosekundenpulsen aus gütegeschalteten Lasersystemen. Dies erweitert den Einsatzbereich der MPC-Technologie erheblich und etabliert einen neuen Ansatz zur nichtlinearen Pulsmanipulation bei Pulsenergien im Millijoule-Bereich, wodurch die Lücke zwischen modengekoppelten und gütegeschalteten Laserplattformen überbrückt wird.

Abschließend untersucht die Dissertation, wie MPCs über die klassische Nachkompression hinaus eingesetzt werden können. Durch die gezielte Anpassung der Ausbreitungsbedingungen und der nichtlinearen Wechselwirkung bei jedem einzelnen Durchlauf können MPCs als Plattform für effiziente Frequenzkonversion und andere nichtlineare optische Prozesse dienen. Insbesondere wird die Erzeugung der zweiten Harmonischen in MPCs als ein Ansatz für eine effiziente breitbandige Wellenlängenkonversion untersucht. Die Ergebnisse zeigen, dass die MPC-basierte Frequenzkonversion, insbesondere die Erzeugung der zweiten Harmonischen, deutlich höhere Effizienzen und größere Bandbreiten erreichen kann als konventionelle Einzelpassansätze, was das Potenzial von MPCs als allgemeine Plattform für die nichtlineare Photonik demonstriert.

Insgesamt präsentiert diese Arbeit MPCs als eine äußerst vielseitige Technologie, die etablierte Ultrakurzpulslaserarchitekturen mit neuartigen Anwendungen der nichtlinearen Optik verbindet. Die in dieser Dissertation vorgestellten Ergebnisse und Konzepte leisten einen Beitrag zu den umfassenderen Bestrebungen, Ultrakurzpulslasersysteme kompakter, besser skalierbar und vielseitiger

zu gestalten und dadurch ihre Nutzbarkeit in der Grundlagenforschung, der angewandten Photonik sowie in industriellen Anwendungen zu erweitern.

1 Introduction

Ultrafast laser technology has evolved rapidly since the invention of the laser in 1960 [7], driven by the quest to generate ever shorter and more intense light pulses. Early advances in mode locking during the 1960s and 1970s enabled the first picosecond and later femtosecond pulses, laying the foundation for ultrafast science and its many applications [8]. In parallel, nonlinear optics emerged as a central discipline in modern photonics, providing the physical mechanisms that make it possible to manipulate light with light and to access regimes far beyond the reach of linear optics, which started from the first observation of the second-harmonic generation of laser in a crystal [9]. Today, nonlinear optical phenomena cover a wide range of transformative technologies and research areas, including frequency conversion [10], harmonic generation [11], optical parametric amplification [12], supercontinuum generation [13], soliton dynamics [14], ultrafast spectroscopy [15], high-harmonic generation [16], and attosecond science [17, 18]. As such, nonlinear optics is not merely a specialized subfield, but a cornerstone of modern laser science, enabling both fundamental discoveries and practical applications across physics, chemistry, materials science, communications, and medicine [18–21].

Among other applications, one of the most central purposes of nonlinear optics is to gain access to wavelength regimes that are not accessible by laser gain materials. This includes not only wavelength conversion, but also the enhancement of the optical bandwidth of laser pulses, enabling much shorter pulse durations than emitted from laser gain materials. Therefore, nonlinear optics is not only responsible for achieving laser pulses in a large range of wavelengths, spanning from the Terahertz (THz) region [22] down to the extreme-ultraviolet (XUV) [16], but also to access pulse durations that can span from the nanosecond (ns) regime down to the picosecond (ps), femtosecond (fs), or even as short as attosecond (as) regime, making it an extremely powerful tool to access insights into the fastest processes in matter [2, 12, 23–25].

Nonlinear optical phenomena cover a broad range of physical regimes, from perturbative frequency conversion to strongly non-perturbative processes such as high-harmonic generation. While the latter effects are of major importance in strong-field and attosecond science, the present work focuses on perturbative nonlinear optics, in particular on processes of second and third-order nonlinear response, which form the basis of many widely used methods for frequency conversion, pulse shaping, and ultrafast light generation [26]. In particular, second- and third-order nonlinear optical processes form the foundation of the phenomena and techniques treated in this work. Second-order nonlinear processes are of particular importance in the present context, as they provide the basis for a broad range of frequency-conversion techniques. These include second-harmonic generation (SHG), sum-frequency generation (SFG), difference-frequency generation (DFG), optical parametric amplification (OPA), and optical rectification (OR), which together enable access to new wavelength regimes and play a central role in the generation and control of ultrafast light [26]. Third-order nonlinear processes are likewise of major importance in nonlinear optics, as they arise in essentially all optical media and provide a broad range of effects that are central to ultrafast photonics. Representative examples include third-harmonic generation, self-phase modulation, four-wave mixing, and stimulated Raman and Brillouin scattering [26, 27]. Through these mechanisms, third-order nonlinear optics enables spectral broadening, wavelength conversion, pulse shaping, and nonlinear propagation effects that are fundamental to many applications in ultrafast science, spectroscopy, and nonlinear laser systems. In particular, self-phase modulation (SPM) and four-wave mixing (FWM) play a key role in the generation and control of broadband optical spectra, while third-harmonic generation (THG) provides access to shorter wavelengths that are otherwise difficult to reach directly.

In the context of nonlinear optics and ultrafast lasers, Herriott-type multi-pass cells (MPC) have emerged as a powerful tool for generating ultrashort laser pulses [24, 28, 29]. In MPCs, the

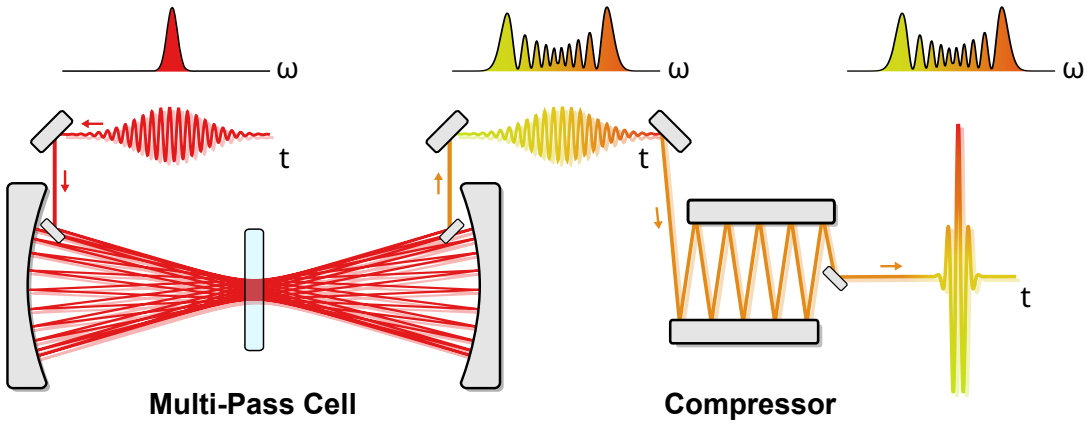


Figure 1: Typical MPC-based post-compression scheme. The annotation "t" indicates the temporal domain and "ω" the frequency domain.

third-order nonlinear effect of SPM is exploited to convert long pulses with a narrow frequency spectrum into broadband spectral bandwidth. Although Herriott-type MPCs were first introduced in 1965 as optical delay lines and spectroscopic tools [30], their use for spectral broadening and pulse post-compression has emerged only in recent years [31]. Since then, Herriott-type MPCs have become an attractive platform for nonlinear pulse post-compression, owing to their long nonlinear interaction lengths, high efficiency, and excellent stability, which together enable high spectral broadening factors while maintaining excellent spectral homogeneity and preserve beam quality at the output. A typical post-compression scheme is illustrated in Fig. 1. An initially long laser pulse is coupled into the MPC consisting of two concave mirrors with a fixed radius of curvature (ROC), placed at a certain distance to each other. The beam passes through the cell multiple times, interacting with a nonlinear medium – either a gas or a solid-state material – via self-phase modulation, which broadens its spectrum. After out-coupling the pulse is compressed to a shorter pulse duration. In recent years, MPCs have emerged as a key platform for the post-compression of ultrafast laser pulses, enabling the generation of shorter pulses from a wide range of laser sources [28, 31]. Early demonstrations were largely centered on ytterbium (Yb)-based lasers, but the field has since expanded substantially, both in terms of the laser systems employed and the performance parameters addressed. Today, MPC-based post-compression is applied across a broad spectral and temporal landscape, spanning different wavelengths, pulse energies, repetition rates, and pulse durations and continues to push the frontiers of ultrafast pulse generation toward ever shorter, more efficient, and more versatile output pulses [31].

In the ongoing quest of extending MPCs towards a broader parameter and application range, a set of key scaling parameters can be identified. We categorize these advancements into eight key scaling parameters that define recent MPC developments. Figure 2 maps out and summarizes representative works related to these development topics. These developments are characterized by the following eight key scaling parameters: **average power, wavelength, pulse energy, peak power, pulse duration, broadening factor, temporal contrast, and nonlinear processes** beyond spectral broadening applications. Each of these parameters represents an active area of current MPC development, and this work addresses several of these topics. A more detailed overview is given in Fig. 3. In the following, we discuss each topic in more detail and provide representative references to ongoing work in the field. In addition, the contributions of this work to these topics are highlighted and placed in the broader context of ongoing MPC research.

We start with the aspect of **average power scaling** in MPCs. Works on average power scaling have been reported in the literature of up to 1 kW of average power [32, 33]. In these works, the underlying laser technology are highly power-scalable ytterbium (Yb)-based laser systems, which are post-compressed by MPCs down to much shorter pulse durations. Yb-based laser systems are

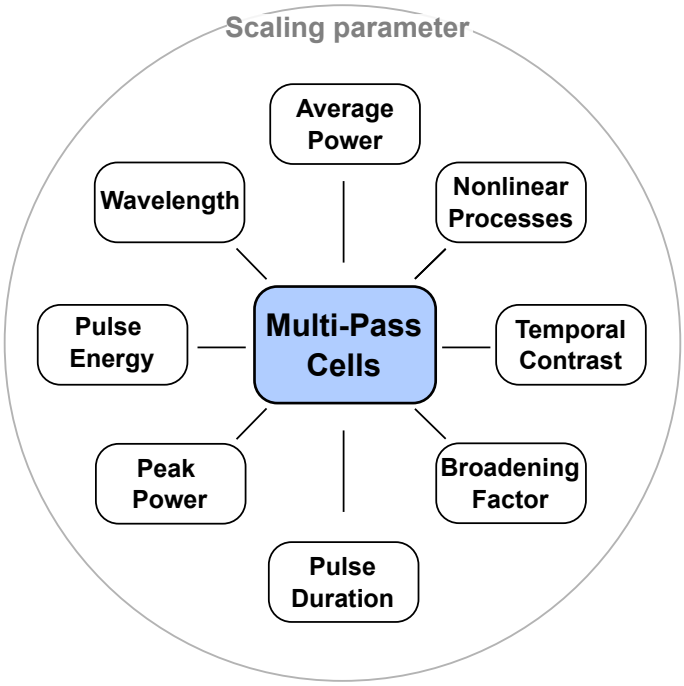


Figure 2: Overview of eight key parameters driving current MPC research.

highly power-scalable [34], but their inherently low gain bandwidth limits the pulse duration to the 100s of femtoseconds or few picoseconds range. Thus, this laser architecture by itself provides large average powers, but only relatively long pulses. MPCs have been established as an excellent tool to overcome these bandwidth limitations, enabling large average powers while at the same time delivering short laser pulses [31]. Yb-based laser systems typically deliver pulses centered at a wavelength of 1030 nm.

In addition, laser systems operating at different **wavelengths** can also be post-compressed. Current developments in MPCs aim to extend the wavelength range in which they can be used, making them a more versatile tool for post-compression across a broad range of spectra. Until now, post-compression in MPCs has been demonstrated in the middle-infrared (MIR), short-wave near-infrared (SWIR), near-infrared (NIR), and visible (VIS) spectral regions, and has even been extended toward the ultraviolet[1] (UV) range [4, 24, 35–39].

Another important line of work focuses on the **pulse energy scaling** of MPC post-compression. The topic of energy scaling in MPCs is a major part of this work and is discussed extensively in Chapter 2. In recent years, a number of MPC pulse energy scaling techniques have been developed [1, 3, 40–48]. One of the major limitations in MPC-based post-compression schemes is the laser-induced damage threshold (LIDT) of the mirrors employed in the MPC. Exceeding a certain threshold fluence on these mirrors, typically defined by the optical coatings, can cause catastrophic damage and lead to irreversible loss of performance. Thus, techniques to overcome LIDT limitations while maintaining, or even decreasing, the size of the setup are necessary in order to enable post-compression of higher pulse energies in a compact setup. In this work, the different techniques are classified into three major branches of methods. The first branch is the simplest approach, in which the MPC dimensions are scaled to accommodate higher pulse energies, with pulse energy increasing linearly with MPC length, while the underlying geometry does not change. Here, post-compression has been demonstrated for up to 200 mJ laser pulses in a 10 m long cell [40]. The second branch comprises non-geometric scaling techniques. These approaches are characterized by modifying the laser beam or pulse structure before coupling into, and optionally after coupling out of, the MPC and thereby decreasing the effective fluence on the mirrors. Here,

[1] Post-compression of UV pulses is one of the secondary topics covered in this thesis.

two main approaches have been demonstrated. In the first approach the spatial properties of the laser beams are modified towards higher-order Laguerre-Gaussian (LG) modes. Increasing the azimuthal order of the beam prior to in-coupling into the MPC significantly reduces the peak fluence of the beam, enabling higher pulse energies in the MPC [41–43]. The second approach is based on the modification in the temporal instead of the spatial domain. In particular, pulse division and coherent recombination approaches have been demonstrated in MPCs, where the pulse is split into multiple replicas with a certain temporal delay and coupled into the MPC, therefore effectively reducing the fluence on the mirrors [44–46]. After spectral broadening, the pulses are coherently recombined to yield a single pulse. In the third branch of pulse energy scaling in MPCs, the MPC geometry is modified in order to scale up the pulse energy, or equivalently, reduce the size of an MPC at a given pulse energy acceptance. We thus summarize this topic as the geometric scaling techniques. Here, four key techniques can be identified, including the 4f-MPC[2], convex-concave MPC (cx-cv MPC), Bow-Tie MPC (BT-MPC) and the compact, folded MPC (CMPC) [1, 3, 47, 48]. This work therefore places strong emphasis on geometric scaling, since one of the major works (CMPC) and one of the secondary works (BT-MPC) employ a geometric scaling method. Each of these techniques is discussed in detail in Section 2.5.

Another important scaling parameter in MPC development is **pulse duration**. In this context, two complementary aspects are relevant. First, a central goal of MPC technology is the generation of the shortest possible output pulses. The production of ultrashort, few-cycle pulses has driven extensive research in MPCs and remains a major objective in the field [50, 52, 53]. Second, pulse duration is also critical on the input side. In particular, post-compression of long pulses becomes increasingly difficult as the input pulse duration increases, since longer pulses typically exhibit lower peak power and therefore provide less efficient driving of the nonlinear spectral broadening process. To the best of our knowledge, the longest pulses post-compressed in an MPC were demonstrated in the nanosecond MPC (nMPC) [2]. In this work, post-compression of a Q-switched laser in an MPC is reported for the first time. The nMPC is part of this work and is discussed in Chapter 3.

Closely related to pulse duration is **peak power**, which is determined by both pulse energy and pulse duration. As with pulse duration, peak power is an important scaling target in MPCs: on the one hand, post-compression aims at the highest possible output peak power, and on the other hand, it seeks to handle the lowest possible input peak power. While terawatt (TW)-level output peak powers after post-compression have been achieved in Yb-based laser systems using high-energy pulses ($> 100\,\mathrm{mJ}$) [40, 41], close-to-TW few-cycle pulses have also been generated from lower-energy systems [49–51]. At the opposite end of the scale, low pulse energies combined with long pulse durations result in low peak power, which poses a challenge for MPC post-compression. To efficiently induce spectral broadening, a sufficient intensity in the nonlinear medium is required, implying a minimum peak power threshold. In MPCs, spectral broadening with peak powers down to 6.5 MW in the pico- to femtosecond regime has been demonstrated using solid-state media [29]. For nanosecond lasers, post-compression of pulses with a peak power of 2 MW has been achieved in the nMPC by using long glass-rods [2].

When the pulse duration is relatively long, a large **broadening factor** is of interest. In MPCs this can be achieved by employing multiple, cascaded MPCs [24, 51]. Here, a broadening factor of close to, or exceeding a factor of 100 has been achieved in multiple works. When simple, compact systems are required, it can be desirable to reach similar broadening factors in a single stage. Examples of high single-stage post-compression factors above 30 have been demonstrated in references [24, 41]. The work on the nanosecond-MPC (nMPC) provides a concept of how to reach even higher broadening factors (>100) specifically for very long pulses in the nanosecond (ns) regime, and how to post-compress them into the picosecond regime [2].

[2]This naming is specific to this work and defined in Chapter 2

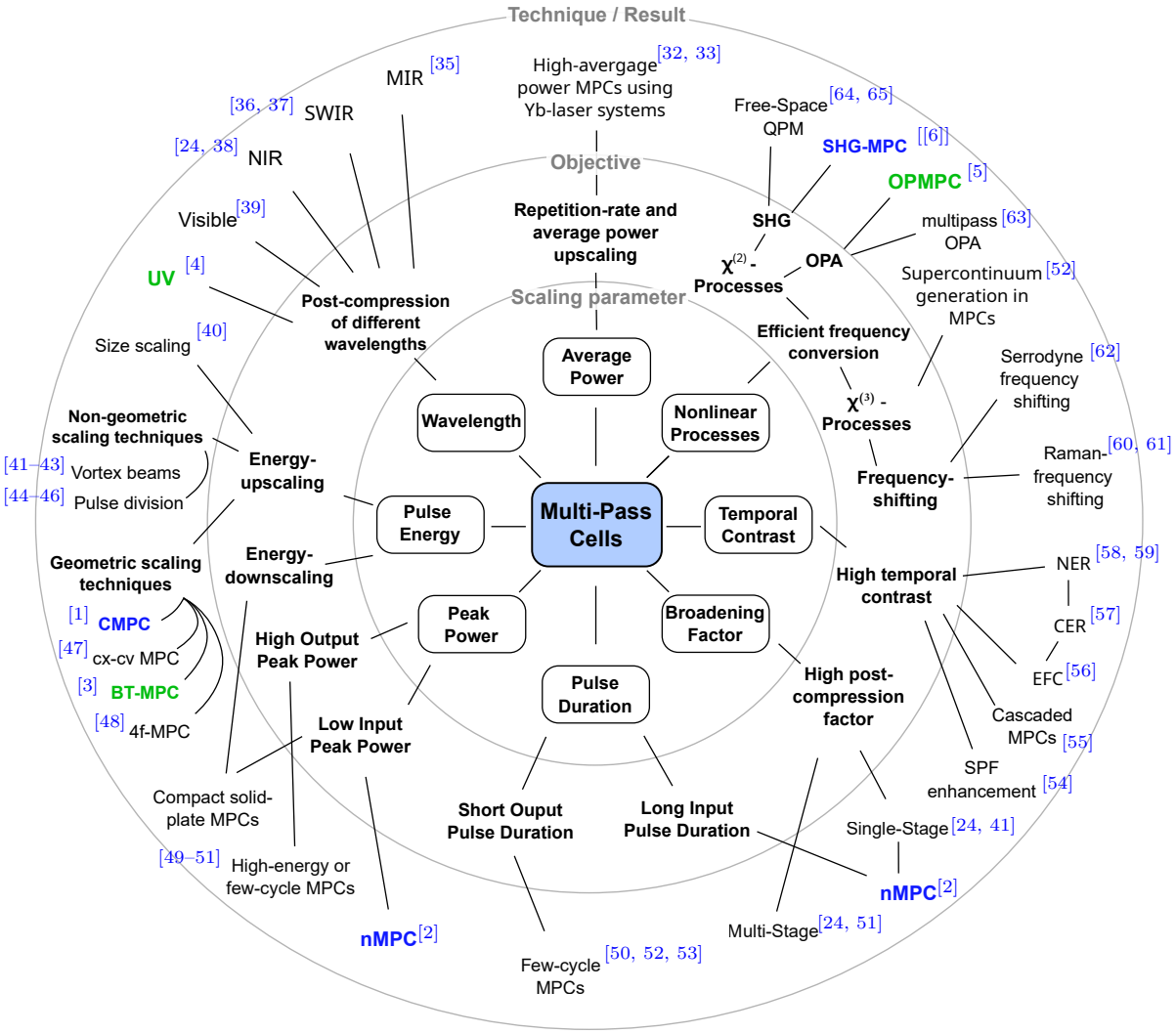


Figure 3: Detailed overview map of scaling parameters and current MPC topics in MPC development. In the center are multi-pass cells and in the inner circle are the scaling parameters. In the next "objective" circle, the goals of scaling the parameters are located. In the outermost "Technique/Result"-circle, examples of works on these topics are provided with the respective references. The topics that are discussed as the main contributions to this thesis are highlighted in blue. The secondary topics are highlighted in green.

Large broadening factors, on the other hand, can degrade the **temporal contrast** of the post-compressed pulse. This degradation is mainly caused by strong spectral and phase modulations induced during spectral broadening via self-phase modulation (SPM), which cannot be effectively compensated by simple compressor systems based only on group-delay dispersion (GDD) compensation. Several techniques have been developed in MPCs to improve the temporal contrast of post-compressed pulses, such as nonlinear ellipse rotation (NER) [58, 59], enhanced frequency chirping (EFC) [56], by using short-pass filters (SPF) [54], or even by employing cascaded MPCs [57]. A recently demonstrated technique combines NER and EFC into chirped ellipse rotation (CER), where both effects are exploited simultaneously for contrast enhancement [55].

In recent years, the scope of applications of MPCs has been extended towards other **nonlinear effects** beyond post-compression. A major topic of this development has been to further exploit the third-order nonlinearity (of which SPM is a subcategory) towards different kinds of light sources. Examples are supercontinuum generation in MPCs [52], or frequency shifting using different mechanisms, such as the delayed response of molecular gases or solid-state media (Raman-response) [60, 61] or by shaping the temporal pulse shape in the serrodyne frequency-shifting scheme [62]. Due to their quasi-waveguide properties, where the laser pulse is propagated repeatedly in the cell, MPCs can be tailored such that the phase- and amplitude can be tuned at each pass using either

the MPC mirrors or additional optical elements. This can be exploited to drive phase-matched second-order nonlinear processes such as second-harmonic generation (SHG) in MPCs with high efficiency via free-space quasi-phase-matching (free-space QPM) [64, 65] or even increase the efficiency and bandwidth of optical-parametric amplification (OPA) processes [5, 63]. One of the major topics of this work is the efficient SHG in MPCs (SHG-MPC) for broadband, ultrashort pulses [6]. This topic is discussed in great detail in Chapter 4.

In summary, the development of MPCs is currently driven by the pursuit of scaling several key parameters, including average power, wavelength, pulse energy, peak power, pulse duration, broadening factor, temporal contrast, and nonlinear processes beyond spectral broadening. Together, these directions define the present frontiers of MPC research and reflect the broader effort to transform MPCs from specialized pulse-post-compression tools into versatile platforms for ultrafast nonlinear optics.

Within this broader context, the present work contributes to multiple aspects of MPC development, with a primary focus on pulse-energy and peak power scaling in the compact, folded MPC (CMPC), long-pulse post-compression, broadening-factor and peak power scaling in the nanosecond MPC (nMPC), as well as the extension of MPCs to nonlinear processes beyond post-compression in the second-harmonic MPC (SHG-MPC). In addition, the work includes secondary contributions, which are not explicitly discussed in this thesis. These secondary contributions include wavelength scaling of MPCs in the ultraviolet MPC (UV-MPC), pulse-energy and peak power scaling of MPC-based post-compression in the bow-tie MPC (BT-MPC), and the extension of MPCs to other nonlinear processes in the optical-parametric MPC (OPMPC). Taken together, this work contributes to the research and development of MPC technology, expanding its scope as a platform for nonlinear optics and ultrafast light generation.

The thesis is structured as follows: in Chapter 2, a general review of energy-scaling concepts for MPC-based post-compression is provided. The CMPC concept (reference [1]), as one of the main publications of this thesis, is included as part of this discussion.[3] In Chapter 3, the publication about the nanosecond-MPC (reference [2]) is summarized and discussed.[4] Chapter 4 summarizes the work on the second-harmonic MPC[5] (reference [6]). The thesis is concluded in Chapter 5.

[3]The publication is attached in Appendix A.
[4]The publication is attached in Appendix B.
[5]The publication is attached in Appendix C.

2 Energy Scaling of MPC-based Post-Compression

This chapter discusses strategies for scaling the pulse energy of multi-pass-cell (MPC) based post-compression systems. After introducing the fundamental limits imposed by mirror damage and nonlinear effects in gas-filled MPCs, different routes to higher energy acceptance are reviewed, including simple size scaling, non-geometric approaches based on modified input pulse or beam structure, and geometric approaches that alter the MPC layout itself. A particular focus is placed on the compact, folded MPC (CMPC) concept as described in reference [1], which is one of the main publications relevant to this work and forms the basis of the experimental results presented in Appendix A of this thesis.

2.1 Introduction

In recent years, advances in MPC technology have been a major driving force in the development of ultrashort, high peak- and average-power laser sources, particularly in the near-infrared (NIR) based on ytterbium (Yb) laser systems [24, 28, 31]. Yb lasers approaching or exceeding the terawatt scale while operating at high repetition rates can routinely be generated using MPC-based post-compression technology [40, 49–51]. In order to further push parameters toward even more powerful laser sources, energy up-scaling is the natural progression for further development. The energy acceptance of an MPC system is fundamentally limited by one important parameter, namely the laser-induced damage threshold (LIDT) of the mirror coatings used in the cell [31]. The LIDT is typically defined in terms of the peak fluence of the laser beam on the mirror surface [66], i.e., the maximum optical energy density incident on the coating, usually expressed in units of J/cm^2. Accordingly, energy scaling of MPC systems can be pursued along two principal directions: either by increasing the LIDT of the mirror coatings, or by reducing the fluence on the mirrors for a given pulse energy. Since coating performance is ultimately constrained by available mirror technology, the latter approach is often the more practical route for further scaling, which is the aim of this work.

A second limitation, which is particularly relevant for gas-filled MPCs, is ionization of the nonlinear medium in the focus [49]. In this case, the relevant constraint is not fluence but peak intensity, since ionization is governed primarily by the local electric-field strength [67]. Once the intensity approaches the ionization threshold of the gas, nonlinear propagation effects such as plasma formation, defocusing, and additional loss can strongly degrade the compression process and limit the maximum achievable pulse energy [31, 68]. Thus, ionization is especially pronounced in strongly focused MPC geometries. To mitigate this, such systems often use vacuum chambers filled with high-ionization-threshold gases such as helium or neon, or adopt solid-state approaches in which the solid plate is positioned close to the MPC mirrors, where the beam diameter is large enough to keep the intensity low.

2.2 Self-phase modulation in gas-filled MPCs

Before examining the various MPC post-compression energy scaling strategies, it is useful to recall the physical mechanism that provides the spectral broadening on which post-compression relies. In gas-filled MPCs the nonlinear phase that drives the compression originates from self-phase modulation (SPM) generated by the optical Kerr effect Consequently, any technique that changes the beam size, the number of passes, or the peak intensity will directly influence the accumulated B-integral and, therefore, the achievable bandwidth. The following subsection briefly revisits the SPM process and the formalism that is used throughout the rest of this chapter.

The spectral broadening employed in gas-filled multi-pass cells (MPCs) originates from self-phase modulation (SPM), which arises from the optical Kerr effect. In an isotropic medium the

refractive index depends on the instantaneous pulse intensity according to

$$n(I) = n_0 + n_2 I(t), \tag{1}$$

where n_0 is the linear refractive index and n_2 denotes the nonlinear Kerr coefficient. As a result, different temporal portions of the pulse experience different phase velocities and accumulate different optical phases during propagation.

A rigorous description of pulse propagation in a dispersive nonlinear medium is provided by the unidirectional pulse propagation equation (UPPE), which is derived directly from Maxwell's equations under the assumption of predominantly forward propagation. In the frequency domain it can be written as [69]

$$\frac{\partial \tilde{E}(z,\omega)}{\partial z} = ik_z(\omega)\tilde{E}(z,\omega) + i\frac{\omega}{2\varepsilon_0 c^2 k_z(\omega)}\tilde{P}_{\mathrm{NL}}(z,\omega), \tag{2}$$

where $\tilde{E}(z,\omega)$ denotes the spectral electric field, $k_z(\omega)$ is the longitudinal propagation constant including the linear dispersion of the medium, and $\tilde{P}_{\mathrm{NL}}$ is the Fourier transform of the nonlinear polarization. The first term describes linear propagation of the optical field, whereas the second term accounts for nonlinear light–matter interaction.

For an isotropic gas with an instantaneous electronic Kerr response, the nonlinear polarization is

$$P_{\mathrm{NL}}(t) = \frac{4}{3}\varepsilon_0 n_0 n_2 |E(t)|^2 E(t), \tag{3}$$

which is equivalent to a third-order nonlinear susceptibility $\chi^{(3)}$. The Kerr polarization modifies the refractive index according to Eq. 1 and gives rise to the nonlinear phase accumulated by the pulse

$$\phi_{\mathrm{NL}}(t) = \frac{2\pi}{\lambda}\int_0^L n_2 I(z,t)\,\mathrm{d}z, \tag{4}$$

Here λ denotes the central wavelength, L the interaction length, and I_p the on-axis peak intensity. Since the nonlinear phase follows the temporal intensity profile of the pulse, it induces the instantaneous frequency shift

$$\omega_{\mathrm{inst}}(t) = \omega_0 - \frac{\partial \phi_{\mathrm{NL}}}{\partial t}, \tag{5}$$

which is the physical origin of self-phase modulation and the resulting spectral broadening.

To quantify the overall strength of the nonlinear interaction, it is convenient to introduce the *B-integral*. Throughout this thesis, the B-integral is defined as the accumulated on-axis nonlinear phase,

$$B = \frac{2\pi}{\lambda}\int_0^L n_2 I_p(z)\,\mathrm{d}z, \tag{6}$$

where $I_p(z)$ denotes the peak intensity on the optical axis. For an MPC with N effective passes, the total accumulated nonlinear phase is

$$B = N\,B_{\mathrm{pass}}. \tag{7}$$

It should be noted that an alternative definition is frequently found in the literature, where the nonlinear phase is expressed in terms of the pulse power,

$$\phi_{\max} = \frac{2\pi}{\lambda}\int_0^L n_2 \frac{P(z)}{A_{\mathrm{eff}}(z)}\,\mathrm{d}z, \tag{8}$$

with $P(z)$ the pulse peak power and $A_{\text{eff}}(z)$ the effective mode area. For a Gaussian beam,

$$I_p = \frac{2P}{A_{\text{eff}}}, \tag{9}$$

such that the two definitions are related by

$$B = 2\phi_{\max}. \tag{10}$$

The spectral broadening factor scales approximately linearly with the accumulated nonlinear interaction [31]

$$K \equiv \frac{\Delta\omega_{\text{out}}}{\Delta\omega_{\text{in}}} \approx \frac{B}{\pi}, \tag{11}$$

showing that the achievable compression factor is directly linked to the accumulated nonlinear phase. In practice, the maximum usable B-integral is limited by the onset of ionization, self-focusing, the laser-induced damage threshold of the cavity optics, and the specific geometry of the MPC, as discussed in the following.

In the next sections, different approaches to energy scaling in MPC post-compression are reviewed with a particular focus on avoiding damage limits imposed by laser-induced damage of the optics and optical-field ionization of the gas. These approaches can be broadly divided into three categories: straightforward geometric scaling of the MPC, non-geometric approaches that modify the pulse or beam properties independently of the resonator geometry, and geometric approaches that alter the MPC design itself to increase the energy acceptance or, equivalently, enable more compact implementations.

2.3 MPCs for post-compression and MPC size scaling

Since every MPC configuration – similar to optical cavities [70] – defines a specific spatial eigenmode of the laser to ensure a periodically invariant beam size, the beam size on the mirrors cannot be modified independently within a given MPC configuration. Thus, the MPC configuration needs to be altered to increase the beam size homogeneously for each reflection and thus reduce the peak fluence. The most typical configuration for MPCs is the symmetric case with two mirrors of same radius of curvature (ROC), which also fulfills the re-entrant condition. The re-entrant condition is defined by the relation [31]

$$\frac{L}{R} = 1 - \cos\left(\xi/2\right) , \quad \xi = 2\pi k/N , \tag{12}$$

where L is the MPC length, R the ROC, N the number of round-trips and k the MPC configuration parameter. The phase term ξ represents the angular advance of the beam on the mirrors per round-trip and is equivalent to the accumulated Gouy phase [31]. Since ξ is the angular advance per round-trip, the angular advance after N round-trips accumulates to $N\xi = 2\pi k$. Thus, when k is integer, the phase advance is a multiple of 2π and the beam ends up at its entry point in the MPC, fulfilling the re-entrant condition. An MPC operating in a regime where a periodically repeating spatial mode is defined is called q-preserving MPC, which is the case if $0 < k < N$. If in addition the re-entrant condition is imposed, the condition for k becomes restricted to integers with $k = 1, ..., N$. The spatial Gaussian mode defined by a q-preserving MPC can be calculated using the linear transfer-matrix formalism, also known as the ABCD formalism. Using the propagator function for the q-parameter $f_M(q) = \frac{Aq+B}{Cq+D}$ with $M = \left(\begin{smallmatrix} A & B \\ C & D \end{smallmatrix}\right) = \left(\begin{smallmatrix} 1-2L/R & L \\ -2/R & 1 \end{smallmatrix}\right)$ and the condition

for q-preservation $f_M(q) = q$, the Gaussian mode of the MPC in the focus is determined by

$$w_0^2 = \frac{R\lambda}{2\pi}\sqrt{\frac{L}{R}\left(2-\frac{L}{R}\right)} = \frac{R\lambda}{2\pi}\sin\left(\pi k/N\right) . \tag{13}$$

The beam size on the mirror can be calculated using $w_m = w(L/2) = -1/\mathrm{Im}(\frac{1}{q(L/2)})$, yielding

$$w_m^2 = \frac{R\lambda}{\pi}\sqrt{\frac{\frac{L}{R}}{2-\frac{L}{R}}} = \frac{R\lambda}{\pi}\tan\left(\pi k/2N\right) . \tag{14}$$

Assuming a Gaussian beam, we can calculate the peak intensity in the focus using $I_0 = 2P/\pi w_0^2$ with $P \approx E/\tau$ the power, E the pulse energy and τ the full width half maximum (FWHM) pulse duration. Similarly, the fluence on the mirror can be calculated using $F_m = 2E/\pi w_m^2$. Using equations (13) and (14) the formula for peak mirror fluence and peak intensity are [3]

$$I_0 = \frac{4E}{\tau R\lambda}\frac{1}{\sin\left(\pi k/N\right)} \tag{15}$$

$$F_m = \frac{2E}{R\lambda}\frac{1}{\tan\left(\pi k/2N\right)} . \tag{16}$$

From the above equations it is clear that both I_0 and F_m scale inversely proportional to R. On the other hand, increasing R requires L to increase simultaneously, according to Eq. (12) to maintain the MPC configuration. If we define a certain threshold F_{th} for the mirror fluence and I_{th} for the peak intensity in the focus, then from equations (15) and (16) follows immediately the formula for the energy acceptance of the MPC [3]

$$E \leq \min\left[\frac{F_{\mathrm{th}}R\lambda}{2}\tan\left(\pi k/2N\right),\ \frac{\tau R\lambda}{4}\sin\left(\pi k/N\right)\right] =: E_{\mathrm{max}} . \tag{17}$$

Specifically for gas-filled MPCs, which are typically used for high-energy MPCs, a scaling that keeps L/R constant falls under the category of scale-invariant nonlinear optical systems in gases [71]. This means that if the pulse energy and gas pressure are adjusted accordingly, the resulting output pulse from the MPC will have the same properties (e.g. spectrum) for different values of R and L. Thus, the simplest way to scale the energy is to simply increase the size of the setup by increasing the ROC of the mirrors and the length of the MPC.

The MPC with the highest energy demonstrated so far has been demonstrated by Pfaff et al., where 200 mJ pulses from an Yb laser system have been post-compressed from 500 fs down to 32 fs [40] by an MPC with a length of close to 10 m. Increasing the system to even larger pulse energies would require an even larger cell, which could be impractical for laboratory-scale applications.

There are however alternative routes for pulse energy scaling of MPC-based post-compression.

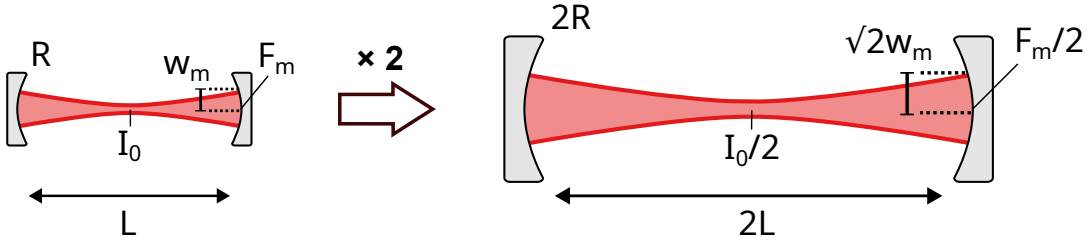


Figure 4: Simple size-scaling of an MPC. Here the main scaling parameters are the radius of curvature R and the length L, which are doubled on the right side. At constant pulse energy, this leads to half the fluence on the mirrors F_{m}, half the peak intesnity in the focus I_0 and a factor of $\sqrt{2}$ larger beam radius w_{m}

Instead of increasing the system size, one can attempt to decrease the fluence by modifying the MPC geometry or the input beam and pulse properties.

2.4 Non-geometric approaches for energy-scaling

Besides modifying the cavity geometry itself, the energy handling capability of a multi-pass cell can also be increased through non-geometric approaches. These methods leave the MPC geometry unchanged and instead alter the properties of the injected beam or pulse. Here, we summarize two different MPC energy-scaling methods: one that modifies the spatial properties and one that modifies the temporal properties of the laser.

Laguerre-Gauss Mode Scaling One non-geometric approach is to deviate from purely Gaussian beams and use higher-order spatial modes in order to decrease the peak fluence on the mirrors. Kaumans et al. demonstrated post-compression of 112 mJ pulses using a first-order Laguerre-Gauss (LG_{01}) mode as the input beam in a 7.8 m MPC, which set the record in pulse energy at that time [41]. Energy scaling using LG_{pl}-modes has further been investigated by Koltalo et al. and 'Ierano et al. [42, 43]. In reference [42] it is shown that the peak intensity scales with the azimuthal index l by

$$\frac{I_{lp}^{\mathrm{LG}}}{I^{\mathrm{G}}} = \frac{|l|!}{(|l|/e)^{|l|}} \ , \tag{18}$$

where $e = 2.71828...$ is the Euler constant. In this scaling law, p is always set to zero. They further demonstrate numerically that, when self-phase modulation (SPM) effects are included while keeping the resulting output Fourier-transform-limited (FTL) pulse duration constant, the energy-scaling law $E \propto l^{0.57}$ is obtained, which is very close to the scaling law described by Eq. (18). The energy acceptance of the MPC thus scales with the azimuthal index l of the LG beam. With these findings, the energy-scaling equation for LG-beam scaling is similar to Eq. (17) but with an additional factor

$$E \leq E_{\mathrm{max}} \cdot (a + b \cdot l^{0.57}) \ , \tag{19}$$

with a and b being fitting parameters that are not disclosed in the referenced source [42], but can be estimated to be close to $a = 1$ and $b = 2$. This method can bring several advantages, as the MPC geometry does not have to be modified, but instead the input beam is simply changed by suitable optical elements beforehand. It can especially be useful for applications requiring ultrashort, high-energy, and high-peak power pulses pulses, where the spatial beam structure does not need to be Gaussian. On the other hand, since Gaussian beams are required for many applications, the back-conversion of a spectrally broadened LG mode into a Gaussian beam can possibly create losses [42].

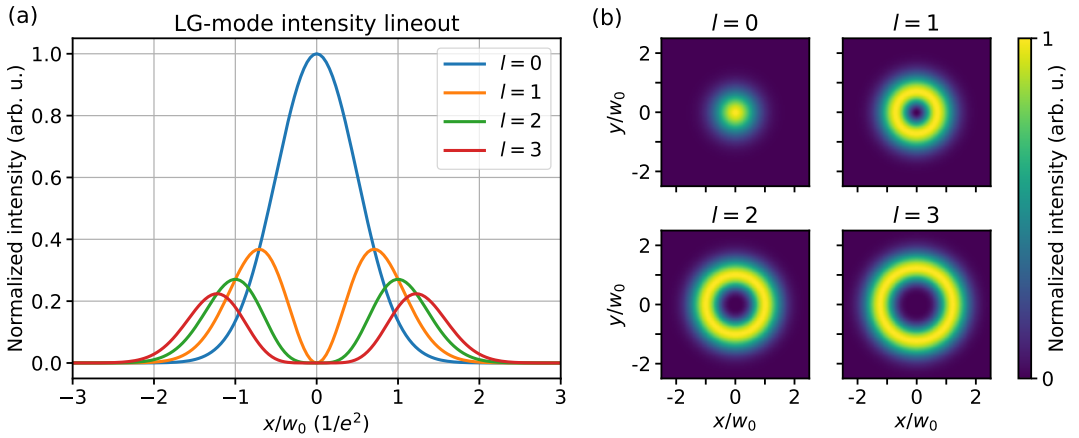


Figure 5: Laguerre-Gauss (LG) mode structure for four different $\mathrm{LG}_{0,l}$ beams with azimuthal numbers $l = 0, 1, 2, 3$. (a) Intensity-lineouts of the cross-section in the center of the beams. (b) Beam profiles of the Laguerre-Gauss modes.

Divided-Pulse Energy-Scaling A different non-geometric approach is the modification of the temporal structure of the pulse rather than its spatial profile. One technique is to divide the pulse into several replicas with a defined temporal delay between them before injection into the MPC [44–46]. The delay is chosen to be longer than the characteristic timescales of the dominant ultrafast laser-induced damage mechanisms. In the ultrashort-pulse regime, damage initiation is primarily governed by electron dynamics, such as the generation and excitation of free carriers in the material [66]. As a result, each replica interacts with the material independently, reducing the peak intensity experienced by the optical components while maintaining the total pulse energy. This enables operation at higher energies without exceeding the laser-induced damage threshold. Thus, dividing the pulses with delays longer than the decay time of these excitations results in a reduced effective fluence on the mirror by a factor of the number of pulse replicas ξ. The energy-scaling equation is simply the maximum energy of any given MPC geometry times the number of replicas

$$E \;\leq\; E_{\mathrm{max}} \cdot \xi \;. \tag{20}$$

After division, the pulses can be spectrally broadened in an MPC with a ξ-fold reduced pulse energy and peak fluence. Subsequently, these pulses can be coherently recombined. In the work of Stark et al. a pulse with 3.4 mJ and 175 fs was divided into four replicas ($\xi = 4$) by polarization rotation and two birefringent crystals, then spectrally broadened, coherently recombined, and compressed down to 34 fs with an overall efficiency of 90% [44]. In another work, Schygulla et al. demonstrated pulse division into eight replicas ($\xi = 4$) by using calcite crystals, with a subsequent post-compression and recombination in an MPC with a recombination efficiency of 95% [45]. Both works showcase the potential of pulse division and recombination as a tool for energy scaling of MPCs using only passive optical elements.

2.5 Geometric approaches for energy-scaling of MPCs

Another route for energy scaling is to modify the overall geometry of MPCs. As stated before, the eigenmode supported by an MPC is determined by its specific geometry [31]. In a standard, symmetric MPC with two curved mirrors of the same ROC, the largest beam size on the mirrors is achieved when the mirror distance, i.e. the MPC length L, is close to $2R$, according to Eq. (14). However, different MPC geometries and configurations can be advantageous specifically for energy up-scaling of MPCs. Similar to optical cavities, MPCs can employ two mirrors with

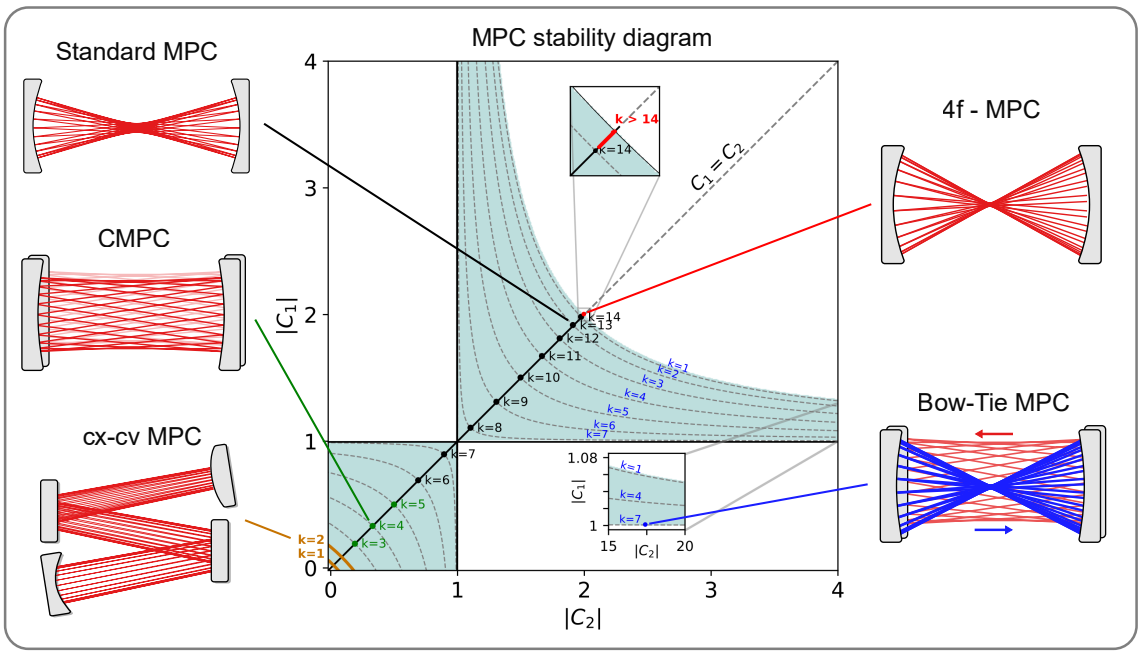


Figure 6: Stability diagram and different MPC geometries. The blue area shows the area where stable configurations with repeating eigenmodes are possible, as a function of $|C_1| = |L_1/R_1|$ and $|C_2| = |L_2/R_2|$, according to Eq. (21). Here the number of round-trips is set to $N = 15$. The dashed lines indicate the re-entrant condition, where the configuration number k is an integer and $1 \leq k \leq N - 1$. The solid black line indicates symmetric MPC configurations $|C_1| = |C_1|$, where Eq. (12) applies. The position of the different types of MPCs is color-coded and indicated in the diagram.

different ROCs or include more than two mirrors. Figure 6 provides an overview of different MPC geometries that were either proposed or implemented in different works concerning MPC energy scaling. The main diagram in Fig. 6 plots the so-called stability region in which self-repeating eigenmodes can exist. Each type of MPC is located inside the region of stability (marked in light blue), where they are typically operated. The stability diagram is defined by the possible solution space of Eq. (21). In this case, we arbitrarily chose the number of round-trips $N = 15$, which is a typical choice in many experiments. We identify four main approaches for energy-scaling in MPCs using alternative geometries that have been proposed in the literature, apart from the size scaling. The four approaches are the 4f-MPC[6] [48], convex-concave MPC (cx-cv MPC) [47], Bow-Tie MPC (BT-MPC) [3], and the compact, folded MPC (CMPC) [1]. In the following, we describe each approach in detail and provide equations for the energy limits of each method. We begin with the 4f-MPC approach, followed by the cx-cv MPC and the BT-MPC, and conclude with a detailed description of the CMPC approach, which is part of the work presented in this thesis.

4f-MPC When $L = 2R$, the configuration is called concentric, meaning that the ROC R of the mirrors forms a perfect circle if the spherical curvature is continued over the whole space. One round-trip in a concentric MPC corresponds to a 4f optical system. Since this configuration is unstable according to Eq. (12), going only close to this limit can lead to a stable configuration with mirror beam sizes getting larger with ever increasing L, while the beam size in the focal position of the cell decreases. Thus, increasing L while approaching $2R$, decreases the fluence on the mirrors, but increases the intensity in the focus. Since the cell constitutes a system close to a 4f geometry, we call this method 4f-MPC. In the context of MPC post-compression, this approach has been demonstrated by Jimenez et al. [72] and Manz et al. [48]. In the former, a double-stage MPC was used for post-compression, where in the second MPC stage low-LIDT chirped mirrors were used to compensate for linear dispersion in the MPC. Due to the low LIDT of the

[6]This naming is specific to this work

chirped mirrors, the MPC length was tuned closer to $2R$ geometry, leading to a lowered fluence on the mirrors, such that the MPC could be operated for a 0.6 mJ, 50 fs input pulse in a roughly 40 cm length, overcoming the limitation of the mirror LIDT. In the second example, Manz et al. demonstrated energy scaling in a bulk-based MPC setup, tuning the previously reported 10 mJ input pulses to 30 mJ by simply increasing the distance of the MPC mirrors closer to $2R$, which is equivalent to $k \to N$ (Eq. (12)). This minimal adjustment already leads to a significant increase in energy acceptance, without changing the overall size of the setup and while maintaining good beam quality and spatio-spectral homogeneity [48].

In the 4f-MPC approach, due to the decreasing focal length and increasing peak intensity in the focus according to Eq. (15), gases are more easily ionized when $k \to N$, hence decreasing the MPC energy limit imposed by ionization. Thus, it is generally necessary to use a vacuum environment in order to avoid ionization. Instead of gas, solid fused silica (FS) plates are used as the nonlinear medium, which are placed close to the mirrors, where the beam is still large. As an alternative, gases with high ionization thresholds like helium can be used to circumvent the challenge of ionization [40]. Another challenge when tuning the length too close to the stability edge of the cell can is the increasing sensitivity to variations in the cell length. Small deviations of the length can already yield a significant difference in beam size, making the 4f-MPC very sensitive to mechanical perturbations when tuned too close to the stability edge.

Convex-Concave MPC In the above examples, the MPC geometry was only moderately modified by increasing the spacing between the MPC mirrors. However, there also exist energy-scaling approaches that employ substantial modifications to the MPC geometry. One possibility is to move away from symmetric MPC configurations and consider non-symmetric designs, in which either different mirrors are used for the two propagation directions or the propagation lengths within the MPC differ. The former has been realized most notably by convex-concave (cx-cv) MPCs [47]. In cx-cv MPCs, one convex mirror is employed instead of a concave mirror in a standard, symmetric MPC. Similar to optical cavities, this results in MPC eigenmodes where the focal plane resides outside of the cavity, which is often called a virtual focal plane. These modes exhibit only minor variations in size throughout the MPC, while avoiding a focus of the beam. Since the radii of curvature of the mirrors are now different, with R_1 the concave and R_2 the convex mirror, the formula for the re-entrant condition with $C_{1,2} = L/R_{1,2}$ generalizes to

$$C_1 + C_2 - C_1 C_2 = \sin^2(\pi k/N) \tag{21}$$

and the formulas for the beam sizes on the mirrors become

$$w_1^2 = \frac{L\lambda}{\pi}\sqrt{\frac{g_2}{g_1(1-g_1g_2)}} = \frac{L\lambda}{\pi}\frac{\sqrt{\frac{1-C_2}{1-C_1}}}{\sin(\pi k/N)} \tag{22}$$

$$w_2^2 = \frac{L\lambda}{\pi}\sqrt{\frac{g_1}{g_2(1-g_1g_2)}} = \frac{L\lambda}{\pi}\frac{\sqrt{\frac{1-C_1}{1-C_2}}}{\sin(\pi k/N)}\,, \tag{23}$$

with $g_{1,2} = 1 - C_{1,2}$. Here, the MPC configuration parameter is restricted to $0 < k < N/2$, and as in the symmetric MPC case, k defines a re-entrant condition if it is an integer. The length of the cx-cv MPC can be calculated using

$$L = \frac{1}{2}\left(R_1 + R_2 + \sqrt{R_1^2 + R_2^2 + 2R_1R_2\cos(2\pi k/N)}\right)\,. \tag{24}$$

In case of $R_1 = R_2 = -R$, the beam radii are $w_1 = w_2$ and equations (22) and (23) simplify to the beam radii on the mirrors in the symmetric MPC case as in Eq. (14). Similarly, equations (21)

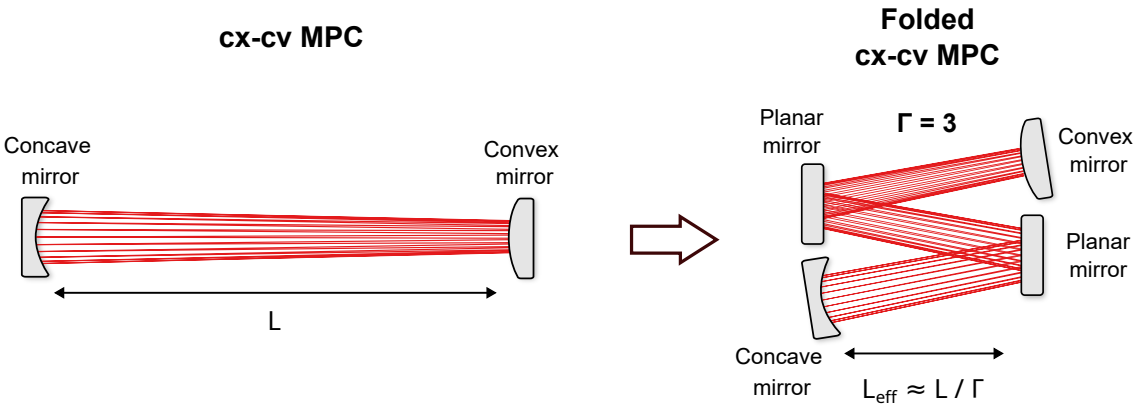


Figure 7: Convex-concave (cx-cv) MPC (left) and a folded convex-concave MPC (right). The folding factor on the folded cx-cv MPC is $\Gamma = 3$, using two additional, planar mirrors. The effective length $L_{\text{eff}} \approx L/\Gamma$ is reduced roughly a factor of three compared to the actual cx-cv MPC length L.

and (24) then both become Eq. (12) in this case. Assuming perfect mode-matching and linear propagation, the maximum fluence occurs at the convex mirror. Without loss of generality, we can assume $R_1 < R_2$, where negative R are associated with concave and positive R with convex mirrors. Thus, the fluence at the convex mirror can be found by $F_2 = 2E/\pi w_2^2$, which yields

$$F_2 = \frac{2E}{L\lambda}\sqrt{\frac{g_2(1-g_1g_2)}{g_1}} = \frac{2E}{L\lambda}\sqrt{\frac{1-C_2}{1-C_1}}\,\sin\left(\pi k/N\right)\,. \tag{25}$$

Avoiding the focus inside the MPC brings along several beneficial consequences for energy-scaling using cx-cv MPCs. One consequence is that the issue of ionization is circumvented for all practical cases by avoiding a focus within the propagation. Furthermore, it allows for folding the MPC by using additional mirrors, reducing the size of the system by the number of foldings Γ. The folding number reduces the MPC length L into an effective length L_{eff}, which roughly relates to the cx-cv MPC length as $L_{\text{eff}} \approx L/\Gamma$, assuming that the spacing of all mirrors is the same. Summarizing this into a formula, the energy-scaling equation for a folded cx-cv MPC for a given threshold fluence F_{th} thus reads

$$E \;\leq\; \frac{\Gamma L_{\text{eff}} F_{\text{th}}\lambda}{2}\sqrt{\frac{g_1}{g_2(1-g_1g_2)}} = \frac{\Gamma L_{\text{eff}} F_{\text{th}}\lambda}{2}\frac{\sqrt{\frac{1-C_1}{1-C_2}}}{\sin(\pi k/N)}\,. \tag{26}$$

Thus, setting a certain constant effective length L_{eff}, the energy acceptance can be increased by increasing the folding number Γ. A similar folding approach is pursued in the Bow-Tie MPC (BT-MPC) and the compact MPC (CMPC), which are discussed later in this chapter. The cx-cv MPC has been demonstrated for nonlinear post-compression in several works [47, 73]. In particular, Hariton et al. proposed folding of the cx-cv MPC as a means for reducing the size of the system, effectively scaling the pulse energy. A major limitation associated with the cx-cv MPC scheme is the reduced nonlinear phase or the B-integral that can be accumulated in one round-trip. If we assume Gaussian beams and define the B-integral per pass as the on-axis accumulated nonlinear phase $B_{\text{pass}} := 2\pi/\lambda \int_0^L n_2 I(z)dz$, one can show that the B-integral in gas-filled (or in general material-filled) MPCs is limited by [31]

$$B_{\text{pass}} = 4\pi^2\frac{n_2 P}{\lambda^2}\frac{k}{N} < 2\pi\frac{k}{N}\,, \tag{27}$$

showing that the maximum B-integral per pass has a limit that corresponds to the Gouy phase $\xi = 2\pi k/N$ per round-trip for a given wavelength λ and nonlinear refractive index n_2. The limit $B \to 2\pi k/N$ is reached when the peak power approaches the critical power of the material

$P \to P_{\mathrm{crit}} \approx \lambda^2/(2\pi n_0 n_2)$. Due to the fact that the cx-cv MPC is typcially operated at values of k close to 1, the amount of spectral broadening that can be achieved in this scheme is significantly lower than in the standard MPC case, where typically $k = N - 1$.

Bow-Tie MPC The cx–cv MPC represents a non-symmetric MPC configuration that generalizes the symmetric MPC by introducing different ROC for the two MPC mirrors, thereby breaking the symmetry of the cavity. Similarly, the bow-tie MPC constitutes a non-symmetric configuration in which two different propagation lengths L_1 and L_2 occur within a single round-trip, while the radii of curvature R of the mirrors are the same. Defining $C_1 = L_1/R$ and $C_2 = L_2/R$, the bow-tie MPC obeys the same equation (21) as the cx-cv MPC. Here, typically one chooses $L_1 < L_2$, and the ratio $L_2/L_1 \approx \Gamma$ defines the folding ratio Γ of the long path L_2. Figure 8 illustrates the bow-tie MPC geometry. The division of the paths in a short "forward" path L_1 and a long "backward" path L_2 leads to a beam caustic where a strong focus occurs in the short path, while the beam is close to collimation in the long path. Furthermore, arranging the beam pattern on the mirrors into a line as shown in Fig. 8(a)(iii) enables folding of the long path using additional mirrors. In the work of Heyl et al. [3], the BT-MPC scheme is demonstrated numerically for high-energy pulses of 125 mJ at 1030 nm, starting from 1 ps pulses and going down to about 50 fs. They use two focusing mirrors (FM) with $R = 2\,\mathrm{m}$, but adjust the long path to $L_2 = 35\,\mathrm{m}$ with $N = 17$ round-trips and $k = (N-1)/2 = 8$. The length L_2 is chosen such that the eigenmode possesses beam sizes on the mirror such that the fluence level is compatible with the LIDT values of available optical coatings [3]. The short path length is then determined by Eq. (21) to $L_1 = R + \delta$, where $\delta = 2\,\mathrm{mm}$. Thus, the effective length of the BT-MPC is equal to $L_{\mathrm{eff}} = L_1$, which is always approximately the ROC of the mirrors R. Since in the short arm L_1, the beam experiences a strong focus, the whole setup needs to be operated in vacuum, where 1 mm thick solid plates of fused silica are used as the nonlinear medium for spectral broadening. Two plates are placed close to the focusing mirrors on each side, where the beam size is still large (Fig. 8(a)). In another study, Heyl et al. numerically show post-compression of a 1 J pulse using a similar geometry as in the 125 mJ case, but with an increased long-arm length of $L_2 = 75\,\mathrm{m}$, matching the fluence level of the previous case. Here they demonstrate post-compression down to about 100 fs. The energy-scaling relation for the BT-MPC can be written as [3]

$$E \leq \frac{R\lambda F_{\mathrm{th}}}{4}(C_2 - 1)\tan\left(\pi k/N\right) \overset{k/N \to 1/2}{\approx} \frac{NR\lambda F_{\mathrm{th}}}{2\pi}(C_2 - 1)\ , \tag{28}$$

where we again set a threshold fluence F_{th} for the mirror coatings. We define the scaling parameter in terms of the folding ratio $\Gamma \approx L_1/L_2 \equiv C_1/C_2$ and can thus write the energy-scaling relation as a function of Γ as

$$E \lesssim \frac{NR\lambda F_{\mathrm{th}}}{2\pi}(\Gamma - 1)\ , \tag{29}$$

where we also used $L_1 \approx R$ and thus $C_1 \approx 1$.

The BT-MPC technique can potentially enable post-compression of high-energy pulses on a table-top sized setup. For the experimental realization, however, the BT-MPC faces some challenges that need to be addressed. The most critical challenge is posed by the narrow margin of the short arm length L_1, which affects the stability of the system. For the 125 mJ case described above, these margins may shrink to just a few millimeters, making stabilization of the cell length necessary. On the other hand, the MPC length lies well within the range that has been demonstrated for solid-state laser oscillators operating at a repetition rate of 8.6 MHz [3, 74]. Increasing the length of the long arm L_2 further toward higher energy acceptance further narrows the acceptable margins of L_1, leading to increased demands on cavity-length stabilization systems. A

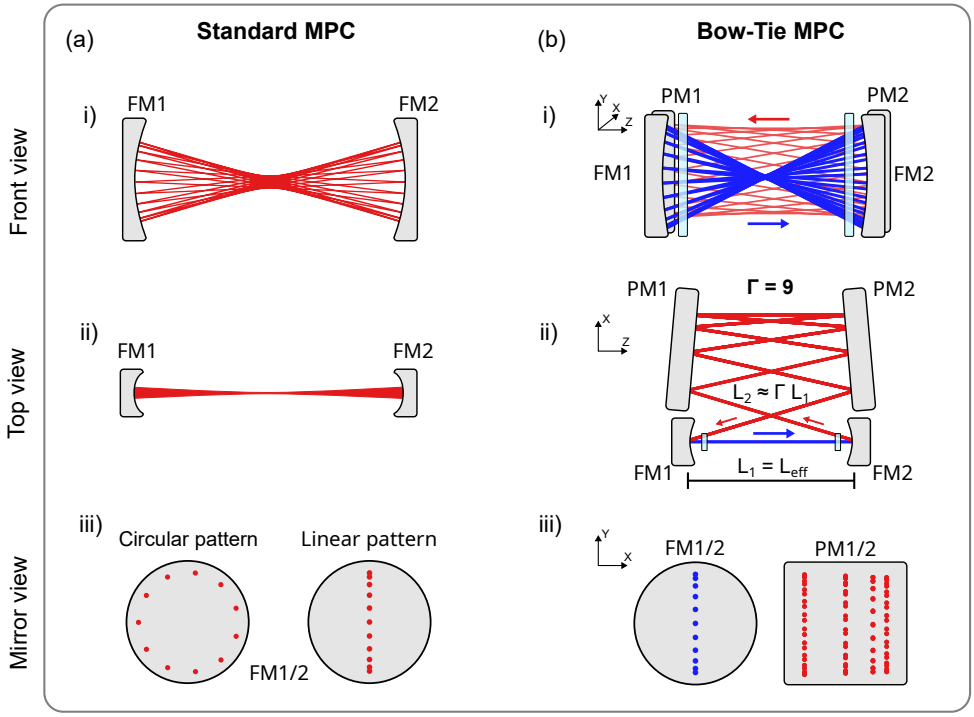


Figure 8: Bow-Tie MPC geometry in comparison to a standard MPC. (a) Standard MPC geometry. (i) Front view on a standard MPC, consisting of two concave focusing mirrors (FM1 and FM2). (ii) Top view on a standard MPC, when a linear pattern in the y-direction is applied. (iii) View on the mirrors and comparison of a circular versus a linear MPC pattern. The BT-MPC scheme uses a linear pattern. (b) Bow-Tie MPC geometry. (i) Front view on the BT-MPC. Here, two additional planar mirrors (PM1 and PM2) are used to fold the beam, which are here placed behind the focusing mirrors. The blue beams indicate the beams propagating in the short arm and the red beams in the long arm. In the short arm, two thin FS plates are placed symmetrically close to FM1 and FM2. (ii) Top view on the BT-MPC. Here, the folding number is $\Gamma = 9$. Thus, the long-arm length is $L_2 \approx \Gamma L_1$, where the effective length is exactly equal to the short-arm length $L_{\text{eff}} = L_1$. (iii) View on one of the FM and one PM, showing the patterns on the mirrors.

minor challenge is the angle of the focusing mirrors in the horizontal ("x") direction, as shown in Fig. 8(b)(ii). This can lead to an accumulation of astigmatism on the beam. On the other hand, the potential beam quality degradation due to astigmatism has been investigated in the work of Beaufort et al., where in a circular arrangement of (curved) MPC mirrors the beam reflects on these curved mirrors with certain angles, potentially leading to astigmatism [75]. However, no astigmatism-related degradation is expected, since due to the re-entrant condition, which implies input-to-output imaging, the output beam is – in the ideal case – the exact image of the input beam. Since the same condition applies to the BT-MPC, beam degradation due to astigmatism is not expected to occur. Thus, astigmatism may not pose a challenge in the context of BT-MPC post-compression.

Compact, folded MPC There is a technique, however, to circumvent the stability and astigmatism challenge, while still maintaining the energy-scalability of the BT-MPC. The compact, folded MPC (CMPC) similarly uses two focusing mirrors with the same ROC and two additional planar folding mirrors similar to the BT-MPC. In contrast to the BT-MPC, the CMPC is a symmetric MPC, where both propagation arms have the same length L. It follows the same equation (12) as a standard MPC and can be viewed as a variation of it, where typically $k < N/2$ is chosen. The CMPC is one of the main parts of this work and will be discussed in detail in the following. Here the relevant publication can be found under reference [1] and is also added to the Appendix A. Similar to the BT-MPC and the cx-cv MPC, the CMPC has an eigenmode caustic such that the beam – in this case in both propagation directions – does not experience a tight focus, but stays

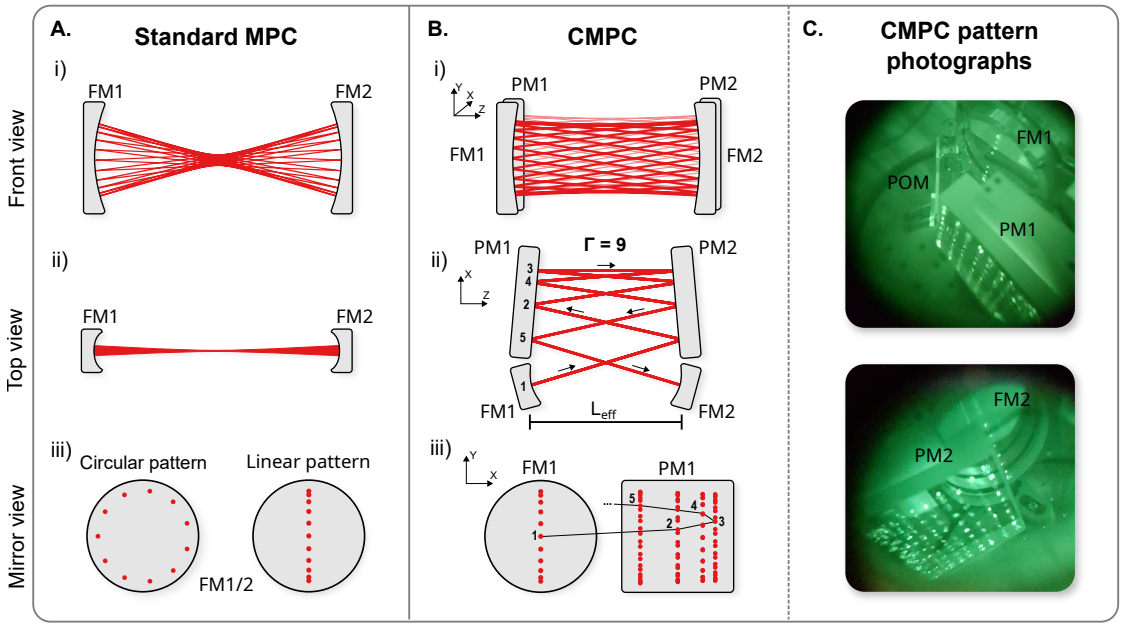


Figure 9: Comparison of a standard MPC and a CMPC. (A) Standard MPC geometry and beam pattern considering a linear beam pattern alignment (FM1/2: focusing mirrors). View of the beam path from the front (i) and from the top (ii). (iii) Resulting patterns for circular/linear alignment on FM1/2. (B) CMPC geometry and beam patterns. (i) Front view with additional planar mirrors (PM1/2) behind FM1/2. (ii) Top view onto the CMPC with beam folding ratio $\Gamma = 9$. The numbers (1-5) indicate the order of reflections of the first pass. (iii) Beam patterns on the mirrors FM1/2 and PM1/2. The black line follows the beam reflections 1-5 on the mirrors. (C) Photographs of experimental beam patterns with $N = 11$, $k = 3$ and $\Gamma = 25$. POM: pick-off mirror. Reprinted with permission from reference [1].

close to collimation over the whole cell length. This property can again be utilized to fold the beam using the additional planar mirrors. Figure 9 illustrates the CMPC geometry and compares it to a standard MPC configuration. The determining parameter for the choice of the ROC R and the length is again the threshold fluence F_{th} set by the mirror coating LIDT. In the CMPC, folding of the beam leads to reflections on the mirrors at any given position of the laser beam in the cell. This means that the relevant quantity to determine the energy acceptance is the fluence at the point of the smallest beam size, i.e. the focal plane. The focal beam size of a symmetric MPC is given by Eq. (13) for a mode-matched, self-repeating beam. The fluence in this position can then be determined using $F_0 = 2E/\pi w_0^2$ and reads

$$F_0 = \frac{4E}{R\lambda} \frac{1}{\sin\left(\pi k/N\right)} \ , \tag{30}$$

where we use Eq. (13). Setting the threshold fluence to $F_{\mathrm{th}} \geq F_0$, we rearrange Eq. (30), which yields the energy acceptance equation for the CMPC

$$E \leq \frac{R\lambda F_{\mathrm{th}}}{4} \sin\left(\pi k/N\right) \ . \tag{31}$$

Similar to the BT-MPC and cx-cv MPC, we can introduce a folding ratio $\Gamma = L/L_{\mathrm{eff}}$ representing the number of how many times the beam is folded. Using Eq. (12), we rewrite the above equation as a function of Γ and L_{eff}, yielding

$$E \leq \frac{\lambda F_{\mathrm{th}} \Gamma L_{\mathrm{eff}}}{4 \tan\left(\pi k/2N\right)} := E_{\mathrm{max}}^{\mathrm{cmpc}} \ . \tag{32}$$

This equation determines the energy acceptance for a certain CMPC geometry with ROC R, folding ratio Γ and the resulting effective length $L_{\mathrm{eff}} = L/\Gamma$. Therefore, by setting a fixed setup length L_{eff},

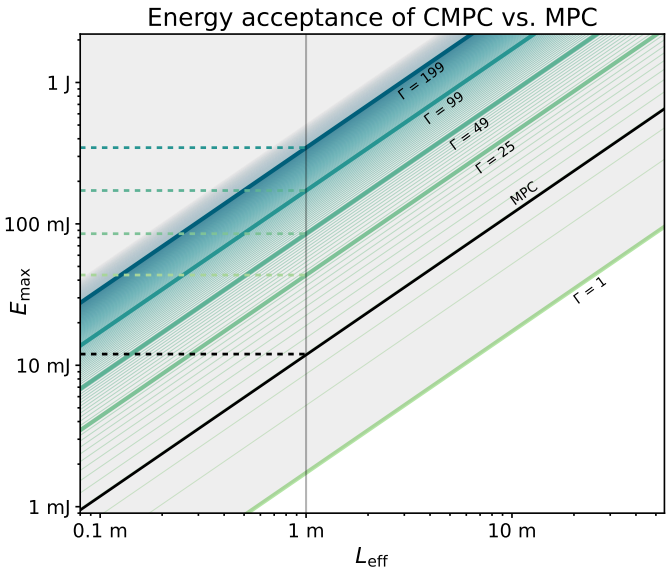


Figure 10: Energy scaling characteristics of a CMPC compared with a standard MPC, showing the calculated pulse-energy acceptance E_{max} as a function of effective length L_{eff}. The solid black line indicates a standard MPC as reported in reference [40] (Eq. (17)). Each colored solid line represents a CMPC with folding ratio Γ (Eq. (32)). The gray line indicates the the effective length of 1 m. The dashed lines show the corresponding pulse energies for selected values of Γ. We set the threshold fluence to $F_{\mathrm{th}} = 0.3\,\mathrm{J/cm^2}$.

the energy acceptance scales proportionally to the folding number. Figure 10 compares the energy acceptance of a standard MPC with a CMPC with folding number Γ for a fixed $F_{\mathrm{th}} = 0.3\,\mathrm{J/cm^2}$. In this plot, we consider $N = 15$ round-trips for both CMPC and MPC with $k = 4$ and $k = 14$, respectively. With these parameters, the scaling factor for $\Gamma = 25$ is about $E^{\mathrm{cmpc}}_{\mathrm{max}}/E^{\mathrm{mpc}}_{\mathrm{max}} \approx 5.8$ and with $\Gamma = 49$ it is 11.4. Thus, for a cell of 1 m length and a threshold fluence of $F_{\mathrm{th}} = 0.3\,\mathrm{J/cm^2}$, a standard MPC energy acceptance would be $E \leq 7.43\,\mathrm{mJ}$ according to equation (17), while for a CMPC it is $E \leq 43.3\,\mathrm{mJ}$ for $\Gamma = 25$ or even $E \leq 85\,\mathrm{mJ}$ for $\Gamma = 49$. This demonstrates that an order-of-magnitude scaling (or down-sizing) can very realistically be achieved with the CMPC technique.

In order to demonstrate this technique, we conduct experiments employing the CMPC post-compression scheme. As shown in Appendix A, we demonstrate post-compression of 1030 nm, 8 mJ, 1.1 ps pulses down to about 50 fs using the CMPC and air as the nonlinear medium in a setup with a length of about 45 cm and a low linear fluence of $0.17\,\mathrm{J/cm^2}$. The setup for the experiment is shown in Fig. 11. We use a commercial 1030 nm, 1.1 ps, 8.4 mJ Yb-based laser as the starting point. After mode-matching (MM) using a curved-mirror telescope, the beam is coupled into the vacuum chamber and then into the CMPC using the first pick-off mirror (POM1), where the pulse energy of 8 mJ is measured. The CMPC consists of two 4 inch focusing mirrors (FM) with $R = 25$ m ROC and two additional planar mirrors (PM) with dimensions $10\,\mathrm{cm} \times 10\,\mathrm{cm}$. The number of round-trips is $N = 11$ with $k = 3$, yielding an MPC length of $L = 8.63$ m. The additional planar mirrors enable folding of $\Gamma = 25$ times, resulting in an effective length of $L_{\mathrm{eff}} = L/\Gamma \approx 34.5$ cm. In this setup, the focusing mirrors are placed behind the planar mirrors, leading to an effective length of about 45 cm (Fig. 11(b)). After POM1, the beam propagates onto PM1 and then PM2. These mirrors are positioned at a small angle in the horizontal (x) direction relative to each other. After 23 reflections, the beam reaches FM2, where it is reflected back onto PM1 and undergoes another 23 reflections on PM1 and PM2, with a slight displacement in the vertical (y) direction. Due to the re-entrant condition of the CMPC, the beam reaches POM1 again after $N = 11$ round-trips in total and is coupled out at a different angle in y-direction than the input beam, enabling separation of input and output using POM2. The total number of reflections amounts to $2N\Gamma = 550$ and the total

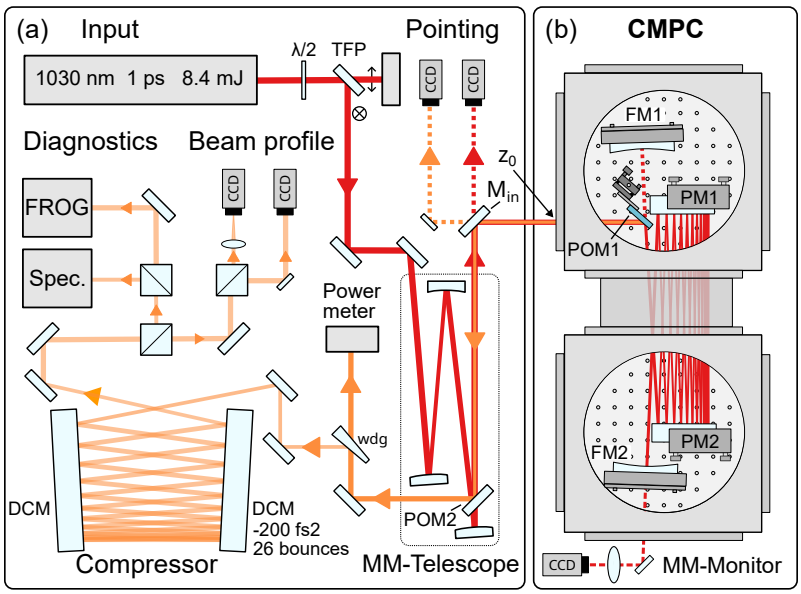


Figure 11: Setup of the CMPC experiment. The CMPC input beam is shown in red and the output beam in orange. FM: focusing mirrors; PM: planar mirrors; POM: pick-off mirrors; M_{in}: input/output mirror; MM: mode-matching optics; DCM: double-chirped mirrors; CCD: cameras; z_0: reference position for stabilization measurements; TFP: thin-film polarizer; wdg: wedge. (A) Input beam path, telescope, and diagnostic components used in the experiment. (B) CMPC configuration integrated with a vacuum chamber. Reprinted with permission from reference [1].

propagation length to approximately 190 m. We nevertheless measure a total throughput of 89% through the CMPC, with an estimated efficiency per reflection of approximately 99.98%, including clipping losses. Thus, even for a large folding number of $\Gamma = 49$, an efficiency of approximately 80% can be expected.

In our first post-compression experiment, we choose air as a nonlinear medium for spectral broadening. Air is composed of about 79% nitrogen (N_2) and 21% oxygen (O_2), both of which exhibit complex nonlinear couplings due to the molecular nature of the gases. This enables larger broadening factors, thereby circumventing the limitations set by the critical power (Eq. (27)) at the expense of the compressibility and temporal contrast of the resulting post-compressed pulses [1, 76]. The main contributions to the nonlinear spectral broadening in molecular gases are the virtually instantaneous electronic response and the delayed rotational mode response on the order of 100 fs [77]. This delayed response is frequently referred to as the Raman-Kerr interaction, and it can lead to an enhancement of the amount of spectral broadening, as we demonstrate in our work [1].

With air as the nonlinear medium, we spectrally broaden the pulses from about 1.1 ps to a compressed duration of 51 fs, while only a small fraction of the pulse is sampled by a wedge (wdg) reflection and compressed using a chirped mirror compressor (DCM). We use 26 reflections with $-200\,\text{fs}^2$ of group-delay dispersion (GDD), amounting to a total GDD of $-5200\,\text{fs}^2$. We keep the pressure at 1 bar due to deformations and misalignments observed at changing pressures in the vacuum chamber. In principle, this can be compensated using electronically actuated mirror mounts, which we did not employ in this setup. The results are shown in Fig. 12. The simulated pulse and spectrum are obtained using a radially symmetric Hankel-transform-based (2+1)D nonlinear pulse propagation model, taking into account SPM as well as the Raman-Kerr interaction in air. The propagation model is described in the publication in Appendix A. Both the measured and simulated pulses agree very well (Fig. 12(a)). They both exhibit a long tail toward the leading edge of the pulse, corresponding to uncompressed red-shifted spectral components, as also visible in the measured and retrieved FROG traces in Figs. 12(c) and (d). Similar pulse features have been observed in other post-compression works employing molecular gases — specifically air — as

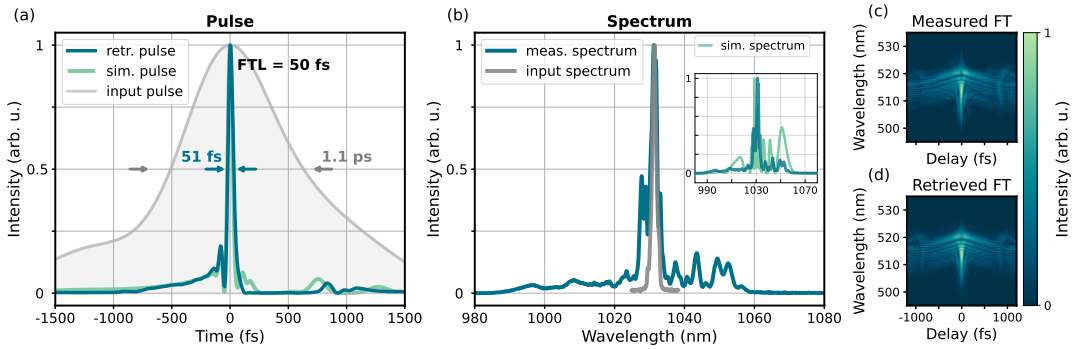


Figure 12: Experimental results of the CMPC experiment in air. (a) Measured input and output pulse shape, along with the simulated pulse using the model described in reference [1]. (b) Measured input and output spectra. The inset shows the measured spectrum along with the simulated one. (c) Measured and retrieved FROG traces. Reprinted with permission from reference [1].

the nonlinear medium [76]. Furthermore, a small side pulse is observed at the trailing edge, about 700 fs away from the center of the pulse. Since this strong nonlinear interaction can also lead to spatio-temporal couplings (STC) and hence to spatio-spectral inhomogeneities, we further conduct STC measurements on the spatio-spectral properties of the beam and pulse using the technique described in reference [78]. The STC is measured using a quantity $V(x, y)$ that calculates the spectral overlap of the spectrum $I(\omega, x, y)$ with the spectrum measured at the beam center $I(\omega, 0, 0)$ using the equation [29]

$$V(x,y) = \frac{\left[\int I_0(\omega)\, I(\omega,x,y)\,\mathrm{d}\omega\right]^2}{\int I_0^2(\omega)\,\mathrm{d}\omega \int I^2(\omega,x,y)\,\mathrm{d}\omega} \,. \tag{33}$$

The spatial average value V_{avg} is the calculated as the normalized integral over the spatial dimensions weighted with the fluence-profile of the beam

$$V_{\mathrm{avg}} = \frac{\int_{-w}^{w} V(x,y)\, F(x,y)\mathrm{d}x\mathrm{d}y}{\int_{-w}^{w} F(x,y)\mathrm{d}x\mathrm{d}y} \,. \tag{34}$$

With the above definitions, the measured spatio-spectral homogeneity (SSH) of the beam after spectral broadening in air amounts to $V_{\mathrm{avg}} = 90.6\%$. For comparison, the performance of a typical MPC in a monoatomic gas can typically exceed 95%, as seen in Fig. 13(b) and in references [32, 68].

A legitimate concern regarding the CMPC is that, for this number of reflections and propagation distance, the beam stability can be significantly affected. However, since an MPC in a re-entrant condition is an input-to-output imaging system, any pointing or translation variation in the input translates one-to-one at the output, rendering an MPC inherently stable.

Other sources of beam position or pointing fluctuations might come from mechanical instability or gas turbulence in the beam path. In order to verify beam stability, we perform measurements on the beam position stability (near field). Over a total recording time of 5 minutes, the output beam position stability increases by only 5% compared to the input stability. Furthermore, the FTL of the spectrum recorded over five minutes fluctuates by only 0.65%. Both measurements show that the CMPC can be operated with high stability, despite the large number of reflections and the propagation distance. For more details, refer to Fig. 7 in Appendix A.

In the second experiment, we measured spectral broadening using krypton as the nonlinear medium and investigated the SSH in terms of $V(x, y)$ and V_{avg} of the output beams. We measured the SSH for pulses at 1 bar of krypton with four pulse energy values, approaching the limit given by equation (27). Figure 13 shows the results of these measurements. In Fig. 13(a), the development

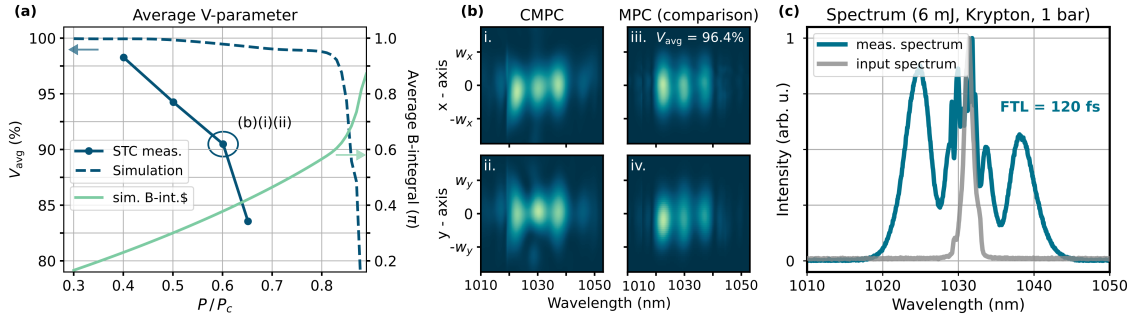


Figure 13: Results of the STC measurements. (a) Measured averaged V-parameter calculated according to Eq. (34) as a function of P/P_{crit}. The simulated V-parameter is indicated as the dashed line. The simulated average B-integral per pass is indicated in green on the right axis. (b) Spatio-spectral distribution of the CMPC output spectrum using krypton as the nonlinear gas at $P = 0.65P_{\mathrm{crit}}$, compared to a standard MPC using the same laser system as input. The standard MPC is the system described in reference [51]. (c) Input- and broadened output spectra measured in a spectrometer at $P = 0.65P_{\mathrm{crit}}$. Reprinted and modified with permission from [1]

of an averaged V-parameter is shown as a function of the peak power P divided by the critical power $P_{\mathrm{crit}} \approx 7\,\mathrm{GW}$ in 1 bar of krypton. As the calculated peak power P is increased from $0.4P_{\mathrm{crit}}$ to $0.6P_{\mathrm{crit}}$, we observe a steady decline of V_{avg} from about 98% to 91%. At $P = 0.65P_{\mathrm{crit}}$, the decline becomes more pronounced and at $P = 0.7P_{\mathrm{crit}}$ (not shown in the plot) the beam collapsed in the experiment. This behaviour is in accordance with standard gas-filled MPCs, where the peak power is typically kept below half the critical power for the best homogeneity performance [31]. We compare the measured SSH data from the STC measurements with those of a standard MPC in Fig. 13(b) under a similar spectral broadening using the same input pulses. Thus, in both MPCs the same amount of B-integral has been accumulated. The standard MPC configuration is $N = 17$, $k = 16$, $R = 1\,\mathrm{m}$ and the corresponding work can be found in reference [51]. This observation can be explained using 27 in combination with the formula for the temporal compression ratio K in gas-filled MPCs [31]

$$K \approx 8\pi \frac{n_2 P k}{\lambda^2} \approx \frac{B}{\pi}\ , \tag{35}$$

where $B = N_{\mathrm{pass}} \cdot B_{\mathrm{pass}}$ is the total B-integral accumulated over N_{pass} passes through the MPC. If we define the peak power $P = \alpha P_{\mathrm{crit}}$, where $\alpha = P/P_{\mathrm{crit}}$ and substitute the formula of the critical power $P_{\mathrm{crit}} = \frac{\lambda^2}{2\pi n_0 n_2}$ with $n_0 \approx 1$ into 27, the spectral broadening formula for $N_{\mathrm{pass}} = 2N$ passes is simply

$$K \approx \frac{B}{\pi} \approx 4\alpha k\ . \tag{36}$$

In the CMPC, we start with a 1.1 ps pulse with an FTL of about 1 ps and end up with a measured FTL of 135 fs at $\alpha = 0.6$ (Fig. 13(a)); the compression ratio amounts to about $K_{\mathrm{meas}} \approx 7.4$. Given the CMPC configuration at $N = 11$, $k = 3$, we can see that for $\alpha = 0.6$, Eq. (36) estimates a value of $K_{\mathrm{calc}} \approx 7.2$, which is in good agreement with the measured value. On the other hand, in the MPC case (Fig. 13(b)(iii) and (iv)) operating at $N = 17$, $k = 16$, the same broadening factor can be achieved with a much lower $\alpha \approx 0.11$, resulting in a significantly higher homogeneity. These measurements demonstrate how a standard MPC and the CMPC differ and the limitations that can arise in certain energy-scaling techniques. This illustrates that trade-offs always exist when MPC geometries or even the pulse or eigenmode structure is modified.

2.6 Summary and Outlook

In this chapter, various concepts for energy scaling in MPC-based post-compression systems were presented. These concepts can be broadly classified into three categories: simple size scaling of MPCs, non-geometric approaches that are independent of the MPC geometry, and geometric approaches in which the MPC geometry itself is modified. The non-geometric approaches include the Laguerre–Gauss mode technique and the divided-pulse scaling technique. The geometric approaches include the 4f-MPC, the convex–concave MPC (cx-cv MPC), the Bow-Tie MPC, and the CMPC. Each concept presents distinct advantages and limitations, which determine its suitability for different application scenarios. For each approach, an energy-scaling relation has been derived, allowing the energy acceptance to be calculated for a fixed system length. Using these scaling relations (Eqs. (17), (19), (20), (26), (29), and 32), the potential energy acceptance of each technique is evaluated for different effective lengths of the system, as shown in Fig. 14. A meaningful comparison of the various concepts requires several assumptions about the achievable scaling parameters. In particular, realistic ranges must be established for parameters such as the folding ratio Γ of the cx-cv MPC and the CMPC, as these ultimately determine the feasibility of implementing a practical post-compression system.

It should be emphasized that the maximum values assumed for the scaling parameters are not intended to represent fundamental limits. Rather, they reflect estimates of what may be realistically achievable with current technology and practical implementation constraints. The comparison presented in this chapter should therefore be understood as an estimate of the relative scaling potential of the different concepts rather than a definitive prediction of their ultimate performance and limitations.

Besides the effective length, the other common parameters in each system are the threshold fluence determined by the LIDT of the mirror coatings, which we set to $F_{\mathrm{th}} = 0.3\,\mathrm{J/cm^2}$, and the number of round-trips, set to $N = 15$. Fig. 14(b) shows a comparison of the energy acceptance of each technique at a fixed effective length $L_{\mathrm{eff}} = 1\,\mathrm{m}$.

Among the geometric scaling techniques, the BT-MPC exhibits comparatively strong energy-scaling capability. As discussed in the previous section, the BT-MPC is typically operated at values of $k \approx (N-1)/2$ (see Fig. 6), which enables a moderately high B-integral per pass when gas is used as the nonlinear medium. However, the BT-MPC also presents several challenges. First, its implementation is comparatively complex, requiring the alignment of a complicated beam pattern. Second, operation close to the stability edge makes the system particularly sensitive to small variations in the MPC length and other alignment parameters. Consequently, maintaining stable long-term operation can be demanding, especially in high-energy implementations. Third, the strong focusing geometry requires operation in a vacuum environment due to high intensities occurring in the short arm of the BT-MPC, leading to ionization of the gas. Instead of gas, a thin solid plate placed close to the mirrors, where the beam is still large, can be used [3]. Fourth, the BT-MPC geometry necessarily results in the beam being reflected at specific angles on the curved mirrors, which may distort the beam profile. For the BT-MPC, the scaling parameter is the folding ratio $\Gamma \approx L_1/L_2$, which we set to $\Gamma = 17$ in Fig. 14 as reported in reference [3]. This yields a maximum energy acceptance of 118 mJ according to Eq. (29).

As an alternative, the CMPC constitutes a simpler approach than the BT-MPC, reducing the sensitivity to cavity length significantly while eliminating reflections at angles on curved mirrors as well as strong focal beam caustics. It can therefore be operated with gases, as demonstrated in this work, and potentially with solids. However, as shown experimentally (Appendix A), the CMPC faces certain limitations on the total spectral broadening, which restricts the achievable B-integral per pass to approximately one-third to one-quarter of that in a standard MPC [1]. Conversely, even with a large degree of folding, resulting in up to 550 reflections in this work, we

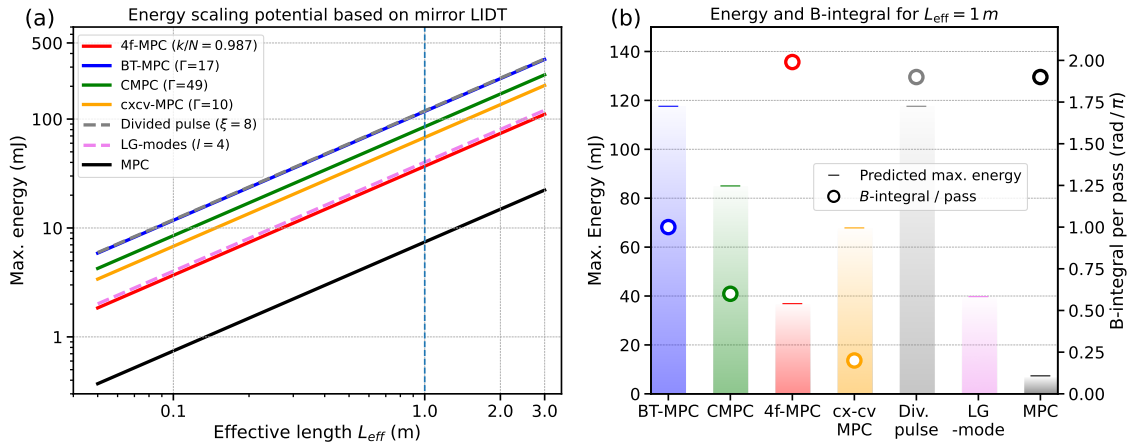


Figure 14: Estimated energy scaling potential of different MPC-based post-compression techniques. (a) Energy scaling potential for the different scaling techniques as a function of the effective length L_{eff}. Here, the maximum estimated value for the energy acceptance for a threshold fluence of $F_{\text{th}} = 0.3\,\text{J/cm}^2$ is assumed. (b) Bar chart of the estimated energy scaling potential of the different techniques, along with the maximum B-integral per pass (circles).

demonstrated a high throughput of 89%, enabling even greater degrees of folding and thus higher energy scalability. In Fig. 14, we therefore choose $\Gamma = 49$, as this still yields a throughput of close to 80%, corresponding to approximately 85 mJ in a 1 m long cell according to Eq. (32).

The 4f-MPC constitutes a very practical technique for energy scaling. The energy acceptance follows the same equation as the standard MPC (Eq. (17)), but the scaling parameter now is the k/N ratio, which translates into directly changing the L/R ratio, according to Eq. (12). This typically requires a geometry where, instead of using only two MPC mirrors, a single mirror is used for each pass, allowing free adjustment of the distance without altering the number of passes of the MPC. However, similarly to the BT-MPC, **it** creates a strong focus in the center and thus needs to be operated in a vacuum environment using solid plates as the nonlinear medium placed close to the MPC mirrors [48]. Demonstrations have shown that the 4f-MPC can be operated at $k/N = 0.96$ [48]. In Fig. 14, we assume that stable operation can still be achieved at values $k/N = 0.98$, which corresponds to $L/R = 0.999$. For a cell with $R = 0.5\,\text{m}$, this implies that the distance between the mirrors is tuned 1 mm away from the stability edge, which is a realistic value for a passively stable MPC [3]. According to Eq. (17), in this roughly 1 m long cell, the maximum achievable pulse energy could reach 37 mJ.

One of the simplest, yet B-integral-restrictive approaches is the cx-cv MPC. Here, one concave mirror of a standard MPC is replaced by a convex mirror, and the beam can be folded using an additional mirror per fold. Thus, while simple in design, it requires many more optical elements than the CMPC or BT-MPC. Furthermore, the B-integral per pass is the lowest among all geometric approaches, at approximately $2\pi/N$ per pass. Although the simplicity of the cx-cv MPC makes it attractive for energy-scaling of systems that do not require large compression factors, its lower B-integral acceptance should be considered. In Fig. 14, we choose a folding ratio of $\Gamma = 10$, which, according to the scheme described in the previous section, would require nine additional folding mirrors. With this value, the maximum achievable energy acceptance is 68 mJ. It should be noted that the value of Γ can be realized with fewer optical elements and can potentially be even higher.

Among the non-geometric approaches, we discuss the pulse-division and the Laguerre-Gauss-mode approaches. Both approaches are completely agnostic to the MPC geometry and can be placed in front of any MPC type. The advantage of pulse-division is the unchanged mode size and properties of the beam. For the pulse-division MPC, division into $\xi = 8$ replicas has been demonstrated with a transmission through the setup of 95% [45]. Furthermore, we demonstrate

a folding factor of $\Gamma = 25$ in the CMPC with 89% transmission, which, according to the CMPC energy scaling equation (32), has an energy acceptance of about 43 mJ. This implies an interesting pathway for further MPC up-scaling: by placing a pulse-division and recombination unit that splits into $\xi = 8$ replicas in front of a CMPC with $\Gamma = 25$, an energy acceptance of $E \leq 8{\times}43\,\mathrm{mJ} = 344\,\mathrm{mJ}$ can potentially be achieved in an $L_{\mathrm{eff}} = 1\,\mathrm{m}$ long setup, representing an almost 50-fold increase in energy scaling capability compared to a standard MPC of 1 m with $E \leq 7.3\,\mathrm{mJ}$ (Fig. 14), while still yielding a high total transmission exceeding 80%. When both methods are scaled toward $\Gamma = 49$ for the CMPC and $\xi = 16$ for the divided-pulse MPC, energy scaling beyond 1 J in a 1 m cell could potentially be accomplished. In principle, this can also work with the LG-mode approach, but its disadvantage compared to the divided-pulse technique is the enlargement of the beam sizes, potentially requiring larger optics. The basic principle, however, is clear: geometric and non-geometric approaches can easily be combined to yield an MPC with unprecedented energy scalability. It can potentially provide a way to reduce the MPC size requirements for 100 mJ-level or even Joule-level pulses from a large experimental hall to a table-top size setup, fitting into a standard laboratory.

3 Post-Compression of Nanosecond Pulses in Multi-Pass Cells

This chapter develops and demonstrates a method to post-compress nanosecond pulses from Q-switched lasers to the picosecond regime using SPM in a nanosecond multi-pass cell (nMPC). After introducing the nMPC concept and its key design ideas (geometry, dispersion, and damage considerations, as well as coating-based spectral filtering), the chapter discusses the main limitations for nanosecond post-compression. Finally, a proof-of-principle experiment is presented, demonstrating post-compression from 0.5 ns to 24 ps. This chapter largely follows the work presented in reference [2], which is included in Appendix B as one of the main publications of this work.

3.1 Introduction

The timescale of optical pulses considered in ultrafast optics typically resides in the range from picoseconds down to femto- or even attoseconds [17, 79, 80]. Within this range, many applications utilize these timescales to resolve dynamics in matter [17], accelerate electrons in compact laser-plasma accelerators (LPA) [81, 82], generate high-harmonics and attosecond sources [25, 83], or simply wield or cut material with extreme precision [84]. The number of industrial and scientific applications is vast and can hardly be listed in its entirety here, underlining their importance in laser-based technology. These lasers are generally produced using mode-locking technology [85] and further amplified via chirped-pulse amplification (CPA) [86]. Two important gain materials for generating ultrafast pulses are Titanium-Sapphire (Ti:Sa) and Yb-doped crystals. While Ti:Sa laser systems are known for their large gain bandwidths, producing laser pulses down to a few femtoseconds with large pulse energies, they suffer from a large quantum defect, resulting in significant heat generation and high cooling requirements, which limit the average power of these systems to a few tens of watts [87]. On the other hand, Yb-based gain media typically produce longer pulses in the picosecond to hundreds-of-femtoseconds range but offer high average power scalability [88].

On the other end of the temporal scale of pulsed lasers, nanosecond laser pulses represent a well-established regime in laser science and technology. They are commonly generated by Q-switching, a technique in which energy is first stored in the gain medium and then released in a short, intense pulse by rapidly increasing the cavity quality factor [89, 90]. Compared to ultrafast systems, Q-switched nanosecond lasers typically deliver relatively high pulse energies at lower repetition rates, making them highly suitable for applications such as material processing, light detection and ranging (LiDAR), and various medical applications [91–94]. A key feature of Q-switched lasers is their overall simplicity: they can be built in a compact, cost-efficient, and robust manner, whereas mode-locked lasers are more complex, larger in footprint, and more expensive. Q-switched lasers can deliver high pulse energies in the millijoule to joule range and average powers up to the kilowatt level [95]. However, a major gap between mode-locked and Q-switched laser technology remains the pulse duration. Their orders-of-magnitude longer pulses limit the achievable peak powers, especially in the millijoule range. Overcoming this gap by generating ultrashort pulses in the pico- to femtosecond range using Q-switched lasers can lead to a substantial simplification of ultrafast laser systems compared to mode-locked systems. This is particularly attractive for applications requiring compactness, cost-efficiency, or robustness. Therefore, realizing ultrashort pulse durations with Q-switched lasers requires the use of additional pulse-shortening and nonlinear compression strategies.

In recent decades, many different post-compression techniques have been developed to shorten the duration of laser pulses after their generation. Most notably, self-phase-modulation (SPM) is one of the major nonlinear effects for generating broader bandwidths and providing a platform for post-compression of laser pulses [31]. SPM interaction can be achieved in various ways, using

direct free-space propagation in gases or bulk material [96], waveguide technology in bulk or gases [23, 97], or quasi-waveguide schemes, most notably multi-pass cells (MPCs) [31]. Recently, MPC technology has been established as a versatile and reliable tool for post-compressing mode-locked laser systems. Applied to Yb-based lasers, MPC post-compression enables both peak power and average power scaling, producing pulse durations comparable to those of Ti:Sa lasers while simultaneously overcoming the average power limitations of Ti:Sa systems [33]. Today, lasers in the tens-of-fs range with mJ-level pulse energies and kW-level average powers can be produced from post-compressed Yb-based laser systems [32].

As a successful approach for mode-locked lasers, a technology based on spectral broadening via SPM would seem to be an obvious path for overcoming the pulse duration gap between nanosecond Q-switched lasers and pico- to femtosecond mode-locked lasers. However, there are various challenges and limitations that arise when using nanosecond pulses, and in particular Q-switched lasers, in combination with SPM spectral broadening methods. Apart from SPM, a common approach is the use of stimulated Brillouin scattering (SBS) for post-compression of nanosecond laser pulses [98, 99], which can be achieved in gases, liquids, and solids with high efficiency, typically exceeding 80% [100–103]. The energy range of operation of such systems lies in the hundreds of mJ or even Joule level, where the achievable pulse durations are limited by the phonon lifetime of the material, typically yielding pulses at the level of 100 ps or higher [99]. Although a very established method, further compression to the few-ps level requires different techniques. Using SPM as the underlying nonlinear process, nanosecond pulses have been post-compressed in the past using solid-core optical fibers [104–106]. However, these efforts were limited mainly by competing nonlinear effects, such as stimulated Raman scattering (SRS), as well as by energy scalability. SRS is an inelastic, stimulated scattering process in which photons are downshifted in energy by an amount determined by the vibrational modes of the medium [27]. In fused silica, the Stokes wave is shifted to a lower frequency by about 13.6 THz [107]. Similar to SBS, SRS becomes significant only above a certain intensity threshold. Because of the relatively large frequency shift, dispersion between the pump pulse and the Stokes pulse can affect the SRS dynamics [27]. SRS has long been a major limiting factor for spectral broadening in fibers [108]. Although spectral broadening factors as high as 80 have been demonstrated in fibers [105, 106], SRS restricts the achievable pulse energies to well below 1 µJ.

In order to address the challenge of scaling nanosecond pulse post-compression down to much shorter pulses and bridge the gap between mode-locked and Q-switched lasers, we propose a method based on SPM and MPCs. As a quasi-waveguide technique, MPCs enable tuning of phase and amplitude after each pass by using for instance suitable mirror coatings. In contrast to the SHG-MPC method described in Chapter 4, the nanosecond MPC focuses on amplitude tunability instead of phase tunability. As discussed later in this chapter, different competing nonlinear effects can be addressed using specific mirror coatings to filter parasitic effects that arise alongside the spectral broadening process. In this chapter, we develop the concept of the nMPC. In the experimental part, we demonstrate post-compression of 0.5 ns pulses down to 24 ps as the first demonstration of mJ-level post-compression of nanosecond pulses down to the picosecond regime. We further discuss approaches to enhance spectral broadening by compressing the pulse duration from the nanosecond regime to the few-picosecond regime at mJ-level pulse energies. Numerical simulations are presented to demonstrate that post-compression factors exceeding 100 are achievable under suitable conditions, even when the dominant parasitic nonlinear effects are included in the model.

3.2 Concept

The nMPC shares many similarities with standard post-compression MPCs used for post-compression of picosecond or femtosecond pulses [31]. However, due to the completely different pulse duration

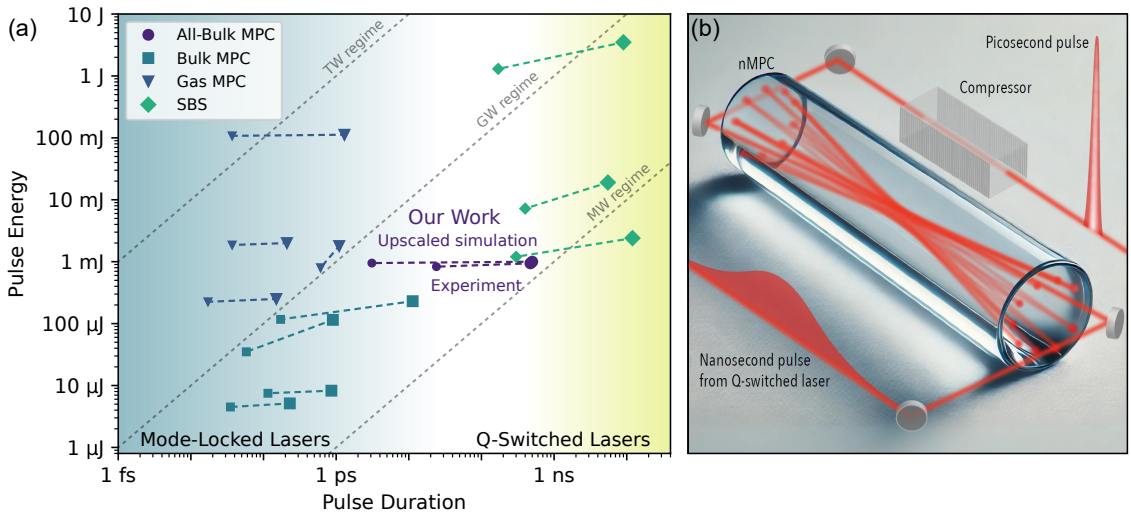


Figure 15: Post-compression methods covering the parameter space from nanoseconds to femtoseconds. (a) Parameter overview of representative laser pulse post-compression studies. Q-switched laser systems (green) have been post-compressed via SBS (diamonds), while gas-filled (triangles) or bulk (squares) MPCs are widely used for compressing mode-locked laser systems (blue) [29, 41, 98, 99, 109–115]. Our work (purple) bridges the gap between these two laser regimes via post-compression of Q-switched lasers in a Herriott-type bulk-rod MPC. The experimental output data point takes into account the output pulse duration measured at reduced energy, scaled to the full energy transmitted through the MPC. (b) Illustration of the proposed nanosecond MPC concept. Reprinted with permission from reference [2].

regime, certain modifications are necessary to allow for efficient spectral broadening of nanosecond pulses produced by Q-switched lasers. First of all, the comparatively low peak power of mJ-level nanosecond pulses needs to be addressed. The overall lower peak power in the range of a few megawatts (MW) makes it difficult to use a gas medium due to the low nonlinearity at pressures close to atmospheric pressure. Typical gas-based MPCs are used for pulses in the range of gigawatts (GW) [31]. A suitable substitute for gases is solid media, providing order-of-magnitude larger nonlinear responses than gases. Solid plates are routinely used for spectral broadening of picosecond to femtosecond pulses in the 10s of MW regime [31]. The lowest peak power so far used in solid-plate MPCs for post-compression has been 6.5 MW [29]. In comparison, a pulse with a duration of 0.5 ns and an energy of 1 mJ (our experimental values) only has about 2 MW of peak power, thus necessitating solid media and a longer interaction length. In the nMPC, the long interaction length is realized by much longer bulk material and many more passes through the nMPC. However, passing the MPC many times can create significant losses due to reflection on optical interfaces between air and the bulk material. In the nMPC concept, this is circumvented by using a full-bulk, monolithic setup, as shown in Fig. 15(b).

The nMPC makes use of the following key features that enable efficient spectral broadening of nanosecond pulses with large broadening factors. First, by using high-reflectivity- (HR-) coated curved surfaces at both ends of the bulk material, the beam propagation can take place without traversing any optical interfaces. This keeps the losses per pass at a minimum, mostly limited only by very small HR-coating losses. Second, although picosecond- or femtosecond-duration input pulses would be strongly affected by the high dispersion in the bulk material, nanosecond pulses are much less sensitive to dispersion due to their narrow spectral bandwidth. Third, the laser-induced damage threshold (LIDT) for nanosecond pulses increases dramatically compared to picosecond- or femtosecond-level pulses. While the LIDT for ps- to fs-level pulses ranges around $1\,\mathrm{J/cm^2}$ or lower, different damage mechanisms increase the LIDT for ns pulses to $10\,\mathrm{J/cm^2}$ or even higher [116, 117]. This enables MPC configurations using much smaller beams, overcoming space constraints due to tight packing of reflections on the mirrors and thus increasing the interaction

length. Fourth, the optical coatings function as spectral filters at each round trip, suppressing competing nonlinear optical processes—such as Raman scattering and four-wave mixing—which would otherwise strongly limit pulse compressibility (see Section 3.3 for more details).

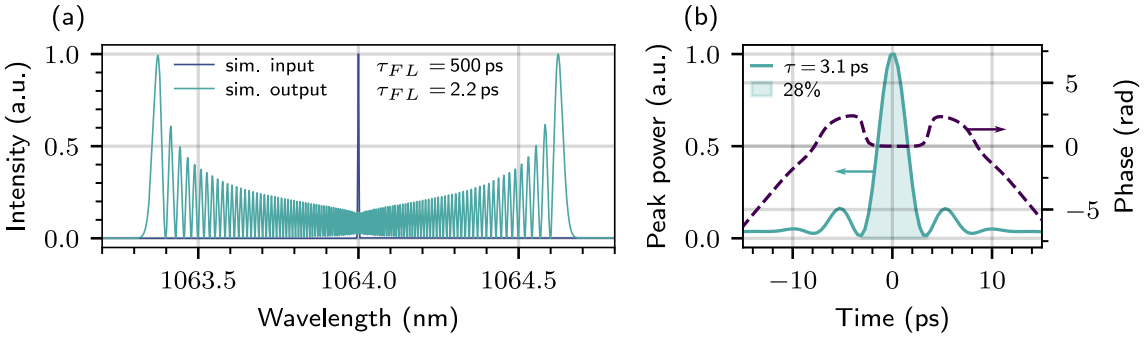


Figure 16: Simulated post-compression using the nMPC concept. (a) Input and output spectra demonstrating a high compression rate in the proposed full-bulk nMPC. (b) Corresponding compressed pulse, where the phase is compensated using GDD only. Reprinted with permission from reference [2].

Based on this concept, simulations are carried out to demonstrate the potential of the nMPC using an input pulse energy of 1 mJ, a Gaussian laser pulse with a duration of 0.5 ns, and 150 round-trips (N=150, k=91). The simulation is performed using a symmetric split-step Fourier algorithm to solve the Unidirectional Pulse Propagation Equation in (2+1) dimensions, assuming radial symmetry [2, 69]. We consider an FS glass block with curved surfaces of $R = 10$ cm, a length $L = 25.43$ cm, and an MPC configuration parameter $k = 91$ [31]. The input and output coupling can be achieved through a small uncoated – or alternatively an anti-reflective (AR) coated – spot on one cell surface. Using a diameter of 3 inches (7.62 cm) for the curved surfaces, the necessary 150 reflections can fit onto the area of the surfaces. As an alternative route, a denser round-trip pattern can be employed, overcoming geometric limitations of a simple circular pattern [118]. Figure 16 shows the results of the simulation. The spectral bandwidth of the input $\Delta\lambda_{10\mathrm{dB}} = 6$ pm increases by a factor of 220 to $\Delta\lambda_{10\mathrm{dB}} = 1.32$ nm, supporting a pulse duration of 2.2 ps (Fig. 16(a)). Following second-order phase compensation (103 ps^2), a compressed pulse with a duration of 3.1 ps is obtained, showing very good compressibility. This results in a temporal compression by a factor of 161 and a final peak power of 82 MW (Fig. 16(b)). We note that large compression factors typically lead to the emergence of pedestals and limit the energy content in the main pulse, as shown in Fig. 16(b). However, strategies exist to mitigate this effect and optimize the pulse contrast; see Section 3.3 for more details.

Due to the inherent property of input-to-output beam imaging in MPCs [31], fluctuations in the input beam pointing are not amplified within the nMPC, even for a large number of round trips (here $N = 150$) and the resulting long propagation distances. MPCs have been demonstrated to exhibit high stability even with many reflections and long propagation distances [1]. Additionally, the all-bulk geometry mitigates the effects of ambient airflow and mechanical instability of the optical mounts, thereby further increasing the system's stability.

In the all-bulk monolithic scheme, the main sources of loss are the coated end facets of the bulk material and the absorption in the medium. With modern manufacturing methods, these losses can be kept very low, allowing the realization of such an MPC with an efficiency >90%. Considering commercially available transmission gratings with efficiencies of >98%, the total transmission of the setup can be of the order of 90%. Alternatively, slightly less efficient but very compact compression can be achieved using a dispersive volume Bragg grating (CVBG). The efficiency within the required parameter regime of the CVBG is >90 %. This enables a total post-compression efficiency >80 % while maintaining a very small footprint.

The nMPC can potentially be further scaled to higher pulse energies and longer pulses, subject

to limitations imposed mainly by SBS and the critical power of the material. While SBS imposes limits on the pulse duration and intensity, critical self-focusing can lead to beam collapse when the critical power is exceeded. In the current configuration, the input pulse energy can be scaled up to 10 mJ when using a 4 ns pulse, where the peak power is roughly half the critical power of fused silica ($P_{\mathrm{crit,FS}} \approx 5\,\mathrm{MW}$) and the SBS limit has not yet been exceeded (see Fig. 19 in Section 3.3).

The nMPC concept provides a promising and unprecedented path towards ultrafast, ps-level pulses from compact, cost-efficient, and robust Q-switched laser systems. However, apart from the advantages of nanosecond laser pulses in the context of spectral broadening, the long pulse durations pose many challenges for post-compression that must be addressed before the required high broadening factor can be achieved. In the following section, these challenges are addressed and potential solutions are presented.

3.3 Challenges of post-compression of nanosecond pulses

In the context of a potential realization of an nMPC, five phenomena that pose challenges and limitations can be identified, each of which needs to be addressed. These phenomena are the temporal quality of post-compressed pulses, longitudinal mode beating of Q-switched lasers [119], stimulated Brillouin scattering (SBS) [27, 120, 121], stimulated Raman scattering (SRS) [27], and degenerate quasi-phase-matched four-wave-mixing (QPM-FWM) [122].

3.3.1 Temporal quality of post-compressed Q-switched pulses

Post-compression via SPM leads to a degradation of the pulse contrast and a reduction in the resulting peak power of the post-compressed pulse. This is a known phenomenon for single-stage MPC post-compression schemes [57]. The same effect naturally occurs in the nMPC, and it becomes more severe as the broadening factor increases. In the simulations in Fig. 16(b), this effect leads to a severely reduced energy content in the main peak of 28% for a post-compression factor of about 161. Here, Gaussian pulses are employed as input to the nMPC. In this case, the broadened spectrum exhibits the typical modulated shape shown in Fig. 16, which reduces the pulse contrast for large broadening factors. One approach to address this issue is to move away from Gaussian pulses and employ different pulse shapes. Pulse shaping techniques are widely employed across different timescales. In the pico- or femtosecond regime, pulse shaping is commonly realized using a spatial mask placed in the Fourier plane [123–125]. In contrast, in the nanosecond regime, the same goal can be achieved with direct temporal pulse-shaping technologies, which are readily available for sub-nanosecond operation with picosecond resolution [126, 127]. Figure 17 shows the result

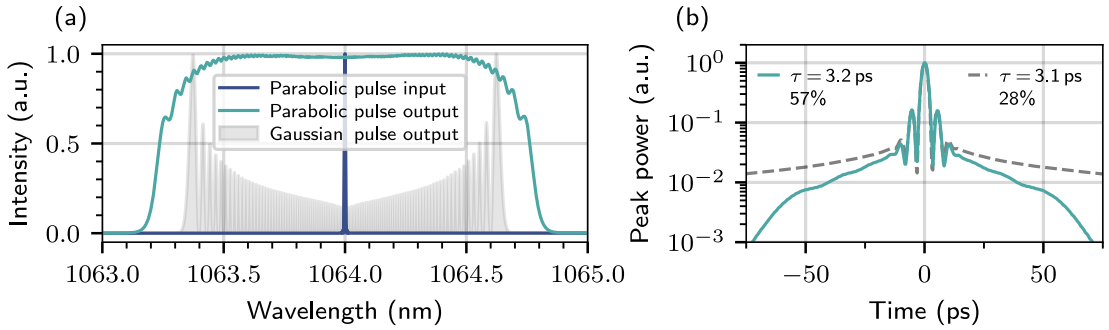


Figure 17: Simulated nMPC post-compression using a parabolic temporal pulse shape. (a) Spectral broadening of a temporally parabolic shaped pulse in comparison to a Gaussian pulse (identical to the data displayed in Fig. 16). (b) Corresponding GDD-compensated pulses, along with the energy fraction contained in the main pulse. Reprinted with permission from reference [2].

of simulations using parabolic pulses instead of Gaussian pulses as the input. The broadened

spectrum exhibits much fewer modulations and resembles a flat-top spectral shape as shown in Fig. 17. After removing the GDD, the pulse contrast improves significantly, increasing from 28% to 57%. The pulse contrast depends on the amount of B-integral accumulated per pass through the nMPC; accordingly, a lower B-integral yields a larger pulse contrast. In the simulations, the average B-integral per pass is around $B_{\text{pass}} = 0.2\pi$, where the configuration was chosen to be $N = 225$ round-trips for a pulse energy of 0.5 mJ and a pulse duration of 0.5 ns, resulting in a spectral broadening matching the FTL in Fig. 16. It is important to note that the dependence of the temporal contrast on B_{pass} does not occur in (1+1)D simulations, where the spatial domain is modeled using the ABCD matrix formalism (see for example Section 4.3.11). Instead, it requires the full spatio-temporal dependence in the model, either in radially symmetric (2+1)D or full (3+1)D simulations, indicating that this effect emerges from spatio-temporal couplings. In Fig. 17, radially symmetric (2+1)D simulations are used as described in Appendix B and reference [2].

Other approaches to improving the pulse contrast include using multi-stage compression schemes, enhanced-frequency chirping, and nonlinear polarization-ellipse rotation [56, 59, 128]. Due to the narrow bandwidth of nanosecond pulses, enhanced-frequency chirping is particularly challenging, as it would require exceedingly large amounts of GDD. Apart from this limitation, these techniques could be applied to nanosecond pulses, and thus constitute promising strategies for future nMPC experiments.

3.3.2 Longitudinal mode-beating in Q-switched lasers

Multiple longitudinal modes (LMs) emitted by Q-switched lasers pose another challenge that must be addressed for further development of the nMPC. This can occur because additional LMs are generated by the laser itself, a typical phenomenon in Q-switched lasers [129]. Additional LMs are emitted alongside the main LM, separated by multiples of the free spectral range of the laser cavity [130]. Since LMs are not mutually coherent, they interfere with the main LM, producing a modulation in the temporal domain. In the context of spectral broadening via SPM, these additional modes can have a particularly strong influence on the phase of the broadened spectrum. For the passively Q-switched laser used in our experiment, the manufacturer specifies that single-LM operation is achieved with less than 0.1 % of the pulse energy distributed among different longitudinal modes. We simulate this effect on spectral broadening in the nMPC using radially symmetric (2+1)-D simulations, as described in Appendix B and Ref. [2]. Figure 18 summarizes the numerical results for the degradation of the post-compressed pulse quality caused by a second LM. Here we simulate the experimental scenario using an nMPC with $R = 10$ cm radius-of-curvature (ROC) mirrors, $N = 31$ round-trips, and $k = 24$, and a 10 cm fused-silica glass block as the nonlinear medium. The pulse energy of the main mode, called single-mode (SM), is 1 mJ with a 0.5 ns duration and a Gaussian temporal shape. Here, however, an additional weak LM is introduced into the calculation, with an energy equal to 0.1% of the SM pulse energy. The spectrum of this input is shown in Fig. 18(a). The output spectra after spectral broadening in the nMPC are shown in Fig. 18(b). We observe significant changes in the spectra when the second LM is present, compared with SM operation. Furthermore, the spectral shape depends on the relative phase between the second LM and the first LM. Figures 18(c)–(d) show the temporal-domain modulations of the input pulse that give rise to the changes observed in Fig. 18(b). Fig. 18(e) displays the spectral phase after broadening. When the group-delay dispersion (GDD) is removed, the resulting spectral phase is shown in Fig. 18(f). In the SM case, removing the GDD is sufficient to obtain a flat spectral phase. In contrast, when a second LM is present, the spectral phase becomes considerably more complex, requiring higher-order phase compensation that is typically impractical. This behaviour is reflected in the post-compressed temporal profiles shown in Fig. 18(g): the SM case yields a clean, compressed pulse, whereas the case with a second LM produces a pulse that remains

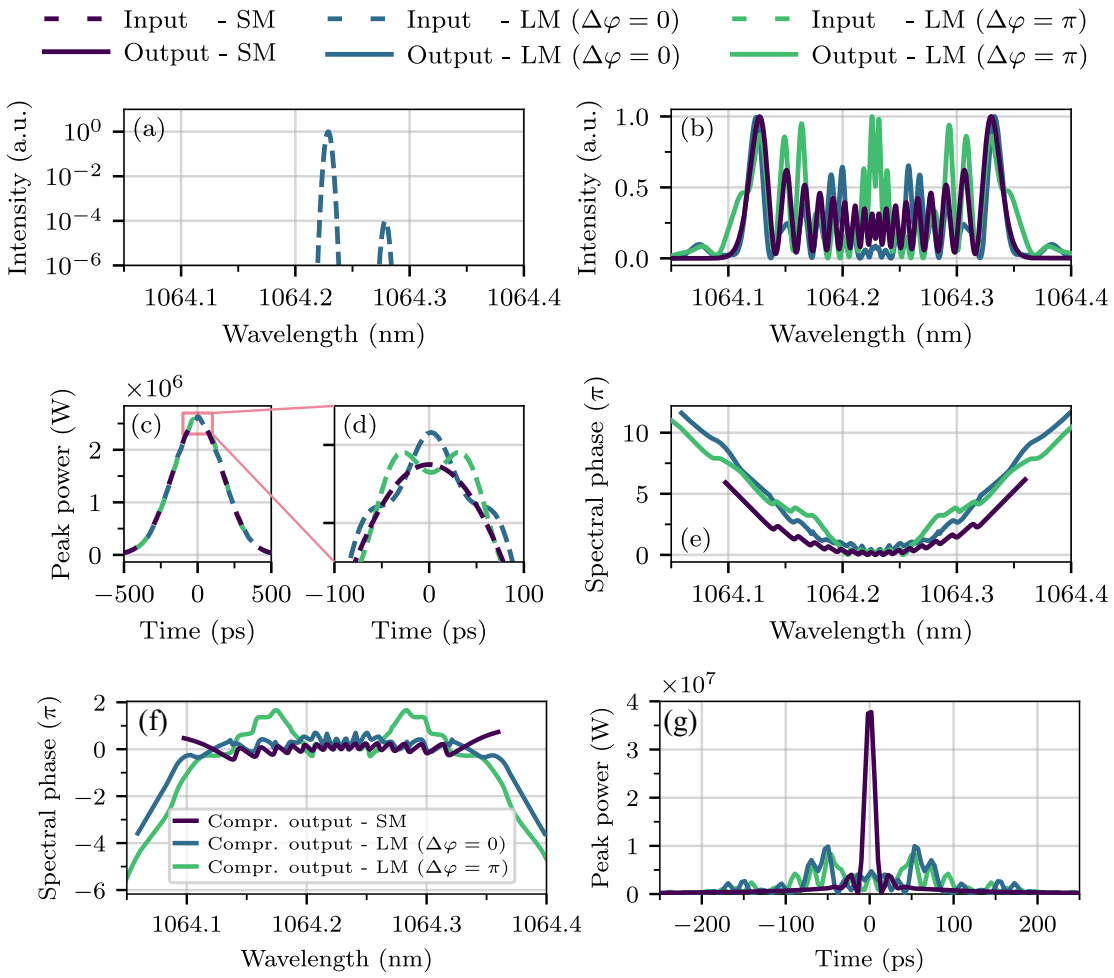


Figure 18: Simulation results visualizing the influence of a secondary longitudinal mode on the compressibility of the MPC output. (a) Input spectrum with a secondary longitudinal mode (LM) with 0.01% of the energy (b) Spectral broadening performance for single longitudinal mode operation (SM) and for multiple LM operation. The broadening is shown for two different relative phases $\Delta\varphi$ between the LMs. (c,d) Temporal intensity profile, with oscillations caused by interference with the second LM. (e) Spectral phase generated by SPM, which must be compensated for pulse compression. (f) Spectral phase after GDD removal. (g) Pulse shape after GDD removal. The amount of GDD removed is obtained by optimizing the peak power of the pulse in the temporal domain. Reprinted with permission from reference [2].

uncompressed and exhibits strong modulation even after GDD removal.

The SM operation is achieved when the strength of the second LM is reduced by a factor of 100, i.e., to 0.001 %. In our experiments this degradation is clearly observed, indicating that mode-cleaning before spectral broadening in the nMPC is necessary. To suppress the influence of the unwanted LMs, we therefore place an etalon before the nMPC. For future development of the nMPC, it is thus important to account for additional LMs that may be present in a Q-switched laser system. Nevertheless, our experiments demonstrate that LM cleaning can be achieved straightforwardly, for example by using a simple optical element like a Fabry-Pérot etalon filter.

3.3.3 Stimulated Brillouin scattering

Stimulated Brillouin Scattering (SBS) originates from a nonlinear interaction between an incoming optical field (the pump) and the medium's acoustic modes. Through electrostriction, this coupling induces a periodic modulation of the material density, which in turn leads to the generation of a back-scattered Stokes wave. For pulse energies above a material-dependent threshold intensity, the laser pulse transfers energy to a backward-propagating Stokes wave. This Stokes wave is shifted in

frequency by a few-GHz relative to the incident light [27, 120, 121]. Although it can be employed in SBS-based post-compression schemes for nanosecond pulses [100–103], it can also completely suppress spectral broadening in the nMPC when most of the light is transferred to the Stokes wave. The onset of SBS occurs rapidly when a certain threshold intensity I^{th} is exceeded [131]. This threshold intensity depends on the pulse duration τ and the phonon lifetime T_{B}. For pulses that are longer than the phonon lifetime of the material ($\tau \gg T_{\mathrm{B}}$; for fused silica $T_{\mathrm{B}} \simeq 5\,\mathrm{ns}$), the SBS-threshold peak intensity I_{th} can be calculated using the steady-state SBS gain coefficient g_B and the threshold parameter Θ [132]. These material-dependent quantities together with the interaction length L define the single-pass peak-intensity threshold as

$$I_{\mathrm{th}} = \frac{\Theta}{g_B\, L} \approx \frac{\Theta}{g_B\, z_R}, \quad \tau \gg \frac{2 z_R}{v_g}\ , \tag{37}$$

where L is the interaction length in the medium and v_g is the group-velocity of the pulse [131]. Conversely, if the pulse is shorter than the phonon lifetime $\tau < T_B$, the interaction with the material is confined to the pulse length, which may be shorter than the medium length L. The threshold intensity can then be calculated using [131]

$$I_{\mathrm{th}} = \frac{2\Theta}{g_B v_{\mathrm{g}} \tau}\left(\frac{T_B \Theta}{\tau} + 1\right), \qquad \tau \leq 2L/v_{\mathrm{g}}. \tag{38}$$

Since the equations above assume a constant spatial-mode diameter (as in optical fibers), we must quantify a free-space-propagating beam in the nMPC. To do this we assume that the interaction length L equals the MPC length, $L = L_{\mathrm{MPC}}$. Furthermore, we define an effective intensity I_{eff} for a single pass through the nMPC that would produce the same nonlinearity—i.e., the same B-integral—as propagation in a fiber with the corresponding constant mode size.

$$B_{\mathrm{pass}} = \frac{2\pi}{\lambda}\, n_2\, L_{\mathrm{MPC}}\, I_{\mathrm{eff}}. \tag{39}$$

Considering the basic geometry of an MPC filled with a nonlinear medium, the B-integral can be written as [31]

$$B_{\mathrm{pass}} = 4\pi^2\, \frac{n_2 P}{\lambda^2}\, \frac{k}{N}. \tag{40}$$

Using Eqs. 39 and 40, we obtain the effective intensity

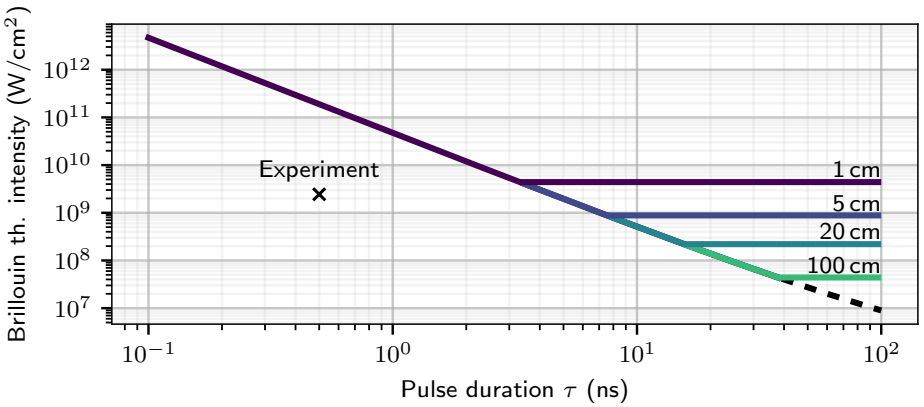


Figure 19: SBS threshold in an nMPC. The dependence of the Brillouin threshold intensity is plotted as a function of the input pulse duration (Eq. 38). For long-pulses, the threshold is dominated by the interaction length (Eq. 37). Our experimental parameters are well below the SBS threshold (Eq. 41). The following parameters were used: $g_B = 5\,\mathrm{cm/GW}$, $T_B = 5\,\mathrm{ns}$, $n_{\mathrm{FS}} = 1.45$, $\Theta = 22$ and $n_2 = 2.19 \cdot 10^{-16}\,\mathrm{cm^2/W}$ [26, 27, 131, 133]. Reprinted with permission from Ref. [2].

$$I_{\text{eff}} = \frac{\pi P\, n}{\lambda\, L_{\text{MPC}}}\, \frac{k}{N}. \tag{41}$$

where P is the peak power and n is the refractive index of the medium. The effective intensity is used for comparison with the threshold intensity I_{th}.

Figure 19 shows the calculated threshold intensity I_{th} obtained from Eq. 38 for various medium interaction lengths as a function of pulse duration. In general, the threshold intensity decreases with increasing pulse duration τ. However, the medium interaction length imposes a limit, beyond which the threshold intensity remains constant. In our experiment we remain well below the threshold intensity, with $I^{\text{eff}}_{\text{nMPC}}/I^{\text{th}}_{\text{SBS}} = 0.013$. If the intensity is kept constant as in our experiment, the pulse duration could be scaled up to 5 ns with an energy of 10 mJ, when $I^{\text{eff}}_{\text{nMPC}}/I^{\text{th}}_{\text{SBS}} \approx 1$. Longer pulses are possible, but this comes at the expense of pulse energy and the B-integral per pass, because $I^{\text{eff}}_{\text{nMPC}}$ would need to be reduced to remain below $I^{\text{th}}_{\text{SBS}}$.

3.3.4 Stimulated Raman Scattering

Stimulated Raman scattering (SRS) is a third-order nonlinear process in which an intense pulse interacts coherently with the vibrational modes of a medium, or with rotational modes in molecular gases, generating a frequency down-shifted field known as the Stokes wave [27]. The Raman frequency shift is material-specific and is determined by the relevant vibrational or rotational resonances. In fused silica, the Raman response is broadband and peaks at a Stokes frequency shift of approximately 13.6 THz [107]. SRS becomes dominant in nonlinear optical interactions when a certain intensity threshold is exceeded [27]. This threshold can be estimated by the [27]

$$I^{\text{SRS}}_{\text{th}} = \frac{32}{L_{\text{W}}\, g_{\text{R}}}\,, \tag{42}$$

where g_{R} is the Raman-gain parameter, approximately $g_{\text{R}} = 1 \cdot 10^{-13}$ m/W for a wavelength of 1 µm in fused silica. $L_{\text{W}} = \tau/\left|v_{\text{gp}}^{-1} - v_{\text{gs}}^{-1}\right|$ is the walk-off length, i.e., the distance after which the pump and Stokes pulses separate temporally, limiting further Raman gain. Here v_{gp} and v_{gs} are the group velocities of the pump and the generated Stokes pulse, respectively. For sufficiently short pulses, when $L_{\text{W}} < L$ (with L the medium interaction length), the walk-off length is short enough to suppress SRS effectively [105]. However, for long pulses in the nanosecond regime, the temporal walk-off may not be sufficient to suppress SRS, and the Stokes wave can build up efficiently over long distances.

Although large broadening factors of up to 80 have been demonstrated in fibers [105, 106], SRS limits the attainable pulse energy to well below 1 µJ and remains the dominant constraint on spectral broadening in fibers [108].

Here we perform numerical simulations using the (1+1)D model described in Section 4.3.11, following the implementation of SRS from Ref. [134]. We simulate the nMPC using the configuration described in the concept Section 3.2, with $N = 150$ round trips ($2N = 300$ passes), $k = 91$, mirror ROC $R = 10$ cm, and 0.5 ns pulses of 1 mJ energy. We simulate SPM spectral broadening together with SRS and evaluate the temporal quality of the pulses in terms of the peak power enhancement $\Pi = P_{\text{peak}}/P_0$ after post-compression, where P_{peak} is the output peak power and P_0 the input peak power. To determine the required suppression of SRS, we perform four simulations employing 0%, 10%, 20% and 30% loss on the Stokes wave after each nMPC pass. Here the Stokes field is initialized with random noise following a Gaussian distribution via the one-photon-per-mode method [27]. Figure 20 shows the results of this simulation. For 0% (no suppression), 10% and 20% suppression, SRS dominates after a certain number of passes, before the full 300 passes are reached. Here, Π degrades quickly when SRS becomes prominent, altering the temporal structure of the pulse, as seen in panels A-C of Fig. 20(b). In the case of 30% suppression of the Stokes wave

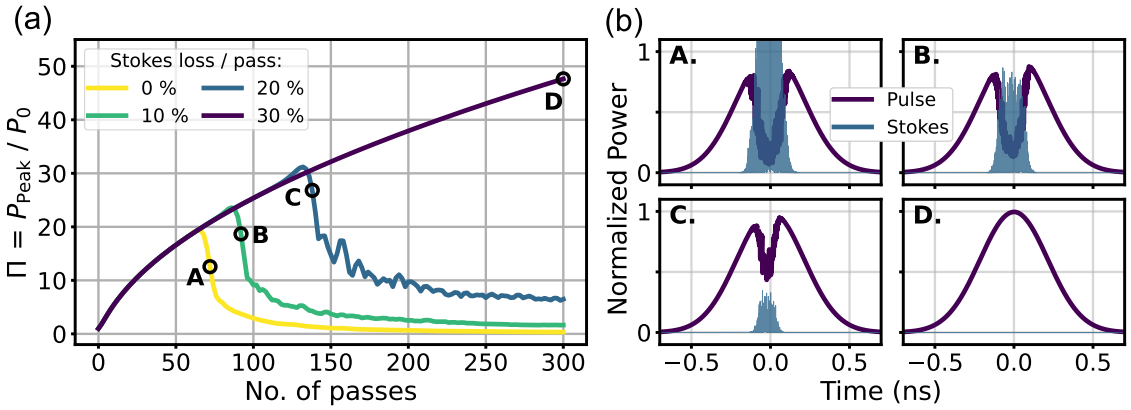


Figure 20: Impact of SRS in an nMPC for various Stokes losses. (a) Simulated peak power enhancement $\Pi = P_{\text{peak}}/P_0$ after spectral broadening of 1 mJ 0.5 ns pulses in an all-bulk fused-silica nMPC with $N = 150$, $k = 91$, $R = 0.1$ m. P_{peak} is obtained by applying the optimized GDD to the output pulses; P_0 denotes the input peak power. The figure displays Π for different values of loss applied per pass to the Stokes pulse. (b) Uncompressed pulses and Stokes fields for the different Stokes losses corresponding to the data shown in (a). The data correspond to different numbers of passes in the nMPC, as indicated by the circles in (a). Figure reprinted with permission from Ref. [2].

per pass, SRS does not visibly affect the pulse, resulting in a peak power enhancement of about 50. We thus conclude that suppressing the Stokes wave by merely 30% is sufficient to suppress SRS for this nMPC configuration. In practice, considering the relatively large THz-level frequency shift of SRS in fused silica, even larger suppression factors are achievable by using suitable mirror coatings, for example a quarter-wave-stack coating architecture [135]. In the next section we show that both SRS and another competing nonlinear effect, namely quasi-phase-matched four-wave mixing, can be effectively suppressed using suitable quarter-wave-stack coating designs for the nMPC.

3.3.5 Quasi-phase-matched four-wave-mixing

In multi-pass cells, single-stage spectral broadening factors above about 20 are routinely achievable [31]. However, operating in this regime can introduce detrimental effects that limit the usable spectral broadening, particularly when even higher broadening factors are targeted. One of the known effects is the degenerate quasi-phase-matched four-wave-mixing (QPM-FWM) [122]. Similar to SRS, this effect can severely limit spectral broadening by generating spectral side-bands that introduce strong temporal modulations of the pulse.

In any symmetric MPC, including the nMPC, QPM-FWM occurs under phase-matching conditions that are typically satisfied in these systems. It is a third-order effect that can be described as the generation of two photons with frequencies ω_2 and ω_3 from two photons of the fundamental field $\omega_1 + \omega_1 \rightarrow \omega_2 + \omega_3$. Here the subscript 1 denotes the fundamental, while 2 and 3 label the FWM components. The nonlinear polarization for this interaction can be written as

$$P(t,z) \propto E_1^*(t,z)\, E_1^*(t,z) E_2(t,z)\, E_3(t,z)\, \mathrm{e}^{i\Delta k(\omega_1,\omega_2\omega_3)z}\,, \tag{43}$$

where the wave-vector mismatch $\Delta k = 2k(\omega_1) - k(\omega_2) - k(\omega_3)$ determines the phase-matching conditions. QPM-FWM occurs in an MPC when the dispersion in a single pass in the MPC with length L is matched such that the condition

$$\Delta\varphi_{\text{pass}} = \Delta k\, L = (2k(\omega_1) - k(\omega_2) - k(\omega_3))\, L \overset{!}{\approx} 2\pi n \quad n \in \mathbb{Z} \tag{44}$$

is approximately fulfilled within the relevant nonlinear interaction region in the MPC. For symmetric, strongly focused MPCs with a Rayleigh length $z_R \ll L$, this condition is fulfilled for certain

frequencies ω_2 and ω_3, which depend on the specific dispersion landscape of the MPC [122]. This effect then leads to the amplified generation of spectral side-bands, which can cause temporal modulations of the pulse and ultimately degrade its temporal quality and compressibility.

We investigate this effect numerically in the nMPC and propose a scheme to mitigate it by suppressing the side-bands generated via QPM-FWM after each pass. Because the effect is similar to SRS, we apply the same principle used to suppress SRS and employ specifically designed quarter-wave-stack coatings to filter out the generated spectral components after each pass in the nMPC. The reflection bands of these coatings are designed for high reflectivity in the spectral region of interest, while spectral components outside that region are partially transmitted, to sufficiently suppress the effect. Figure 21 shows the simulation results for the nMPC configuration, in which

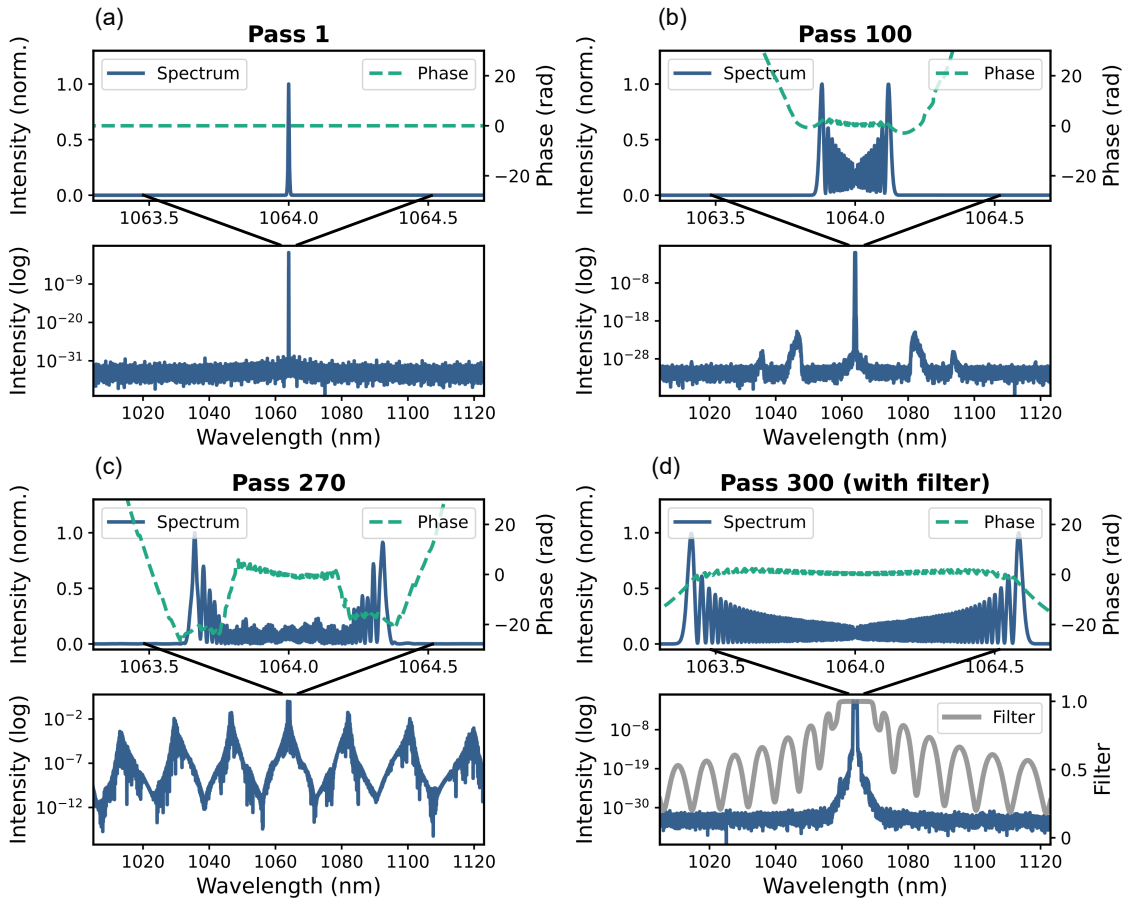


Figure 21: Impact of QPM-FWM in an nMPC. The QPM-FWM contribution is simulated after (a) 1, (b) 100, and (c) 270 passes without using a spectral filter. (d) shows the broadened spectrum when a spectral filter is applied after each pass. In each of the panels (a)-(d), the spectrum is plotted on a linear scale (upper plot) and on a logarithmic scale (lower plot, which is a zoomed view of the upper plot). The spectral phase is plotted after subtracting the optimized GDD for the highest peak power. The gray line in the lower panel of (d) visualizes the spectral filter. Figure reprinted with permission from Ref. [2].

a 0.5 ns, 1 mJ pulse is propagated through a full-bulk fused-silica nMPC with $R = 10\,\text{cm}$, $N = 150$ and $k = 91$ (corresponding to $2N = 300$ passes) using the (1+1)D simulation model described in Section 4.3.11 and Ref. [122]. We combine both SRS and QPM-FWM in this simulation and use the spectral filter to eliminate the spectral components of the two effects simultaneously. Figures 21(a)-(c) show the effect of QPM-FWM on the broadened spectrum after 1, 100, and 270 passes through the nMPC. In these cases no spectral filter is applied, and both the spectrum and the spectral phase degrade. Here the build-up of additional spectral components can be observed in the logarithmic plot, symmetrically placed around the original spectrum where Eq. (44) is

satisfied. Conversely, Fig. 21(d) shows the case in which the spectral filter is applied, yielding a clean, compressible spectrum and spectral phase without discontinuities. Comparing the two cases, Figures 21(c) and (d) make it clear that QPM-FWM must be accounted for in the design of a future large-broadening-factor nMPC. It further shows that, in practice, full suppression of parasitic spectral components from SRS and QPM-FWM can be achieved with suitable mirror coatings.

3.4 Experiment

In the first experimental demonstration, we take a simplified approach to show that spectral broadening and post-compression of ns pulses in an MPC is, in principle, possible. Instead of a monolithic cell, we use two curved mirrors with a standard high-reflectivity (HR) coating, without the filter effect described in the previous section. Furthermore, a glass block of fused silica (FS) is used as the nonlinear medium for spectral broadening. We demonstrate that efficient spectral broadening with a transmission of 83% through the MPC and post-compression from about 0.5 ns to 24 ps is possible, even with this simplified approach. Figure 22 schematically shows the experimental

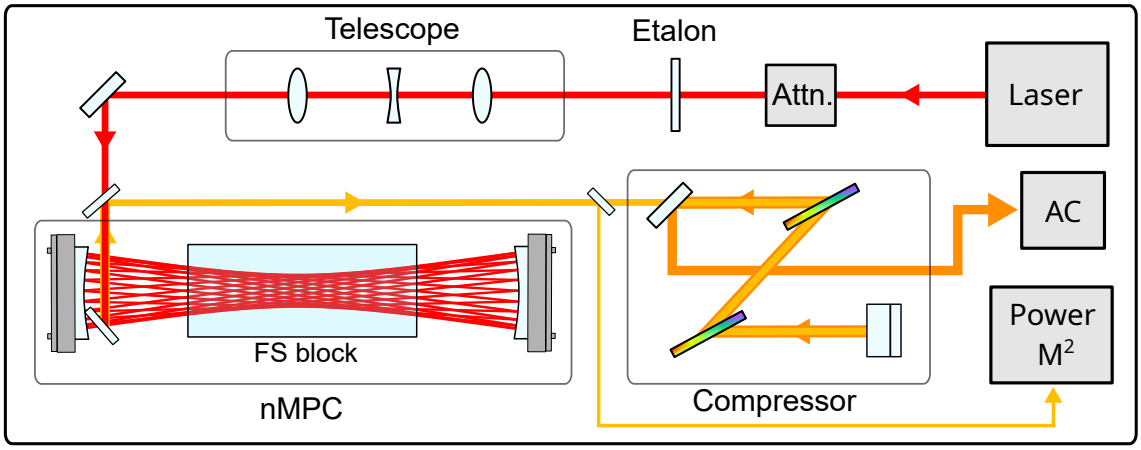


Figure 22: Sketch of the experimental setup used in the nMPC experiments. After the laser and the attenuator (Attn.), the beam is mode-matched in the telescope and coupled into the MPC. The MPC consists of two mirrors with a radius of curvature $R = 10\,\text{cm}$; a configuration with $N = 32$ round-trips and $k = 24$ is used. In the centre of the MPC, the 10 cm-long fused-silica (FS) block is placed as the nonlinear medium. The length of the MPC is about 21 cm. Then the beam is sent to the diagnostics, where the power and M^2 are measured. In an alternative path, the beam is directed to the compressor unit and then into the autocorrelation (AC) unit, where the pulse duration after compression is measured.

setup. We use a commercial Q-switched, diode-pumped Nd:YAG laser (MPL2310, QS Lasers), delivering pulses with 2 mJ energy, 0.4 ns duration, at a wavelength of 1064 nm. After thermal stabilisation, the cavity operates in single-mode emission, with less than 0.1 % of the total energy distributed among adjacent longitudinal modes (LM). As discussed in the previous Section 3.3.2, this LM contrast is not high enough for SPM spectral broadening in the nMPC. We therefore employ additional LM cleaning using an etalon with a free-spectral range of 230 pm and a finesse of 41, reducing the adjacent LM—spaced about 50 pm from the main spectrum—by approximately 24 dB. This results in an estimated contrast of <0.001% , which is sufficient for SPM spectral broadening, as we show numerically in Section 3.3.2. After attenuation and the etalon, the beam is mode-matched in a three-lens telescope to match the eigenmodes of the nMPC. As mentioned above, a simplified version of the nMPC is used: the beam is coupled into an MPC formed by two curved mirrors with radii of curvature $R = 100\,\text{mm}$ and a fused-silica (FS) block of dimensions $L \times W \times H = 100\,\text{mm} \times 75\,\text{mm} \times 75\,\text{mm}$ placed in the centre of the MPC. The MPC configuration has $N = 31$ round-trips (i.e. $2N = 62$ passes) with $k = 24$. Taking into account the refractive index of fused silica ($n \approx 1.45$ at 1064 nm) and the resulting shortening of the optical path, the

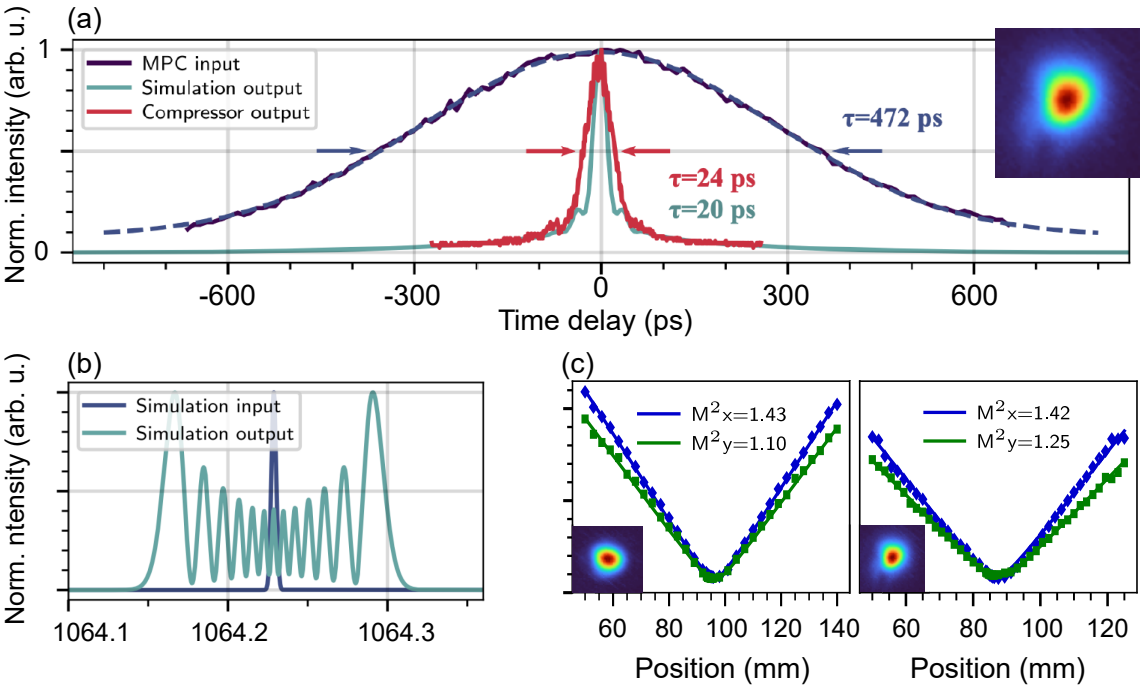


Figure 23: Results of the nMPC experiment. (a) Autocorrelation measurements of the input and output pulses. The pulse duration indicates the full-width-at-half-maximum (FWHM) duration after deconvolution. The simulated pulse is plotted together with the measurements. (b) Simulated spectrum compared with the Gaussian input spectrum. (c) Beam quality measurements. Reprinted and modified with permission from reference [2].

MPC length is about 21 cm. In this configuration, the fluence on the mirrors in the linear case (no Kerr-lensing) is about 0.3 J/cm^2, which is well below the typical laser-induced damage thresholds (LIDTs) of optical coatings (10 J/cm^2 for nanosecond pulses) [116, 117]. The peak intensity in the focus is about 10 GW/cm^2, still lower than the optical-breakdown threshold of fused silica (55 GW/cm^2 for nanosecond pulses) [136]. The pulse coupled into the MPC has an initial energy of 0.94 mJ and a duration of 0.47 ns; the slight narrowing caused by the etalon is measured with an autocorrelator (AC). After 62 round-trips through the MPC, the beam is extracted by the scraper mirror, which also serves as the input coupler.

We measure a transmission of about 83 % at full power, which is in good agreement with the calculated efficiency of 86 %, considering the reflectivity of the cell mirrors and the fused-silica (FS) bulk surfaces as specified by the manufacturer. After spectral broadening, the pulse is sent to a compressor consisting of two transmission gratings with a line density of 1740 lines/mm. With the compressor we obtain a total group-delay dispersion (GDD) of about $-1100\,\mathrm{ps}^2$ for optimal compression, which is close to the simulated value of $-1370\,\mathrm{ps}^2$. The diffraction efficiency of the gratings is unfortunately limited to about 60 %, resulting in a compressor throughput of only 12 %. These gratings were chosen for availability reasons and can be significantly improved by using state-of-the-art transmission gratings with >99.5 % diffraction efficiency [137]. Alternatively, a compact chirped volume Bragg-grating (CVBG) can be employed for compression. Contemporary CVBGs can provide the necessary GDD while offering a high efficiency of 90% and supporting energies of more than 1 mJ and average powers of 250 W, all in a device only a few centimeters long [138]. After the grating compressor, the pulse is sent to the AC unit and the pulse duration is measured. Figure 23 shows the results of the measurements. The measured autocorrelation (AC) for the input, the output, and the simulated compressed pulse are shown in Fig. 23(a). The values plotted in Fig. 23(a) represent the de-convoluted pulse durations. Here we measure a post-compression from 0.472 ns down to 24 ps, corresponding to a compression factor of 20. The simulated pulse duration of 20 ps is in good agreement with the measured value. The corresponding

simulated spectra are shown in Fig. 23(b). Figure 23(b) shows only a minor decline in beam quality in one axis, from $M^2 = 1.1$ to $M^2 = 1.25$, while the M^2 of the orthogonal axis remains around $M^2 = 1.4$.

3.5 Conclusion and Outlook

In this chapter we introduce the concept of a nanosecond multi-pass cell (nMPC): a quasi-waveguide, Herriott-type bulk-rod approach that enables self-phase-modulation (SPM)-based spectral broadening of nanosecond pulses from Q-switched lasers. The central idea is to adapt the MPC post-compression paradigm—well established for ps and fs sources—to the fundamentally different operating conditions of ns pulses (much lower peak power, narrow intrinsic bandwidth, and stronger sensitivity to parasitic nonlinear processes over many round trips). This is achieved by an all-bulk monolithic geometry (to avoid air-bulk interface losses), by exploiting the reduced dispersion sensitivity and elevated laser-induced damage thresholds of ns pulses, and by using the optical coatings as an additional degree of freedom to suppress competing nonlinear effects such as stimulated Raman scattering (SRS) and quasi-phase-matched four-wave mixing (QPM-FWM).

Experimentally, we performed a first proof-of-principle demonstration using a simplified nMPC implementation with standard high-reflectivity mirrors and a fused-silica bulk medium. Starting from ≈ 0.5 ns Q-switched pulses at 1064 nm, we achieved post-compression down to 24 ps after propagation through 62 passes, corresponding to a compression factor of ≈ 20. The result confirms that nanosecond post-compression via multi-pass SPM is feasible and that mJ-level pulse energies can be transferred into the picosecond regime even without the fully optimised monolithic and spectrally-filtering design.

The chapter also provides a pathway toward substantially larger compression factors. Numerical simulations based on (2+1)D and (1+1)D propagation models indicate that, under suitable conditions and with an optimised nMPC geometry and coating-based spectral filtering, compression factors >100 are realistic even in the presence of the dominant parasitic processes. In particular, we identified and quantified key limitations related to temporal pulse quality and contrast degradation at high broadening factors, including longitudinal-mode beating intrinsic to Q-switched lasers, stimulated Brillouin scattering (SBS) as an intensity- and pulse duration-dependent threshold limitation, and stimulated Raman scattering (SRS) as well as quasi-phase-matched four-wave-mixing (QPM-FWM), which can generate unwanted spectral sidebands and prevent clean compressibility. We further showed that longitudinal-mode cleaning (e.g., with an etalon) can restore compressibility, and that only moderate suppression of Stokes components may already be sufficient to keep SRS from dominating. Finally, we argued that coating designs (e.g., quarter-wave stack concepts) can be engineered to filter out the spectral components responsible for QPM-FWM while preserving the desired SPM-broadened spectrum. It remains future work—particularly experimental—to identify other challenges that may arise during the spectral-broadening process in an nMPC and to develop corresponding solutions.

In conclusion, this experiment demonstrates that efficient post-compression of nanosecond pulses from Q-switched lasers into the picosecond regime is possible even in a simplified nMPC setup. Further work is required to push the broadening factors to levels where the pulse duration and bandwidth gap between Q-switched and mode-locked laser technologies closes, enabling ps- to fs-level pulses to be generated with simple, compact, cost-efficient Q-switched lasers as the source platform.

4 Second-Harmonic Generation in Multi-Pass Cells

This chapter discusses the use of multi-pass cells (MPCs) to enhance second-order nonlinear optical processes. It introduces the basic physical concepts, develops a theoretical description of the relevant frequency-conversion mechanisms, and presents experimental and numerical results for second-harmonic generation in an MPC geometry. The chapter is structured as follows. First, an overview of second-order nonlinear interactions and their relevance in the context of MPCs is given. This is followed by a conceptual discussion of the second-harmonic MPC (SHG-MPC), including the role of phase matching and group-delay matching. Subsequently, a theoretical treatment is developed, starting from the Maxwell equations and leading to an analytical model for SHG in an MPC under the non-depleting-pump approximation. The theory section also introduces the numerical model used for simulations. Afterwards, the experimental implementation of the SHG-MPC is presented and compared with numerical simulations for both longer and shorter pulses. Finally, the chapter concludes with a discussion of the the experimental results achieved within the work of this thesis, including an outlook on possible extensions such as higher-order dispersion compensation, energy scaling, and the applicability of the concept to other second-order nonlinear processes. The chapter largely follows the work summarized in [6], attached in Appendix C.

4.1 Introduction

Second-harmonic generation (SHG) of light in crystals was discovered in 1961, shortly after the invention of the laser in 1960 [7, 9]. The short gap between these two discoveries is directly linked to the invention of the laser. As a coherent light source, the laser provided peak powers and intensities orders of magnitude higher than conventional sources at the time, satisfying the requirements for nonlinear optical phenomena. With lasers as the source of coherent and intense light, other nonlinear phenomena were discovered and studied since. Among a plethora of other nonlinear phenomena, many important applications are based on the second-order nonlinearity. The entirety of these second-order phenomena are sum-frequency generation (SFG), difference-frequency generation (DFG) giving rise to optical parametric amplification (OPA), optical rectification (OR), and second-harmonic generation (SHG) [26]. Each of these processes has a variety of applications. SFG is used for converting two different laser wavelength into a laser with shorter wavelength, typically not accessible by using standard gain media [139, 140]. Important example are the third harmonic generation, often used to efficiently generate ultraviolet (UV) light [141–143], for instance of a ytterbium (Yb) laser system typically centered at 1030 nm [144]. Here, the second-harmonic at 515 nm is mixed with the fundamental wavelength 1030 nm, resulting in a wavelength of 343 nm. Optical rectification is used to generate terahertz (THz) light [145, 146]. DFG on the other hand is widely employed in many systems for generating lasers in a wide variety of wavelengths. Not only can lasers be generated at wavelengths resulting from the difference of the frequency of their driving fields, resulting typically in the middle-infrared (mid-IR) regime [147–149], but more importantly, DFG is the underlying process for optical-parametric amplification (OPA) [26, 150]. OPA systems are widely used in many applications, as they provide a method for generating broadband, highly wavelength-tunable laser sources [12, 151, 152]. In the context of MPCs, several works on OPA in MPCs have recently been reported [5, 63]. Employing MPCs for OPA, many key limitations on standard, single-pass OPA systems have been considerably improved, in particular the overall efficiency and bandwidth of the resulting field. This shows that using MPCs for second-order nonlinear processes can be highly beneficial, highlighting the utility and flexibility of MPCs as an important technique in the field of nonlinear optics. Another process that benefits from MPCs is SHG, which is the topic of this work. The publication of this work is attached in Appendix C. Apart from this work, MPC-based free-space quasi-phase-matching (QPM) has been demonstrated

for nanosecond-level pulse durations [64, 65]. Here, the phase-mismatch of the fundamental and second-harmonic field accumulated inside the crystal during the conversion process is compensated by the dispersion of the gas within a pass through the MPC. Thus, after each pass, the total phase-mismatch, i.e. relative phase, is a multiple of 2π upon re-entrance into the crystal, leading to an efficient SHG process. This scheme is similar to a standard QPM process in a single periodically-poled crystal, where typically a periodically-poled Lithium-Niobate (PPLN) crystal is used for this effect. However, for ultrashort pulses in the femtosecond range, a challenge arises when only the "zeroth"-order phase-mismatch is compensated, as it is done in QPM. In order to achieve SHG with broad bandwidth and high efficiency, not only the phase velocity needs to be matched, but higher-order phases become relevant. If the higher-order phase-mismatches, in particular the relative group-delay (GD) between the fundamental and second harmonic, are not accounted for, the phase-matching condition is typically satisfied only over a limited spectral bandwidth, which reduces conversion efficiency and leads to spectral narrowing of the frequency-converted pulse [26]. To address this limitation – particularly in SHG – several advanced approaches have been developed, including adiabatic frequency conversion [153], prism-based phase and group-delay matching [154, 155], and microstructured fiber-based phase and group-delay (GD) matching [156], the latter of which has so far only been proposed conceptually. While these methods offer promising routes toward efficient SHG, they generally rely on single- or few-pass free-space configurations or waveguides, where tunability of the relative phases remains limited. In this work, we address this challenge by employing MPCs as the mechanism for matching both the phase and the GD simultaneously. In this way, both limitations on bandwidth and efficiency can be overcome and highly efficient, broadband second-harmonic pulses can be generated, exhibiting high temporal contrast as well as excellent beam quality. In the next session we describe the concept of the second-harmonic MPC (SHG-MPC), followed by a theoretical treatment and an analytical model in the non-depleting pump approximation. Afterwards, the experimental and numerical results are shown, followed by an outlook for possible future developments of the SHG-MPC.

4.2 Concept

The most important feature of the SHG-MPC is the dispersion after each pass through the cell. It can be tailored such that both after each pass through the crystal, both the fundamental and second-harmonic fields experience the same phase-shift of a multiple of 2π within a wide wavelength range. The phase-mismatch experienced by two coupled laser fields stems from the wavenumber-mismatch in a given material. The frequency- and material-dependent wavenumber $k(\omega)$ is defined as $k(\omega) = \omega/c_0 n(\omega)$, where $n(\omega)$ is the refractive index of a material and $c_0 = 299{,}792{,}458\,\mathrm{m/s}$ the speed of light in vacuum. It can be expanded in a power series of ω around a center frequency $\bar{\omega} = 2\pi/\lambda$ with λ the center wavelength such that

$$k(\omega) = k^{(0)} + k^{(1)} \cdot (\omega - \bar{\omega}) + \frac{1}{2} k^{(2)} \cdot (\omega - \bar{\omega}) + \dots \quad , \tag{45}$$

where the coefficients $k^{(n)} := \frac{\partial^n k}{\partial \omega^n}\big|_{\omega=\bar{\omega}}$ are the nth derivatives of $k(\omega)$ at the center frequency $\bar{\omega}$ and $k^{(0)} := \bar{\omega}/c_0\, n(\bar{\omega}) = 2\pi/\lambda\, n(\bar{\omega})$. If there are two fields present with center-frequencies $\bar{\omega}_1$ and $\bar{\omega}_2$, propagating in two different axes in a non-isotropic medium with refractive indices n_1 and n_2, we label each wavenumber by $k_p(\omega_p) = \omega_p/c_0\, n_p(\omega_p)$ with $p = 1, 2$ and define the "zeroth"-order wavenumber-mismatch as

$$\Delta k^{(0)} = 2k_1^{(0)}(\bar{\omega}_1) - k_2^{(0)}(\bar{\omega}_2) = \frac{\bar{\omega}_2}{c_0} \left(n_1(\omega_1) - n_2(\omega_2)\right) \ , \tag{46}$$

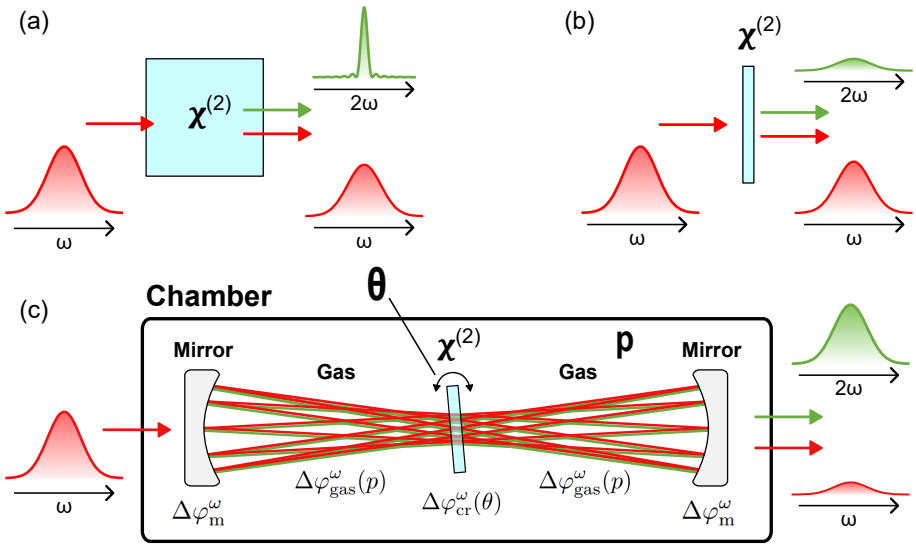


Figure 24: Illustration of the SHG-MPC in comparison to SHG in thick and thin crystals. (a) In a thick crystal, even if the phase-matching angle is matched, the efficiency and the spectral bandwidth of the SHG process is limited by the narrow phase-matching bandwidth of the crystal. (b) A thin crystal provides a large bandwidth, but is limited in interaction length, rendering the SHG process inefficient. (c) The SHG-MPC can provide both, high efficiencies and large bandwidth by suitably tuning phase- and GD-mismatch after every pass through a thin crystal. Reprinted with permission from [6].

which, for a given material length L results in the zeroth-order phase-mismatch $\Delta\phi^{(0)} = \Delta k^{(0)} \cdot L$. Phase-matching is achieved when $\Delta k^{(0)} = 0$. Equation (46) describes a special case of phase-matching which is called type I phase-matching, where the fundamental field $p = 1$ is polarized orthogonally to the second-harmonic field $p = 2$. However, for achieving phase-matching, $\Delta k^{(0)} = 0$ in general needs to be fulfilled, even for other phase-matching schemes, such as type II phase-matching, QPM or even in general for other second- or higer-order multi-wave-mixing processes [26]. In the end, $\Delta k^{(0)}$ describes the mismatch in phase-velocity $v_p^{\mathrm{ph}} = \bar{\omega}_p / k_p^{(0)}$ experienced by the light at a certain frequency $\bar{\omega}_p$. If $v_1^{\mathrm{ph}} = v_2^{\mathrm{ph}}$, the fundamental and second-harmonic waves propagate with identical phase velocities, so their relative phase remains constant along the propagation direction. As a result, no phase mismatch accumulates ($\Delta k^{(0)} = 0$), and efficient phase-matching is achieved, enabling coherent buildup of the second-harmonic field over the full interaction length L. In type I phase-matching, as described by Eq. (46), a birefringent medium – typically an optical crystal – is used to achieve phase-matching. In a uni- or bi-axial crystal with a second-order nonlinear response in the orthogonal direction to the polarization of the fundamental field, the induced second-harmonic polarization is likewise orthogonal to the fundamental field. The birefringence property can then be used to tune the phase-velocity of the orthogonal second-harmonic field to match the fundamental phase-velocity, typically done via angle-tuning or temperature tuning of the crystal [26]. Figure 25 schematically shows the geometry of matching the refractive indices in the case of type I phase-matching for a uniaxial crystal such as BBO. The ellipsoids in the plot show the areas (or lines) of constant $n_p(\lambda_p)$, where $p = 1$ is the fundamental and $p = 2$ the second-harmonic. In type I phase-matching, the fundamental is polarized along the xy-plane, propagating in the ordinary direction. On the other hand, the second-harmonic is polarized along the plane spanned by $\vec{k}$ and the z-axis, commonly referred to as the optical axis of the crystal. The $\vec{k}$-vector has an angle θ relative to the z-axis and the extraordinary refractive index is dependent on it. When both ordinary and extraordinary ellipsoids intersect, both refractive indices are the same, i.e. $n_1(\lambda_1) = n_2(\lambda_2)$ and phase-matching is achieved (Eq. (46)).

When the relative phase is matched, i.e. $\Delta k^{(0)} = 0$, high efficiencies can be generally achieved for narrowband pulses. However, in the ultrashort pulse regime of the order of 10s of femtoseconds, higher-order relative phase terms can become significant, leading to a reduction of SHG bandwidth

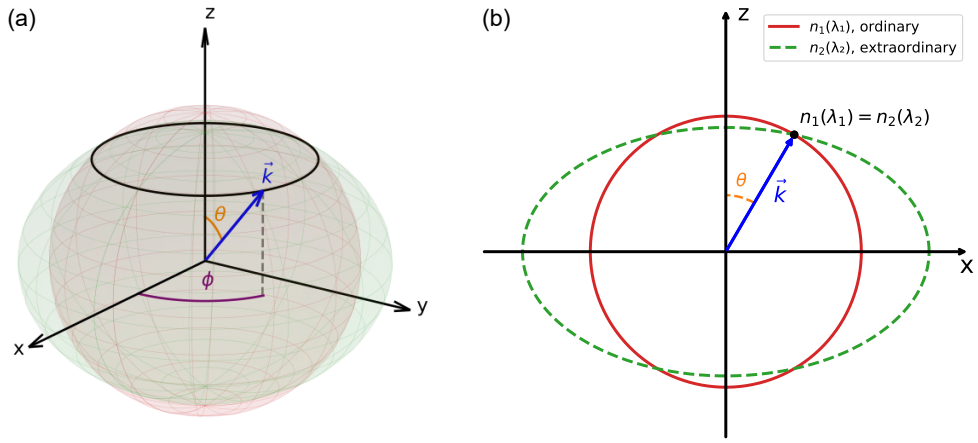


Figure 25: Index ellipsoids of a negative uniaxial crystal for type I phase-matching. (a) Three dimensional view on the two index ellipsoids. The red ellipsoid represents the refractive index $n_1(\lambda_1)$ for the fundamental, polarized in the xy-plane (ordinary). The green represents $n_2(\lambda_2)$ the second-harmonic, polarized in the plane spanned by $\vec{k}$ and the z-axis (extraordinary). The black circle marks the intersection of both. (b) Cross-section of the xz-plane. At the intersections at a certain angle θ, $n_1(\lambda_1) = n_2(\lambda_2)$, meaning phase-matching is achieved.

and efficiency. The next order to zeroth-order wavenumber-mismatch as in Eq. (46) is the first-order wavenumber-mismatch

$$\Delta k^{(1)} = k_1^{(1)}(\bar{\omega}_1) - k_2^{(1)}(\bar{\omega}_2) \ , \tag{47}$$

where $\Delta\phi^{(1)} = \Delta k^{(1)} \cdot L$ is also known as the relative group-delay (GD) between fundamental and second-harmonic field and L the medium length. Here, as mentioned before, $k_p^{(1)}(\bar{\omega}_p) = \frac{\partial k_p(\omega)}{\partial \omega}\big|_{\bar{\omega}_p}$ is the first derivative of $k_p^{(1)}(\omega)$ evaluated at the center frequency $\bar{\omega}_p$ and $p = 1, 2$ for fundamental and second-harmonic. In general, even if $\Delta k^{(0)}$ is matched, $\Delta k^{(1)}$ is not simultaneously matched as well. Thus, a different method needs to be employed to match both the phase and GD. Here MPCs offer a possibility for adjusting the relative phase of the fundamental and second-harmonic after each pass through the crystal. In the second-harmonic MPC (SHG-MPC) discussed in this work a phase-matched nonlinear crystal can be placed in the center of the cell, where at each pass the SHG process takes place. The resulting relative GD can then be compensated after each pass using suitable GD-compensating mirror coatings.

Figure 24 illustrates the SHG-MPC scheme and compares it to single-pass generation schemes. In Fig. 24(a), a thick crystal reduces the bandwidth of the generated second-harmonic spectrum. A thin crystal as shown in Fig. 24(b) results in a large bandwidth, but the efficiency is low due to a small interaction length. Placing a thin crystal inside an SHG-MPC, as illustrated in Fig. 24(c), can increase the effective interaction length. This approach avoids the bandwidth limitations of a thick bulk crystal by tailoring the dispersion so that both the phase and group delay between the fundamental and second-harmonic waves are simultaneously matched during each pass. Thus, in order to do so, we consider the relative phases and wavenumbers (Eq. 45) up to first order in ω and consider the ω-dependent relative phase per MPC pass. In the SHG-MPC, $\Delta\varphi^{\omega}_{\text{pass}}$ consists mainly of three contributions

$$\Delta\varphi^{\omega}_{\text{pass}}(\theta, p) = \underbrace{\Delta\varphi^{\omega}_{\text{cr}}(\theta)}_{\text{Crystal}} + \underbrace{\Delta\varphi^{\omega}_{\text{gas}}(p)}_{\text{Gas}} + \underbrace{\Delta\varphi^{\omega}_{\text{m}}}_{\text{Mirror}} + \Delta\varphi_0 \ , \tag{48}$$

where the superscripted ω indicates the frequency-dependence and the $\Delta\phi_0$ is a constant offset. The $\Delta\varphi^{\omega}_{\text{pass}}$ is now a function of two parameters: the pressure p and the angle of the wavevector

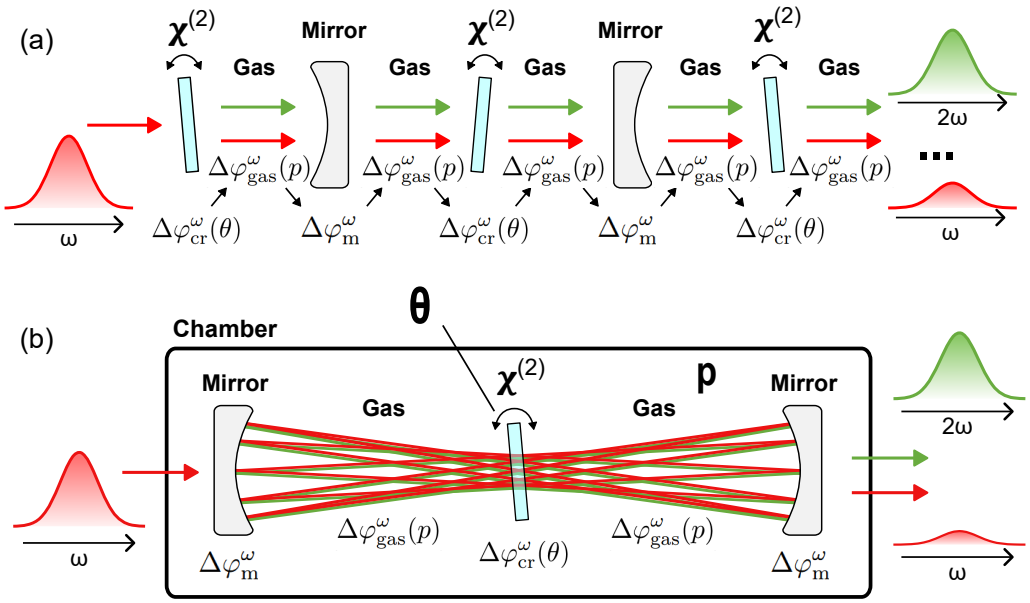


Figure 26: Illustration of the SHG-MPC in consecutive order (a) and the actual configuration (b). Parts of the figure reprinted with permission from [6].

relative to the optical axis of the crystal θ. The pressure dependence comes from the phase contribution from gas in the gas-cell $\Delta\varphi^{\omega}_{\mathrm{gas}}(p)$, where it acts as one of the tuning parameters. The angle dependence arises from the phase accumulated in the crystal $\Delta\varphi^{\omega}_{\mathrm{cr}}(\theta)$, where θ acts as the second tuning parameter to adjust the MPC dispersion by tuning the extraordinary axis in which the second-harmonic field propagates.

We write each contribution up to first order in ω

$$\Delta\varphi^{\omega}_{\mathrm{cr}}(\theta) = \Delta\varphi^{(0)}_{\mathrm{cr}}(\theta) + \Delta\varphi^{(1)}_{\mathrm{cr}}(\theta)\cdot(\omega-\bar{\omega}_2) \tag{49}$$

$$\Delta\varphi^{\omega}_{\mathrm{gas}}(p) = \Delta\varphi^{(0)}_{\mathrm{gas}}(p) + \Delta\varphi^{(1)}_{\mathrm{gas}}(p)\cdot(\omega-\bar{\omega}_2) \tag{50}$$

$$\Delta\varphi^{\omega}_{\mathrm{m}} = \Delta\varphi^{(0)}_{\mathrm{m}} + \Delta\varphi^{(1)}_{\mathrm{m}}\cdot(\omega-\bar{\omega}_2)\ , \tag{51}$$

with $\bar{\omega}_2 = 2\bar{\omega}_1$ being the center frequency of the second-harmonic field, which is two times the center frequency of the fundamental field $\bar{\omega}_1$. The terms $\Delta\varphi^{(0)} = 2\varphi^{(0)}_1 - \varphi^{(0)}_2$ are the zeroth-order relative phase mismatches (phase-matching terms) and $\Delta\varphi^{(1)} = \varphi^{(1)}_1 - \varphi^{(1)}_2$ is the first-order relative phase-mismatches (GD-matching terms). Phase- and GD matching in a single pass in the SHG-MPC is achieved when

$$\Delta\varphi^{(0)}_{\mathrm{pass}}(\theta,p) = \Delta\varphi^{(0)}_{\mathrm{cr}}(\theta) \ + \ \Delta\varphi^{(0)}_{\mathrm{gas}}(p) + \Delta\varphi_0 \ \stackrel{!}{=}\ 2\pi n\ , \tag{52}$$

where n is an integer. Since $\Delta\varphi^{(0)}_{\mathrm{m}}$ is constant, it is absorbed in the $\Delta\varphi_0$ term. At the same time, for the first order terms, the condition

$$\Delta\varphi^{(1)}_{\mathrm{pass}}(\theta,p) = \Delta\varphi^{(1)}_{\mathrm{cr}}(\theta) \ + \ \Delta\varphi^{(1)}_{\mathrm{gas}}(p) + \Delta\varphi^{(1)}_{m} \ \stackrel{!}{=}\ 0 \tag{53}$$

needs to be fulfilled to ensure GD matching. The amount of GD that is then required to be compensated by the mirrors can be determined by

$$\Delta\varphi^{(1)}_{\mathrm{m}} = -\ \left(\Delta\varphi^{(1)}_{\mathrm{cr}}(\theta_{\mathrm{pm}}) \ + \ \Delta\varphi^{(1)}_{\mathrm{gas}}(p_{\mathrm{ref}})\right)\ , \tag{54}$$

where θ_{pm} is the phase-matching angle ($\theta_{\mathrm{pm}} = 23.4°$ for BBO) and p_{ref} the reference pressure of

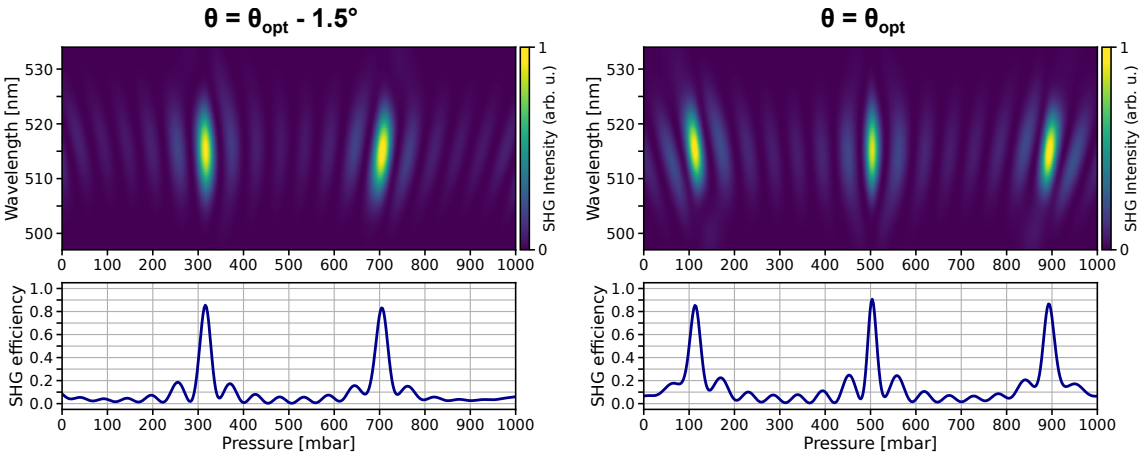


Figure 27: Simulated idealized spectrograms of the SH pulse for two different crystal angles. The simulation parameters are matched with the experiment, but ideal Gaussian beams are used as the fundamental input pulses. The input is a 1030 nm, 60 fs, 50 µJ pulse and the MPC parameters are $R = 1\,\mathrm{m}$, $N = 4$, $k = 1$ with 8 passes in total through a BBO with 100 µm thickness. We compensate the relative GD by 15 fs at each mirror reflection, delaying the fundamental pulse. The simulations are carried out using the model described in supplement section S1. The optimal angle here is $\theta_{\mathrm{opt}} = 23.8°$. (a) Unmatched relative GD. (b) Matched GD. Reprinted with permission from [6].

the gas that can be arbitrarily set. In our experiments, we choose $p_{\mathrm{ref}} = 500\,\mathrm{mbar}$ of air, in order to allow for full tunability from 0-1 bar in the cell. Figure 26(a) shows the "unraveled" system and the phase contributions in consecutive order in comparison to the realistic SHG-MPC (Fig. 26(b)).

With the GD-compensating mirrors in place, we can now use the two tuning parameters θ and p to fine-tune phase- and GD matching in the SHG-MPC. The systematic approach is as follows: first the air pressure p in the gas-cell is tuned and the spectra are recorded as a function of p, resulting in p-ω spectrograms (or p-λ in our experiments). The output power is recorded simultaneously. Figure 27 shows such spectrograms obtained via simulations based on the model described in Section 4.3.10. In both plots, a spectrogram as well as the conversion efficiency is shown. In both, one can observe major maxima, which correspond to the case where the condition Eq. (52) is fulfilled and "zeroth"-order phase-matching is achieved. The distance between the two major maxima is determined approximately only by the gas dispersion $\Delta\phi^{(0)}_{\mathrm{gas}} = \Delta k^{(0)}_{\mathrm{gas}}\, L$, which itself depends on the gas-type, pressure and the MPC length $L_{\mathrm{MPC}} \approx L$. The mirrors and the crystal contribute only weakly to this separation, since the crystal is operated close to the phase-matching angle, where $\Delta k_{\mathrm{cr}} \approx 0$. The number of minor maxima between the two major maxima depends on the number or passes through the cell and is $N_{\mathrm{pass}} - 2$, as we will show in Section 4.3. Figure 27(a) shows such spectrogram when the angle θ is off by 1.5°. Here the maxima appear tilted, indicating that, while the phase is matched (i.e. Eq. ((52) is fulfilled), the GD is not matched at these pressures and Eq. (53) is not fulfilled. By tuning θ such that $\theta = \theta_{\mathrm{opt}}$, the major maximum at about 500 mbar now appears vertical, indicating that for each wavelength across the spectrum the phases are matched at the same pressure. This means that now both conditions are fulfilled and phase and GD are matched simultaneously.

4.3 Theory

In this section we develop the basic theory for the nonlinear frequency conversion based on the second-order nonlinear response of materials within the framework of MPCs. In many textbooks, such as [26], analytical equations are obtained by considering only monochromatic fields, where effects from higher-order phases, such as the group-delay (GD) are not taken into account. Apart from phase-matching itself, these effects, in particular the relative GD between the fields, eventually limit the bandwidth and efficiency of the nonlinear process. This section will start from the Maxwell

equations, then going to the wave equation for scalar fields, where only the temporal domain and scalar fields are considered. Then, an analytical model for the SHG-MPC is derived in the non-depleting pump approximation.

4.3.1 General equations for second-order nonlinear conversion

In this part of the derivation, we partially follow the calculations in [26]. We start from the Maxwell equations

$$\nabla \cdot \tilde{\mathbf{D}} = \rho_{\text{free}} \qquad \text{(Gauss's law)} \tag{55}$$

$$\nabla \cdot \tilde{\mathbf{B}} = 0 \qquad \text{(Gauss's law for magnetism)} \tag{56}$$

$$\nabla \times \tilde{\mathbf{E}} = -\frac{\partial \tilde{\mathbf{B}}}{\partial t} \qquad \text{(Faraday's law)} \tag{57}$$

$$\nabla \times \tilde{\mathbf{H}} = \mathbf{J}_{\text{free}} + \frac{\partial \tilde{\mathbf{D}}}{\partial t} \qquad \text{(Ampère-Maxwell law)} \tag{58}$$

where the tilde indicates rapid oscillations in time. We assume no free electron charges $\rho_{\text{free}} = 0$ and no free currents $\mathbf{J}_{\text{free}} = 0$. Further, the material should not possess a magnetic response with $\tilde{\mathbf{B}} = \mu_0 \tilde{\mathbf{H}}$.

We take the curl of the Faraday's law equation (Eq. (57))

$$\nabla \times \nabla \times \tilde{\mathbf{E}} = -\nabla \times \frac{\partial \tilde{\mathbf{B}}}{\partial t} = -\frac{\partial}{\partial t} \nabla \times \tilde{\mathbf{B}} = -\mu_0 \frac{\partial}{\partial t} \nabla \times \tilde{\mathbf{H}} \tag{59}$$

and use the equation $\nabla \times \tilde{\mathbf{H}} = \frac{\partial \tilde{\mathbf{D}}}{\partial t}$ (Eq. (56)) and the identity

$$\nabla \times \nabla \times \tilde{\mathbf{E}} = \nabla(\nabla \cdot \tilde{\mathbf{E}}) - \nabla^2 \tilde{\mathbf{E}} \tag{60}$$

and assume that from Gauss's law $\nabla \cdot \tilde{\mathbf{D}} = 0$ follows $\nabla \cdot \tilde{\mathbf{E}} = 0$, which according to Boyd (4th edition, pp. 71-72) is not necessarily true for nonlinear optics, but good enough, especially in the slowly-varying amplitude approximation (SVEA) [26] . Then the first term on the right-hand side of Eq. (60) vanishes and we end up with

$$\nabla^2 \tilde{\mathbf{E}} - \mu_0 \frac{\partial^2}{\partial t^2} \tilde{\mathbf{D}} = 0 \tag{61}$$

The electric displacement field $\tilde{\mathbf{D}} = \epsilon_0 \tilde{\mathbf{E}} + \tilde{\mathbf{P}}$ contains the electric field as well as the full material response $\tilde{\mathbf{P}}$. The material response can be separated into two main components, the linear and the nonlinear part $\tilde{\mathbf{P}} = \tilde{\mathbf{P}}^{(1)} + \tilde{\mathbf{P}}^{\text{NL}}$. We define the linear electric displacement as $\tilde{\mathbf{D}}^{(1)} = \epsilon_0 \tilde{\mathbf{E}} + \tilde{\mathbf{P}}^{(1)}$ and insert $\tilde{\mathbf{D}} = \tilde{\mathbf{D}}^{(1)} + \tilde{\mathbf{P}}^{(\text{NL})}$ into Eq. (61), yielding

$$\nabla^2 \tilde{\mathbf{E}} - \frac{1}{\epsilon_0 c^2} \frac{\partial^2}{\partial t^2} \tilde{\mathbf{D}}^{(1)} = \frac{1}{\epsilon_0 c^2} \frac{\partial^2}{\partial t^2} \tilde{\mathbf{P}}^{\text{NL}} \ , \tag{62}$$

where we used $\mu_0 = 1/\epsilon_0 c^2$. The fields in the above equation are functions of space and time, e.g. $\tilde{\mathbf{D}}^{(1)} = \tilde{\mathbf{D}}^{(1)}(x, y, z, t)$. Since the aim here is to work only in the temporal domain, the dependencies on x and y can be dropped. As usual, z is defined as the direction of propagation. Thus, in the first term on the l.h.s. of equation (62), the ∇^2 becomes $\frac{\partial^2}{\partial z^2}$ and the fields are now scalar and not vectors anymore. The new equation reads

$$\frac{\partial^2}{\partial z^2} \tilde{E}(z,t) - \frac{1}{\epsilon_0 c^2} \frac{\partial^2}{\partial t^2} \tilde{D}^{(1)}(z,t) = \frac{1}{\epsilon_0 c^2} \frac{\partial^2}{\partial t^2} \tilde{P}^{\text{NL}}(z,t) \ , \tag{63}$$

where $\tilde{E}(z,t)$ is the full electric field including both the fundamental and the SH field. The term $\tilde{D}^{(1)}(z,t)$ is the linear dielectric displacement and $\tilde{P}^{\mathrm{NL}}(z,t)$ is the nonlinear polarization of the material. The constants ϵ_0 and c are the dielectric constant and the speed of light in vacuum respectively. Now the fields can be expanded into their constituents. It is important to note that each constituent in this treatment is distinct from each other, meaning that these fields don't overlap in the spectral domain and are not degenerate in any way.

4.3.2 Fourier expansions of the fields

The expanded fields into their distinct field components can be written as the sums of their components

$$\tilde{E}(z,t) = \frac{1}{2}\sum_p E_p(z,t) + \text{c.c.} \tag{64}$$

$$\tilde{D}^{(1)}(z,t) = \frac{1}{2}\sum_p D_p^{(1)}(z,t) + \text{c.c.} \tag{65}$$

$$\tilde{P}(z,t) = \frac{1}{2}\sum_p P_p(z,t) + \text{c.c.} \tag{66}$$

where the indices p run over all fields that potentially couple to each other via some nonlinear interaction and c.c. stands for the complex conjugate. For a three-wave mixing process in a second-order nonlinear interaction, $p = 1, 2, 3$ and for a second-harmonic generation process, $p = 1$ stands for the fundamental and $p = 2$ for the second-harmonic field. Inserting equations Eqs. (64)-(66) into Eq. 63, the evolution equation for each distinct field is

$$\frac{\partial^2}{\partial z^2}E_p(z,t) - \frac{1}{\epsilon_0 c^2}\frac{\partial^2}{\partial t^2}D_p^{(1)}(z,t) = \frac{1}{\epsilon_0 c^2}\frac{\partial^2}{\partial t^2}P_p^{\mathrm{NL}}(z,t)\ , \tag{67}$$

omitting the complex conjugates. The left-hand side of Eq. (67) describes the linear propagation of one of the distinct fields (i.e. "pulses"), while the right hand side acts as a source term, where the pth field couples to the other field via the nonlinear polarization P_p^{NL}. The nonlinear polarization term incorporates all nonlinear interaction effects that do not include free electric charges or charge transfers, since the terms ρ_{free} and $\mathbf{J}_{\mathrm{free}}$. The specific shape of P_p^{NL} for certain interaction such as SHG will be discussed in the next section. We further expand each distinct field $\tilde{E}_p(z,t)$ and $D_p^{(1)}(z,t)$ into their Fourier components

$$E_p(z,t) = \int_{-\infty}^{\infty} E_p'(z,\bar{\omega}_p+\omega)\,\mathrm{e}^{-i(\bar{\omega}_p+\omega)t}\,d\omega \tag{68}$$

$$D_p^{(1)}(z,t) = \int_{-\infty}^{\infty} D_p^{'(1)}(z,\bar{\omega}_p+\omega)\,\mathrm{e}^{-i(\bar{\omega}_p+\omega)t}\,d\omega\ \ . \tag{69}$$

The prime indicates the Fourier transformed fields and the frequencies $\bar{\omega}_p$ stand for the central frequencies of the fields. The Fourier-expanded fields in Eqs. (68) - (69) can be written in terms of the complex amplitudes $E_p'(z,\bar{\omega}_p+\omega) = A_p(z,\omega)\,\mathrm{e}^{ik_p(\bar{\omega}_p+\omega)z}$

$$E_p(z,t) = \int_{-\infty}^{\infty} A_p(z,\omega)\,\mathrm{e}^{ik_p(\bar{\omega}_p+\omega)z}\,\mathrm{e}^{-i(\bar{\omega}_p+\omega)t}\,d\omega \tag{70}$$

$$D_p^{(1)}(z,t) = \int_{-\infty}^{\infty} \epsilon_0 n_p^2(\bar{\omega}_p+\omega)A_p(z,\omega)\,\mathrm{e}^{ik_p(\bar{\omega}_p+\omega)z}\,\mathrm{e}^{-i(\bar{\omega}_p+\omega)t}\,d\omega\ \ , \tag{71}$$

where we use that $D_p^{'(1)}(z,\bar{\omega}_p+\omega) = \epsilon_0 n_p^2(\bar{\omega}_p+\omega)E'_p(z,\bar{\omega}_p+\omega)$. The wavenumber is defined as $k_p(\bar{\omega}_p+\omega) = n(\bar{\omega}_p+\omega)\ (\bar{\omega}_p+\omega)/c$. Now plugging the expressions (70) and (71) into the r.h.s. of Eq. (67) and employing the slowly-varying envelope approximation $|\frac{\partial^2}{\partial z^2}A_p(z,\omega)| \ll |k_p(\omega)\frac{\partial}{\partial z}A_p(z,\omega)|$ (SVEA) for both fields, we arrive at two (coupled) evolution equations for the complex electric field amplitudes

$$2i\int \Big[\frac{\partial}{\partial z}A_p(z,\omega)\Big]k_p(\omega)\ \mathrm{e}^{i(k_p(\omega)z-(\bar{\omega}_p+\omega)t)}\,d\omega = \frac{1}{\epsilon_0 c^2}\frac{\partial^2}{\partial t^2}P_p^{\mathrm{NL}}(z,t)\ . \tag{72}$$

Equation (72) acts as a starting point for further derivations for analytical equations describing the evolution of the fields for different second-order nonlinear processes, such as SHG, DFG or SFG. For each interaction the nonlinear polarization $P_p^{\mathrm{NL}}(z,t)$ takes a specific form. We continue this treatment specifically for SHG, as it is the main focus of this work.

4.3.3 Coupled wave equations for second-harmonic generation

The second-harmonic generation process can be regarded as a three-wave mixing process such as SFG, where the the two mixing fields creating the third are fully degenerate. Therefore, two electric fields $E(z,t) = \frac{1}{2}(E_1(z,t)+E_2(z,t))$ (Eq. (64)) are involved in the process. For an SHG process where the two (here degenerate) fundamental fields are polarized orthogonally to the second-harmonic field, commonly referred to as type I phase-matching [157], the polarizations can be written as [26]

$$P_1^{\mathrm{NL}}(z,t) = 4\epsilon_0 d_{\mathrm{eff}}\ E_1^*(z,t)\cdot E_2(z,t) \tag{73}$$

$$P_2^{\mathrm{NL}}(z,t) = 2\epsilon_0 d_{\mathrm{eff}}\ E_1(z,t)\cdot E_1(z,t)\ . \tag{74}$$

Inserting the Fourier decompositions of E_1 and E_2 in Eq. (70) into the r.h.s., then plugging Eqs. (73) and (74) into Eq. (72) yields the evolution equations, one for the complex amplitudes A_1 of the fundamental and the other one for the amplitude A_2 of the second-harmonic field. For simplicity, we treat only the equation for A_2 for now, since the treatment is analogous for A_1. The equation for A_2 then reads

$$2i\int k_2(\omega)\Big(\frac{\partial}{\partial z}A_2(z,\omega)\Big)\ \mathrm{e}^{i(k_2(\omega)z-(\bar{\omega}_2+\omega)t)}\,d\omega = \tag{75}$$

$$= -\frac{2d_{\mathrm{eff}}}{c^2}\iint_{-\infty}^{\infty}(2\bar{\omega}_1+\omega'+\omega'')^2\ A_1(z,\omega')A_1(z,\omega'')\,\mathrm{e}^{i[k_1(\omega')+k_1(\omega'')]z}\mathrm{e}^{-i(2\bar{\omega}_1+\omega'+\omega'')t}\,d\omega'\,d\omega''\ , \tag{76}$$

where the time-derivatives $\partial^2/\partial t^2$ on $P^{\mathrm{NL}}(z,t)$ were performed. Due to energy conservation, the frequencies on the left hand side of the equation above must be the sum of the frequencies of the fields on the r.h.s., i.e. $\bar{\omega}_2+\omega = \bar{\omega}_1+\omega'+\bar{\omega}_1+\omega''$. We also identify the center frequency as $\bar{\omega}_2 = 2\bar{\omega}_1$ and thus $\omega'' = \omega-\omega'$ and $d\omega'' = d\omega'$. Inserting these relations into the equation above yields

$$2i\int k_2(\omega)\Big(\frac{\partial}{\partial z}A_2(z,\omega)\Big)\ \mathrm{e}^{i(k_2(\omega)z-(\bar{\omega}_2+\omega)t)}\,d\omega =$$

$$= -\frac{2d_{\mathrm{eff}}(\bar{\omega}_2+\omega)^2}{c^2}\iint_{-\infty}^{\infty}A_1(z,\omega')A_1(z,\omega-\omega')\,\mathrm{e}^{i[k_1(\omega')+k_1(\omega-\omega')]z}\mathrm{e}^{-i(2\bar{\omega}_1+\omega)t}\,d\omega'\,d\omega\ , \tag{77}$$

which, by omitting the integrals $\int d\omega$ on both sides yields the evolution equation for each single frequency component ω for the second-harmonic amplitudes A_2, as well as, - in an analogous

treatment - the amplitudes A_1 of the fundamental field

$$\frac{\partial}{\partial z}A_1(z,\omega) = i\frac{2(\bar{\omega}_1+\omega)d_{\text{eff}}}{n_1(\omega)c}\int_{-\infty}^{\infty} A_1^*(z,\omega')A_2(z,\omega+\omega')\,\mathrm{e}^{-i\Delta k(\omega,\omega')z}\,d\omega' \tag{78}$$

$$\frac{\partial}{\partial z}A_2(z,\omega) = i\frac{(\bar{\omega}_2+\omega)d_{\text{eff}}}{n_2(\omega)c}\int_{-\infty}^{\infty} A_1(z,\omega')A_1(z,\omega-\omega')\,\mathrm{e}^{i\Delta k(\omega,\omega')z}\,d\omega'\ , \tag{79}$$

where we used $k_p(\omega) = n_p(\omega)\ (\bar{\omega}_p+\omega)/c$. The term

$$\Delta k(\omega,\omega') := k_1(\omega') + k_1(\omega-\omega') - k_2(\omega) \tag{80}$$

is the material-dependent wavevector-mismatch. The phase-mismatch after propagation through a material with length L is simply $\Delta\varphi = \Delta k \cdot L$ and thus

$$\Delta\varphi(\omega,\omega') := \varphi_1(\omega') + \varphi_1(\omega-\omega') - \varphi_2(\omega)\ . \tag{81}$$

Equations (78) and (79) determine the evolution of the fundamental and second-harmonic amplitude in a nonlinear medium. Since the accumulated phase in a medium will play an important role, we transform these equation into their electric field representations $E_p(z,\omega) = A_p(z,\omega)\,\mathrm{e}^{-k_p(\omega)z}$. Inserting this relation into Eqs. (78) and (79) yields

$$\frac{\partial}{\partial z}E_1(z,\omega) = ik_1E_1(z,\omega) + i\frac{2(\bar{\omega}_1+\omega)d_{\text{eff}}}{n_1(\omega)c}\int_{-\infty}^{\infty} E_1^*(z,\omega')E_2(z,\omega+\omega')\,d\omega' \tag{82}$$

$$\frac{\partial}{\partial z}E_2(z,\omega) = ik_2E_2(z,\omega) + i\frac{(\bar{\omega}_2+\omega)d_{\text{eff}}}{n_2(\omega)c}\int_{-\infty}^{\infty} E_1(z,\omega')E_1(z,\omega-\omega')\,d\omega'\ . \tag{83}$$

In the next section, the non-depleting pump approximation will be applied in order to arrive at an analytical equation for the second-harmonic field evolution in the SHG-MPC.

4.3.4 Equation for SHG in MPCs in the non-depleting pump approximation

In this section, we develop a simplified analytical model for the SHG-MPC. In order to solve the equation for the complex second-harmonic amplitude Eq. (79), we make the assumption of a non-depleting fundamental pulse by setting the equation for amplitude of the fundamental field (Eq. (78)) to

$$\frac{\partial}{\partial z}A_1(z,\omega) = 0\ . \tag{84}$$

Using this relation and inserting $A_1(z,\omega) = E_1(z,\omega)\,\mathrm{e}^{-ik_1(\omega)z}$, Eq. (82) results in the non-depleting evolution equation for the electric field of the fundamental beam

$$\frac{\partial}{\partial z}E_1(z,\omega) = ik_1(\omega)E_1(z,\omega)\ , \tag{85}$$

which can be immediately solved such that

$$E_1(z,\omega) = E_1(z_0,\omega)\,\mathrm{e}^{ik_1(\omega)(z-z_0)}\ , \tag{86}$$

where we choose $z_0 = 0$. Thus, the amplitude fundamental field is unchanged, i.e. non-depleting, and the phase evolves depending on the linear response of the material the field propagates in. In the SHG-MPC, two different types of material are present: the crystal in the center of the MPC that is the nonlinear medium and the rest of the MPC, for example the gas and the mirrors, where the propagation is purely linear. The contribution to the phase of the fundamental field from the

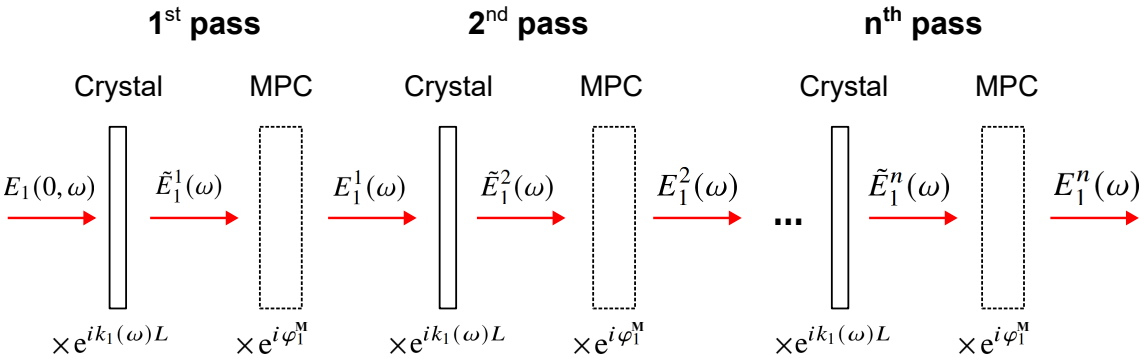


Figure 28: Schematical representation of the evolution of the non-depleting fundamental field $E_1(\omega)$, as in equations (89) and (90).

passage through a distance z the crystal is denoted here by $k_1(\omega)z$, while the contributions from the linear part of the MPC are summarized in φ_1^{M}. Thus, after propagation through the crystal with length L, the fundamental field is

$$\tilde{E}_1(L,\omega) = E_1(0,\omega)\,\mathrm{e}^{ik_1(\omega)L}\ , \tag{87}$$

where we denote the field right at the exit of the crystal with a tilde. After subsequent propagation through the MPC excluding the crystal, the field acquires the phase denoted by $\varphi_1^M(\omega)$

$$E_1(L,\omega) = \tilde{E}_1(L,\omega)\mathrm{e}^{i\varphi_1} = E_1(0,\omega)\,\mathrm{e}^{i(k_1(\omega)L+\varphi_1^M(\omega))}\ . \tag{88}$$

After n passes, we define the fundamental field after n passes through the MPC

$$E_1^n(\omega) = E_1(\omega)\,\mathrm{e}^{in[k_1(\omega)L+\varphi_1^M(\omega)]}\ , \tag{89}$$

with the initial fundamental field $E(\omega) := E_1(0,\omega)$ and $\varphi_1(\omega) := k_1(\omega)L + \varphi_1^M(\omega)$. This describes the evolution of the non-depleting fundamental field. After n passes through the MPC system, the fundamental field simply acquired the accumulated linear phase of $n\,\varphi_1(\omega)$. Figure 28 schematically shows the evolution of the non-depleting fundamental field. The fundamental field after n passes through the SHG-MPC system is then given by

$$E_1^n(z,\omega) = E_1^n(\omega)\,\mathrm{e}^{ik_1(\omega)z} = E_1(\omega)\,\mathrm{e}^{in\varphi_1(\omega)}\mathrm{e}^{ik_1(\omega)z}\ . \tag{90}$$

The evolution of the second-harmonic field is governed by Eq. (83), which is a non-homogeneous, first-order ordinary differential equation in z of the form $\frac{\partial}{\partial z}y(z) = a(z)y(z) + b(z)$. This type of equation has the general solution

$$y(z) = \left(\int_{z_0}^{z} b(z')\,\mathrm{e}^{-\int_{z_0}^{z'} a(z'')\mathrm{d}z''}\,\mathrm{d}z' + c\right)\mathrm{e}^{\int_{z_0}^{z} a(z')\mathrm{d}z'}\ . \tag{91}$$

In Eq. (91), we associate the functions and coefficients by comparing it to Eq. (83)

$$y(z) = E_2(z,\omega)\ , \quad a(z) = ik_2(\omega)\ , \quad c = E_2(z_0,\omega) \tag{92}$$

$$b(z) = i\tilde{c}\int_{-\infty}^{\infty} E_1(z,\omega')E_1(z,\omega-\omega')\,d\omega'\ , \tag{93}$$

where we set $\tilde{c} := \frac{(\bar{\omega}_2+\omega)d_{\text{eff}}}{n_2(\omega)c}$ and the constant $c = E_2(z_0,\omega)$ is the initial second-harmonic field at the entrance of the crystal. This results in the solution

$$E_2(z,\omega) = \left(\int_{z_0}^{z} i\tilde{c} \int E_1(z',\omega')E_1(z',\omega-\omega')\,\mathrm{e}^{-ik_2(\omega)(z'-z_0)}\;\mathrm{d}\omega'\,\mathrm{d}z' + E_2(z_0,\omega)\right) \times \\ \times\, \mathrm{e}^{ik_2(\omega)(z-z_0)}\;, \tag{94}$$

In a similar treatment as for the fundamental field, the first pass through the nonlinear medium is calculated by setting $z_0 = 0$ and $z = L$ and $E(0,\omega) = 0$ as the initial condition

$$E_2(L,\omega) = \Big(\int_0^L i\tilde{c} \int E_1(z,\omega')E_1(z,\omega-\omega')\,\mathrm{e}^{-ik_2(\omega)z}\;\mathrm{d}\omega'\,\mathrm{d}z\Big)\,\mathrm{e}^{i(k_2(\omega)L+\varphi_2^M(\omega))} \tag{95}$$

$$= \Big(\int_0^L i\tilde{c} \int E_1(\omega')E_1(\omega-\omega')\,\mathrm{e}^{i\Delta k(\omega,\omega')z}\;\mathrm{d}\omega'\,\mathrm{d}z\Big)\,\mathrm{e}^{i\varphi_2(\omega)}\;, \tag{96}$$

where again $\Delta k(\omega,\omega') = k_1(\omega') + k_1(\omega-\omega') - k_2(\omega)$ and $\varphi_2(\omega) = k_2(\omega)L + \varphi_2^M(\omega)$ is the phase the second-harmonic field accumulates in a single pass in the MPC. To simplify calculations, we define the n-th pass integral as

$$dE^n := \int_0^L i\tilde{c} \int E_1^n(z,\omega')E_1^n(z,\omega-\omega')\,\mathrm{e}^{-ik_2(\omega)z}\;\mathrm{d}\omega'\,\mathrm{d}z \tag{97}$$

$$= \int_0^L i\tilde{c} \int E_1(\omega')\,\mathrm{e}^{in\varphi_1(\omega')}E_1(\omega-\omega')\,\mathrm{e}^{in\varphi_1(\omega-\omega')}\,\mathrm{e}^{i\Delta k(\omega,\omega')z}\;\mathrm{d}\omega'\,\mathrm{d}z \tag{98}$$

$$= \tilde{c}\int E_1(\omega')E_1(\omega-\omega')\,\frac{\mathrm{e}^{i\Delta k(\omega,\omega')L}-1}{\Delta k(\omega,\omega')}\;\mathrm{e}^{in[\varphi_1(\omega')+\varphi_1(\omega-\omega')]}\;\mathrm{d}\omega'\;, \tag{99}$$

where the integral over z from 0 to L was carried out in the last step and we used Eq. (90) for $E_1^n(z,\omega)$. With the above definition, the propagation through the MPC is divided into a nonlinear part, where a field dE^n is added to the second-harmonic field E_2^{n-1} and a linear part, where the linear phases are multiplied onto the resulting field $E_2^n = (E_2^{n-1} + dE^n)\cdot \mathrm{e}^{i\varphi_1(\omega)}$. Figure 29 illustrates the calculation scheme that is used here. For simplicity, we start with the very first pass through the MPC and rewrite Eq. (96) using the definition (99), which writes

$$E_2^1(\omega) = dE^1\mathrm{e}^{i\varphi_2}\;, \tag{100}$$

And then for the second pass

$$E_2^2(\omega) = (dE^2 + dE^1\mathrm{e}^{i\varphi_2})\mathrm{e}^{i\varphi_2}\;, \tag{101}$$

and for N passes

$$E_2^N(\omega) = (dE^N + (dE^{N-1} + (dE^{N-2} + \dots)\mathrm{e}^{i\varphi_2})\mathrm{e}^{i\varphi_2})\mathrm{e}^{i\varphi_2}\;. \tag{102}$$

This recursive formula can be expressed explicitly in a sum

$$E_2^N(\omega) = \sum_{n=0}^{N} dE^N\,\mathrm{e}^{i(N-n)\varphi_2}\;, \tag{103}$$

where $dE^0 = 0$. Inserting the definition (99) for dE^n results in

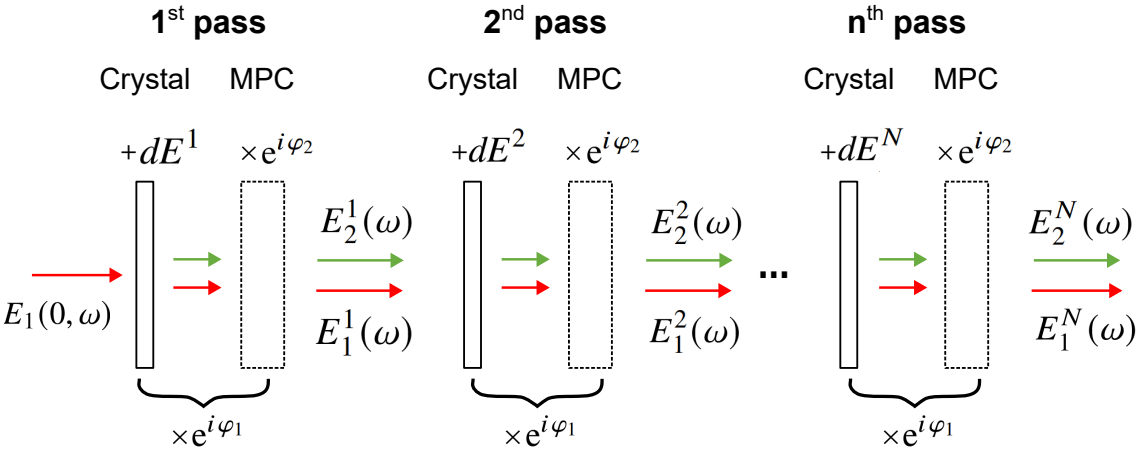


Figure 29: Schematic of the solution to the evolution equation (94) of the second-harmonic electric field in the non-depleting pump approximation. The solution of Eq. (94) is done consecutively by first calculating the nonlinear part, adding dE_2^n to the second-harmonic field and then multiplying the phase $e^{i\varphi_2}$ originating from the linear interactions. In the lower part, the schematic evolution of the non-depleting fundamental field is shown, which propagates linearly in this approximation and only acquires a phase of $e^{i\varphi_1}$ per pass, according to Eq. (90).

$$E_2^N = \sum_{n=0}^{N} \tilde{c} \int_{-\infty}^{\infty} E_1(\omega')E_1(\omega-\omega') \frac{e^{i\Delta kL}-1}{\Delta k(\omega,\omega')} e^{in[\varphi_1(\omega')+\varphi_1(\omega-\omega')]} e^{i(N-n)\varphi_2(\omega)}\, d\omega' \tag{104}$$

$$= \tilde{c}\, e^{iN\varphi_2(\omega)} \int_{-\infty}^{\infty} E_1(\omega')E_1(\omega-\omega') \frac{e^{i\Delta kL}-1}{\Delta k(\omega,\omega')} \sum_{n=0}^{N} \left(e^{i\Delta\varphi(\omega)}\right)^n \mathrm{d}\omega' \,, \tag{105}$$

where we wrote the relative phase between fundamental and second-harmonic as $\Delta\varphi = \varphi_1(\omega') + \varphi_1(\omega-\omega') - \varphi_2(\omega)$ as in Eq. (81). The sum in the integral can be identified as the partial geometric sum of the form $\sum_{n=0}^{k} s^n = \frac{1-s^{k+1}}{1-s}$. Applying this relation to Eq. (105) results in

$$E_2^N(\omega) = \tilde{c}\, e^{iN\varphi_2(\omega)} \int_{-\infty}^{\infty} E_1(\omega')E_1(\omega-\omega') \frac{e^{i\Delta k(\omega,\omega')L}-1}{\Delta k(\omega,\omega')} \frac{1-e^{iN\Delta\varphi(\omega,\omega')}}{1-e^{i\Delta\varphi(\omega,\omega')}} d\omega' \,. \tag{106}$$

In order to further progress with the analytic equation and solve the integral over ω', it is now necessary to linearize the phase terms inside the integral with respect to ω and ω'. Up to linear order, the integral can still be solved analytically without any further approximations. As we will show later, evaluating the integral while including higher-order phase expansions requires further approximations. In the following the linearization of the phase terms in the integral in Eq. (106) are discussed.

4.3.5 Linearization of the phase-terms

The phase terms in equation (106) are expanded up to their first order in ω. The first term is the crystal dispersion described by the relative wavenumber $\Delta k(\omega,\omega') = k_1(\omega') + k_1(\omega-\omega') - k_2(\omega)$. Here we expand each term individually around their central frequency ω_p with $p = 1, 2$. Since we defined $k_p(\omega) \equiv k_p(\bar{\omega}_p + \omega)$, where $\bar{\omega}_p$ is the center frequency of fundamental ($p = 1$) or the second harmonic ($p = 2$), the expansions are

$$k_1 = k_1(\bar{\omega}_1 + \omega) \approx k_1^{(0)} + k_1^{(1)}\omega \tag{107}$$

$$k_2 = k_2(\bar{\omega}_2 + \omega) \approx k_2^{(0)} + k_2^{(1)}\omega \tag{108}$$

and similarly for the phases accumulated outside of the crystal in the MPC

$$\varphi_1 = \varphi_1(\bar{\omega}_1 + \omega) \approx \varphi_1^{(0)} \; + \; \varphi_1^{(1)}\omega \tag{109}$$

$$\varphi_2 = \varphi_2(\bar{\omega}_2 + \omega) \approx \varphi_2^{(0)} \; + \; \varphi_2^{(1)}\omega \; , \tag{110}$$

so that we can expand both the relative wavenumber $\Delta k(\omega, \omega')$ (Eq. (80))

$$\begin{aligned}\Delta k(\omega,\omega') =& k_1(\omega') + k_1(\omega-\omega') - k_2(\omega') \approx \\ &\approx \; k_1^{(0)} \; + \; k_1^{(1)}\omega' + k_1^{(0)} \; + \; k_1^{(1)}(\omega-\omega') - k_2^{(0)} \; + \; k_2^{(1)}\omega \\ &= \; 2k_1^{(0)} - k_2^{(0)} \; + \; (k_1^{(1)} - k_2^{(1)})\omega \\ \\ \Leftrightarrow \qquad & \Delta k(\omega) := \; \Delta k^{(0)} \; + \; \Delta k^{(1)}\omega \end{aligned} \tag{111}$$

and analogously the phase terms $\Delta\varphi(\omega, \omega')$ (Eq. (81))

$$\Delta\varphi(\omega) := \; \Delta\varphi^{(0)} \; + \; \Delta\varphi^{(1)}\omega \; , \tag{112}$$

where it shows that both terms are now independent of ω' and thus can be taken out if the integral in Eq. (106).

4.3.6 Analytic SHG-MPC equation

Now inserting the linearized phase terms in Eqs. (111) and (112) into the formula Eq. (72)

$$E_2^N(\omega) = \tilde{c} \int_{-\infty}^{\infty} E_1(\omega')E_1(\omega-\omega') \; \frac{\mathrm{e}^{i\Delta k(\omega)L} - 1}{\Delta k(\omega)} \; \frac{1 - \mathrm{e}^{i(\Delta k(\omega)L + \Delta\varphi(\omega))\,N}}{1 - \mathrm{e}^{i(\Delta k(\omega)L + \Delta\varphi(\omega))}} \, d\omega'. \tag{113}$$

and taking the phase terms out of the integral, the evolution equation becomes

$$E_2^N(\omega) = \tilde{c} \; \frac{\mathrm{e}^{i\Delta k(\omega)L} - 1}{\Delta k(\omega)} \; \frac{1 - \mathrm{e}^{i\Delta\varphi(\omega)\,N}}{1 - \mathrm{e}^{i\Delta\varphi(\omega)}} \int_{-\infty}^{\infty} E_1(\omega')E_1(\omega-\omega') \, d\omega' \; , \tag{114}$$

where one can immediately identify the convolution integral $E_1(\omega) * E_1(\omega) := \int_{-\infty}^{\infty} E_1(\omega')E_1(\omega - \omega') \, d\omega'$, such that the above equation can be re-written into

$$E_2^N(\omega) = \tilde{c} \; \frac{\mathrm{e}^{i\Delta k(\omega)L} - 1}{\Delta k(\omega)} \cdot \frac{1 - \mathrm{e}^{i\Delta\varphi(\omega)N}}{1 - \mathrm{e}^{i\Delta\varphi(\omega)}} \cdot \big[E_1(\omega) \, * \, E_1(\omega)\big] \; . \tag{115}$$

We further turn Eq. (115) into an equation for the intensity by $I_2^N(\omega) = \frac{n(\omega)\eta_0 c_0}{2}|E_2^N(\omega)|^2$ and $|\tilde{c}_2|^2 := \frac{\epsilon_0 c_0 \, n_2(\omega)}{2}|\tilde{c}|^2$

$$\boxed{I_2^N(\omega) = |\tilde{c}_2|^2 L^2 \; \mathrm{sinc}^2\big(\Delta k(\omega)L\big) \cdot \; |E_1(\omega) * E_1(\omega)|^2 \cdot \; |\Phi^N(\Delta\varphi)|^2} \tag{116}$$

$$\text{with} \qquad \Phi^N(\Delta\varphi) := \frac{1 - \mathrm{e}^{i\Delta\varphi(\omega)\,N}}{1 - \mathrm{e}^{i\Delta\varphi(\omega)}} \; . \tag{117}$$

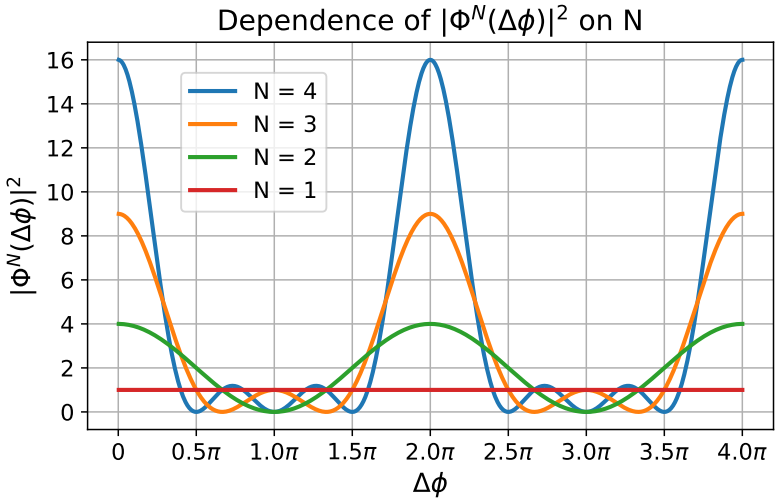


Figure 30: The function $|\Phi^N(\Delta\varphi)|^2$ appearing in Eq. 118 plotted as a function of the relative phase $\Delta\varphi$ between fundamental and SH per pass for different numbers of passes N.

Taking the absolute square, the factor $|\Phi^N(\Delta\varphi)|^2$ can be simplified to

$$|\Phi^N(\Delta\varphi)|^2 = \frac{\sin^2\left\{\frac{N}{2}\Delta\varphi(\omega)\right\}}{\sin^2\left\{\Delta\varphi(\omega)\right\}} \ , \tag{118}$$

which is the oscillating factor arising from the periodic passes through the MPC system, or a quasi-waveguide in general, where the nonlinear medium is placed in the center of each pass, and where outside of the crystal the propagation is purely linear.
The oscillating function $|\Phi^N(\Delta\varphi)|^2$ represents the contribution of the multi-pass cavity (MPC) geometry. This function depends explicitly on the number of passes N and the total accumulated phase shift per pass $\Delta\varphi(\omega)$. Figure 30 illustrates how $|\Phi^N(\Delta\varphi)|^2$ varies with both $\Delta\varphi(\omega)$ and N. For the case of a single pass ($N = 1$), the function simplifies to $|\Phi^1(\Delta\varphi)|^2 = 1$, and equation (116) describes single-pass second harmonic generation

$$I_2^N(\omega) = |\tilde{c}_2|^2 L^2 \ \mathrm{sinc}^2\big(\Delta k(\omega)L\big) \cdot \ |E_1(\omega) * E_1(\omega)|^2 \tag{119}$$

for a medium with length L. When $N > 1$, the function becomes modulated, exhibiting a main maximum at $\Delta\varphi_{\mathrm{pass}} = 2\pi \cdot n$, where n is an integer. Additionally, there are $N-2$ minor maxima and $N-1$ minima within a 2π interval. The positions of these minima can be determined from the numerator of $|\Phi^N|^2$, which locates minima at $\Delta\varphi = 2\pi/N \cdot n$ with $n = 1, .., N-1$. On the other hand, the locations of the minor maxima cannot be easily derived analytically. Furthermore, the height of the main maxima scales proportionally to N^2. This quadratic dependence indicates that when the medium is traversed N times, the phase-matched second harmonic generation efficiency increases quadratically with N, leading to the same enhancement as in an N times longer crystal, assuming phase-matching and negligible depletion of the fundamental field.

This characteristic behavior is observed in both the simulated spectrograms, such as Fig. 27, and the experimental spectrograms, such as Fig. 37 in Section 4.4, recorded as functions of the ambient gas pressure (p) and optical frequency ω at a fixed crystal angle θ. It manifests as the modulation patterns in the spectrograms, originating from the properties of $|\Phi^N(\Delta\varphi)|^2$. Figure 31 illustrates how these spectrograms can be decomposed into the spectral part $|E_1(\omega) * E_1(\omega)|^2$, with Gaussian pulses as $E_1(\omega)$ and the MPC part $|\Phi^N(\Delta\varphi(p))|^2$ as a function of the total accumulated relative phase per pass $\Delta\varphi(p)$, tuned by the parameter p. Here we see that the resulting spectrogram

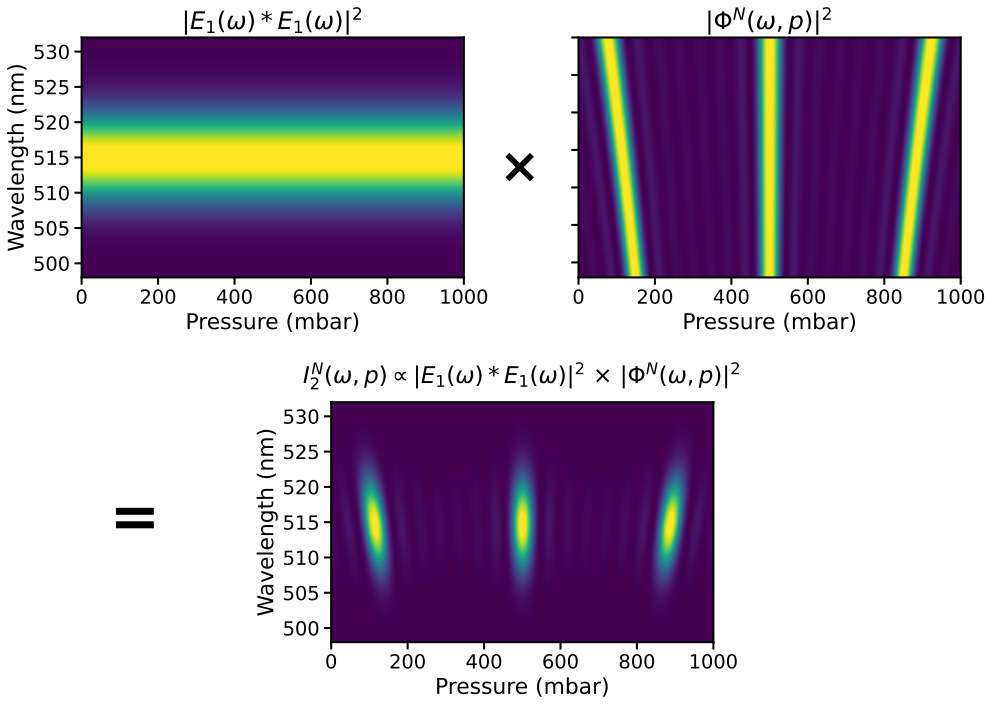


Figure 31: Figure illustrating the origin of the features of the pressure spectrograms similar to the experiments. Multiplying $|E_1(\omega) * E_1(\omega)|^2$ (upper left), which we chose here to be Gaussian shaped, with $|\Phi^N(\Delta\varphi(p))|^2$ (upper right) results in the typical shape of the spectrogram (lower plot), which plots the second-harmonic spectral intensity $I_2^N(\omega)$ (Eq. 116) over pressure p.

fundamentally is comprised of these two contributions.

4.3.7 Comparison of the analytical model to experimental data

We compare the analytical model derived in the previous section to the experimental results in the main manuscript. Since in the experiment, we use the mirrors to compensate for group delay (GD) and furthermore the crystal angle θ and the gas pressure p to fine-tune phase- and GD-matching, the linearized phase-terms will be comprised of the contributions

$$\Delta\varphi^\omega(\theta, p) = \underbrace{\Delta\varphi^\omega_{\mathrm{cr}}(\theta)}_{\text{Crystal}} + \underbrace{\Delta\varphi^\omega_{\mathrm{gas}}(p)}_{\text{Gas}} + \underbrace{\Delta\varphi^\omega_{\mathrm{m}}}_{\text{Mirror}} , \tag{120}$$

where we follow the main manuscript and superscript the ω dependency, since the relevant tuning parameters are now θ and p. For better overview, we define $\Delta\varphi^\omega_{\mathrm{cr}}(\theta) := \Delta k^\omega_{\mathrm{cr}}(\theta) L$. Each relative phase contribution now is comprised of a 0^{th} order and 1^{st} order in the following way

$$\Delta\varphi^\omega_{\mathrm{cr}}(\theta) = \Delta\varphi^{(0)}_{\mathrm{cr}}(\theta) + \Delta\varphi^{(1)}_{\mathrm{cr}}(\theta)\ \omega \tag{121}$$

$$\Delta\varphi^\omega_{\mathrm{gas}}(p) = \Delta\varphi^{(0)}_{\mathrm{gas}}(p) + \Delta\varphi^{(1)}_{\mathrm{gas}}(p)\ \omega \tag{122}$$

$$\Delta\varphi^\omega_{\mathrm{m}} = \Delta\varphi^{(0)}_{\mathrm{m}} + \Delta\varphi^{(1)}_{\mathrm{m}}\ \omega\ . \tag{123}$$

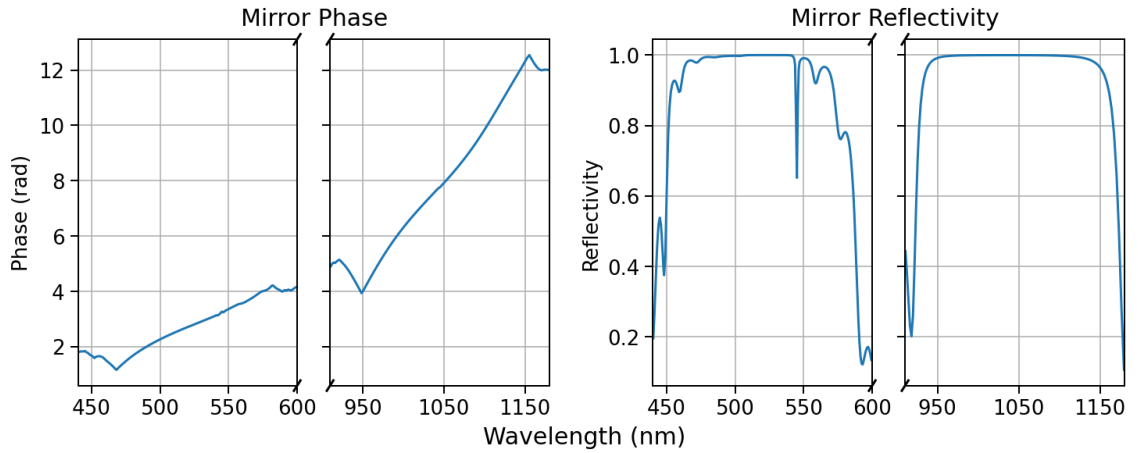


Figure 32: Mirror data for the mirrors used in the experiments and simulations, as provided by the manufacturer LAYERTEC GmbH. Reprinted and modified with permission from [6]

We approximate the θ-dependencies of the crystal terms in the following linearized manner and represent the phase in terms of the wavenumbers

$$\Delta\varphi_{\mathrm{cr}}^{(0)}(\theta) = \Big(\underbrace{\Delta k_{\mathrm{cr}}^{(0)}(\theta_{\mathrm{pm}})}_{\approx\, 0} + \frac{d\Delta k_{\mathrm{cr}}^{(0)}(\theta)}{d\theta}\Big|_{\theta=\theta_{\mathrm{pm}}} \cdot (\theta - \theta_{\mathrm{pm}}) \Big)\, L_{\mathrm{cr}} \tag{124}$$

$$\Delta\varphi_{\mathrm{cr}}^{(1)}(\theta) = \Big(\Delta k_{\mathrm{cr}}^{(1)}(\theta_{\mathrm{pm}}) + \frac{d\Delta k_{\mathrm{cr}}^{(1)}(\theta)}{d\theta}\Big|_{\theta=\theta_{\mathrm{pm}}} \cdot (\theta - \theta_{\mathrm{pm}}) \Big)\, L_{\mathrm{cr}} \ . \tag{125}$$

The first term in Eq. (124) is the phase-mismatch introduced for a single pass through the crystal in phase-matching angle 23.4°, which is naturally very close to zero. The second term in Eq. (124) describes the linear dependency of the phase-mismatch depending on the detuning angle θ. Similarly, the first term in Eq. (124) is the GD-mismatch at phase-matching angle, while the second term is the dependency of the GD-mismatch dependent on the detuning angle θ. The dependency on the pressure in the gas terms can be caluclated by

$$\Delta\varphi_{\mathrm{gas}}^{(0)}(p) = \Delta k_{\mathrm{gas}}^{(0)}(p_{\mathrm{atm}})\, L_{\mathrm{cr}} \cdot \frac{p}{p_{\mathrm{atm}}} \tag{126}$$

$$\Delta\varphi_{\mathrm{gas}}^{(1)}(p) = \Delta k_{\mathrm{gas}}^{(1)}(p_{\mathrm{atm}})\, L_{\mathrm{cr}} \cdot \frac{p}{p_{\mathrm{atm}}} \ . \tag{127}$$

In the gas terms, the dispersion, phase and GD, scale proportionally with the pressure p. Here we set the reference to the atmospheric pressure of $p_{\mathrm{atm}} = 1013\,\mathrm{mbar}$.

Following the experiment described in the main manuscript, we use a $L_{\mathrm{cr}} = 95\,\mu\mathrm{m}$ BBO as the crystal, Krypton as the gas and mirrors with GD compensation. The MPC is comprised of two identical mirrors with ROC of $R = 1\,\mathrm{m}$, $N' = 4$ number of round-trips ($N = 8$ passes) and a length of about $L_{\mathrm{MPC}} = 29.5\,\mathrm{cm}$. We summarize the parameters of the equations (124) - (125) for BBO in Table 1 and the parameters in Eqs. (126)-(127) for krypton in Table 2. We also provide the mirror phase coefficients in table 3. We calculate similar spectrograms following the experimental data.

$\Delta k_{\mathbf{cr}}^{(0)}(\theta_{\mathbf{pm}})$	$\frac{d\Delta k_{\mathbf{cr}}^{(0)}}{d\theta}\big\vert_{\theta=\theta_{\mathbf{pm}}}$	$\Delta k_{\mathbf{cr}}^{(1)}(\theta_{\mathbf{pm}})$	$\frac{d\Delta k_{\mathbf{cr}}^{(1)}}{d\theta}\big\vert_{\theta=\theta_{\mathbf{pm}}}$
$\approx\ 0$	$1.167 \cdot 10^{6}\,(\mathrm{deg\,m})^{-1}$	$-9.15 \cdot 10^{4}\,\mathrm{fs\,m}^{-1}$	$3.62 \cdot 10^{5}\,\mathrm{fs\,(deg\,m)}^{-1}$

Table 1: BBO coefficients. Table showing the coefficients for equations (124) - (125). The reference value for the crystal angle is chosen at the phase-matching angle for BBO at 1030 nm at $\theta_{\mathrm{pm}} = 23.4°$. The values are determined using the Sellmeier-equations from references [158, 159].

In the analytic traces, we use a crystal angle of $\theta = 23.6°$, a number of passes of $N = 8$ and an

$\Delta k^{(0)}_{\mathbf{Kr}}(p_{\mathbf{atm}})$	$\Delta k^{(1)}_{\mathbf{Kr}}(p_{\mathbf{atm}})$	$\Delta k^{(0)}_{\mathbf{Air}}(p_{\mathbf{atm}})$	$\Delta k^{(1)}_{\mathbf{Air}}(p_{\mathbf{atm}})$
$-103.48\,\mathrm{m}^{-1}$	$-87.64\,\mathrm{fs\,m}^{-1}$	$-55.17\,\mathrm{m}^{-1}$	$-46.5\,\mathrm{fs\,m}^{-1}$

Table 2: Gas coefficients for Krypton and Air. Table showing the coefficients for equations (126) - (127). The reference value for the krypton pressure is chosen at 1 atmospheric pressure with $p_{\mathrm{atm}} = 1013\,\mathrm{mbar}$. The values are determined using the Sellmeier-equations from references [159, 160].

$\Delta\varphi^{(0)}_{\mathbf{m}}$	$\Delta\varphi^{(1)}_{\mathbf{m}}$
$2.85\,\pi$	16.5 fs

Table 3: Table showing the relative phase and group-delay introduced by the mirrors (one reflection). Due to the manufacturing tolerances provided by the manufacturer LAYERTEC GmbH of $15\,\mathrm{fs} \pm 5\,\mathrm{fs}$ for the group delay, we adjust the provided phase data for the mirrors in the simulation well within the tolerances by about a factor of 1.1, resulting in 16.5 fs. The mirror data is provided in Fig. 32.

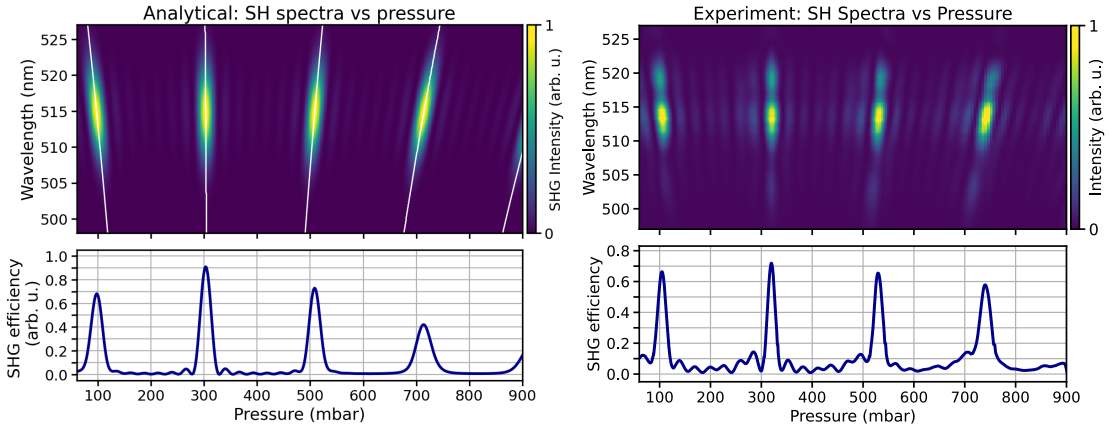


Figure 33: Comparison between the analytical model (left plot) and the measurements in the experiment (right plot) for krypton as the ambient gas medium. The right plot consists of the data obtained in Experiment A (Section 4.4, Fig. 37). We use Eq. (116), Eqs. (121)-(127), as well as the coefficients from tables 1 - 3. The white lines indicate the positions where the relative zeroth-order phase per pass is $\Delta\varphi_{\mathrm{pass}} = n\,2\pi$ with n integer.

input pulse duration of 56 fs, matching the experimental conditions of experiment A. The results for Experiment A (Appendix C, Section 3A or in Section 4.4 in this chapter) are shown in Fig. 33 in comparison to the calculated results using Krypton as the ambient gas. Furthermore, the results of the experiment in air with the same pulse parameters are shown in Fig. 34. We see a very good correspondence between the calculated spectrograms using Eq. (116) and the experimental traces. The positions of the maxima are well reproduced and the spectra exhibit similar tilts at different pressures p. At the same time, the number of minor maxima between the major (phase-matched) maxima is defined by the number of passes $N - 2 = 6$, which can be seen in both, the analytical and the experimental case. This oscillation is intruduced by the factor Eq. (118), as explained in the previous section. On the other hand, some differences can be identified as well. First, the shapes of the spectra are different, which is due to the fact that we use Gaussian beams in the analytical traces, while in the experiment, the input spectra are based on SPM-modulated pulses. Further, the relative height of the efficiency peaks in Fig. 33 is different as well. This difference can be explained by saturation effects in the actual experiment. In the analytic equation, saturation is not included due to the non-depleting pump approximation. In the experiment on the other hand, depletion of the pump pulse leads to a reduced conversion from fundamental to the SH, such that the highest efficiency maximum increases slower than the other maxima after some passes, leading to a smaller deviation between them. And lastly, we observe SPM to a certain small degree in the experiment, which is not included in Eq. (116).

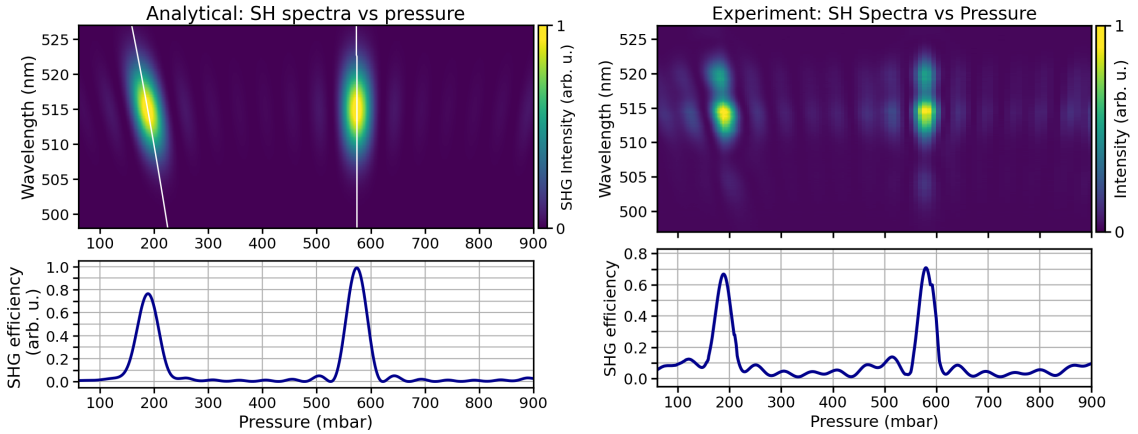


Figure 34: Comparison between the analytical model (left plot) and the measurements in the experiment (right plot) for air as the ambient gas medium. The right plot consists of the data obtained in Experiment A (Section 4.4, Fig. 38). We use Eq. (116), Eqs. (121)-(127), as well as the coefficients from tables 1 - 3. The white lines indicate the positions where the relative zeroth-order phase per pass is $\Delta\varphi_{\text{pass}} = n\,2\pi$ with n integer.

4.3.8 Expansion of the relative phase up to second order

In order to obtain an even broader conversion bandwidth into the second-harmonic, it may become necessary to compensate for higher-order relative phase-mismatches, such as the GDD, which describes the second-order dispersion. The phase terms in equation (106) are now expanded up to their second order in ω. The first term is the crystal dispersion described by the relative wavenumber $\Delta k(\omega, \omega') = k_1(\omega') + k_1(\omega - \omega') - k_2(\omega)$. Here we expand each term individually around their central frequency ω_p with $p = 1, 2$. Since we defined $k_p(\omega) \equiv k_p(\bar{\omega}_p + \omega)$, where $\bar{\omega}_p$ is the center frequency of fundamental ($p = 1$) or the second harmonic ($p = 2$), the expansions are now

$$k_1 = k_1(\bar{\omega}_1 + \omega) \approx k_1^{(0)} + k_1^{(1)}\omega + \frac{1}{2}k_1^{(2)}\omega^2 \tag{128}$$

$$k_2 = k_2(\bar{\omega}_2 + \omega) \approx k_2^{(0)} + k_2^{(1)}\omega + \frac{1}{2}k_2^{(2)}\omega^2 \tag{129}$$

$$\varphi_1 = \varphi(\bar{\omega}_1 + \omega) \approx \varphi_1^{(0)} + \varphi_1^{(1)}\omega + \frac{1}{2}\varphi_1^{(2)}\omega^2 \tag{130}$$

$$\varphi_2 = \varphi(\bar{\omega}_2 + \omega) \approx \varphi_2^{(0)} + \varphi_2^{(1)}\omega + \frac{1}{2}\varphi_2^{(2)}\omega^2 \tag{131}$$

Now expanding the relative wave-vector mismatch up to second order:

$$\Delta k_2(\omega, \omega') = k_1(\omega') + k_1(\omega - \omega') - k_2(\omega) \approx \tag{132}$$

$$\approx \Delta k_2^{(0)} + \Delta k_2^{(1)}\,\omega + \frac{1}{2}\left(k_1^{(2)}\omega'^2 + k_1^{(2)}(\omega - \omega')^2 - k_2^{(2)}\omega^2\right) \tag{133}$$

$$= \Delta k_2^{(0)} + \Delta k_2^{(1)}\,\omega + \underbrace{k_1^{(2)}\omega'^2 + \frac{1}{2}k_1^{(2)}\omega^2 - k_1^{(2)}\omega\omega' - \frac{1}{2}k_2^{(2)}\omega^2}_{\text{second order term } \Delta k^{(2)}(\omega,\omega')} \tag{134}$$

The second order term cannot be rearranged such that ω' is canceled from the equation. And analogously for the linear phase term

$$\Delta\varphi_2^{(0)} + \Delta\varphi_2^{(1)}\,\omega \;+\; \underbrace{\varphi_1^{(2)}\omega'^2 + \frac{1}{2}\varphi_1^{(2)}\omega^2 - \varphi_1^{(2)}\omega\omega' - \frac{1}{2}\varphi_2^{(2)}\omega^2}_{\text{second order term } \Delta\varphi^{(2)}(\omega,\omega')} \;. \tag{135}$$

We summarize the second order terms into

$$\Delta\varphi_{\text{tot}}^{(2)}(\omega,\omega') = \Delta k^{(2)}(\omega,\omega')\,L_{\text{cr}} + \Delta\varphi^{(2)}(\omega,\omega') \tag{136}$$

$$= (k_1^{(2)}L_{\text{cr}} + \varphi_1^{(2)})\omega'^2 + \frac{1}{2}(k_1^{(2)}L_{\text{cr}} + \varphi_1^{(2)})\omega^2 \tag{137}$$

$$- (k_1^{(2)}L_{\text{cr}} + \varphi_1^{(2)})\omega\omega' - \frac{1}{2}(k_2^{(2)}L_{\text{cr}} + \varphi_2^{(2)})\omega^2 \tag{138}$$

$$= \varphi_{1,\text{tot}}^{(2)}\omega'^2 + \frac{1}{2}\varphi_{1,\text{tot}}^{(2)}\omega^2 - \varphi_{1,\text{tot}}^{(2)}\omega\omega' - \varphi_{2,\text{tot}}^{(2)}\omega^2 \tag{139}$$

where $\varphi_{1,\text{tot}}^{(2)}$ is the total accumulated GDD inside the MPC in one pass for the fundamental and $\varphi_{2,\text{tot}}^{(2)}$ for the SHG. In order to compensate for the GDD, we introduce a second-order mirror dispersion $\Delta\varphi_{\text{M}}^{(2)}$ onto the SHG pulse, such that

$$\varphi_{1,\text{tot}}^{(2)}\omega'^2 + \frac{1}{2}\varphi_{1,\text{tot}}^{(2)}\omega^2 - \varphi_{1,\text{tot}}^{(2)}\omega\omega' - \frac{1}{2}\varphi_{2,\text{tot}}^{(2)}\omega^2 \;-\; \frac{1}{2}\Delta\varphi_{\text{M}}^{(2)}\omega^2 = 0 \tag{140}$$

Since there is no non-trivial solution to find the coefficient $\varphi_{2,\text{M}}^{(2)}$, we make the approximation that $\omega = \omega'$. Then from the equation (140) it follows immediately that

$$\Delta\varphi_{\text{M}}^{(2)} \approx \varphi_{1,\text{tot}}^{(2)} - \varphi_{2,\text{tot}}^{(2)} \tag{141}$$

so the mirror GDD to be compensated is approximately the difference between the GDD accumulated by the fundamental beam in one pass and the GDD of the SHG pulse. By employing the approximation $\omega = \omega'$, we neglect the effects that arise from the dispersion of the fundamental pulse, thus treating the second-order relative phase term inside the convolution integral as if the convolution was a simple multiplication in order to still be able to find an analytical solution.

4.3.9 Gouy phase contribution

In this whole section we did not consider the Gouy phase as a contributing term for the relative phases up to the first order. We here calculate the contribution of the relative Gouy phase to the SHG process up to first order in the frequency ω. We show that this contribution can in practice be neglected as a phase-mismatch term inside the crystal for most application scenarios of the SHG-MPC.

We start with the definition of the Gouy phase, which is

$$\Psi(z) = \arctan\left(\frac{z}{z_{\text{R}}}\right), \quad z_{\text{R}} = \frac{\pi w_0^2}{\lambda}\,, \tag{142}$$

where w_0 is the beam waist radius in the focus. Since the crystal is typically short compared to the Rayleigh length $L_{\text{cr}} \ll z_{\text{R}}$, we can replace the arctan with the first-order Taylor expansion, which is just $\arctan(x) \approx x$. Furthermore, expressing the wavelength $\lambda = 2\pi c_0/\omega'$, where $\omega' = \bar{\omega} + \omega$ and $\bar{\omega}$ is the center frequency and then applying the Taylor expansion on the term $1/(\bar{\omega}+\omega) \approx 1/\bar{\omega} - \omega/\bar{\omega}^2$

up to first order, the Gouy phase writes

$$\Psi(z,\omega) \approx \frac{z}{z_\mathrm{R}} = \frac{2c_0 z}{w_0^2}\frac{1}{\bar{\omega}+\omega} \approx \frac{2c_0 z}{w_0^2}\left(\frac{1}{\bar{\omega}} - \frac{\omega}{\bar{\omega}^2}\right) . \tag{143}$$

The relative Gouy phase can now be calculated using $\Delta\Psi(z,\omega) = \Psi_1(z,\omega')+\Psi_1(z,\omega-\omega')-\Psi_2(z,\omega)$ (see Eq. (80)), yielding

$$\Delta\Psi(z,\omega) = \Delta\Psi^{(0)} + \Delta\Psi^{(1)}\omega = \frac{2c_0 z}{w_0^2}\Big(\overbrace{\frac{1}{\bar{\omega}_1}}^{0^{\mathrm{th}}\text{ order}} - \overbrace{\frac{3\omega}{4\bar{\omega}_1^2}}^{1^{\mathrm{st}}\text{ order}} \Big) . \tag{144}$$

For example, inserting the experimental parameters $z = L_\mathrm{cr}$, $w_0 = 400\,\mu\mathrm{m}$, $\lambda = 1030\,\mathrm{nm}$ and $\bar{\omega}_1 = 2\pi c_0/\lambda$ results in a zeroth-order relative Gouy phase of $\Delta\Psi^{(0)} \approx 0.19\,\mathrm{mrad}$, which is negligibly small. For the first order, we obtain $\Delta\Psi^{(1)} \approx -8\cdot10^{-5}\,\mathrm{fs}$ of group-delay, which is negligible as well. We therefore conclude that the Gouy phase mismatch contribution within the interaction length of the crystal is small and can be neglected.

4.3.10 Numerical model (3+1)D

The simulation model used in this work is mainly described by the Unidirectional Pulse Propagation Equation (UPPE) [69]

$$\partial_z\, E(k_x,k_y,\omega,z) = iK_z(k_x,k_y,\omega)\, E(k_x,k_y,\omega,z) + iQ(k_x,k_y,\omega)\frac{P(k_x,k_y,\omega,z)}{2\varepsilon_0} , \tag{145}$$

where $K_z(k_x,k_y,\omega) = \sqrt{k^2(k_x,k_y,\omega) - k_x^2 - k_y^2}$ and $k(k_x,k_y,\omega) = \frac{\omega}{c_0}n(k_x,k_y,\omega)$. The propagation equation is treated in a non-field resolved manner, where the rapidly oscillating center frequency terms $\bar{\omega}$ are multiplied out by $\tilde{E}(\bar{\omega}+\omega) = E(\omega)\mathrm{e}^{i\bar{\omega}t}$ The wavenumber dependent refractive index is calculated self-consistently according to reference [161], giving rise to spatial propagation effects in non-isotropic media, for example and most notably the spatial walk-off of the second harmonic in the crystal [161]. The nonlinear propagation coupling is defined as $Q(k_x,k_y,\omega) = \frac{\omega^2}{c^2 K_z(k_x,k_y,\omega)}$, where we make an isotropic approximation $K_z(k_x,k_y,\omega) \approx k(\omega)$ (but only in the nonlinear part, the dependency is kept in the linear part). The nonlinear polarization $P_{\mathrm{o/e}}(x,y,t,z)$ for ordinary (o) and extraordinary (e) field is as usual solved in time-domain and takes into account second-order $\chi^{(2)}$ effects as well as self-phase modulation (SPM). The nonlinear polarization for the second-order nonlinearities is defined as [161]

$$P_{\mathrm{o/e}}(x,y,t,z) = P^{(2)}_{\mathrm{o/e}}(x,y,t,z) + P^{(3)}_{\mathrm{o/e}}(x,y,t,z) \tag{146}$$

$$P^{(2)}_{\mathrm{o}} = \frac{\kappa_o}{4}\Big(\overbrace{2E_eE_o^*}^{\text{SHG process}} + E_eE_e + E_eE_e^* + E_oE_e^* + E_eE_o\Big) \tag{147}$$

$$P^{(2)}_{\mathrm{e}} = \frac{\kappa_e}{4}\Big(\overbrace{E_oE_o}^{\text{SHG process}} + 2E_oE_e^* + E_eE_o^* + E_eE_o + E_oE_o^*\Big) , \tag{148}$$

where we indicate the nonlinear processes that are responsible for the SHG generation in BBO with type I phase-matching. The pre-factors (coupling parameters) are $\kappa_{o/e} = 2\varepsilon_0\frac{\omega d_\mathrm{eff}}{n_{o/e}(\omega)}$, with the d_eff as the medium and its orientation dependent second-order response. The additional factor of 1/4 in the above equations arises from the convention used to calculate the intensity from the electric field $I = \frac{1}{2}nc_0\varepsilon_0|E|^2$, as opposed to $I = 2nc_0\varepsilon_0|E|^2$ used in reference [161] and by other authors [26]. For an explanation of these convention differences, refer to the preface of reference

[162].
The effect of SPM as a third-order polarization is modeled as

$$P_{\mathrm{o/e}}^{\mathrm{SPM}}(x,y,t,z) = (1-f_{\mathrm{R}})\,\gamma_{o/e}\,|E_{o/e}(x,y,t,z)|^2\,E_{o/e}(x,y,t,z)\ , \tag{149}$$

with $\gamma_{o/e} = \frac{1}{2}\varepsilon_0^2 c_0 n_{o/e}^2 n_{2,o/e}$. The factor f_{R} denotes the Raman fraction, taking values $0 \leq f_{\mathrm{R}} \leq 1$ [77]. It represents the fraction between the instantaneous electronic response and the delayed molecular response with $f_{\mathrm{R}} = 0$ when no delayed response is present. In order to model the delayed Raman-response (stimulated Raman scattering, SRS) of a medium, the additional third order, time-delayed polarization term is introduced

$$P_{\mathrm{o/e}}^{\mathrm{SRS}}(x,y,t,z) = f_{\mathrm{R}}\ \gamma_{o/e}\int_0^\infty R(t-t')|E_{o/e}(x,y,t',z)|^2\mathrm{d}t'\ E_{o/e}(x,y,t,z)\ , \tag{150}$$

which is the single damped oscillator model described in [77]. The response function $R(t)$ is modeled as such using

$$R(t) = \frac{\Gamma^2/4+\Lambda^2}{\Lambda}\exp(-\Gamma t/2)\sin(\Lambda t)\ , \tag{151}$$

with Λ as the characteristic frequency of the Raman-oscillator and $1/\Gamma$ the characteristic damping time [77]. This model is used in the numerical simulations in Chapter 2 to model the Raman-response of Air, in Chapter 3 for the Raman-response of fused silica and in this chapter to include the nonlinear interaction when air is used as the ambient gas medium for dispersion compensation (which typically is comparatively small).

We use an in-house developed code for the numerical evaluation of Eq. (145), which is solved using a Fourier split-step method. The linear part is solved in the k-number and frequency domain and the nonlinear part is solved in real space and time domain using the Runge-Kutta 4 (RK4) method.

4.3.11 ABCD-formalism-based (1+1)D model

In addition to the (3+1)D model including all spatio-temporal effects, we use a (1+1)D model, where the spatial domain is modeled using the Gaussian ABCD matrix formalism, additionally taking into account Kerr lensing [122]. This hybrid approach enables fast numerical calculations of MPC post-compression as well as the SHG-MPC by summarizing the two spatial variables x and y into a simple ABCD-matrix based calculation, while capturing the same nonlinear effects of the temporal and spatial domain as the (3+1)D model. The temporal and spatial domain is modeled by equation 145, but without the spatial coordinates

$$\partial_z\,E(\omega,z) = ik_z(\omega)\,E(\omega,z) + iQ(\omega)\frac{P(\omega,z)}{2\varepsilon_0}\ , \tag{152}$$

where $k_z = \frac{\omega}{c_0}n(\omega)$ and $Q(\omega) = \frac{\omega^2}{c_0^2 k_z}$. Again, nonlinear polarization $P_{\mathrm{o/e}}(t,z)$ for ordinary (o) and extraordinary (e) field is as usual solved in time-domain and takes into account second-order $\chi^{(2)}$ effects as well as self-phase modulation (SPM). The nonlinear polarization for the second-order nonlinearities is defined as [161]

$$P_{\mathrm{o/e}}(t,z) = P_{\mathrm{o/e}}^{(2)}(t,z) + P_{\mathrm{o/e}}^{(3)}(t,z) \tag{153}$$

$$P_{\mathrm{o}}^{(2)} = \frac{\kappa_o}{4}\Big(\overbrace{2E_eE_o^*}^{\text{SHG process}} + E_eE_e + E_eE_e^* + E_oE_e^* + E_eE_o\Big) \tag{154}$$

$$P_{\mathrm{e}}^{(2)} = \frac{\kappa_e}{4}\Big(\overbrace{E_oE_o}^{\text{SHG process}} + 2E_oE_e^* + E_eE_o^* + E_eE_o + E_oE_o^*\Big) \ , \tag{155}$$

where we indicate the nonlinear processes that are responsible for the SHG generation in BBO with type I phase-matching. The pre-factors (coupling parameters) are again $\kappa_{o/e} = 2\varepsilon_0 \frac{\omega d_{\mathrm{eff}}}{n_{o/e}(\omega)}$, with the d_{eff} as the medium and its orientation dependent second-order response. SPM is modeled using

$$P_{\mathrm{o/e}}^{(3)}(t,z) = \gamma_{o/e}\,|E_{o/e}(t,z)|^2\,E_{o/e}(t,z) \ , \tag{156}$$

with $\gamma_{o/e} = \frac{1}{2}\varepsilon_0^2 c_0 n_{o/e}^2 n_{2,o/e}$.
Similar to the 3D case, the delayed Raman response for molecular gases and solids is modeled using

$$P_{\mathrm{o/e}}^{\mathrm{SRS}}(t,z) = f_{\mathrm{R}}\ \gamma_{o/e}\int_0^\infty R(t-t')|E_{o/e}(t',z)|^2\mathrm{d}t'\ E_{o/e}(t,z) \ , \tag{157}$$

with

$$R(t) = \frac{\Gamma^2/4+\Lambda^2}{\Lambda}\exp(-\Gamma t/2)\sin(\Lambda t) \ . \tag{158}$$

Finally, the spatial effects are modeled using the ABCD transfer matrices for translation $M_L = \left(\begin{smallmatrix} 1 & L/n \\ 0 & 1 \end{smallmatrix}\right)$ and focusing $M_f = \left(\begin{smallmatrix} 1 & 0 \\ -1/f & 1 \end{smallmatrix}\right)$. Kerr lensing is accounted for by calculating the Kerr-focal length f_{Kerr} by [122]

$$f_{\mathrm{Kerr}} = 0.47\frac{\pi w^4}{P_{\mathrm{peak}} n_2 dz} \ , \tag{159}$$

where P_{peak} is the peak power. Kerr lensing is then incorporated by altering one propagation step of a distance dz as

$$M_{dz} = M_{dz/2}\cdot M_{f_{\mathrm{Kerr}}}\cdot M_{dz/2} \ . \tag{160}$$

4.4 Experiment and Simulation: Second-Harmonic in MPCs

To demonstrate the broadband SHG-MPC, we performed two experiments at a central wavelength of 1030 nm using pulses with different durations and spectral bandwidths. In the first case, referred to as Experiment A, we frequency-double 50 µJ, 63 fs pulses with a Fourier-transform limit (FTL) of approximately 56 fs. This experiment yields a conversion efficiency of 72 %. In the second case, Experiment B, we convert 15.3 fs pulses to the second-harmonic with an FTL of 10 fs, with a measured efficiency of 47 %. In Experiment B, the generated SH pulses are additionally compressed with chirped mirrors to a duration of 13.8 fs. In both cases, the fundamental pulses are first post-compressed in a conventional self-phase modulation (SPM)-based MPC post-compression stage. The experimental results are furthermore compared to the simulations based on the model described in Section 4.3.10.

Figure 35 illustrates the experimental setups used in both experiments. After spectral broadening and compression, the fundamental pulses are directed to the SHG-MPC chamber, where the beam is mode-matched and guided into the SHG-MPC. Prior to coupling into the SHG-MPC, the beam passes through the first harmonic separator (HS). The SHG-MPC is composed of two curved mirrors with a radius of curvature (ROC) of $R = 1$ m and is set to $N = 4$ round-trips (8 passes)

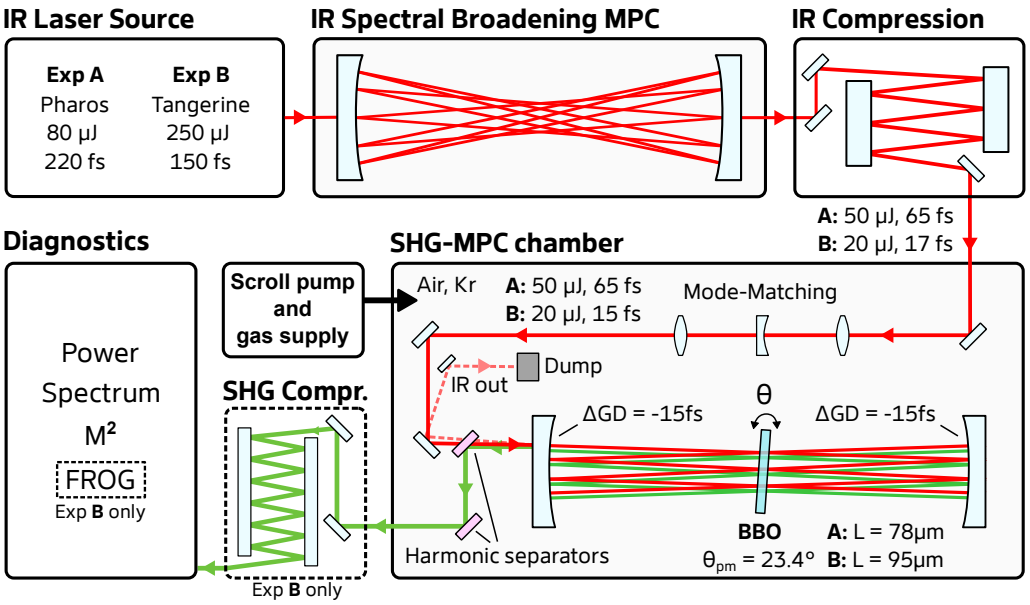


Figure 35: Experimental setup for both the long pulse (Exp A) and the short pulse (Exp B) experiment. Two different laser systems with similar parameters are used. After spectral broadening and post-compression, the pulses are sent into the chamber, where mode-matching and SHG in the SHG-MPC is carried out. Two harmonic separators are used to fully filter out the remaining fundamental light. In Exp B, the SH pulses are compressed using a chirped mirror compressor. The spectrum, M^2 and power is analyzed subsequently. FROG measurements are additionally carried out in experiment B (Exp B). Reprinted with permission from [6].

with an MPC length of $L = 295\,\text{mm}$. The mirror coatings are specifically designed to compensate for a group delay (GD) of approximately $-15\,\text{fs}$ between 1030 nm and 515 nm, corresponding to the relative GD accumulated over a single pass through the MPC at a reference pressure of 500 mbar of air. The nonlinear crystals are two Beta-Barium Borate (β-BaB_2O_4, BBO) crystals with thicknesses of $L_{\text{cr}} = 78\,\mu\text{m}$ and $L_{\text{cr}} = 95\,\mu\text{m}$. Both are cut for the type I phase-matching angle of $\theta_{\text{pm}} = 23.4°$ and have no substrate. In this MPC configuration, the beam is weakly focused, resulting in rather small beam sizes of 385 µm beam radius on the mirrors and 340 µm waist radius in the focus. The BBO crystal is mounted in a way that the actual incidence angle θ can be adjusted according to $\theta = \theta_{\text{pm}} \pm \Delta\theta$, where $\Delta\theta$ denotes the detuning from the phase-matching angle. After 8 passes through the SHG-MPC and the crystal, both the fundamental and SHG beams are coupled out. The fundamental field is then filtered by two harmonic separators to ensure a pure SHG output field.

Measurements are carried out using both air (Experiments A and B) and krypton (A only). To generate spectrograms such as those shown in Fig. 27, the gas pressure in the chamber is scanned from approximately 50 mbar up to 1 bar. By examining the tilt of the spectra at the maxima of the spectrograms, we can determine whether the relative group delay (GD) is matched and adjust the angle θ so that the spectrum at one of the maxima appears vertical. To satisfy both phase- and GD-matching conditions, the pressure is then tuned to this vertical maximum. The SHG beam is subsequently analyzed using the diagnostics. In Experiment B the SHG pulse is additionally compressed with a pair of chirped mirrors providing an average dispersion of $-40\,\text{fs}^2$ per reflection.

A. Long Pulse Conversion

In Experiment A, we use post-compressed pulses with a pulse duration of 63 fs and an FTL of 56 fs. The pulse energy is attenuated to 50 µJ, and the repetition rate is set to 4 kHz. Here, we use the shorter BBO crystal with a thickness of $L_{\text{cr}} = 78\,\mu\text{m}$. By simultaneously recording the spectrum and output power while scanning the pressure in the chamber, we obtain spectrograms together

with the measured conversion efficiency, as shown in Fig. 27. We use both air and Krypton as the ambient gas medium in the SHG-MPC. While air is more practical since it is always available, Krypton allows more phase-matching peaks to be resolved due to its stronger dispersion. Figure

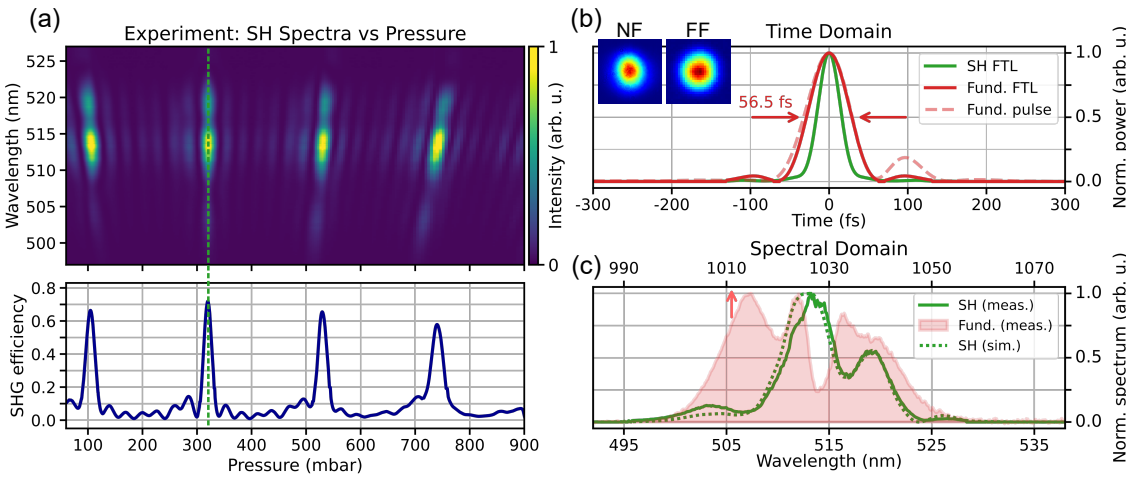


Figure 36: Measurement results of the long pulse experiment. (a) Spectrograms recorded as a function of gas pressure (here: Krypton) and the corresponding measured efficiencies. here, the green dashed line indicates the highest efficiency at around 315 mbar. (b) Measured input and output pulses in temporal and spectral domain. In this experiment the SH pulses are not compressed, thus the FTL pulses are plotted. The simulated spectrum is in very good agreement with the measurement. Reprinted with permission from [6].

36 shows the experimental results for Krypton. In Fig. 36(a), the pressure-scan spectrogram is presented together with the corresponding measured efficiency. In Fig. 36(b), the fundamental and SH pulses at the highest efficiency are shown in both the temporal and spectral domains. Since the SH pulses were not compressed in this case, the FTL pulse is plotted together with the measured input fundamental pulse. In both gases, the bandwidth of the resulting SH pulses around 515 nm supports an FTL of 31.5 fs. We measure a maximum conversion efficiency of 72 % at a pressure of $p = 315$ mbar. The beam quality of the SH pulses is excellent, with $M^2 = 1$ on both axes. The simulated spectrum in Fig. 36 is in excellent agreement with the experimental data.

In the spectrogram shown in Fig. 36(a), the dispersive properties of the SHG-MPC are clearly observable. The four visible main peaks are separated by approximately 205 mbar, which corresponds to a relative phase shift of 2π between the 1030 nm fundamental field and the 515 nm SHG field for the given MPC length of about 29.5 cm. For pressures below 315 mbar, the spectra appear tilted to the left, indicating an anomalous (negative) group-delay dispersion regime for a single pass, in which the group velocity of the 1030 nm pulse is slower than that of the 515 nm pulse. On the other hand, for pressures above 315 mbar, the spectra are tilted to the right, indicating a normal dispersive regime. At 315 mbar, where both group velocities are equal, the highest efficiency of 72 % as well as the largest bandwidth among the main peaks is achieved. At this pressure, both phase and group delay are matched. The resulting pulses at 315 mbar are shown in Fig. 36(b).

The spectrogram also exhibits several minima and local minor maxima between the two main efficiency maxima. Both are determined by the number of passes N_{pass}, where the number of minima is $N_{\text{pass}} - 1$ and the number of minor maxima is $N_{\text{pass}} - 2$. The efficiency minima occur at points where $\Delta\phi_{\text{pass}} = n \cdot 2\pi / N_{\text{pass}}$ with $n = 1, \ldots, N_{\text{pass}} - 1$. A more detailed explanation can be found in Supplementary Section 4.3.

Based on the simulation model described in Section 4.3.10, we further conduct simulations mimicking the experimental conditions. Figures 37 and 38 show the simulated spectrograms and efficiencies for krypton and air, which are used as the ambient gases in the gas cell. Figures 37 and 38 present a comparison between experiment and simulation for a BBO crystal with a thickness

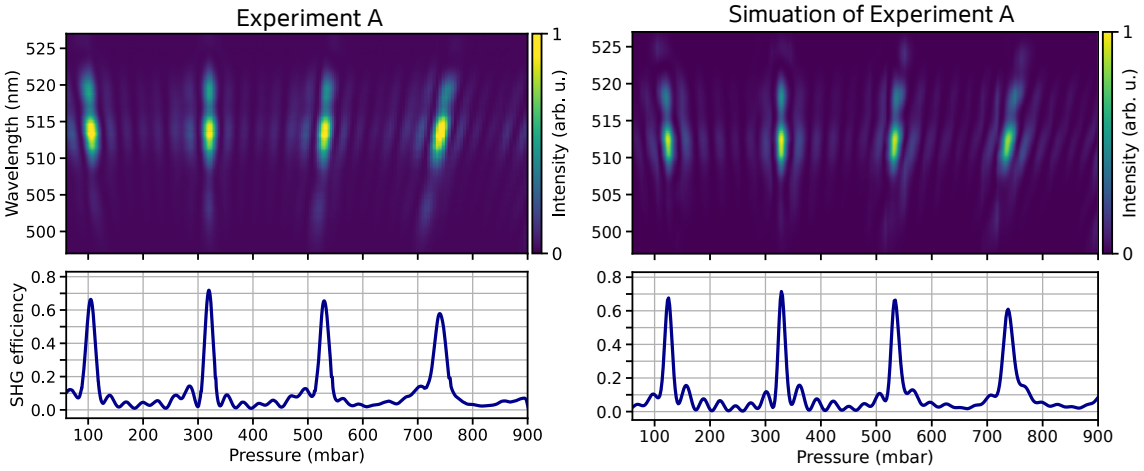


Figure 37: Experimental (left) and simulated (right) spectrograms for experiment A (section 3A in the main manuscript) using Krypton as the ambient gas for 63 fs, 50 µJ fundamental pulses. The data for the input pulse is retrieved from FROG measurements. Reprinted with permission from [6].

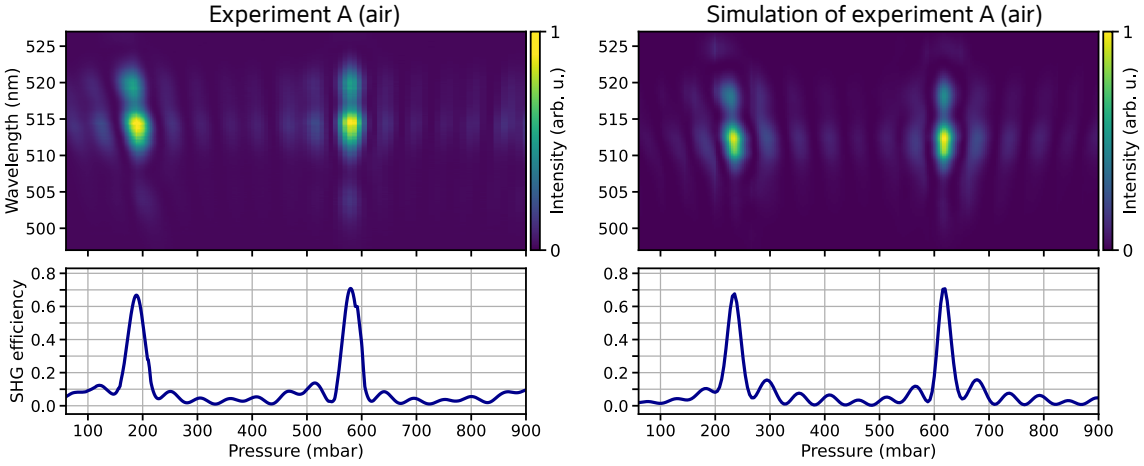


Figure 38: Experimental (left) and simulated (right) spectrograms for experiment A, but with air as the ambient gas (not shown in the main manuscript) for 63 fs, 50 µJ fundamental pulses as the input. The data for the input pulse is retrieved from FROG measurements. Reprinted with permission from [6].

of 78 µm. In both datasets, the input pulses have a central wavelength of 1030 nm, a duration of 63 fs, and an energy of 50 µJ. These pulses correspond to retrieved pulse profiles obtained from FROG measurements (Fig. 36)(b), which are used as input for the simulations. The simulations additionally include the wavelength-dependent phase and reflectivity characteristics of the mirrors, provided by LAYERTECH GmbH (for the mirror data, see Appendix C). The BBO crystal angle relative to the optical axis is set to $\theta = 24°$, and the gas pressure is varied between approximately 60 mbar and 900 mbar. In both cases, excellent agreement between simulation and experiment is observed in the spectrograms as well as in the spectra. The measured second-harmonic (SH) spectrum supports a Fourier-transform-limited (FTL) pulse duration of 31.5 fs, which is in exact agreement with the value obtained from the simulated SH spectrum. We furthermore incorporate an estimated anti-reflective (AR) coating loss of (1 %) for both fields. The simulations yield a maximum efficiency of 71 % for both gases, which is very close to the measured maximum efficiency of (72 %).

B. Short Pulse Conversion

In Experiment B, we use post-compressed pulses with a pulse duration of 15.4 fs, an FTL of 14.5 fs, and a pulse energy of 20 µJ. The post-compressed laser system is the one developed by Siletti

et al. [112]. The repetition rate of the system can be adjusted and is set to 5 kHz. Here, we use air as the dispersive medium in the SHG-MPC, which results in fewer phase-matched peaks due to the lower dispersion of air compared to krypton. We further replace the crystal with a slightly longer one of thickness $L_{\mathrm{cr}} = 95\,\mu\mathrm{m}$. The results are shown in Fig. 39. In the recorded

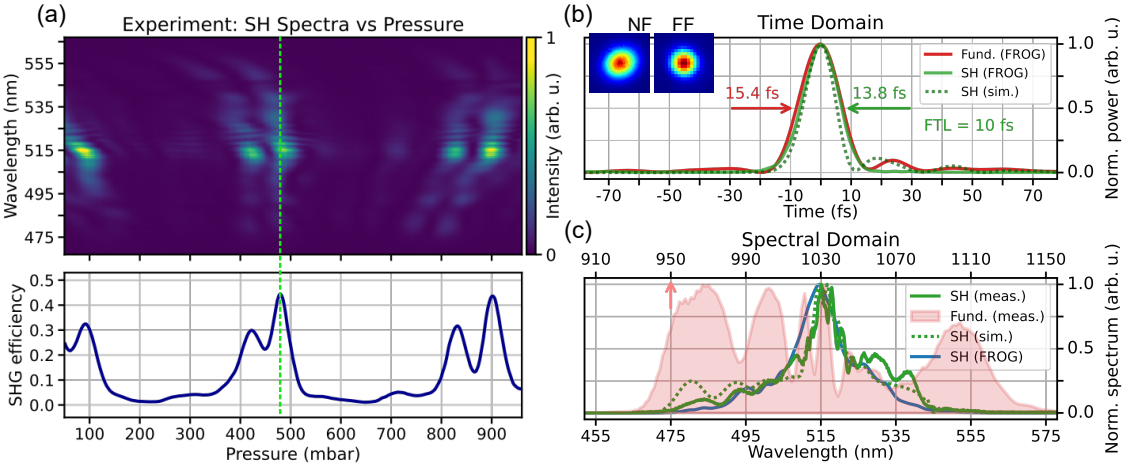


Figure 39: Measurement results of the short pulse experiment (experiment B). (a) Spectrograms recorded as a function of gas pressure (here: air) and the corresponding measured efficiencies. Here, the green dashed line indicates the highest efficiency at around 490 mbar. (b) Measured input and output pulses in temporal and spectral domain. The simulated spectrum agrees well with the experiment. Reprinted with permission from [6].

spectrograms in Fig. 39, we observe a global maximum at around 490 mbar. We further observe spectra that appear curved, effectively reducing the bandwidth and efficiency of the SHG process. The curvature of the spectra results from higher-order relative phases, with the main contribution arising from the relative group-delay dispersion (GDD) between the fundamental and SH fields. The GDD, and higher-order terms, originate from both the phase characteristics of the mirror coatings and the dispersion of the materials in the MPC. In the experiment, we could not account for these contributions. The efficiency maxima exhibit a double-peak structure, which we are not able to reproduce in the simulations (Fig. S3), while the overall shape of the spectra matches very well with the experiments.

After setting the pressure to the maximum efficiency, we compress the pulse using a pair of chirped mirrors. The pulses are characterized by frequency-resolved optical gating (FROG), from which we retrieve a pulse duration of 13.8 fs and a conversion efficiency of 47 %. This efficiency is measured before the chirped-mirror compressor. The total compressor transmission amounts to 93.4 %, and could still be improved by using chirped mirrors with higher reflectivity. Here, the bandwidth measured with the spectrometer supports a pulse duration of 10 fs, whereas the spectrum retrieved from the FROG measurement yields an FTL of 12.6 fs. We attribute this discrepancy to the limited bandwidth of the SHG crystal in the FROG setup, which reduces the measured spectral width. Similarly to the spectrometer-measured FTL, the simulated FTL is also 10 fs, confirming the observation of a narrowed spectrum in the FROG measurement. When SPM is suppressed in the simulations, the resulting FTL decreases to 11.5 fs, again indicating that SPM plays only a minor role in the generation process. The beam quality of the SH pulse is slightly lower than for the longer pulse, with $M^2 = 1.3$ on both axes, compared to a fundamental input beam quality of $M^2 = 1.2$.

We again conduct simulations for the short pulse experiment. Figure 40 shows the experimental and simulated spectrograms for experiment B (see Section 3B of the main manuscript), using air as the ambient gas medium and fundamental input pulses at 1030 nm with a duration of 15.4 fs and an energy of 20 µJ. These input pulses were characterized using FROG measurements (Fig.

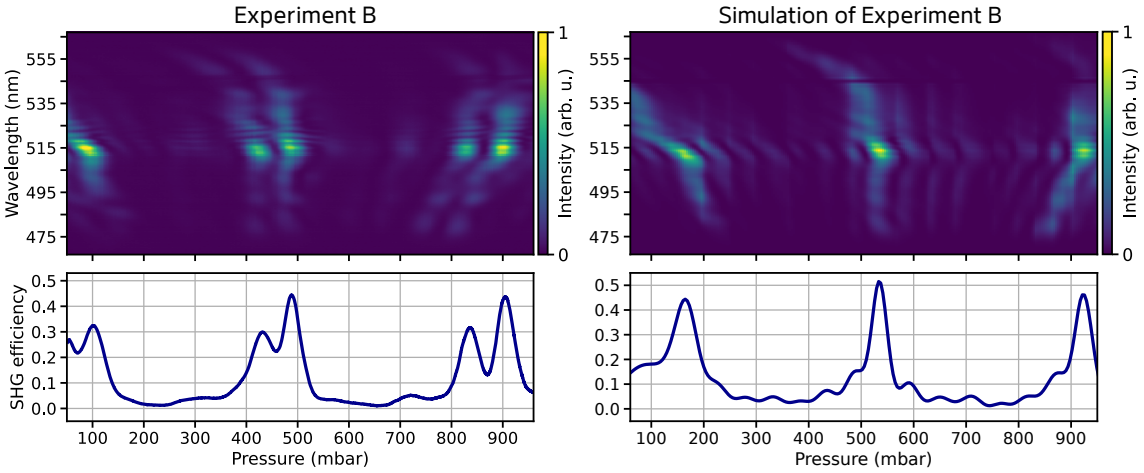


Figure 40: Experimental (left) and simulated (right) spectrograms for experiment B using air as the ambient gas for 15.4 fs, 20 µm input fundamental pulses. The data for the input pulse is retrieved from FROG measurements. Reprinted with permission from [6].

39) and used as input for the simulations. In this simulation, the BBO crystal thickness was increased to 95 µm and the θ angle is set to 23.2°. The overall spectral shape, as well as the positions of the spectral and efficiency maxima, are well reproduced. Furthermore, the measured and simulated SH spectra show good agreement, with both supporting a FTL pulse duration of 10 fs. As discussed in the main manuscript, the spectra retrieved from the FROG measurements exhibit a reduced bandwidth. This narrowing can be attributed to the limited phase-matching bandwidth of the BBO crystal used in the FROG setup. The narrowed retrieved FROG spectrum is plotted in Fig. 39. In this simulation we apply an estimated AR-coating loss of 2% for each field, which results in a maximum conversion efficiency of about 53%, which is reasonably close to the measured efficiency of 47%. The spectrograms show one noticeable differences between experiment and simulation, namely the double peak structure of the efficiencies and spectra in Fig. 40(a). This feature can be reproduced in simulations when a realistic MPC geometry with a round

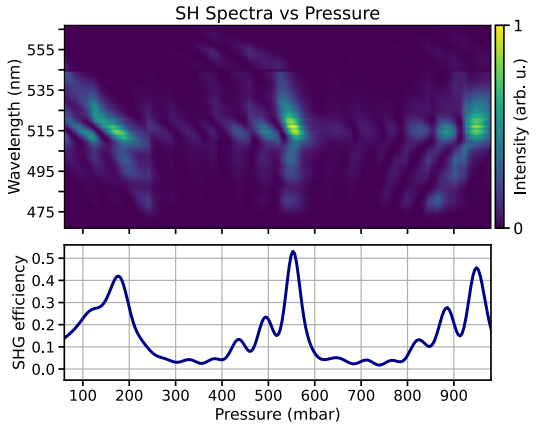


Figure 41: Simulated spectrograms and efficiencies including a θ variation of about ±0.4°, emulating the realistic experimental conditions. The SHG-MPC configuration in this simulation follows the experimental conditions of experiment B.

beam pattern is implemented into the simulation. In particular, a round beam pattern causes a variation in the critical angle θ, changing the dispersion properties in each pass through the SHG-MPC. According to simulations, e.g. in Fig. 41, this can lead to additional, weaker efficiency maxima to appear. However, for θ variations $< \pm 0.5°$, which is the situation in this experiment, the efficiency and bandwidth do not reduce significantly compared to no θ variations, according to

the simulations. The topic of avoiding the θ variation will be discussed in the next section.

4.5 Discussion

In the preceding sections, we introduced the concept of the second-harmonic multi-pass cell (SHG-MPC), developed an analytical description of the underlying nonlinear interaction, and demonstrated its performance experimentally and numerically for both long and ultrashort pulses. The results show that the SHG-MPC enables simultaneous control over phase and group-delay matching, thereby overcoming key limitations of conventional single-pass SHG schemes in terms of bandwidth and conversion efficiency. In particular, the agreement between experiment and simulation confirms the validity of the proposed model and highlights the role of the MPC geometry as a flexible platform for dispersion management in second-order nonlinear frequency conversion. In the following, we discuss the implications of these findings, the remaining limitations of the present implementation, and possible directions for further improvement and extension of the SHG-MPC concept.

4.5.1 Overview of previous SHG works

In the broader context of previous work on second-harmonic generation, we benchmark our experimental results against earlier publications on SHG. Figure 42 shows a collection of data found in the literature on SHG, plotted over the Fourier-transform-limited (FTL) bandwidth and the efficiency of the generation process [153, 155, 163–181]. In this overview plot, many of the published

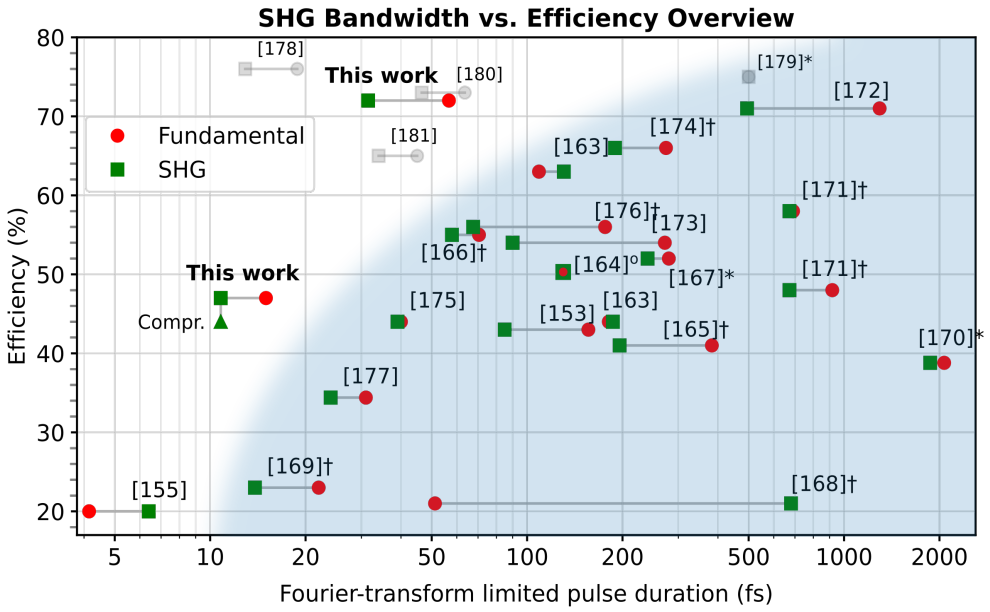


Figure 42: Overview of various works on second-harmonic generation (SHG), relating efficiency to the fundamental (red dots) input and SHG output (green squares) bandwidths, here expressed as the full-width half-maximum (FWHM) of the Fourier-transform limited (FTL) pulses. The green triangle indicates the efficiency after compression of the SH pulse. The gray markers indicate flat-top or non-Gaussian beam systems. †The FTL was calculated using the spectral bandwidth provided in the reference. *The pulse duration was used, since the reference did not provide the FTL or bandwidth. ° No FTL, bandwidth or pulse duration of the SH pulse provided. Reprinted and modified with permission from [6].

results for SHG accumulate in the area marked in light blue. [7] The results from the SHG-MPC

[7] The outliers (marked in gray in the plots) are laser systems using non-Gaussian beams, such as e.g. flat-top beams, for mostly high energy pulses around of exceeding Joule level, avoiding effects such as spatial walk-off and even more important spatial hole-burning, where the fundamental beam is depleted locally where the intensity is highest.

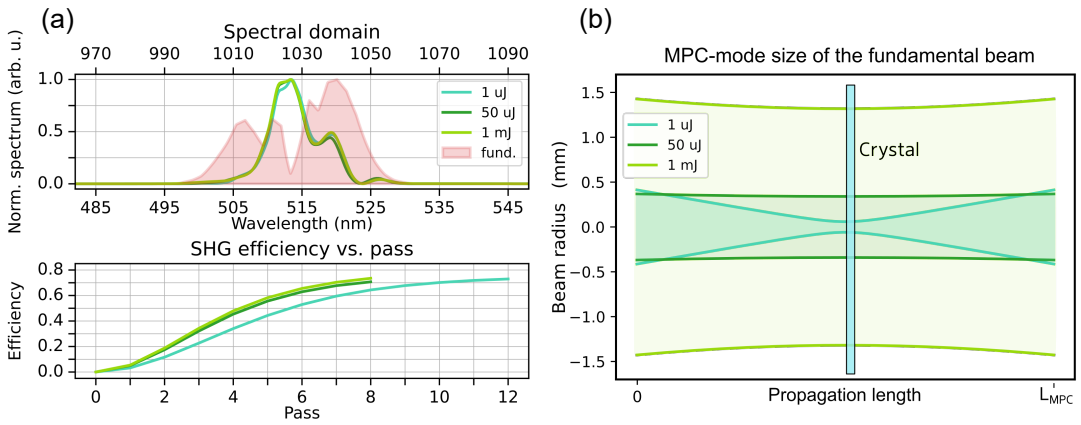


Figure 43: Simulations of energy-scaled SHG-MPCs. Here we use the measured spectrum (FROG) of the fundamental pulse, as it is used in Section 4.4. (a) Upper plot: Simulated spectra and of three different pulse energies (1 µJ, 50 µJ, 1 mJ) of the fundamental pulse, as well as the fundamental spectrum. Lower plot: simulated evolution of the efficiency per pass. (b) Comparison of the MPC mode-sizes of the fundamental beam (1030 nm). Here the MPC geometries are configured such that the maximum peak intensity in the crystal is around 600 GW cm^{-2}. The crystal length is kept at 100 µm for each simulation. Reprinted with permission from [6].

appear outside of the blue area, indicating an improved bandwidth- and efficiency performance compared to the other works. Furthermore, a main characteristic of MPC-generated SHG exhibits high beam quality and pulse contrast, as we showed in the experiment. The good beam quality can be explained by two main features of MPCs, the first being the re-entrance of the crystal from opposite sides, effectively "flipping" and compensating the spatial beam walk-off. The second a characteristic of nonlinear propagation in MPCs, where at each pass through the MPC the beam is not fully re-imaged at the same spot, leading to a mixing of the spatial phase, especially when nonlinear effects are present [31]. On the other hand, the high pulse quality can be simply explained by the fine-tunability of the relative GD, avoiding temporal walk-off between the fundamental and second harmonic pulse, which typically causes ca complicated temporal shape and spectral phase of the resulting second-harmonic field [182].

4.5.2 Pulse energy-scaling of the SHG-MPC

An important aspect of any novel system in the field of ultrafast lasers is its pulse energy-scalability. In Chapter 2 pulse energy scaling of MPC-based post-compression systems are discussed in detail. Similarly, we discuss here the potential of pulse energy up- and down-scaling of the SHG-MPC, in order to make it applicable to a wide range of laser systems. Thus, we discuss two scenarios, each with three different pulse energies and provide simulations for validation. In the first scenario, we choose the same input pulse shape as in experiment A in Section 4.4. In Experiment A we use long pulses with 63 fs pulse duration and a pulse energy of 50 µJ. We numerically analyze SHG for pulses with 1 µJ, 50 µJ and 1 mJ pulse energy. The important parameter that needs to be kept constant is the peak intensity inside the crystal, which we determine to stay at about $I_{\mathrm{peak}} \approx 600\,\mathrm{GW/cm^2}$. In this case, typically a moderate amount of passes (typically 6-12) is sufficient to reach saturation. Figure 43 shows the three cases and the results of the simulations. The spectra in Fig. 43(a) are virtually invariant to this type of scaling, therefore reaching the same bandwidth performance. In the efficiency plot in Fig. 43(a), in all scenarios the same efficiency of >70% is reached, including the 1% losses implemented in the simulation per pass and field. The design of the MPC should always be done with respect to the mode-size in the center of the MPC, where the crystal is typically located, such that the peak intensity of $I_{\mathrm{peak}} \approx 600\,\mathrm{GW/cm^2}$ is roughly kept constant. Example mode-shapes are illustrated in Fig. 43(b). Similar mode-sizes can be achieved in various ways, for example by different geometries such as a convex-concave

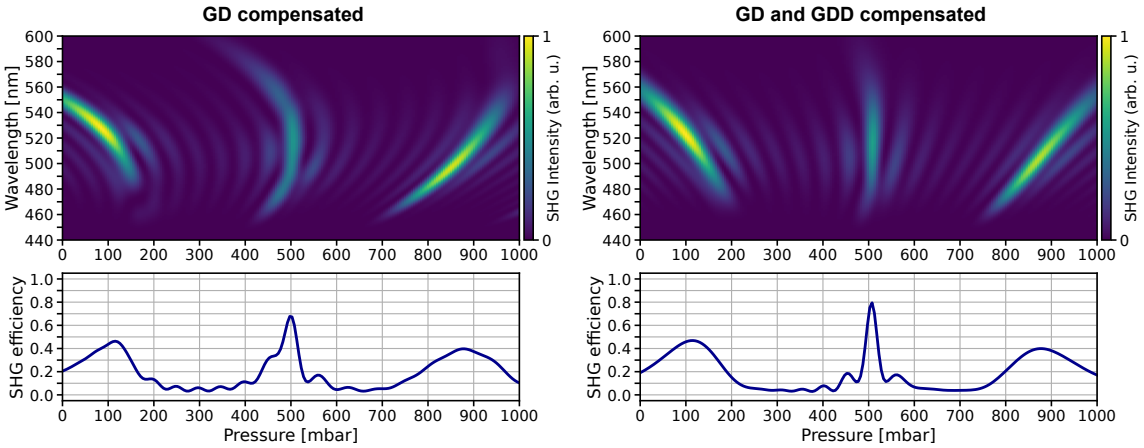


Figure 44: Simulated spectrogram traces and efficiencies for a 7 fs Gaussian pulse input using a 100 µm BBO crystal and air as the ambient gas. (a) GD compensated, but GDD uncompensated. (b) Both GD and GDD compensated using formulas Eq. (54) and Eq. (161). Reprinted with permission from [6].

MPC (cx-cv MPC) [47] as discussed in Section 2.5. The cx-cv MPC is especially useful to go to high energies, as the mode-size can be large, while the MPC can be tuned arbitrarily short [47].

In the second scenario, we analyze energy-scaling for a short pulse as described experiment B, Section 4.4. We use the same input for the fundamental pulse as shown in Fig. 39.

4.5.3 Pulse duration down-scaling and GDD compensation

So far, we focused on compensating both the relative phase and GD of the fundamental and second-harmonic fields. While this is typically enough for pulses around 15 fs pulse duration, as we demonstrate in our experiments, pulses shorter than this can be strongly affected by higher-order phase-mismatch. The next order in line is the second order phase (commonly referred to as group-delay-dispersion, GDD), which can decrease the resulting bandwidth and efficiency of the SHG process. The same way as the first-order relative phase-mismatch (GD) is compensated by the mirrors according to Eq. (54), we write the relative GDD that is required to be compensated per pass by the mirrors according to Eq. (141) as

$$\Delta\varphi_{\mathrm{m}}^{(2)} \approx -\left(\Delta\varphi_{\mathrm{cr}}^{(2)}(\theta_{\mathrm{pm}}) + \Delta\varphi_{\mathrm{gas}}^{(2)}(p_{\mathrm{ref}})\right) , \tag{161}$$

where $\Delta\varphi_{\mathrm{cr}}^{(2)}(\theta_{\mathrm{pm}})$ and $\Delta\varphi_{\mathrm{gas}}^{(2)}(p_{\mathrm{ref}})$ is the accumulated GDD in the crystal and the gas respectively, at phase-matching angle θ_{pm} and reference pressure p_{ref}. Here, the GDD can only be compensated approximately, since the intra-pulse dispersion of the fundamental pulse is neglected, as discussed in Section 4.3.8. However, using this formula, we run simulations for a two-cycle 1030 nm, 7 fs input pulse and compare the case with and without GDD compensation. Here the simulations are idealized, using Gaussian pulses and mirrors that compensate 15 fs of relative GD and about 12 fs^2 of relative GDD. Figure 44 shows the results of this calculation. In the GDD uncompensated case, a clear curvature of the major maxima are observable, leading to a lowered efficiency and bandwidth. On the other hand, the GDD compensated spectrograms exhibit a major maximum at about 500 mbar of air which has almost no curvature except at the edges, resulting in an increased efficiency and bandwidth. While such an optical coating, compensating for GD and GDD at the same time may be challenging to manufacture, GDD compensation can significantly benefit the SHG-MPC scheme for short pulse durations.

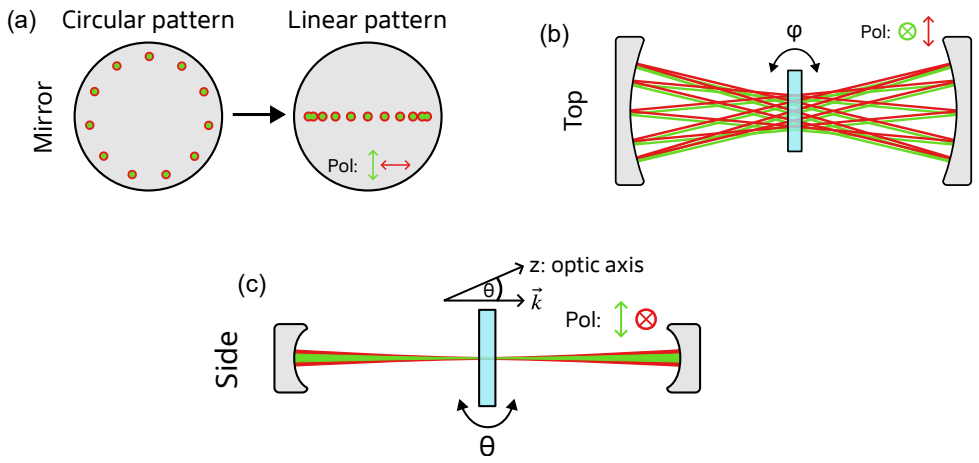


Figure 45: Optimized MPC geometry for an SHG-MPC with a uniaxial crystal, e.g. BBO. The required polarization of the fundamental (red) and SH beam (green) are indicated with arrows. Crosses indicate a polarization vector that points into the plane of the document. (a) A round pattern, typically used in standard MPC configurations versus a linear pattern. (b) View from top of and MPC with linear pattern. From this perspective, the linear and round pattern look the same. (c) View from the side. The beam pattern in a linear pattern looks like a line. Here the SH polarization is in the extraordinary direction. Reprinted with permission from [6].

4.5.4 Geometry considerations for uniaxial crystals

A challenge that can arise in MPCs is that the round beam-pattern geometry may introduce relatively large incidence angles on the crystal, thereby altering the propagation direction of the beams and, consequently, the dispersion relations in a non-isotropic crystal. This issue can be avoided by applying two modifications. First, the beam geometry is switched to a linear pattern, as shown in Fig. 45(a)-(c). Second, uniaxial crystals – for instance BBO – are used, with the beam pattern oriented such that the angular variation occurs only along the ϕ-axis, while the θ-axis, along which the extraordinary SH field propagates, remains unchanged for each pass. Here, the angle θ again refers to the angle of the $\vec{k}$-vector to the optical axis z of the crystal and ϕ is the angle relative to the xz plane [183, 184]. Figure 45 illustrates this type of setup. Figure 45(a) shows how, similar to the case of the Bow-Tie MPC (Fig. 8) or CMPC (Fig. 9), the beam pattern can simply be aligned into a line in the horizontal axis, while assuring that the fundamental field is polarized in the horizontal plane as well. In this way, the beam propagation direction ($\vec{k}$-vector) only varies in the horizontal (x) axis. Looking from the top onto the SHG-MPC, the crystal is oriented such that this angle variation happens in the ordinary xy-plane of the crystal, hence not changing the dispersive properties of the fundamental and second-harmonic field. In the side view in Fig. 45 now one can see that the angle θ, which is a crucial tuning parameter in the SHG-MPC scheme, can be freely tuned to homogeneously tune the relative phases of both fields, by changing the extraordinary propagation axis, in which the second-harmonic field propagates. In this way, all relevant parameters can be controlled precisely without any distorting effects arising from variations in propagation angle.

4.5.5 Mode-matching of the second-harmonic

When operating any type of MPC, mode matching is a crucial prerequisite for achieving stable and controlled performance as well as reproducible results [31]. By using a suitable arrangement of optical elements before coupling into the MPC, the beam caustic will reproduce itself at each pass, if the beam is matched to the eigenmode of the cell. This also applies to the SHG-MPC, where the fundamental beam is mode-matched before the MPC setup. It is however not directly obvious that the generated second-harmonic beam is automatically mode-matched as well. Here we perform simulations using the full (3+1)D model described in 4.3.10 in order to resolve the spatial

properties of the beam. We use the exact same simulations as we performed for the experiment B (Section 4.4). We extract the $1/e^2$ beam size at each propagation step using the python package *laserbeamsize* by Scott Prahl [185]. Figure 46 shows the beam radius of both fundamental and

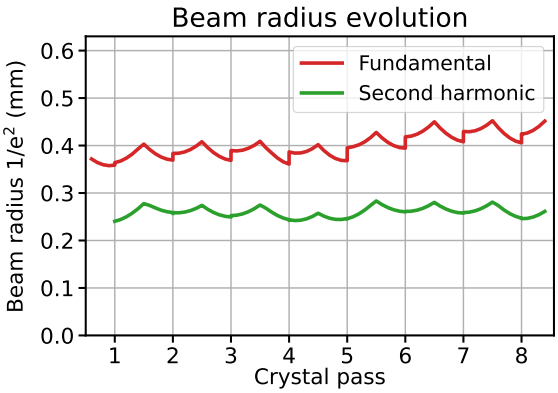


Figure 46: Simulated $1/e^2$ beam radii of the fundamental and second-harmonic beam, plotted along the propagation length. The x-axis indicates the positions of the crystal interaction. Reprinted with permission from [6].

second-harmonic within the full propagation in the MPC. It clearly shows that both beams are reproducing very well at each pass. The second-harmonic beam caustic follows the fundamental beam, and the beam size is about $1/\sqrt{2}$ smaller than the fundamental beam size, which is the typical behaviour for low-order, perturbative harmonic generation [26, 186]. This can be explained as follows: in the generation process, the generated harmonic field follows the spatial phase of the fundamental, where in the picture of Gaussian beams, the harmonic possesses the same curvature R_{ph} of the wavefronts as the fundamental beam [26]. Mode-matching occurs when R_{ph} matches with the curvature of the MPC mirrors [187]. With the radius of curvature of a Gaussian wavefront $R_{\mathrm{ph}} = z(1 + \frac{z_{\mathrm{R}2}}{z^2})$ and $z_{\mathrm{R}} = \pi w_0^2/\lambda$ the Rayleigh length, setting

$$R^1_{\mathrm{ph}} = R^2_{\mathrm{ph}} \quad \Leftrightarrow \quad z(1 + \frac{z^2_{\mathrm{R}1}}{z^2}) = z(1 + \frac{z^2_{\mathrm{R}2}}{z^2}) \quad \Rightarrow \quad z_{\mathrm{R}1} = z_{\mathrm{R}2} \tag{162}$$

and with $z_{\mathrm{Rp}} = \pi w_{0p}^2/\lambda_p$, $p = 1, 2$ for fundamental and second-harmonic respectively, it follows with $\lambda_1 = 2\lambda_2$ that $w_{01} = \sqrt{2}w_{02}$, meaning that the waist of the second-harmonic is $\sqrt{2}$ times smaller than the fundamental. Typically in standard single-pass SHG, this is approximately valid for the regime of low conversion, where the fundamental beam does not deplete locally too much. However, interestingly, in the SHG-MPC, our findings suggest that this is still valid for high conversion efficiency. Therefore, the quasi-waveguide properties of MPCs, and specifically the SHG-MPC lead to clean beams with high quality wavefronts, avoiding local depletion and hole-burning in the fundamental beam.

Another implication of these findings is that the ABCD-formalism-based (1+1)D simulations as described in Section 4.3.10 are indeed a very good approximation to the (3+1)D problem, because the spatial properties can be modeled as Gaussian throughout the whole propagation through the MPC.

4.6 Conclusion

In this work, we demonstrated efficient second-harmonic generation in a multi-pass cell (MPC) and showed that this geometry offers a versatile way to improve both the efficiency and bandwidth of second-order nonlinear frequency conversion. By combining a thin nonlinear crystal with dispersive propagation in the MPC, as well as GD-compensating mirrors, the relative phase and group delay between the fundamental and second-harmonic fields can be tuned simultaneously, enabling efficient

broadband conversion. We developed an analytical model for SHG in the MPC under the non-depleting-pump approximation, which captures the main features of the process and explains the observed pressure-dependent spectrograms. The model shows how the crystal phase-matching, gas dispersion, and mirror dispersion together determine the conversion behavior, and it also indicates how higher-order dispersion becomes relevant for few-cycle pulses. Experimentally, we realized an SHG-MPC based on a free-standing BBO crystal and a symmetric two-mirror cavity. For 63 fs, 1030 nm pulses, we achieved 72 % conversion efficiency and generated SH pulses with 31.5 fs Fourier-transform-limited duration. For shorter 15.4 fs pulses, we obtained 47 % conversion efficiency and SH pulses supporting durations down to 10 fs. In both experiments, the SH output exhibited excellent beam quality and good agreement with numerical simulations. We further demonstrate numerically that the capabilities of the SHG-MPC can be further extended towards few-cycle pulses, as well as pulse energies ranging from the microjoule- up to the millijoule range, enabling the applicability of the SHG-MPC to a wide range of laser systems.

These results show that MPCs are a powerful platform for broadband and efficient second-order nonlinear processes, and they may also be extended to other applications such as sum-frequency generation and optical parametric amplification.

5 Conclusion

Multi-pass cells (MPCs) have evolved from a specialized tool for spectral broadening into a broadly applicable platform for nonlinear ultrafast optics. The central idea underlying all of the work presented in this thesis is that repeated free-space interaction with a nonlinear medium, combined with precise control of the temporal/spectral phase and the nonlinear interaction, allows for tailoring light-matter interaction in ways that are difficult or impossible to realize in conventional single-pass systems. Across the three main topics of this thesis – energy scaling of MPC-based post-compression, post-compression of nanosecond pulses from Q-switched lasers, and broadband second-harmonic generation in an MPC – the results demonstrate that MPCs are a highly versatile technology for scalable nonlinear photonics.

A first major theme of this work was the question of how pulse energy in MPC-based post-compression schemes can be increased while preserving compactness, efficiency and the beam- and pulse quality of the output light. The analysis showed that energy scaling can be pursued along several complementary routes: by increasing the physical size of the setup, by modifying the input beam or pulse structure, or by altering the MPC geometry itself. In particular, the compact folded MPC (CMPC) was developed as a practical solution that combines high energy acceptance with a small footprint and stable operation. The CMPC demonstrates that changing the MPC geometry and folding the propagation path of the beam can strongly reduce the required footprint of the setup without sacrificing the desirable properties of standard MPC post-compression. Together with the discussion of Laguerre-Gauss-mode scaling, divided-pulse scaling, the 4f-MPC, convex-concave MPCs, and bow-tie MPCs, this chapter established a broader design landscape for energy-scalable MPC techniques. The main conclusion is that there is no unique optimum approach; rather, the suitable design depends on the target pulse energy, pulse duration, compression factor and setup size restrictions. Since each technique imposes different trade-offs, a careful analysis of the requirements should precede the decision for a certain approach.

The second major topic was the extension of MPC post-compression to a much longer-pulse regime, namely nanosecond pulses from Q-switched lasers. This work showed that the MPC concept can be transferred into a regime that is fundamentally different from conventional, mode-locked ultrafast laser technology. In the nanosecond MPC (nMPC), spectral broadening via self-phase modulation can be used to bridge the large temporal gap between compact and simple Q-switched sources and mode-locked ultrafast lasers. The proof-of-principle experiment demonstrated post-compression from the nanosecond to the picosecond regime with millijoule-level pulse energies, confirming that MPC-based broadening is not limited to the femtosecond domain and to mode-locked lasers. At the same time, the analysis identified the main challenges that must be addressed to make the nMPC concept truly scalable: longitudinal-mode beating, stimulated Brillouin scattering, stimulated Raman scattering, and quasi-phase-matched four-wave mixing. A central insight of this part of the thesis is that these limitations are not fundamental obstacles, but problems that can in principle be mitigated through improved cavity design, mode cleaning, monolithic all-bulk implementations, and specifically designed mirror coatings. This makes the nMPC a promising route toward compact, cost-efficient, and simple sources of picosecond and potentially even shorter pulses.

The third major topic was the use of MPCs for second-harmonic generation. Here, the MPC is no longer used primarily as a spectral broadening device, but as a tool to control phase and group delay between the fundamental and the generated harmonic. The SHG-MPC concept demonstrated that a thin nonlinear crystal can be placed inside a dispersive multi-pass environment such that both phase matching and group-delay matching are simultaneously optimized. The discussion even extends the phase-matching capabilities towards higher-order phase-mismatches, such as the GDD, enabling even more broadband and efficient wavelength conversion. This enabled high conversion

efficiency together with broad spectral support and excellent beam quality, overcoming the classic trade-off between efficiency and bandwidth encountered in conventional single-pass SHG. The theoretical treatment developed in this thesis provides an analytical framework for understanding the multi-pass enhancement of SHG and for interpreting the observed pressure-dependent spectrograms. The experimental results, together with the numerical simulations, confirm that MPCs can be used not only for third-order nonlinear processes such as spectral broadening, but also for highly efficient, phase-matching-dependent second-order frequency conversion. This broadens the scope of MPC applications from post-compression systems of ultrafast lasers to platforms for nonlinear optical processes. Taken together, the results of this thesis show that MPCs offer a flexible framework for nonlinear optical pulse manipulation.

In conclusion, this thesis demonstrates that multi-pass cells are a powerful and adaptable platform for nonlinear ultrafast optics. By exploiting different cell geometries, phase- and amplitude shaping abilities and controlled nonlinear propagation in a variety of materials, MPCs can be engineered to meet very different scientific and technological requirements. The work presented here establishes energy-scalable post-compression, nanosecond pulse shortening, and broadband second-harmonic generation as three manifestations of the same underlying principle: that repeated nonlinear interaction in a free-space geometry can enable new ways of realizing nonlinear optics, making MPCs an important tool for ultrafast science and technology.

References

[1] Arthur Schönberg, Supriya Rajhans, Esmerando Escoto, Nikita Khodakovskiy, Victor Hariton, Bonaventura Farace, Kristjan Pøder, Ann-Kathrin Raab, Saga Westerberg, Mekan Merdanov, Anne-Lise Viotti, Cord L. Arnold, Wim P. Leemans, Ingmar Hartl, and Christoph M. Heyl. Compact, folded multi-pass cells for energy scaling of post-compression. *Photonics Research*, 13(3):761, 2025. ISSN 2327-9125. doi: 10.1364/PRJ.540977.

[2] Peer Biesterfeld, Arthur Schönberg, Marc Seitz, Nayla Jimenez, Tino Lang, Marcus Seidel, Prannay Balla, Lutz Winkelmann, Jyothish K Sunny, Sven Fröhlich, Philip Mosel, Ingmar Hartl, Francesca Calegari, Uwe Morgner, Milutin Kovacev, Christoph M Heyl, and Andrea Trabattoni. Post-compression of a Q-switched laser in a glass-rod multi-pass cell. *Journal of Physics: Photonics*, 8(1):015013, 2025. ISSN 2515-7647. doi: 10.1088/2515-7647/ae1fc4.

[3] Christoph M. Heyl, Marcus Seidel, Esmerando Escoto, Arthur Schönberg, Stefanos Carlström, Gunnar Arisholm, Tino Lang, and Ingmar Hartl. High-energy bow tie multi-pass cells for nonlinear spectral broadening applications. *Journal of Physics: Photonics*, 4(1): 014002, 2022. ISSN 2515-7647. doi: 10.1088/2515-7647/ac483a.

[4] Victor Hariton, Yujiao Jiang, Arthur Schönberg, Marcus Seidel, Marek Wieland, Mark J. Prandolini, Ingmar Hartl, Markus Drescher, and Christoph M. Heyl. UV 30 fs laser pulse generation using a multi-pass cell. *Optics Letters*, 49(13):3769, 2024. ISSN 1539-4794. doi: 10.1364/OL.527988.

[5] Supriya Rajhans, Nikolas Rupp, Esmerando Escoto, Arthur Schönberg, Dominic Laumer, Malte Sumfleth, Issam Abdallah, Bastian Manschwetus, Caroline Juliano, Nikan Javid, Cord Arnold, TAIS GORKHOVER, Markus Drescher, Robert Riedel, Ingmar Hartl, Christoph Heyl, and Tino Lang. Optical parametric multi-pass cell amplifier. *Optica*, 2026. ISSN 2334-2536. doi: 10.1364/optica.597010.

[6] Arthur Schönberg, Nikolas Rupp, Ana Oliveira e Silva, Lorenzo Pratolli, Yujiao Jiang, Vincent Wanie, Terence Mullins, Francesca Calegari, and Christoph M. Heyl. Efficient broadband second-harmonic generation in a multi-pass cell, 2026. URL `https://arxiv.org/abs/2607.03192`.

[7] T. H. Maiman. Stimulated optical radiation in ruby. *Nature*, 187(4736):493–494, 1960. ISSN 1476-4687. doi: 10.1038/187493a0.

[8] Hermann A. Haus. Mode-locking of lasers. *IEEE Journal of Selected Topics in Quantum Electronics*, 6:1173–1185, 2000. URL `https://api.semanticscholar.org/CorpusID:43518800`.

[9] P. A. Franken, A. E. Hill, C. W. Peters, and G. Weinreich. Generation of optical harmonics. *Physical Review Letters*, 7(4):118–119, 1961. ISSN 0031-9007. doi: 10.1103/PhysRevLett.7.118.

[10] J. A. Giordmaine. Mixing of light beams in crystals. *Physical Review Letters*, 8(1):19–20, 1962. ISSN 0031-9007. doi: 10.1103/PhysRevLett.8.19.

[11] P. D. Maker, R. W. Terhune, M. Nisenoff, and C. M. Savage. Effects of dispersion and focusing on the production of optical harmonics. *Physical Review Letters*, 8(1):21–22, 1962. ISSN 0031-9007. doi: 10.1103/PhysRevLett.8.21.

[12] Giulio Cerullo and Sandro De Silvestri. Ultrafast optical parametric amplifiers. *Review of Scientific Instruments*, 74(1):1–18, 2003. ISSN 1089-7623. doi: 10.1063/1.1523642.

[13] Goëry Genty, Stéphane Coen, and John M. Dudley. Fiber supercontinuum sources (Invited). *Journal of the Optical Society of America B*, 24(8):1771, 2007. ISSN 1520-8540. doi: 10.1364/josab.24.001771.

[14] L. F. Mollenauer, R. H. Stolen, and J. P. Gordon. Experimental Observation of Picosecond Pulse Narrowing and Solitons in Optical Fibers. *Physical Review Letters*, 45(13):1095–1098, 1980. ISSN 0031-9007. doi: 10.1103/physrevlett.45.1095.

[15] Margherita Maiuri, Marco Garavelli, and Giulio Cerullo. Ultrafast Spectroscopy: State of the Art and Open Challenges. *Journal of the American Chemical Society*, 142(1):3–15, 2019. ISSN 1520-5126. doi: 10.1021/jacs.9b10533.

[16] Thomas Brabec and Ferenc Krausz. Intense few-cycle laser fields: Frontiers of nonlinear optics. *Reviews of Modern Physics*, 72(2):545–591, 2000. ISSN 1539-0756. doi: 10.1103/revmodphys.72.545.

[17] Ferenc Krausz and Misha Ivanov. Attosecond physics. *Reviews of Modern Physics*, 81(1):163–234, 2009. ISSN 1539-0756. doi: 10.1103/revmodphys.81.163.

[18] F. Calegari, D. Ayuso, A. Trabattoni, L. Belshaw, S. De Camillis, S. Anumula, F. Frassetto, L. Poletto, A. Palacios, P. Decleva, J. B. Greenwood, F. Martín, and M. Nisoli. Ultrafast electron dynamics in phenylalanine initiated by attosecond pulses. *Science*, 346(6207):336–339, 2014. ISSN 1095-9203. doi: 10.1126/science.1254061.

[19] Andrea Orlando, Filippo Franceschini, Cristian Muscas, Solomiya Pidkova, Mattia Bartoli, Massimo Rovere, and Alberto Tagliaferro. A Comprehensive Review on Raman Spectroscopy Applications. *Chemosensors*, 9(9):262, 2021. ISSN 2227-9040. doi: 10.3390/chemosensors9090262.

[20] Stojan Radic, David J. Moss, and Benjamin J. Eggleton. *Nonlinear optics in communications*, pages 759–828. Elsevier, 2008. ISBN 9780123741714. doi: 10.1016/b978-0-12-374171-4.00020-4.

[21] Christopher B. Marble and Vladislav V. Yakovlev. Biomedical Optics Applications of Advanced Lasers and Nonlinear Optics. *Journal of Biomedical Optics*, 25(4):040902, 2020. doi: 10.1117/1.JBO.25.4.040902.

[22] H. T. Olgun, W. Tian, G. Cirmi, K. Ravi, C. Rentschler, H. Çankaya, M. Pergament, M. Hemmer, Y. Hua, D. N. Schimpf, N. H. Matlis, and F. X. Kärtner. Highly efficient generation of narrowband terahertz radiation driven by a two-spectral-line laser in PPLN. *Optics Letters*, 47(10):2374, 2022. ISSN 1539-4794. doi: 10.1364/ol.448457.

[23] John C. Travers, Teodora F. Grigorova, Christian Brahms, and Federico Belli. High-energy pulse self-compression and ultraviolet generation through soliton dynamics in hollow capillary fibres. *Nature Photonics*, 13(8):547–554, 2019. ISSN 1749-4893. doi: 10.1038/s41566-019-0416-4.

[24] Prannay Balla, Ammar Bin Wahid, Ivan Sytcevich, Chen Guo, Anne-Lise Viotti, Laura Silletti, Andrea Cartella, Skirmantas Alisauskas, Hamed Tavakol, Uwe Grosse-Wortmann, Arthur Schönberg, Marcus Seidel, Andrea Trabattoni, Bastian Manschwetus, Tino Lang, Francesca Calegari, Arnaud Couairon, Anne L'Huillier, Cord L. Arnold, Ingmar Hartl, and Christoph M. Heyl. Postcompression of picosecond pulses into the few-cycle regime. *Optics Letters*, 45(9):2572, 2020. ISSN 1539-4794. doi: 10.1364/OL.388665.

[25] Philippe Antoine, Anne L'Huillier, and Maciej Lewenstein. Attosecond Pulse Trains Using High–Order Harmonics. *Physical Review Letters*, 77(7):1234–1237, 1996. ISSN 1079-7114. doi: 10.1103/physrevlett.77.1234.

[26] Robert W. Boyd. *Nonlinear Optics*. Elsevier, AP Academic Press, London, fourth edition, 2020. ISBN 978-0-12-811002-7.

[27] Govind P. Agrawal. *Nonlinear fiber optics*. Engineering professional collection. Academic Press, Oxford, 5th ed edition, 2013. ISBN 9780123970237. Includes bibliographical references and index.

[28] Jan Schulte, Thomas Sartorius, Johannes Weitenberg, Andreas Vernaleken, and Peter Russbueldt. Nonlinear pulse compression in a multi-pass cell. *Optics Letters*, 41(19):4511, 2016. ISSN 1539-4794. doi: 10.1364/ol.41.004511.

[29] Johannes Weitenberg, Andreas Vernaleken, Jan Schulte, Akira Ozawa, Thomas Sartorius, Vladimir Pervak, Hans-Dieter Hoffmann, Thomas Udem, Peter Russbüldt, and Theodor W. Hänsch. Multi-pass-cell-based nonlinear pulse compression to 115 fs at 75 µJ pulse energy and 300 W average power. *Optics Express*, 25(17):20502, 2017. ISSN 1094-4087. doi: 10.1364/oe.25.020502.

[30] Donald R. Herriott and Harry J. Schulte. Folded Optical Delay Lines. *Applied Optics*, 4(8):883, 1965. ISSN 1539-4522. doi: 10.1364/ao.4.000883.

[31] Anne-Lise Viotti, Marcus Seidel, Esmerando Escoto, Supriya Rajhans, Wim P. Leemans, Ingmar Hartl, and Christoph M. Heyl. Multi-pass cells for post-compression of ultrashort laser pulses. *Optica*, 9(2):197, 2022. ISSN 2334-2536. doi: 10.1364/optica.449225.

[32] Christian Grebing, Michael Müller, Joachim Buldt, Henning Stark, and Jens Limpert. Kilowatt-average-power compression of millijoule pulses in a gas-filled multi-pass cell. *Optics Letters*, 45(22):6250, 2020. ISSN 1539-4794. doi: 10.1364/OL.408998.

[33] Imre Seres, Evgeny Shestaev, Maxim Tschernajew, Péter Jójárt, Christian Gaida, Nico Walther, Tamás Bartyik, Barnabás Gilicze, Zsolt Bengery, Dominik Hoff, Marco Kienel, Tino Eidam, Jens Limpert, Ádám Börzsönyi, Katalin Varjú, and Zoltán Várallyay. Over 400 W average power, sub-two-cycle, carrier-envelope phase-stable fiber laser system. *High Power Laser Science and Engineering*, 14, 2026. ISSN 2052-3289. doi: 10.1017/HPL.2025.10103.

[34] Cesar Jauregui, Jens Limpert, and Andreas Tünnermann. High-power fibre lasers. *Nature Photonics*, 7(11):861–867, 2013. ISSN 1749-4893. doi: 10.1038/nphoton.2013.273.

[35] D. Carlson, M. Tanksalvala, D. Morrill, J. San Roman, E. Conejero Jarque, H. C. Kapteyn, M. M. Murnane, and M. Hemmer. Nonlinear post-compression in multi-pass cells in the mid-IR region using bulk materials. *Optics Letters*, 47(20):5289, 2022. ISSN 1539-4794. doi: 10.1364/OL.471458.

[36] Lucas Eisenbach, Ziyao Wang, Jan Schulte, Tobias Heuermann, Peter Russbüldt, Rudolf Meyer, Philipp Gierschke, Mathias Lenski, Muneo Sugiura, Koichi Tamura, Jens Limpert, and Constantin Häfner. Highly efficient nonlinear compression of mJ pulses at 2 μm wavelength to 20 fs in a gas-filled multi-pass cell. *Journal of Physics: Photonics*, 6(3):035015, 2024. ISSN 2515-7647. doi: 10.1088/2515-7647/ad4cc4.

[37] Ziyao Wang, Warunya Röder, Tobias Heuermann, Chang Liu, Philipp Gierschke, Yi Zhang, Maximilian Karst, Mathias Lenski, Lucas Eisenbach, Robert Klas, Jan Rothhardt, and Jens

Limpert. Multipass-cell-based pulse compression to sub-two-cycle duration at 2 μm. *Optics Letters*, 51(9):2460, 2026. ISSN 1539-4794. doi: 10.1364/OL.586515.

[38] Louis Daniault, Jaismeen Kaur, Geoffrey Gallé, Cedric Sire, François Sylla, and Rodrigo Lopez-Martens. Sub-2-cycle post-compression of multi-mJ energy Ti:sapphire laser pulses in a gas-filled multi-pass cell. *Optics Letters*, 49(23):6833, 2024. ISSN 1539-4794. doi: 10.1364/OL.544563.

[39] Victor Hariton, Ammar Bin Wahid, Gonçalo Figueira, Kilian Fritsch, and Oleg Pronin. Multipass spectral broadening and compression in the green spectral range. *Optics Letters*, 47(5):1246, 2022. ISSN 1539-4794. doi: 10.1364/ol.450200.

[40] Yanik Pfaff, Gaia Barbiero, Michael Rampp, Sandro Klingebiel, Jonathan Brons, Catherine Y. Teisset, Haochuan Wang, Robert Jung, Jasna Jaksic, Abel H. Woldegeorgis, Maximilian Trunk, Andreas R. Maier, Clara J. Saraceno, and Thomas Metzger. Nonlinear pulse compression of a 200 mJ and 1 kW ultrafast thin-disk amplifier. *Optics Express*, 31(14): 22740, 2023. ISSN 1094-4087. doi: 10.1364/OE.494359.

[41] Martin Kaumanns, Dmitrii Kormin, Thomas Nubbemeyer, Vladimir Pervak, and Stefan Karsch. Spectral broadening of 112 mJ, 1.3 ps pulses at 5 kHz in a LG_{10} multipass cell with compressibility to 37 fs. *Optics Letters*, 46(5):929, 2021. ISSN 1539-4794. doi: 10.1364/OL.416734.

[42] V. Koltalo, S. Westerberg, M. Redon, G. Beaufort, A.-K. Raab, C. Guo, C. L. Arnold, and A.-L. Viotti. Energy scaling in a compact bulk multi-pass cell enabled by Laguerre–Gaussian single-vortex beams. *APL Photonics*, 10(4), 2025. ISSN 2378-0967. doi: 10.1063/5.0253348.

[43] Ania Ierano', Michele Natile, Anne-Lise Viotti, Florent Guichard, Marc Hanna, and Patrick Georges. Energy scaling and propagation properties of Laguerre-Gauss modes in gas-filled multipass cells. *Optics Express*, 34(11):19478, 2026. ISSN 1094-4087. doi: 10.1364/OE.597143.

[44] Henning Stark, Christian Grebing, Christian Grebing, Joachim Buldt, Arno Klenke, and Jens Limpert. Divided-pulse nonlinear compression in a multipass cell. *Journal of Physics: Photonics*, 4(3):035001, 2022. ISSN 2515-7647. doi: 10.1088/2515-7647/ac66ab.

[45] Henrik Schygulla, Nayla Jimenez, Yujiao Jiang, Ingmar Hartl, and Marcus Seidel. Divided-pulse Bulk Multi-pass Cell for Generating Sub-50 fs multi-GW Peak Power Pulses. *EPJ Web of Conferences*, 307:04066, 2024. ISSN 2100-014X. doi: 10.1051/epjconf/202430704066.

[46] Nayla Jimenez, Victor Hariton, Henrik Tünnermann, Hüseyin C̈ankaya, Ingmar Hartl, and Marcus Seidel. Passive Coherent Combining for Energy-Scaled Pulse Compression in Multipass Cells. In *Frontiers in Optics + Laser Science 2025 (FiO, LS)*, LS, page LTh3F.5. Optica Publishing Group, 2025. doi: 10.1364/ls.2025.lth3f.5.

[47] Victor Hariton, Kilian Fritsch, Kevin Schwarz, Nazar Kovalenko, Gonçalo Figueira, Gunnar Arisholm, and Oleg Pronin. Spectral broadening in convex-concave multipass cells. *Optics Express*, 31(12):19554, 2023. ISSN 1094-4087. doi: 10.1364/OE.486797.

[48] Jonas Manz, Gaia Barbiero, Sandro Klingebiel, Catherine Y. Teisset, Haochuan Wang, Michael Rampp, Jonathan Brons, Clara J. Saraceno, and Thomas Metzger. Bulk-based nonlinear pulse compression of 30 mJ and 150 W pulses of an ultrafast thin-disk amplifier. *Optics Express*, 33(26):54907, 2025. ISSN 1094-4087. doi: 10.1364/OE.580757.

[49] Martin Kaumanns, Vladimir Pervak, Dmitrii Kormin, Vyacheslav Leshchenko, Alexander Kessel, Moritz Ueffing, Yu Chen, and Thomas Nubbemeyer. Multipass spectral broadening of 18 mJ pulses compressible from 13 ps to 41 fs. *Optics Letters*, 43(23):5877, 2018. ISSN 1539-4794. doi: 10.1364/ol.43.005877.

[50] Michael Müller, Joachim Buldt, Henning Stark, Christian Grebing, and Jens Limpert. Multipass cell for high-power few-cycle compression. *Optics Letters*, 46(11):2678, 2021. ISSN 1539-4794. doi: 10.1364/ol.425872.

[51] Supriya Rajhans, Esmerando Escoto, Nikita Khodakovskiy, Praveen K. Velpula, Bonaventura Farace, Uwe Grosse-Wortmann, Rob J. Shalloo, Cord L. Arnold, Kristjan Põder, Jens Osterhoff, Wim P. Leemans, Ingmar Hartl, and Christoph M. Heyl. Post-compression of multi-millijoule picosecond pulses to few-cycles approaching the terawatt regime. *Optics Letters*, 48(18):4753, 2023. ISSN 1539-4794. doi: 10.1364/ol.498042.

[52] Semyon Goncharov, Kilian Fritsch, and Oleg Pronin. Few-cycle pulse compression and white light generation in cascaded multipass cells. *Optics Letters*, 48(1):147, 2022. ISSN 1539-4794. doi: 10.1364/ol.479248.

[53] Anne-Lise Viotti, Chen Li, Gunnar Arisholm, Lutz Winkelmann, Ingmar Hartl, Christoph M. Heyl, and Marcus Seidel. Few-cycle pulse generation by double-stage hybrid multi-pass multi-plate nonlinear pulse compression. *Optics Letters*, 48(4):984, 2023. ISSN 1539-4794. doi: 10.1364/ol.478790.

[54] Yinfei Liu, Jiajun Song, Xiaoming Lu, Yujie Peng, Yanyan Li, Guanguang Gao, Liya Shen, Junze Zhu, Tianze Xu, and Yuxin Leng. Temporal contrast enhancement by self-phase modulation in a multi-pass cell with excellent beam quality and pointing stability. *Chinese Optics Letters*, 24(2):021401, 2026. ISSN 1671-7694. doi: 10.3788/COL202624.021401.

[55] Esmerando Escoto, Andrea Zablah Ticas, Supriya Rajhans, and Christoph M. Heyl. Post-Compression with Enhanced Temporal Pulse Quality via Chirped Ellipse Rotation. In *2025 Conference on Lasers and Electro-Optics Europe & European Quantum Electronics Conference (CLEO/Europe-EQEC)*, pages 1–1. IEEE, 2025. doi: 10.1109/CLEO/Europe-EQEC65582.2025.11110933.

[56] Maximilian Benner, Maximilian Karst, Cristina Amaya Mendez, Henning Stark, and Jens Limpert. Concept of enhanced frequency chirping for multi-pass cells to improve the pulse contrast. *Journal of the Optical Society of America B*, 40(2):301, 2023. ISSN 1520-8540. doi: 10.1364/josab.479037.

[57] Esmerando Escoto, Anne-Lise Viotti, Skirmantas Alisauskas, Henrik Tünnermann, Ingmar Hartl, and Christoph M. Heyl. Temporal quality of post-compressed pulses at large compression factors. *Journal of the Optical Society of America B*, 39(7):1694, 2022. ISSN 1520-8540. doi: 10.1364/josab.453901.

[58] Viktor Pajer and Mikhail Kalashnikov. High temporal contrast ultrashort pulses generated by nonlinear ellipse rotation in multipass cells. *Laser Physics Letters*, 18(6):065401, 2021. ISSN 1612-202X. doi: 10.1088/1612-202x/abff49.

[59] Esmerando Escoto, Federico Pressacco, Yujiao Jiang, Supriya Rajhans, Nikita Khodakovskiy, Ingmar Hartl, Marcus Seidel, Christoph M. Heyl, and Henrik Tünnermann. Improved temporal characteristics for post-compressed pulses via application-tailored nonlinear polarization ellipse rotation. *Optics Letters*, 49(23):6841, 2024. ISSN 1539-4794. doi: 10.1364/ol.539646.

[60] Nour Daher, Xavier Délen, Florent Guichard, Marc Hanna, and Patrick Georges. Raman wavelength conversion in a multipass cell. *Optics Letters*, 46(14):3380, 2021. ISSN 1539-4794. doi: 10.1364/ol.431675.

[61] Giovanni Cichelli, Gautier Parize, Michele Natile, Xavier Delen, Florent Guichard, Paolo Laporta, Nicola Coluccelli, Marc Hanna, and Patrick Georges. High-energy soliton frequency shifting in a nitrogen-filled multipass cell. *Optics Letters*, 50(21):6714, 2025. ISSN 1539-4794. doi: 10.1364/ol.568548.

[62] Prannay Balla, Henrik Tünnermann, Sarper H. Salman, Mingqi Fan, Skirmantas Alisauskas, Ingmar Hartl, and Christoph M. Heyl. Ultrafast serrodyne optical frequency translator. *Nature Photonics*, 17(2):187–192, 2022. ISSN 1749-4893. doi: 10.1038/s41566-022-01121-9.

[63] Jan H. Nägele, Tobias Steinle, Johann Thannheimer, Philipp Flad, and Harald Giessen. Dispersion-engineered multipass optical parametric amplification. *Nature*, 647(8088):74–79, 2025. ISSN 1476-4687. doi: 10.1038/s41586-025-09665-w.

[64] Nazar Kovalenko, Victor Hariton, Kilian Fritsch, and Oleg Pronin. Free-space quasi-phase matching. *Optics Letters*, 48(23):6220, 2023. ISSN 1539-4794. doi: 10.1364/OL.502825.

[65] Nazar Kovalenko, Ankit Pai, and Oleg Pronin. Free-space quasi-phase matched second harmonic generation in crystalline quartz, 2026.

[66] Praveen Kumar Velpula, Daniel Kramer, and Bedrich Rus. Femtosecond Laser-Induced Damage Characterization of Multilayer Dielectric Coatings. *Coatings*, 10(6):603, 2020. ISSN 2079-6412. doi: 10.3390/coatings10060603.

[67] M. J. Norman, C. Chandre, T. Uzer, and P. Wang. Nonlinear dynamics of ionization stabilization of atoms in intense laser fields. *Physical Review A*, 91(2):023406, 2015. ISSN 1094-1622. doi: 10.1103/physreva.91.023406.

[68] F. Tavella and K. Mecseki. Multi-pass cell spectral broadening at high pulse energies. *Physics of Plasmas*, 29(8), 2022. ISSN 1089-7674. doi: 10.1063/5.0091955.

[69] A. Couairon, E. Brambilla, T. Corti, D. Majus, O. de J. Ramírez-Góngora, and M. Kolesik. Practitioner's guide to laser pulse propagation models and simulation: Numerical implementation and practical usage of modern pulse propagation models. *The European Physical Journal Special Topics*, 199(1):5–76, 2011. ISSN 1951-6401. doi: 10.1140/epjst/e2011-01503-3.

[70] H. Kogelnik and T. Li. Laser Beams and Resonators. *Applied Optics*, 5(10):1550, 1966. ISSN 1539-4522. doi: 10.1364/ao.5.001550.

[71] C. M. Heyl, H. Coudert-Alteirac, M. Miranda, M. Louisy, K. Kovacs, V. Tosa, E. Balogh, K. Varjú, A. L'Huillier, A. Couairon, and C. L. Arnold. Scale-invariant nonlinear optics in gases. *Optica*, 3(1):75, 2016. ISSN 2334-2536. doi: 10.1364/optica.3.000075.

[72] Nayla Jimenez, Victor Hariton, Arthur Schönberg, Ayhan Tajalli, Ingmar Hartl, and Marcus Seidel. Double-stage Compact Multi-pass Cell for Sub-20 fs Pulse Compression. In *CLEO 2025*, page SS147_2. Optica Publishing Group, 2025. doi: 10.1364/CLEO_SI.2025.SS147_2.

[73] Alan Omar, Tim Vogel, Martin Hoffmann, and Clara J. Saraceno. Spectral broadening of 2-mJ femtosecond pulses in a compact air-filled convex–concave multi-pass cell. *Optics Letters*, 48(6):1458, 2023. ISSN 1539-4794. doi: 10.1364/ol.481774.

[74] T. Südmeyer, S. V. Marchese, S. Hashimoto, C. R. E. Baer, G. Gingras, B. Witzel, and U. Keller. Femtosecond laser oscillators for high-field science. *Nature Photonics*, 2(10): 599–604, 2008. ISSN 1749-4893. doi: 10.1038/nphoton.2008.194.

[75] Gaspard Beaufort, Nayla Jimenez, Gunnar Arisholm, Victor Hariton, Ayhan Tajalli, Ingmar Hartl, Anne-Lise Viotti, and Marcus Seidel. Towards direct nonlinear compression of energetic sub-nanosecond pulses to the ultrafast regime. *High Power Laser Science and Engineering*, pages 1–23, 2026. ISSN 2052-3289. doi: 10.1017/hpl.2026.10156.

[76] Chengyong Feng and Jake Bromage. Nonlinear post-compression to sub-20 fs using a single-stage multipass cell filled with ambient air. *Optics Express*, 34(4):6073, 2026. ISSN 1094-4087. doi: 10.1364/oe.588406.

[77] D. Langevin, J. M. Brown, M. B. Gaarde, and A. Couairon. Determination of molecular contributions to the nonlinear refractive index of air for mid-infrared femtosecond laser-pulse excitation. *Physical Review A*, 99(6):063418, 2019. ISSN 2469-9934. doi: 10.1103/physreva.99.063418.

[78] Miguel Miranda, Marija Kotur, Piotr Rudawski, Chen Guo, Anne Harth, Anne L'Huillier, and Cord L. Arnold. Spatiotemporal characterization of ultrashort laser pulses using spatially resolved Fourier transform spectrometry. *Optics Letters*, 39(17):5142, 2014. ISSN 1539-4794. doi: 10.1364/ol.39.005142.

[79] Sibo Niu, Wenwen Wang, Pan Liu, Yiheng Zhang, Xiaoming Zhao, Jibo Li, Maosen Xiao, Yuzhi Wang, Jing Li, and Xiaopeng Shao. Recent Advances in Applications of Ultrafast Lasers. *Photonics*, 11(9):857, 2024. ISSN 2304-6732. doi: 10.3390/photonics11090857.

[80] M Yu Ivanov, R Kienberger, A Scrinzi, and D M Villeneuve. Attosecond physics. *Journal of Physics B: Atomic, Molecular and Optical Physics*, 39(1):R1–R37, 2005. ISSN 1361-6455. doi: 10.1088/0953-4075/39/1/r01.

[81] W. P. Leemans, B. Nagler, A. J. Gonsalves, Cs. Tóth, K. Nakamura, C. G. R. Geddes, E. Esarey, C. B. Schroeder, and S. M. Hooker. GeV electron beams from a centimetre-scale accelerator. *Nature Physics*, 2(10):696–699, 2006. ISSN 1745-2481. doi: 10.1038/nphys418.

[82] K. Põder, J. C. Wood, N. C. Lopes, J. M. Cole, S. Alatabi, M. P. Backhouse, P. S. Foster, A. J. Hughes, C. Kamperidis, O. Kononenko, S. P. D. Mangles, C. A. J. Palmer, D. Rusby, A. Sahai, G. Sarri, D. R. Symes, J. R. Warwick, and Z. Najmudin. Multi-GeV Electron Acceleration in Wakefields Strongly Driven by Oversized Laser Spots. *Phys. Rev. Lett.*, 132 (19):195001, 2024. doi: 10.1103/PhysRevLett.132.195001.

[83] Jie Li, Jian Lu, Andrew Chew, Seunghwoi Han, Jialin Li, Yi Wu, He Wang, Shambhu Ghimire, and Zenghu Chang. Attosecond science based on high harmonic generation from gases and solids. *Nature Communications*, 11(1), 2020. ISSN 2041-1723. doi: 10.1038/s41467-020-16480-6.

[84] Can Kerse, Hamit Kalaycıoğlu, Parviz Elahi, Barbaros Çetin, Denizhan K. Kesim, Önder Akçaalan, Seydi Yavaş, Mehmet D. Aşık, Bülent Öktem, Heinar Hoogland, Ronald Holzwarth, and Fatih Ömer Ilday. Ablation-cooled material removal with ultrafast bursts of pulses. *Nature*, 537(7618):84–88, 2016. ISSN 1476-4687. doi: 10.1038/nature18619.

[85] Hermann A. Haus. Theory of mode locking with a fast saturable absorber. *Journal of Applied Physics*, 46(7):3049–3058, 1975. ISSN 1089-7550. doi: 10.1063/1.321997.

[86] Donna Strickland and Gerard Mourou. Compression of amplified chirped optical pulses. *Optics Communications*, 55(6):447–449, 1985. ISSN 0030-4018. doi: 10.1016/0030-4018(85)90151-8.

[87] Sterling Backus, Charles G. Durfee, Margaret M. Murnane, and Henry C. Kapteyn. High power ultrafast lasers. *Review of Scientific Instruments*, 69(3):1207–1223, 1998. ISSN 1089-7623. doi: 10.1063/1.1148795.

[88] Henning Stark, Joachim Buldt, Michael Müller, Arno Klenke, and Jens Limpert. 1 kW, 10 mJ, 120 fs Coherently Combined Fiber CPA Laser System. *Optics Letters*, 46(5):969, 2021. doi: 10.1364/OL.417032.

[89] F. J. McClung and R. W. Hellwarth. Giant Optical Pulsations from Ruby. *Applied Optics*, 1(S1):103, 1962. ISSN 1539-4522. doi: 10.1364/ao.1.s1.000103.

[90] Jingling Tang, Zhenxu Bai, Duo Zhang, Yaoyao Qi, Jie Ding, Yulei Wang, and Zhiwei Lu. Advances in All-Solid-State Passively Q-Switched Lasers Based on Cr4+:YAG Saturable Absorber. *Photonics*, 8(4):93, 2021. ISSN 2304-6732. doi: 10.3390/photonics8040093.

[91] Stephan Gräf, Gisbert Staupendahl, André Krämer, and Frank A. Müller. High precision materials processing using a novel Q-switched CO 2 laser. *Optics and Lasers in Engineering*, 66:152–157, 2015. ISSN 0143-8166. doi: 10.1016/j.optlaseng.2014.09.007.

[92] Marco Nägele, Klaus Stoppel, and Thomas Dekorsy. Passively Q-switched 914 nm microchip laser for lidar systems. *Optics Express*, 29(15):23799, 2021. doi: 10.1364/OE.432340.

[93] M. Skorczakowski, J. Swiderski, W. Pichola, P. Nyga, A. Zajac, M. Maciejewska, L. Galecki, J. Kasprzak, S. Gross, A. Heinrich, and T. Bragagna. Mid-infrared Q-switched Er:YAG laser for medical applications. *Laser Physics Letters*, 7(7):498–504, 2010. ISSN 1612-202X. doi: 10.1002/lapl.201010019.

[94] Lívia Arroyo Trídico and Carlos Roberto Antonio. Laser quality switched (Q-switched): revisão de suas variações e principais aplicabilidades clínicas. *Surgical & Cosmetic Dermatology*, 11(4), 2019. doi: 10.5935/scd1984-8773.20191141419.

[95] Mike Poulter, Nick Hay, Ben Fulford, Paul Campton, Mike Mason, and David Burns. Q-switched Nd:YAG lasers for high average-power and high peak-power operation. In W. Andrew Clarkson, Norman Hodgson, and Ramesh K. Shori, editors, *Solid State Lasers XVIII: Technology and Devices*, volume 7193, page 719309. SPIE, 2009. doi: 10.1117/12.814927.

[96] Bo-Han Chen, Jia-Xuan Su, Jhan-Yu Guo, Kai Chen, Shi-Wei Chu, Hsuan-Hao Lu, Chih-Hsuan Lu, and Shang-Da Yang. Double-Pass Multiple-Plate Continuum for High-Temporal-Contrast Nonlinear Pulse Compression. *Frontiers in Photonics*, 3, 2022. ISSN 2673-6853. doi: 10.3389/fphot.2022.937622.

[97] Jonathan Hu, Brian S. Marks, Curtis R. Menyuk, Jinchae Kim, Thomas F. Carruthers, Barbara M. Wright, Thierry F. Taunay, and E. Joseph Friebele. Pulse compression using a tapered microstructure optical fiber. *Optics Express*, 14(9):4026, 2006. ISSN 1094-4087. doi: 10.1364/oe.14.004026.

[98] Aleksandr A. Tarasov and Hong Chu. Subnanosecond Nd: YAG laser with multipass cell for SBS pulse compression. In W. Andrew Clarkson and Ramesh K. Shori, editors, *Solid State Lasers XXVI: Technology and Devices*, volume 10082, page 100820Q. SPIE, 2017. doi: 10.1117/12.2248355.

[99] Chengyong Feng, Xiaozhen Xu, and Jean-Claude Diels. High-energy sub-phonon lifetime pulse compression by stimulated Brillouin scattering in liquids. *Optics Express*, 25(11): 12421, 2017. ISSN 1094-4087. doi: 10.1364/oe.25.012421.

[100] David T. Hon. Pulse compression by stimulated Brillouin scattering. *Optics Letters*, 5(12): 516, 1980. ISSN 1539-4794. doi: 10.1364/ol.5.000516.

[101] C.B. Dane, W.A. Neuman, and L.A. Hackel. High-energy SBS pulse compression. *IEEE Journal of Quantum Electronics*, 30(8):1907–1915, 1994. ISSN 0018-9197. doi: 10.1109/3.301654.

[102] H. Yoshida, H. Fujita, M. Nakatsuka, T. Ueda, and A. Fujinoki. Temporal compression by stimulated Brillouin scattering of Q-switched pulse with fused-quartz and fused-silica glass from 1064 nm to 266 nm wavelength. *Laser and Particle Beams*, 25(3):481–488, 2007. ISSN 1469-803X. doi: 10.1017/s0263034607000596.

[103] Masayuki Matsumoto and Genya Miyashita. Efficiency and Stability of Pulse Compression Using SBS in a Fiber With Frequency-Shifted Loopback. *IEEE Photonics Technology Letters*, 29(1):3–6, 2017. ISSN 1941-0174. doi: 10.1109/lpt.2016.2623324.

[104] L. F. Mollenauer, W. J. Tomlinson, R. H. Stolen, and J. P. Gordon. Extreme picosecond pulse narrowing by means of soliton effect in single-mode optical fibers. *Optics Letters*, 8(5): 289, 1983. ISSN 1539-4794. doi: 10.1364/ol.8.000289.

[105] A. M. Johnson, R. H. Stolen, and W. M. Simpson. 80× single-stage compression of frequency doubled Nd:yttrium aluminum garnet laser pulses. *Applied Physics Letters*, 44(8):729–731, 1984. ISSN 1077-3118. doi: 10.1063/1.94897.

[106] J. D. Kafka, B. H. Kolner, T. Baer, and D. M. Bloom. Compression of pulses from a continuous-wave mode-locked Nd:YAG laser. *Optics Letters*, 9(11):505, 1984. ISSN 1539-4794. doi: 10.1364/ol.9.000505.

[107] R. H. Stolen, W. J. Tomlinson, H. A. Haus, and J. P. Gordon. Raman response function of silica-core fibers. *Journal of the Optical Society of America B*, 6(6):1159, 1989. ISSN 1520-8540. doi: 10.1364/josab.6.001159.

[108] Takashi Nakashima, Masataka Nakazawa, Kazuki Nishi, and Hirokazu Kubota. Effect of stimulated Raman scattering on pulse-compression characteristics. *Opt. Lett.*, 12(6):404–406, 1987. doi: 10.1364/OL.12.000404. URL `https://opg.optica.org/ol/abstract.cfm?URI=ol-12-6-404`.

[109] Johannes Weitenberg, Tobias Saule, Jan Schulte, and Peter Rusbuldt. Nonlinear Pulse Compression to Sub-40 fs at 4.5 μ J Pulse Energy by Multi-Pass-Cell Spectral Broadening. *IEEE Journal of Quantum Electronics*, 53(6):1–4, 2017. ISSN 1558-1713. doi: 10.1109/jqe.2017.2761883.

[110] Jiajun Song, Zhaohua Wang, Renchong Lv, Xianzhi Wang, Hao Teng, Jiangfeng Zhu, and Zhiyi Wei. Generation of 172 fs pulse from a Nd: YVO4 picosecond laser by using multi-pass-cell technique. *Applied Physics B*, 127(4), 2021. ISSN 1432-0649. doi: 10.1007/s00340-021-07587-9.

[111] Marcus Seidel, Federico Pressacco, Oender Akcaalan, Thomas Binhammer, John Darvill, Nagitha Ekanayake, Maik Frede, Uwe Grosse-Wortmann, Michael Heber, Christoph M. Heyl, Dmytro Kutnyakhov, Chen Li, Christian Mohr, Jost Müller, Oliver Puncken, Harald Redlin, Nora Schirmel, Sebastian Schulz, Angad Swiderski, Hamed Tavakol, Henrik Tünnermann,

Caterina Vidoli, Lukas Wenthaus, Nils Wind, Lutz Winkelmann, Bastian Manschwetus, and Ingmar Hartl. Ultrafast MHz-Rate Burst-Mode Pump–Probe Laser for the FLASH FEL Facility Based on Nonlinear Compression of ps-Level Pulses from an Yb-Amplifier Chain. *Laser & Photonics Reviews*, 16(3), 2022. doi: 10.1002/lpor.202100268.

[112] Laura Silletti, Ammar bin Wahid, Esmerando Escoto, Prannay Balla, Supriya Rajhans, Katinka Horn, Lutz Winkelmann, Vincent Wanie, Andrea Trabattoni, Christoph M. Heyl, and Francesca Calegari. Dispersion-engineered multi-pass cell for single-stage post-compression of an ytterbium laser. *Optics Letters*, 48(7):1842, 2023. ISSN 1539-4794. doi: 10.1364/ol.476846.

[113] Moritz Ueffing, Simon Reiger, Martin Kaumanns, Vladimir Pervak, Michael Trubetskov, Thomas Nubbemeyer, and Ferenc Krausz. Nonlinear pulse compression in a gas-filled multipass cell. *Optics Letters*, 43(9):2070, 2018. ISSN 1539-4794. doi: 10.1364/ol.43.002070.

[114] Anne-Lise Viotti, Skirmantas Alisauskas, Ammar Bin Wahid, Prannay Balla, Nora Schirmel, Bastian Manschwetus, Ingmar Hartl, and Christoph M. Heyl. 60 fs, 1030 nm FEL Pump–Probe Laser Based on a Multi-Pass Post-Compressed Yb:YAG Source. *Journal of Synchrotron Radiation*, 28(1):36–43, 2021. doi: 10.1107/S1600577520015052.

[115] Chengyong Feng, Xiaozhen Xu, and Jean-Claude Diels. Generation of 300 ps Laser Pulse with 1.2 J Energy at 532 nm by Stimulated Brillouin Scattering in Water. In *CLEO: 2014*, page SM2F.7. OSA, 2014. doi: 10.1364/CLEO_SI.2014.SM2F.7.

[116] M. H. Niemz. Threshold dependence of laser-induced optical breakdown on pulse duration. *Applied Physics Letters*, 66(10):1181–1183, 1995. ISSN 1077-3118. doi: 10.1063/1.113850.

[117] Erikas Atkočaitis, Linas Smalakys, and Andrius Melninkaitis. Pulse temporal scaling of LIDT for anti-reflective coatings deposited on lithium triborate crystals. *Optics Express*, 30 (16):28401, 2022. ISSN 1094-4087. doi: 10.1364/oe.459391.

[118] Claude Robert. Simple, stable, and compact multiple-reflection optical cell for very long optical paths. *Appl. Opt.*, 46(22):5408–5418, 2007. doi: 10.1364/AO.46.005408. URL `https://opg.optica.org/ao/abstract.cfm?URI=ao-46-22-5408`.

[119] John D. Corless, James A. West, Jake Bromage, and C. R. Stroud. Pulsed single-mode dye laser for coherent control experiments. *Review of Scientific Instruments*, 68(6):2259–2264, 1997. ISSN 1089-7623. doi: 10.1063/1.1148056.

[120] R. Y. Chiao, C. H. Townes, and B. P. Stoicheff. Stimulated Brillouin Scattering and Coherent Generation of Intense Hypersonic Waves. *Phys. Rev. Lett.*, 12:592–595, 1964. doi: 10.1103/PhysRevLett.12.592. URL `https://link.aps.org/doi/10.1103/PhysRevLett.12.592`.

[121] E. Armandillo and D. Proch. Highly efficient, high-quality phase-conjugate reflection at 308 nm using stimulated Brillouin scattering. *Opt. Lett.*, 8(10):523–525, 1983. doi: 10.1364/OL.8.000523. URL `https://opg.optica.org/ol/abstract.cfm?URI=ol-8-10-523`.

[122] Marc Hanna, Nour Daher, Florent Guichard, Xavier Délen, and Patrick Georges. Hybrid pulse propagation model and quasi-phase-matched four-wave mixing in multipass cells. *Journal of the Optical Society of America B*, 37(10):2982, 2020. ISSN 1520-8540. doi: 10.1364/josab.395789.

[123] Antoine Monmayrant, Sébastien Weber, and Béatrice Chatel. A newcomer's guide to ultrashort pulse shaping and characterization. *Journal of Physics B: Atomic, Molecular*

and Optical Physics, 43(10):103001, 2010. doi: 10.1088/0953-4075/43/10/103001. URL https://doi.org/10.1088/0953-4075/43/10/103001.

[124] Claire Lefort, Meri Kalashyan, Guillaume Ducourthial, Tigran Mansuryan, Rodney P. O'Connor, and Frederic Louradour. Sub-30-fs pulse compression and pulse shaping at the output of a 2-m-long optical fiber in the near-infrared range. *J. Opt. Soc. Am. B*, 31(10): 2317–2324, 2014. doi: 10.1364/JOSAB.31.002317. URL https://opg.optica.org/josab/abstract.cfm?URI=josab-31-10-2317.

[125] Denis Ilia, Chen Li, Uwe Grosse-Wortmann, Ingmar Hartl, Yujiao Jiang, Christoph Mahnke, Harsha Panuganti, Federico Pressacco, Hamed Tavakol, and Henrik Tünnermann. Advanced pulse shaping for photoinjector lasers. In Peter R. Herman, Roberto Osellame, and Adela Ben-Yakar, editors, *Frontiers in Ultrafast Optics: Biomedical, Scientific, and Industrial Applications XXV*, page 41. SPIE, 2025. doi: 10.1117/12.3050328.

[126] C. E. Rogers and P. L. Gould. Nanosecond pulse shaping at 780 nm with fiber-based electro-optical modulators and a double-pass tapered amplifier. *Opt. Express*, 24(3):2596–2606, 2016. doi: 10.1364/OE.24.002596. URL https://opg.optica.org/oe/abstract.cfm?URI=oe-24-3-2596.

[127] R. A. Meijer, A. S. Stodolna, K. S. E. Eikema, and S. Witte. High-energy Nd:YAG laser system with arbitrary sub-nanosecond pulse shaping capability. *Opt. Lett.*, 42(14):2758–2761, 2017. doi: 10.1364/OL.42.002758. URL https://opg.optica.org/ol/abstract.cfm?URI=ol-42-14-2758.

[128] Yanik Pfaff, Carola Forster, Gaia Barbiero, Michael Rampp, Sandro Klingebiel, Jonathan Brons, Catherine Y. Teisset, Haochuan Wang, Robert Jung, Jasna Jaksic, Abel H. Woldegeorgis, Clara J. Saraceno, and Thomas Metzger. Nonlinear pulse compression of a thin-disk amplifier and contrast enhancement via nonlinear ellipse rotation. *Opt. Express*, 30(7):10981–10990, 2022. doi: 10.1364/OE.455393. URL https://opg.optica.org/oe/abstract.cfm?URI=oe-30-7-10981.

[129] W. R. Sooy. THE NATURAL SELECTION OF MODES IN A PASSIVE Q-SWITCHED LASER. *Applied Physics Letters*, 7(2):36–37, 1965. ISSN 0003-6951. doi: 10.1063/1.1754286. URL https://doi.org/10.1063/1.1754286.

[130] Xuanpu Zhang, Zhihan Wang, Shi Liu, Siyu Gou, Rong Fan, Duo Jin, Zhenao Bai, and Zhenxu Bai. Development of Single-Longitudinal-Mode Selection Technology for Solid-State Lasers. *International Journal of Optics*, 2021:1–13, 2021. ISSN 1687-9384. doi: 10.1155/2021/6667015.

[131] Gregory L. Keaton, Manuel J. Leonardo, Mark W. Byer, and Derek J. Richard. Stimulated Brillouin scattering of pulses in optical fibers. *Opt. Express*, 22(11):13351–13365, 2014. doi: 10.1364/OE.22.013351. URL https://opg.optica.org/oe/abstract.cfm?URI=oe-22-11-13351.

[132] Bin Chen, Zhenxu Bai, Xuanning Hun, Jianping Wang, Can Cui, Yaoyao Qi, Bingzheng Yan, Jie Ding, Kun Wang, Yulei Wang, and Zhiwei Lu. Gain characteristics of stimulated Brillouin scattering in fused silica. *Opt. Express*, 31(4):5699–5707, 2023. doi: 10.1364/OE.480391. URL https://opg.optica.org/oe/abstract.cfm?URI=oe-31-4-5699.

[133] Piotr Kabaciński, Tomasz M. Kardaś, Yuriy Stepanenko, and Czesław Radzewicz. Nonlinear refractive index measurement by SPM-induced phase regression. *Optics Express*, 27(8):11018, 2019. ISSN 1094-4087. doi: 10.1364/oe.27.011018.

[134] Clifford Headley and Govind P. Agrawal. Unified description of ultrafast stimulated Raman scattering in optical fibers. *Journal of the Optical Society of America B*, 13(10):2170, 1996. ISSN 1520-8540. doi: 10.1364/josab.13.002170.

[135] R. Paschotta. Dielectric Mirrors. RP Photonics Encyclopedia, 2005. URL `https://www.rp-photonics.com/dielectric_mirrors.html`. Available online at `https://www.rp-photonics.com/dielectric_mirrors.html`.

[136] Sheila Galt, Mats Sjöberg, Manuel Lopez Quiroga-Teixeiro, and Sverker Hård. Optical breakdown in fused silica and argon gas: application to Nd:YAG laser limiter. *Applied Optics*, 42(3):579, 2003. ISSN 1539-4522. doi: 10.1364/ao.42.000579.

[137] Gitterwerk. 1064 nm Transmission Grating, n.d. URL `https://gitterwerk.com/1064-nm-transmission-grating/`. Accessed: 2026-05-08.

[138] Leonid Glebov, Vadim Smirnov, Eugeniu Rotari, Ion Cohanoschi, Larissa Glebova, Oleg Smolski, Julien Lumeau, Christopher Lantigua, and Alexei Glebov. Volume-chirped Bragg gratings: monolithic components for stretching and compression of ultrashort laser pulses. *Optical Engineering*, 53:051514, 2014. doi: 10.1117/1.OE.53.5.051514.

[139] M. Bass, P. A. Franken, A. E. Hill, C. W. Peters, and G. Weinreich. Optical Mixing. *Physical Review Letters*, 8(1):18–18, 1962. ISSN 0031-9007. doi: 10.1103/physrevlett.8.18.

[140] Shekhar Guha and Joel Falk. The effects of focusing in the three-frequency parametric upconverter. *Journal of Applied Physics*, 51(1):50–60, 1980. ISSN 1089-7550. doi: 10.1063/1.327353.

[141] Lew Goldberg and Dahv A. V. Kliner. Tunable UV generation at 286 nm by frequency tripling of a high-power mode-locked semiconductor laser. *Optics Letters*, 20(15):1640, 1995. ISSN 1539-4794. doi: 10.1364/ol.20.001640.

[142] D. Eimerl, J. M. Auerbach, C. E. Barker, D. Milam, and P. W. Milonni. Multicrystal designs for efficient third-harmonic generation. *Optics Letters*, 22(16):1208, 1997. ISSN 1539-4794. doi: 10.1364/ol.22.001208.

[143] Huaifeng Xiao, Abdul-Haseeb Munj, Ara Minassian, and Michael J. Damzen. High-efficiency deep-UV output from a diode-pumped alexandrite laser. *Optics Express*, 33(19):39229, 2025. ISSN 1094-4087. doi: 10.1364/oe.571272.

[144] Jan Pilar, Martin Divoky, Jonathan Phillips, Martin Hanus, Petr Navratil, Ondrej Denk, Patricie Severova, Tomas Paliesek, Danielle Clarke, Martin Smrz, Thomas Butcher, Chris Edwards, and Tomas Mocek. Half-kilowatt high-energy third-harmonic conversion to 50 J @ 10 Hz at 343 nm. *High Power Laser Science and Engineering*, 12, 2024. ISSN 2052-3289. doi: 10.1017/hpl.2024.80.

[145] Arno Schneider, Max Neis, Marcel Stillhart, Blanca Ruiz, Rizwan U. A. Khan, and Peter Günter. Generation of terahertz pulses through optical rectification in organic DAST crystals: theory and experiment. *Journal of the Optical Society of America B*, 23(9):1822, 2006. ISSN 1520-8540. doi: 10.1364/josab.23.001822.

[146] Koustuban Ravi. Theory of Terahertz Generation by Optical Rectification. S.m. thesis, Massachusetts Institute of Technology, Cambridge, MA, 2014. URL `http://hdl.handle.net/1721.1/93837`.

[147] F Rotermund, V Petrov, and F Noack. Difference-frequency generation of intense femtosecond pulses in the mid-IR (4–12 μm) using HgGa2S4 and AgGaS2. *Optics Communications*, 185(1-3):177–183, 2000. ISSN 0030-4018. doi: 10.1016/s0030-4018(00)00987-1.

[148] R. T. Murray, T. H. Runcorn, E. J. R. Kelleher, and J. R. Taylor. Highly efficient mid-infrared difference-frequency generation using synchronously pulsed fiber lasers. *Optics Letters*, 41 (11):2446, 2016. ISSN 1539-4794. doi: 10.1364/ol.41.002446.

[149] Q. Bournet, F. Guichard, M. Natile, Y. Zaouter, M. Joffre, A. Bonvalet, I. Pupeza, C. Hofer, F. Druon, M. Hanna, and P. Georges. Enhanced intrapulse difference frequency generation in the mid-infrared by a spectrally dependent polarization state. *Optics Letters*, 47(2):261, 2022. ISSN 1539-4794. doi: 10.1364/ol.444908.

[150] S. A. Akhmanov and R. V. Khokhlov. Parametric Amplifiers and Generators of Light. *Soviet Physics Uspekhi*, 9(2):210–222, 1966. ISSN 0038-5670. doi: 10.1070/PU1966V009N02ABEH002870.

[151] A. Shirakawa, I. Sakane, M. Takasaka, and T. Kobayashi. Sub-5-fs visible pulse generation by pulse-front-matched noncollinear optical parametric amplification. *Applied Physics Letters*, 74(16):2268–2270, 1999. ISSN 1077-3118. doi: 10.1063/1.123820.

[152] Matz Liebel, Christoph Schnedermann, and Philipp Kukura. Sub-10-fs pulses tunable from 480 to 980 nm from a NOPA pumped by an Yb:KGW source. *Optics Letters*, 39(14):4112, 2014. ISSN 1539-4794. doi: 10.1364/ol.39.004112.

[153] Asaf Dahan, Assaf Levanon, Mordechai Katz, and Haim Suchowski. Ultrafast adiabatic second harmonic generation. *Journal of Physics: Condensed Matter*, 29(8):084004, 2017. ISSN 1361-648X. doi: 10.1088/1361-648X/29/8/084004.

[154] T. R. Zhang, Heung Ro Choo, and Michael C. Downer. Phase and group velocity matching for second harmonic generation of femtosecond pulses. *Applied Optics*, 29(27):3927, 1990. ISSN 1539-4522. doi: 10.1364/ao.29.003927.

[155] Peter Baum, Stefan Lochbrunner, and Eberhard Riedle. Tunable sub-10-fs ultraviolet pulses generated by achromatic frequency doubling. *Optics Letters*, 29(14):1686, 2004. ISSN 1539-4794. doi: 10.1364/OL.29.001686.

[156] Artemii Tishchenko, Thomas Geernaert, Nathalie Vermeulen, Francis Berghmans, and Tigran Baghdasaryan. Simultaneous modal phase and group velocity matching in microstructured optical fibers for second harmonic generation with ultrashort pulses. *Optics Express*, 30(7):12026, 2022. ISSN 1094-4087. doi: 10.1364/oe.453844.

[157] R. Paschotta. Phase Matching. RP Photonics Encyclopedia, 2021. URL `https://www.rp-photonics.com/phase_matching.html`. Available online at `https://www.rp-photonics.com/phase_matching.html`.

[158] Gintaras Tamošauskas, Gvidas Beresnevičius, Darius Gadonas, and Audrius Dubietis. Transmittance and Phase Matching of BBO Crystal in the 3–5 μm Range and Its Application for the Characterization of Mid-Infrared Laser Pulses. *Optical Materials Express*, 8(6):1410, 2018. doi: 10.1364/OME.8.001410.

[159] Mikhail N. Polyanskiy. Refractiveindex.info database of optical constants. *Scientific Data*, 11(1), 2024. ISSN 2052-4463. doi: 10.1038/s41597-023-02898-2.

[160] A. Bideau-Mehu, Y. Guern, R. Abjean, and A. Johannin-Gilles. Measurement of refractive indices of neon, argon, krypton and xenon in the 253.7–140.4 nm wavelength range. Dispersion relations and estimated oscillator strengths of the resonance lines. *Journal of Quantitative Spectroscopy and Radiative Transfer*, 25(5):395–402, 1981. ISSN 0022-4073. doi: 10.1016/0022-4073(81)90057-1.

[161] T. Lang, A. Harth, J. Matyschok, T. Binhammer, M. Schultze, and U. Morgner. Impact of temporal, spatial and cascaded effects on the pulse formation in ultra-broadband parametric amplifiers. *Optics Express*, 21(1):949, 2013. ISSN 1094-4087. doi: 10.1364/oe.21.000949.

[162] Richard L. Sutherland. *Handbook of Nonlinear Optics*. Marcel Dekker, New York, 2 edition, 2003. ISBN 9780824742430.

[163] Mario Galletti, Hugo Pires, Victor Hariton, Celso Paiva João, Swen Künzel, Marco Galimberti, and Gonçalo Figueira. High efficiency second harmonic generation of nanojoule-level femtosecond pulses in the visible based on BiBO. *High Power Laser Science and Engineering*, 7, 2019. ISSN 2052-3289. doi: 10.1017/HPL.2018.72.

[164] M. Ghotbi, M. Ebrahim-Zadeh, A. Majchrowski, E. Michalski, and I. V. Kityk. High-average-power femtosecond pulse generation in the blue using BiB_3O_6. *Optics Letters*, 29(21):2530, 2004. ISSN 1539-4794. doi: 10.1364/OL.29.002530.

[165] Arkady Major, Daaf Sandkuijl, and Virginijus Barzda. Efficient frequency doubling of a femtosecond Yb:KGW laser in a BiB_3O_6 crystal. *Optics Express*, 17(14):12039, 2009. ISSN 1094-4087. doi: 10.1364/oe.17.012039.

[166] Heyuan Zhu, Tao Wang, Wanguo Zheng, Peng Yuan, Liejia Qian, and Dianyuan Fan. Efficient second harmonic generation of femtosecond laser at 1 μm. *Optics Express*, 12(10):2150, 2004. ISSN 1094-4087. doi: 10.1364/opex.12.002150.

[167] Maximilian Karst, Pauline Pfaller, Robert Klas, Ziyao Wang, Philipp Gierschke, Jan Rothhardt, and Jens Limpert. 22-W average power high pulse energy multipass-cell-based post-compression in the green spectral range. *Optics Letters*, 48(5):1300, 2023. ISSN 1539-4794. doi: 10.1364/OL.482600.

[168] Hong Liu, Hong-Yi Lin, Zhang-Chao Huang, Jian-Jian Ruan, and Dong Sun. Second harmonic generation at 544 nm of a femtosecond laser. *Optik*, 208:164537, apr 2020. ISSN 0030-4026. doi: 10.1016/j.ijleo.2020.164537.

[169] Teruto Kanai, Xiangyu Zhou, Taro Sekikawa, Shuntaro Watanabe, and Tadashi Togashi. Generation of subterawatt, sub-10-fs blue pulses at 1-5 kHz by broadband frequency doubling. *Optics Letters*, 28(16):1484, 2003. ISSN 1539-4794. doi: 10.1364/OL.28.001484.

[170] Yumin Zhang, Jun Liu, Zhongzhong Qin, and Xiaolong Su. Double-pass second-harmonic generation of picosecond pulses with custom-poled KTP crystal. *Optics Continuum*, 3(3): 461, 2024. ISSN 2770-0208. doi: 10.1364/optcon.519697.

[171] Bastian Gronloh, Peter Russbueldt, Bernd Jungbluth, and Hans-Dieter Hoffmann. Ultrafast green laser exceeding 400 W of average power. In Jacob I. Mackenzie, Helena Jelinkova, Takunori Taira, and Marwan Abdou Ahmed, editors, *Laser Sources and Applications II*, volume 9135, page 91350C. SPIE, 2014. doi: 10.1117/12.2051510.

[172] Christoph Röcker, Andre Loescher, Florian Bienert, Philippe Villeval, Dominique Lupinski, Dominik Bauer, Alexander Killi, Thomas Graf, and Marwan Abdou Ahmed. Ultrafast green

thin-disk laser exceeding 1.4 kW of average power. *Optics Letters*, 45(19):5522, 2020. ISSN 1539-4794. doi: 10.1364/ol.403781.

[173] Christoph Röcker, Andre Loescher, Jan-Philipp Negel, Martin Delaigue, Franck Morin, Clemens Honninger, Eric Mottay, Philippe Villeval, Adrien Holvoet, Dominique Lupinski, Thomas Graf, and Marwan Abdou Ahmed. Direct amplification of sub-300 fs pulses in a versatile thin-disk multipass amplifier. *Optics Communications*, 460:125159, 2020. ISSN 0030-4018. doi: 10.1016/j.optcom.2019.125159.

[174] Jan Rothhardt, Tino Eidam, Steffen Hadrich, Florian Jansen, Fabian Stutzki, Thomas Gottschall, Thomas V. Andersen, Jens Limpert, and Andreas Tunnermann. 135 W average-power femtosecond pulses at 520 nm from a frequency-doubled fiber laser system. *Optics Letters*, 36(3):316, 2011. ISSN 1539-4794. doi: 10.1364/ol.36.000316.

[175] Xiang Liu, Liejia Qian, and Frank W. Wise. Efficient generation of 50-fs red pulses by frequency doubling in LiB_3O_5. *Optics Communications*, 144(4-6):265–268, 1997. ISSN 0030-4018. doi: 10.1016/S0030-4018(97)00367-2.

[176] Xuezhi Zhao, Zhengping Wang, Xinle Wang, Fapeng Yu, and Xinguang Xu. Broadband second-harmonic-generation in GdCOB crystals. *Optics Express*, 30(5):6546, 2022. ISSN 1094-4087. doi: 10.1364/oe.451703.

[177] Dongliang Wang, Qi Liu, Zhongchao Li, Xinyue Yuan, Hongyue Wu, Zixi Liu, Wei Liu, and Guoqing Chang. Generation of 1-MHz, 64-W, 26-fs green pulses via second-harmonic generation of nonlinearly compressed pulses at 1.03 μm. *High Power Laser Science and Engineering*, 13, 2025. ISSN 2052-3289. doi: 10.1017/hpl.2025.10056.

[178] C. Aparajit, Kamalesh Jana, Amit D. Lad, Yash M. Ved, Arnaud Couairon, and G. Ravindra Kumar. Efficient second-harmonic generation of a high-energy, femtosecond laser pulse in a lithium triborate crystal. *Optics Letters*, 46(15):3540, 2021. ISSN 1539-4794. doi: 10.1364/OL.423725.

[179] David Hillier, Colin Danson, Stuart Duffield, David Egan, Stephen Elsmere, Mark Girling, Ewan Harvey, Nicholas Hopps, Michael Norman, Stefan Parker, Paul Treadwell, David Winter, and Thomas Bett. Ultrahigh contrast from a frequency-doubled chirped-pulse-amplification beamline. *Applied Optics*, 52(18):4258, 2013. ISSN 2155-3165. doi: 10.1364/ao.52.004258.

[180] S. Yu. Mironov, V. N. Ginzburg, V. V. Lozhkarev, G. A. Luchinin, Aleksei V. Kirsanov, I. V. Yakovlev, Efim A. Khazanov, and A. A. Shaykin. Highly efficient second-harmonic generation of intense femtosecond pulses with a significant effect of cubic nonlinearity. *Quantum Electronics*, 41(11):963–967, 2011. ISSN 1468-4799. doi: 10.1070/qe2011v041n11abeh014694.

[181] O. Gobert, G. Mennerat, R. Maksimenka, N. Fedorov, M. Perdrix, D. Guillaumet, C. Ramond, J. Habib, C. Prigent, D. Vernhet, T. Oksenhendler, and M. Comte. Efficient broadband 400 nm noncollinear second-harmonic generation of chirped femtosecond laser pulses in BBO and LBO. *Applied Optics*, 53(12):2646, 2014. ISSN 2155-3165. doi: 10.1364/AO.53.002646.

[182] Dal-Woo Kim, Gang-Yao Xiao, and Guo-Bin Ma. Temporal properties of the second-harmonic generation of a short pulse. *Applied Optics*, 36(27):6788, 1997. ISSN 1539-4522. doi: 10.1364/ao.36.006788.

[183] Bahaa E. A. Saleh and Malvin Carl Teich. *Fundamentals of photonics*. John Wiley & Sons, Hoboken, NJ, 3 edition, 2019. ISBN 978-1-119-50687-4.

[184] Theresa A. Maldonado and Thomas K. Gaylord. Light propagation characteristics for arbitrary wavevector directions in biaxial media by a coordinate-free approach. *Applied Optics*, 30(18):2465, 1991. ISSN 1539-4522. doi: 10.1364/ao.30.002465.

[185] Scott Prahl. laserbeamsize: ISO 11146 Calculation of Laser Beam Center, Diameter, and M², 2026.

[186] Arthur Schoenberg. Production of coherent 150 nm light via 7^{th} harmonic generation for nuclear spectroscopy applications. Masterarbeit, University of Hamburg, Hamburg, 2021. URL `https://bib-pubdb1.desy.de/record/454846`. Masterarbeit, University of Hamburg, 2021.

[187] Marc Hanna, Louis Daniault, Florent Guichard, Nour Daher, Xavier Délen, Rodrigo Lopez-Martens, and Patrick Georges. Nonlinear beam matching to gas-filled multipass cells. *OSA Continuum*, 4(2):732, 2021. ISSN 2578-7519. doi: 10.1364/osac.418247.

A Appendix: Compact, Folded Multi-Pass Cells for Energy Scaling of Post-Compression

Research Article Vol. 13, No. 3 / March 2025 / Photonics Research 761

PHOTONICS Research

Compact, folded multi-pass cells for energy scaling of post-compression

Arthur Schönberg,[1,*] Supriya Rajhans,[1,2] Esmerando Escoto,[1] Nikita Khodakovskiy,[1] Victor Hariton,[1] Bonaventura Farace,[1] Kristjan Põder,[1] Ann-Kathrin Raab,[3] Saga Westerberg,[3] Mekan Merdanov,[3] Anne-Lise Viotti,[3] Cord L. Arnold,[3] Wim P. Leemans,[1] Ingmar Hartl,[1] and Christoph M. Heyl[1,4,5]

[1]Deutsches Elektronen-Synchrotron DESY, 22607 Hamburg, Germany
[2]Friedrich-Schiller-Universität Jena, 07743 Jena, Germany
[3]Department of Physics, Lund University, SE-221 00 Lund, Sweden
[4]GSI Helmholtzzentrum für Schwerionenforschung GmbH, 64291 Darmstadt, Germany
[5]Helmholtz-Institut Jena, 07743 Jena, Germany
*Corresponding author: arthur.schoenberg@desy.de

Received 3 September 2024; accepted 8 January 2025; posted 10 January 2025 (Doc. ID 540977); published 28 February 2025

Combining high peak power and high average power has long been a key challenge of ultrafast laser technology, crucial for applications such as laser-plasma acceleration and strong-field physics. A promising solution lies in post-compressed ytterbium lasers, but scaling these to high pulse energies presents a major bottleneck. Post-compression techniques, particularly Herriott-type multi-pass cells (MPCs), have enabled large peak power boosts at high average powers but their pulse energy acceptance reaches practical limits defined by setup size and coating damage threshold. In this work, we address this challenge and demonstrate, to our knowledge, a novel type of compact, energy-scalable MPC (CMPC). By employing a novel MPC configuration and folding the beam path, the CMPC introduces a new degree of freedom for downsizing the setup length, enabling compact setups even for large pulse energies. We experimentally and numerically verify the CMPC approach, demonstrating post-compression of 8 mJ pulses from 1 ps down to 51 fs in atmospheric air using a cell roughly 45 cm in length at low fluence values. Additionally, we discuss the potential for energy scaling up to 200 mJ with a setup size reaching 2.5 m. Our work presents a new approach to high-energy post-compression, with up-scaling potential far beyond the demonstrated parameters. This opens new routes for achieving the high peak and average powers necessary for demanding applications of ultrafast lasers.

Published by Chinese Laser Press under the terms of the Creative Commons Attribution 4.0 License. Further distribution of this work must maintain attribution to the author(s) and the published article's title, journal citation, and DOI.
https://doi.org/10.1364/PRJ.540977

1. INTRODUCTION

Ultrafast laser technology has experienced immense progress within recent years. Ultrashort, high-peak-power lasers are used in a vast range of applications, including attosecond science and high-harmonic generation [1–4], laser-plasma acceleration [5,6], or high-field science including laser-based nuclear fusion [7]. However, developing a laser source that is simultaneously average and peak power scalable remains a major challenge.

The invention of mode-locked solid-state laser technology, in particular titanium-doped sapphire (Ti:Sa) lasers in combination with chirped-pulse amplification (CPA), enabled ultrashort, few-cycle pulses with unprecedented pulse energy [8–10]. Nowadays, peak powers exceeding the terawatt regime are routinely employed [9]. While excelling in peak power performance, Ti:Sa amplifiers are commonly constrained in average power to a few tens of watts, which can be attributed to their large quantum defect [11]. As an alternative to laser amplification in active gain media, optical parametric processes can be employed. In particular optical parametric chirped-pulse amplifiers (OPCPAs) offer broad bandwidths supporting few-cycle pulses and simultaneously high average powers [10,12]. However, OPCPA systems suffer from low pump-to-signal efficiencies typically around 10%–20% for pulses in the range of 10s of femtoseconds (fs) [13]. Ultrafast ytterbium (Yb)-based laser architectures on the other hand provide excellent average power scalability exceeding 10 kW [14], but pulse durations limited to 100s of femtoseconds up to about 1 picosecond (ps). Combining Yb lasers with efficient post-compression methods supporting large (>10) compression factors and high pulse energies can offer an excellent solution to the power scaling challenge.

In recent years, a number of post-compression techniques have been developed, mostly relying on self-phase modulation (SPM) as the nonlinear process for spectral broadening [15]. In particular, gas-based technologies provide excellent tools for post-compression of high-power lasers. Example systems rely on gas-filled hollow-core fibers (HCF) [16–18], cascaded focus and compression (CASCADE) [19], white-light filaments [20], as well as Herriott-type multi-pass cells (MPCs) [15,21–23]. In HCFs, post-compression of 70 mJ 220 fs pulses down to 30 fs has been demonstrated in a 3 m long fiber [24]. Post-compression of very high pulse energies in the multiple Joule range has been achieved via thin-film spectral broadening techniques. However, typical compression factors lie in the range of only two to five [25,26]. Similar to HCFs, MPCs enable large compression factors reaching 10–20 or more while supporting a wide range of pulse energies. In addition, MPCs support high average powers [27] and outperform HCFs in system footprint especially for large compression factors [15]. The maximum attainable energy acceptance in a standard, two-mirror MPC is directly proportional to its size [15,28]. A record of 200 mJ has been achieved in a 10 m long MPC setup [29]. Further energy up-scaling leads to MPC sizes that are impractical for standard laboratory settings. The development of a highly efficient post-compression method supporting large compression factors and high pulse energies thus remains a key challenge.

We here introduce a new MPC type, the compact MPC (CMPC), which possesses a weakly focused fundamental mode as well as a linear beam pattern on the focusing mirrors. This geometry allows us to fold the beams inside the MPC using two additional planar mirrors, thus introducing a new energy scaling parameter, the folding ratio Γ. The CMPC in principle allows for an arbitrary amount of folding and thus, very compact setup sizes while sharing key properties of standard MPCs such as high average power support, excellent beam quality, and efficiency. We experimentally demonstrate spectral broadening of 1030 nm, 8 mJ, 1 ps pulses in a CMPC in atmospheric air using a setup with an effective length of around 45 cm. We keep the maximum mirror fluence at a moderate level of around 170 mJ/cm^2 and demonstrate compressibility of 1 ps input pulses down to 51 fs with an MPC throughput reaching 89% while maintaining excellent spatio-temporal pulse characteristics.

2. CONCEPT

Most MPCs demonstrated for post-compression to date rely on two identical concave mirrors, resembling the most basic optical cavity arrangement. However, more complex designs employing a convex mirror and a concave mirror [30,31] or even multiple additional mirrors can provide advantageous mode-forming capabilities. MPCs with more than two mirrors have been proposed in previous works focusing on energy scaling of MPCs [31,32]. Other energy scaling methods that do not rely on modifications on the MPC geometry include divided pulse nonlinear post-compression [33,34], or using higher-order Laguerre beams to decrease the fluence on the mirrors [35]. These techniques can be combined with geometrical scaling methods. With the CMPC we demonstrate a new geometrical approach. The concept of the CMPC is based on a weakly focused beam and folding of the beam path via multiple reflections on two additional, planar mirrors in each pass through the cell, as shown in Fig. 1. This provides an additional tuning parameter, namely, the folding ratio Γ, which reduces the length of the CMPC by $L_{\mathrm{eff}} \approx L/\Gamma$. Figures 1(A) and 1(B) depict the principle of beam folding and the effective size reduction of the cell together with the configuration regimes for standard MPCs and the CMPC. In Fig. 1(B) the original beam path is divided into three parts and then folded such that the setup length reduces by approximately a factor of three and thus $\Gamma = 3$.

In general, the geometry of a symmetric Herriott-type MPC—including a CMPC—is fully determined by three of the following four parameters: radius-of-curvature (ROC) of the mirrors R, the propagation length between the two focusing mirrors L, the number of round-trips N, and the configuration parameter k. These parameters are related by [15]

$$\frac{L}{R} = 1 - \cos\left(\frac{\pi k}{N}\right). \tag{1}$$

Typically, k is chosen to be integer and prime to the number of round-trips N, in order to ensure the re-entrant condition of the MPC. Moreover, the parameter k determines the angular

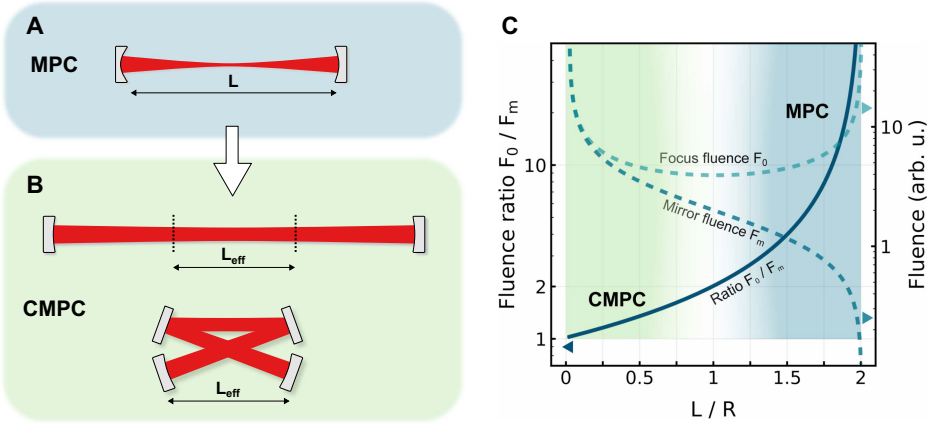


Fig. 1. MPC and CMPC schematic and configuration regimes. (A) Standard MPC mode. (B) CMPC mode without and with folding. In the unfolded geometry the CMPC is typically longer than a comparable MPC, reducing to much shorter length L_{eff} after folding. (C) Typical configuration regimes and corresponding fluence characteristics of MPC and CMPC within the stability range.

advance of the beam on the MPC mirror, which is equivalent to the Gouy phase per pass $\phi_G^{(1)} = \pi k/N$ [15]. The amount of Gouy phase per pass determines the caustic of the beam in the MPC. For a standard MPC, $\phi_G^{(1)}$ approaches π, which leads to a large mode size w_m on the mirrors and a small waist w_0 in the focus. In the CMPC, the beam propagates within the Rayleigh-range, where the accumulated Gouy phase per pass is $\phi_G^{(1)} < \pi/2$. This is the case when $L/R < 1$, where the beam radius at the mirror w_m is comparable to the beam radius at focus w_0. The peak fluence of the beam follows a similar behavior, with $F_0/F_m < 2$ for $L/R < 1$ [Fig. 1(C)]. This weak focusing geometry with small fluence variations enables the placement of additional optical components within the beam path of the CMPC and thus folding of the beam. In addition, a weakly focused mode eliminates pulse energy limitations arising due to ionization in standard gas-filled MPCs. Figure 2 illustrates the CMPC scheme. In Fig. 2(A) the setup schematic of a standard MPC with linear pattern alignment is shown. Here, the strongly focused beams propagate directly between the two focusing mirrors FM1 and FM2, without any optical components in-between. In the CMPC [Fig. 2(B)], two additional planar mirrors PM1 and PM2 are placed behind FM1 and FM2. As seen in Fig. 2(B-ii), the beam propagates from FM1 to PM2 and PM1, where it is folded multiple times before reaching FM2. Here, the depicted folding ratio is $\Gamma = 9$. The total path length between FM1 and FM2 is the length determined by Eq. (1). However, the effective length is now reduced by $L_{eff} \approx L/\Gamma$, which under the correct choice of R and Γ can become significantly shorter than that of a standard MPC with similar pulse energy acceptance.

The pulse energy acceptance of a gas-filled MPC can be estimated considering the mirror fluence and the focus intensity. The beam waist radius in the focus and on the mirrors in an MPC can be calculated using the equations $w_0^2 = (R\lambda/2\pi)\sin(\pi/kN)$ and $w_m^2 = (R\lambda/\pi)\tan(\pi k/2N)$, respectively, where λ is the wavelength of the laser [32]. The parameters L/R can be directly mapped to k/N according to Eq. (1). Assuming a laser with Gaussian pulses and pulse energy E, the maximum peak fluence in the focus $F_0 = 2E/\pi w_0^2$, as well as the peak fluence on the mirror $F_m = 2E/\pi w_m^2$ can be calculated [32]. For a standard MPC consisting of two identical focusing mirrors, the fluence on these mirrors should not exceed the threshold fluence F_{th}, yielding a maximum pulse energy of

$$E_{MPC} \le \frac{R\lambda F_{th}}{2}\tan(\pi k/2N). \tag{2}$$

For simplicity, the second energy limitation that can arise at high focus intensity due to ionization is omitted in this discussion as it has little or no relevance for the CMPC. In a CMPC, where beam folding is achieved by additional mirrors (Fig. 2) the beam can be reflected at almost any point between the focusing mirrors including the focus. Therefore, the condition for avoiding damage needs to be $F_0 \le F_{th}$ and thus

$$E_{CMPC} \le \frac{R\lambda F_{th}}{4}\sin(\pi k/N). \tag{3}$$

In addition, replacing R with L using Eq. (1) and writing L in terms of $L_{eff} \approx L/\Gamma$, we obtain

$$E_{CMPC} \le \frac{\lambda F_{th}\Gamma L_{eff}}{4\tan(\pi k/2N)}. \tag{4}$$

Equations (2)–(4) illustrate the energy scaling possibilities of MPCs. For standard MPCs [Eq. (2)], the energy scaling options are restricted to maximizing the ratio $k/N \to 1$, increasing the ROC of the mirrors R (which increases L proportionally at constant k/N), or increasing the threshold fluence F_{th}. In the case of CMPCs, energy scaling can be achieved differently. Since k/N is generally smaller, the energy acceptance for the same set of parameters R and F_{th} is typically reduced according

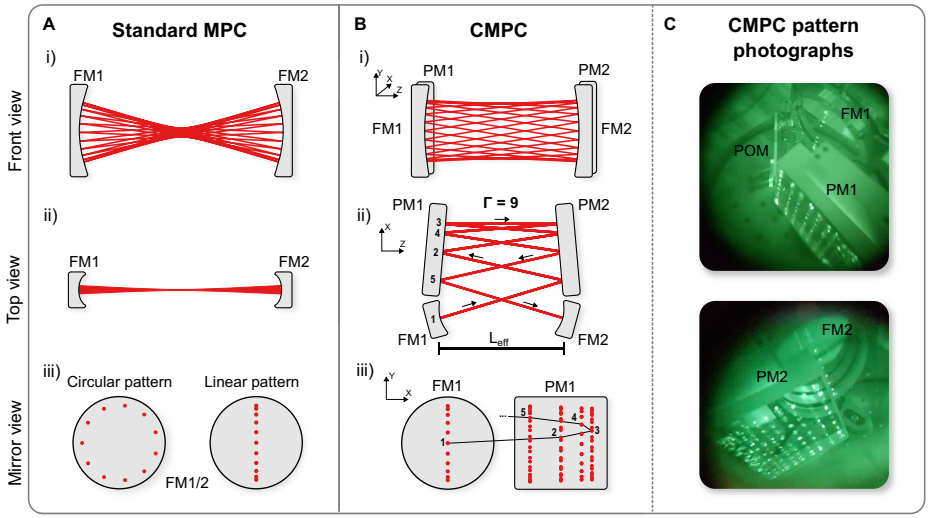


Fig. 2. Schematics of standard MPC and CMPC. (A) Standard MPC geometry and beam pattern considering a linear beam pattern alignment (FM1/2: focusing mirrors). View of the beam path from the front (i) and from the top (ii). (iii) Resulting patterns for circular/linear alignment on FM1/2. (B) CMPC geometry and beam patterns. (i) Front view with additional planar mirrors (PM1/2) behind FM1/2. (ii) Top view onto the CMPC with beam folding ratio $\Gamma = 9$. The numbers (1–5) are indicating the order of reflections of the first pass. (iii) Beam patterns on the mirrors FM1/2 and PM1/2. The black line follows the beam reflections 1–5 on the mirrors. (C) Photographs of experimental beam patterns with $N = 11$, $k = 3$, and $\Gamma = 25$. POM: pick-off mirror.

to Eq. (3). Thus, the first step of scaling is achieved by adjusting R in Eq. (3) such that $E_{\mathrm{CMPC}} = E_{\mathrm{MPC}}$. This typically increases L, i.e., $L_{\mathrm{CMPC}} > L_{\mathrm{MPC}}$. The second step is to fold the beam by the factor Γ and decrease the length of the system by exploiting $L_{\mathrm{eff}} = L/\Gamma$.

To illustrate the discussion with an example, we use a typical set of parameters for a standard MPC with $R = 1$ m and a $\lambda = 1030$ nm, 1 ps level laser. The threshold fluence for quarter-wave-stack high-reflectance dielectric coatings can, e.g., be set to $F_{\mathrm{th}} = 0.17$ J/cm^2 (corresponding to the linear fluence in our experiment), leaving headroom to damage. With $N = 15$ round-trips and $k = 14$, we arrive at $E_{\mathrm{MPC}} \leq 8.3$ mJ and a length of close to 2 m. To match the pulse energy acceptance of the CMPC to the MPC, we first set $k = 4$, and increase the ROC to $R = 25$ m and the length to $L = 8.27$ m. Now folding the beam $\Gamma = 25$ times, we arrive at $E_{\mathrm{CMPC}} \leq 8.1$ mJ with an effective length of $L_{\mathrm{eff}} = 33$ cm. A second example is illustrated in Fig. 3. Here we refer to the works reported by Pfaff *et al.*, where 200 mJ pulses have been compressed in a 10 m long MPC, with a fluence on the mirrors of approximately 0.5 J/cm^2 [29]. Figure 3 shows that the energy acceptance increases with larger folding ratio and effective system length. At 10 m length, a folding ratio of $\Gamma = 25$ supports an energy of 700 mJ and at $\Gamma = 49$, the accepted energy exceeds 1 J. At these parameters, the CMPC with 1 J energy acceptance and $\Gamma = 49$ would require an ROC of $R > 1$ km with a focusing mirror diameter of 60 cm and a planar mirror size of 60 cm × 68 cm [see Eqs. (A3)–(A5) in Appendix A]. In particular the large ROCs can become a limiting factor, as discussed in Section 4. Conversely, for a pulse energy of 200 mJ, the CMPC size can be scaled down to about 3 m or 1.5 m considering $\Gamma = 25$ and $\Gamma = 49$, respectively. As visible in Fig. 3, for $\Gamma = 1$, the fully "unfolded" CMPC is generally longer than the standard MPC considering an identical threshold fluence for both cases. This is due to the fact that the CMPC operates in the $L/R < 1$ regime while the MPC operates at $L/R \approx 2$.

A second limitation in MPCs, which we omitted in the above discussion, typically arises due to the peak intensity of the laser exceeding the ionization threshold of the gas in the MPC [15]. Due to the loose focusing geometry of the CMPC however, this problem is fully avoided here, as the limitation due to the LIDT of the coating typically sets in much earlier. For example, in the above discussed system with $k/N = 4/15$ and $R = 25$ m, ionization of a gas with an ionization threshold of $I_{\mathrm{th}} = 1 \times 10^{13}$ W/cm^2 would set in at 478 mJ for 1 ps pulses [32].

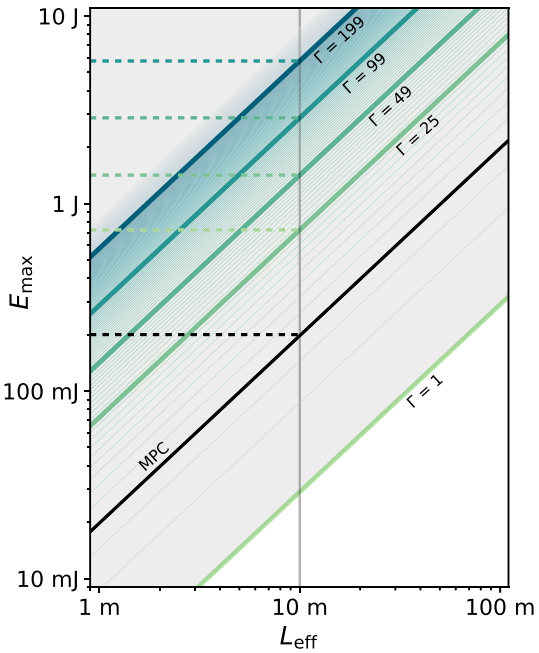


Fig. 3. Energy scaling characteristics: calculated pulse energy acceptance E_{max} as a function of effective length L_{eff}. The solid black line indicates a standard MPC as reported in Ref. [29] [Eq. (2)]. Each colored solid line represents a CMPC with a folding ratio Γ [Eq. (4)]. The gray line indicates an effective length of 10 m. The dashed lines show the corresponding pulse energies for selected values of Γ. We set the threshold fluence to $F_{\mathrm{th}} = 0.5$ J/cm^2.

3. EXPERIMENT

Our experimental setup displayed in Fig. 4 uses a commercial innoslab Yb laser system (AMPHOS GmbH), delivering 1030 nm 1 ps pulses at a repetition rate of 1 kHz with a pulse energy of >8 mJ. After suitable mode-matching, the beam is sent onto the pick-off mirror POM1 and into the CMPC [Fig. 4(B)]. The CMPC consists of two concave 4 inch mirrors with $R = 25$ m and two planar folding mirrors with size 10 cm × 10 cm. The configuration is set to $N = 11$ round-trips and $k = 3$, which corresponds, according to Eq. (1), to an unfolded MPC length of $L = 8.63$ m. Following in-coupling at the pick-off mirror POM1, the beam is sent onto the planar folding mirror PM2 and is subsequently reflected by PM1, with both mirrors being aligned in a V-shaped configuration and separated by about 34 cm. The beam continues its path as described in Fig. 2, forming the typical CMPC pattern. A folding ratio of $\Gamma = 25$ results in an effective CMPC length

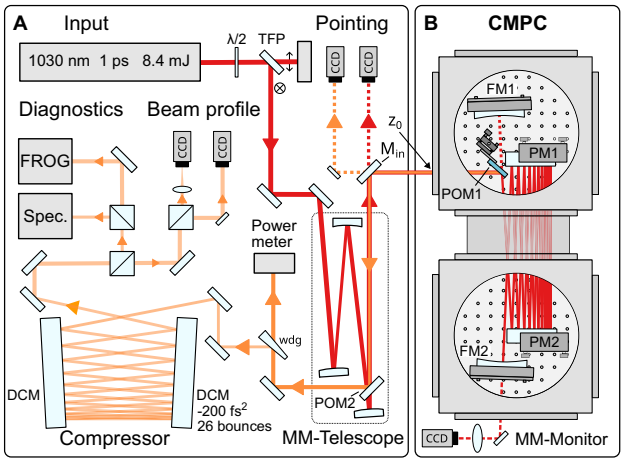


Fig. 4. Experimental setup. The CMPC input beam is indicated in red, and the output beam in orange. FM: focusing mirror. PM: planar mirror. POM: pick-off mirror. M_{in}: input/output mirror. MM: mode-matching. DCM: double-chirped mirror. CCD: camera. z_0: reference point for stability measurements. TFP: thin-film polarizer. wdg: wedge. (A) Beam input, telescope, and diagnostics used in the experiment. (B) CMPC setup with vacuum chamber.

of $L_{\text{eff}} = 34.5$ cm. However, due to spatial constraints, the two focusing mirrors FM1 and FM2 are placed a few centimeters behind PM1 and PM2, making the total CMPC length slightly larger, resulting in around 45 cm [see Fig. 4(B)]. After propagating $N = 11$ round-trips (22 passes), the beam returns on PM1 and is coupled out with a different angle in the vertical direction. The total number of mirror reflections amounts to $2N\Gamma = 550$ and the total propagation length is roughly 190 m. We use ambient air at atmospheric pressure (1006 mbar) as the nonlinear medium for spectral broadening. Nevertheless, a chamber or housing is necessary to avoid beam fluctuations due to turbulences in air.

After out-coupling, the spectrally broadened beam is separated from the input beam with another pick-off mirror POM2 [Fig. 4(A)]. Here, we measure an output power of around 7.1 W and thus a total transmission of roughly 89%. This corresponds to a reflectance of the mirrors of at least 99.98% per reflection, disregarding clipping losses. Subsequently, a wedge is used for beam sampling, reflecting around 8%, corresponding to roughly 570 mW. The transmission of the wedge is sent onto a power meter. The wedge-reflected pulse is compressed using a chirped-mirror compressor with 26 reflections corresponding to about −5200 fs^2 of compensated second-order dispersion.

We analyze the compressed pulses using frequency-resolved optical gating (FROG) and measure the spectrum. In addition, the beam quality parameter M^2 is analyzed using the same wedge reflection. We furthermore record input and output near-field pointing using the input/output mirror (M_{in}) transmission of both input and output beams. For direct comparison of input and output, both cameras are placed in the exact same distance $d = 42$ cm from a common reference point z_0, located at the vacuum chamber input window. The spectrum and FROG results are shown in Fig. 5. The input pulse has a pulse duration of about 1.1 ps with a Fourier-transform-limit (FTL) of about 1 ps. After spectral broadening in the CMPC, the output pulse FTL reaches 50 fs. Following compression, we reach 51 fs [Fig. 5(A)]. We simulate the spectral broadening process using the measured input pulse [Fig. 5(A)]. The simulations are conducted using our in-house developed (2 + 1)D radially symmetric simulation code based on Hankel-transforms in the spatial dimension, which is described in Appendix A [Eqs. (A1) and (A2)]. The simulated output pulse agrees very well with the measured output pulse, exhibiting similar temporal characteristics after compression. In both measurement and simulation, we observe a temporal pedestal likely stemming from uncompressed spectral components in the longer wavelength range. On the trailing edge, a post-pulse appears at around 800 fs, which we attribute to a pulse-breakup caused by the delayed response of the Raman-Kerr contribution in air. The measured and simulated spectra [Fig. 5(B)] also show similar characteristics as well as similar broadening, except for the strength of the side lobes compared to the background close to 1030 nm.

The molecular nature of air results in a broadened spectrum that qualitatively deviates from a typical "SPM-like" spectrum, obtained from atomic gases. We therefore conduct spectral broadening measurements in Krypton as well, in order to demonstrate typical SPM broadening and compare it with

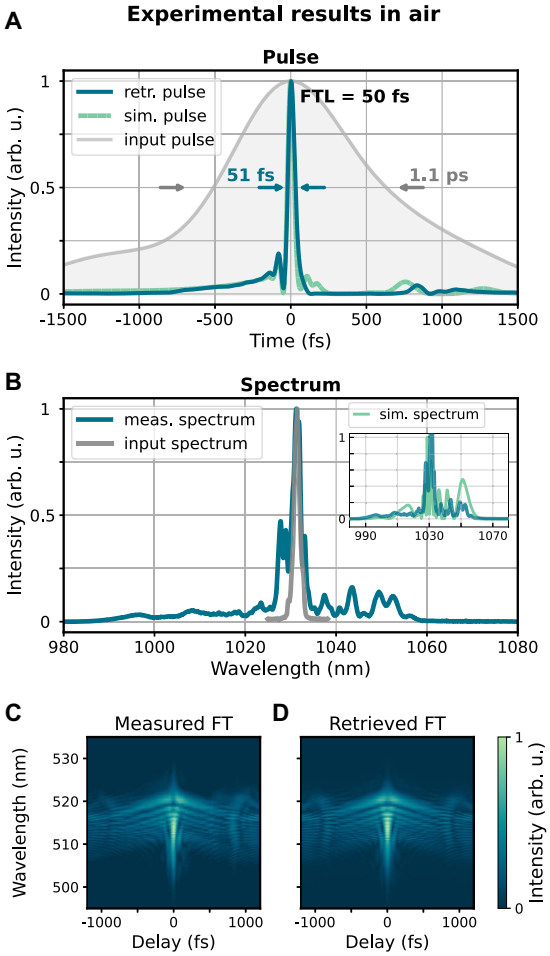


Fig. 5. Measured and simulated pulse characteristics after CMPC spectral broadening and subsequent compression in 1 bar of air. (A) Reconstructed input and output temporal pulse. (B) Measured input spectrum and broadened spectrum. The inset shows the measured broadened spectrum along with simulated spectrum. (C) Measured FROG trace (FT). (D) Retrieved FROG trace (FROG error = 0.73% on a 1024 × 1024 grid).

the simulations. Due to technical constraints originating from mechanical instabilities of the vacuum chamber, the chamber could only be operated at 1 bar pressure. We measure the spectral broadening with 6.5 mJ pulse energy and the results are shown in Fig. 6, where we reach an FTL of approximately 120 fs.

The beam path inside the CMPC involves 550 reflections and a long propagation path of about 190 m. The beam is particularly sensitive to displacements of the folding mirrors PM1 and PM2 (Fig. 4), where most of the reflections take place. Thus, it is important to characterize the stability of the beam. Figures 7(A) and 7(B) show the measured beam position stability for both input and output beams. We conduct the measurements separately within a few minutes. The measurements show only a very slight increase in the RMS beam position deviation of approximately 5% in the output, compared to the input. This demonstrates the spatial stability owing to the input-to-output imaging property of the CMPC, also known

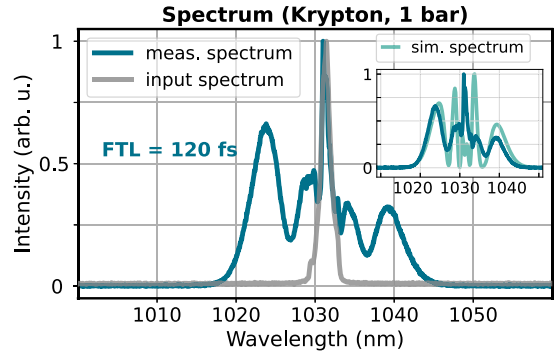


Fig. 6. Spectral broadening of 6.5 mJ pulses in 1 bar of Krypton. CMPC input (gray line) and measured output (dark blue line) spectra are shown. The inset shows the simulated spectrum along with the measured output spectrum.

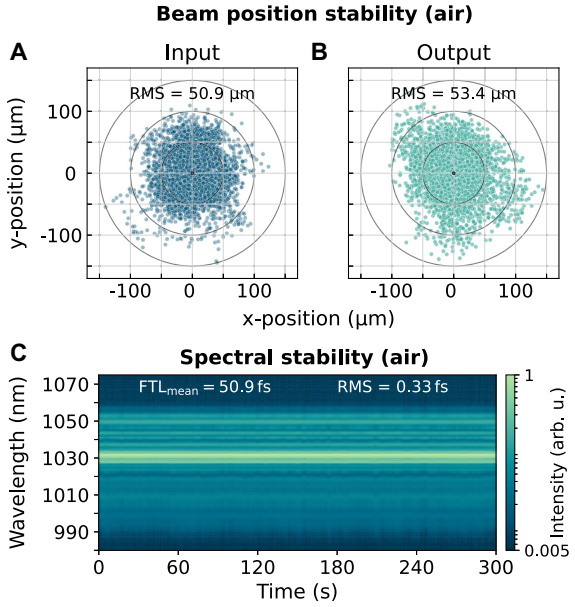


Fig. 7. Beam position and spectral stability, measured in 1 bar of air. (A), (B) Scatter-plots of the beam position of input (A) and output (B) beams. Measurements are taken separately; the data span for each measurement is 7.5 min and 4000 data points, with a few minutes between measurements. In both measurements, the camera is placed at exactly 42 cm distance from the common reference point z_0 (Fig. 4). Circles indicate deviations of 50, 100, and 150 µm from the mean value. The measurements are in accordance with the medium-term beam position stability measurements defined in EN ISO 11670:2003. (C) Measured broadened spectrum recorded over 5 min with 10 points per minute at full broadening (logarithmic scale). The RMS deviation of the FTL amounts to 0.65%.

from standard MPCs. In addition, we measure the spectral stability of the system over 5 min [Fig. 7(C)]. We measure RMS fluctuations of the FTL of 0.33 fs, with a mean value of 50.9 fs, resulting in a relative RMS deviation of 0.65%, indicating that the spectral broadening is stable.

We further measure the beam quality parameter M^2 of the input beam after the mode-matching telescope and the output beam. We observe a beam quality degradation from $M^2 = 1.36$ at the input to 1.76 at the output at full power. As this observation may indicate spatio-temporal coupling (STC) effects, we decided to further investigate the spatio-spectral pulse characteristics using spatially resolved Fourier-transform spectrometry [36]. The STC measurements provide information about the spatially dependent spectral homogeneity of the pulse $V(x,y)$, which we calculate via the spectral overlap integral as defined in Eqs. (A6) and (A7) in Appendix A. An average spectral overlap V_{avg} is then computed by weighting the $V(x,y)$ with the fluence $F(x,y)$ obtained from the same dataset and averaging over an area defined by the measured $1/e^2$ diameter of the beam. In air (Fig. 12, Appendix A), we measure $V_{\mathrm{avg}} = 90.6\%$ at full power, confirming a slight degradation of the spatio-spectral homogeneity compared to the input beam, which exhibits an almost perfect homogeneity of $V_{\mathrm{avg}} \approx 99\%$. We further investigate more generally how the spatio-spectral homogeneity behaves in atomic gases as a function of the input peak power P of the pulse, compared to the critical power P_{c} of the gas. The measurement is performed using Krypton as the nonlinear medium at 1 bar pressure and the same CMPC configuration is used as described in the beginning of this section. We carry out STC measurements at four different pulse energies and thus four different values for P/P_{c} and measure an STC trace for each point. Figure 8 summarizes the STC measurement results. From the first measurement point [Fig. 8(A)] at $P/P_{\mathrm{c}} \approx 0.4$ to the third at $P/P_{\mathrm{c}} \approx 0.6$, we observe a linear decline from 98.3% to 90.5%. The fourth point at $P/P_{\mathrm{c}} \approx 0.65$ exhibits a stronger deterioration. We compare our results with simulations considering again the measured input pulse as input for the simulation. Here we observe an onset of homogeneity reduction [Fig. 8(A)] at approximately $P/P_{\mathrm{c}} = 0.55$ and an overall weaker deterioration compared to the measurements. However, the simulations reproduce the measured behavior qualitatively including the onset of homogeneity degradation at around $P/P_{\mathrm{c}} \approx 0.6$ well. At $P/P_{\mathrm{c}} \approx 0.8$, the simulations predict a beam collapse causing a sharp decline of V_{avg}. The faster degradation of the spatio-spectral homogeneity in the experimental data might be related to imperfect input beam characteristics in the experiment and/or possible spatial phase distortions arising due to many beam reflections on the CMPC mirrors.

For an example point at $P/P_{\mathrm{c}} \approx 0.6$, the spatio-spectral distribution obtained via an STC scan is shown in Fig. 8(B). We compare the results with a spectrally broadened pulse from a standard gas-filled MPC with $N = 17$, $k = 16$, and $R = 1$ m at similar spectral broadening characteristics. The corresponding spatio-spectral distribution is shown in Fig. 8(C). Both measurements indicate rather homogeneous spatio-spectral characteristics and thus a similar spectral broadening performance for both MPC types, with $V_{\mathrm{avg}} = 96.4\%$ for the standard MPC and a slightly reduced $V_{\mathrm{avg}} = 90.5\%$ for the CMPC. We can further compare our measured V_{avg} values to another non-standard MPC, where a convex-concave MPC arrangement was used for spectral broadening. In Ref. [31], a value of $V_{\mathrm{avg}} = 98\%$ was achieved, albeit with a lower spectral broadening factor corresponding to compression from 260 fs to 50 fs (spectral broadening factor of approximately five) and

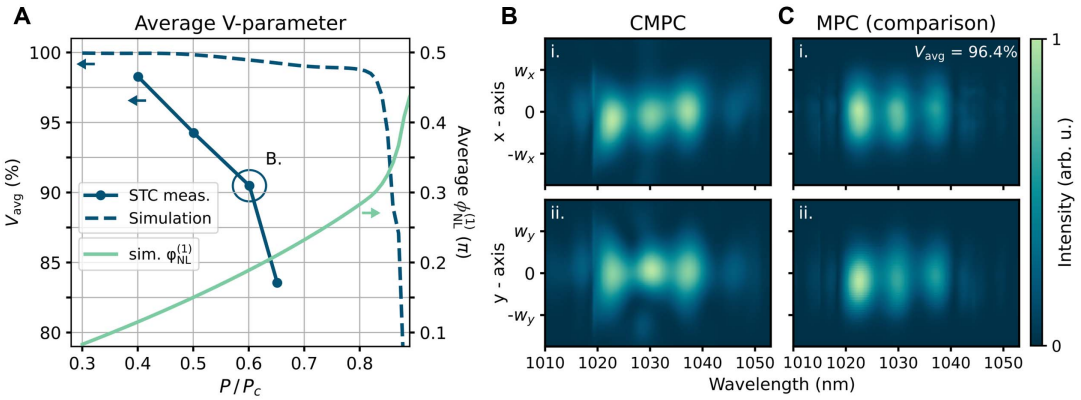


Fig. 8. Measured spatio-spectral beam characteristics. (A) Measured and simulated average spectral overlap V_{avg} and simulated accumulated nonlinear phase $\phi_{NL}^{(1)}$ as a function of peak power P normalized to the critical power P_c. (B) Example data set of a single measurement point, indicated by a circle in (A). (i), (ii) Spectral distribution of the pulse over the spatial x-direction, integrated over the y-direction and vice versa. (C) Corresponding STC traces for a standard MPC with similar broadening. w_x and w_y represent the $1/e^2$ beam radii.

in a solid medium. Another experiment using a convex-concave MPC and a solid medium yielded $V_{avg} = 90\%$ [30], with a spectrum that supports 133 fs, starting from 670 fs. In the latter example, the bandwidth of the broadened spectrum is roughly similar to our measurements in air, where we measure $V_{avg} = 90.6\%$.

4. DISCUSSION

The CMPC enables post-compression for high pulse energies at compact setup length, tunable via the folding ratio Γ [Eq. (3)] while exhibiting excellent characteristics known from conventional MPCs. These include support for large compression factors, excellent beam quality and pointing properties, as well as high transmission efficiency. In principle, Γ can be increased to arbitrarily large values, enabling very compact systems. There are, however, practical limitations. The mirror size, in particular the length (corresponding to the x-dimension in Fig. 2), sets a limit on Γ [a mirror dimension estimate is provided in Eqs. (A3)–(A5) in Appendix A]. Increasing Γ also gives rise to a larger amount of total reflections. This can lead to a decreased throughput and lower efficiency of the system. The large number of reflections in a CMPC further restricts the mirror coatings to low GDD and at the same time high reflectivity. Typical coatings fulfilling these properties are quarter-wave-stack coatings with bandwidths supporting pulse durations of around 30 fs at 1030 nm. Consequently, post-compression to few-cycles cannot be achieved using the CMPC scheme. In our experiment we measure a throughput of 89% at 550 reflections corresponding to an average mirror reflectivity of >99.98%. Moreover, a large number of reflections can cause wavefront distortions, which we minimize by using mirrors with a high surface flatness of $\lambda/20$. Another factor that can restrict energy scalability is the radius-of-curvature of the mirror substrate. While mirrors with an ROC of 2 km can be manufactured [37], large ROCs can become more strongly affected by mirror distortions, such as mechanical stress or thermal effects, which could potentially limit the average power acceptance of the CMPC.

As discussed in Section 2 the CMPC scheme requires a regime where the beam inside the cell is loosely focused in order to enable beam folding on additional mirrors. This in turn fundamentally limits the amount of nonlinear phase $\phi_{NL}^{(1)}$ that can be accumulated per pass to smaller values compared to a strongly focused geometry. In gas-filled MPCs, the accumulated Gouy phase per pass $\phi_{NL}^{(1)}$ sets a theoretical limit on the nonlinear phase $\phi_{NL}^{(1)} \leq \phi_G^{(1)}$ [15], which is directly related to the MPC geometry via $\phi_G^{(1)} = \pi k/N$. In standard MPCs with $k/N \to 1$ this limit approaches $\phi_{NL}^{(1)} = \pi$, whereas in the CMPC typically k/N is lower. In our experiment, the configuration is set to $N = 11$ and $k = 3$ and thus $\phi_{NL}^{(1)} \leq 0.27\pi$. Getting close to this limit, the peak power approaches the critical power of the medium P_c and spatio-temporal couplings can become more pronounced leading to a sudden degradation of the spatio-spectral homogeneity. However, this effect is not necessarily a limiting factor for spectral broadening in a CMPC. The generally smaller $\phi_{NL}^{(1)}$ in a CMPC can be compensated by simply employing more passes through the cell, while keeping the ratio k/N approximately constant. For both MPC types, operation at $P < P_c$ ensures that excellent spatio-spectral and thus spatio-temporal pulse characteristics can be reached.

5. OUTLOOK AND CONCLUSION

In our proof-of-principle experiment we demonstrate post-compression of 8 mJ pulses in a compact setup. However, we can further scale up the energy by increasing the mirror sizes as well as the radius-of-curvature R of the mirrors. As an outlook for high-energy CMPC operation, we simulate the post-compression of 200 mJ, 1 ps pulses at 1030 nm central wavelength in a CMPC using 50 mbar of argon as the nonlinear medium. We show that post-compression down to 80 fs can be achieved, with a transmission of almost 80%. Figure 9 summarizes the simulation results for this scenario, indicating excellent post-compression performance. Here, we assume a mirror reflectivity of 99.98% and consider the influence of the mirror on the spectral phase of the pulse. We include the effects of all reflections on the mirrors in the simulations, which amount to $2N\Gamma = 1170$. Using focusing mirrors with

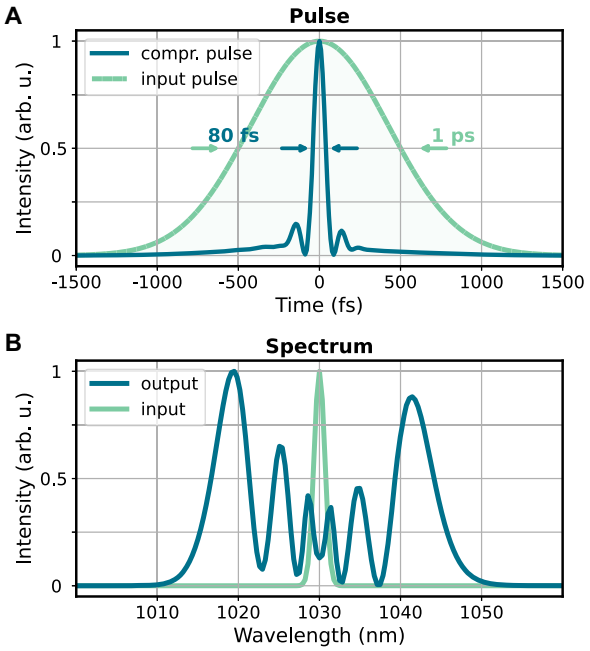


Fig. 9. CMPC simulation for 200 mJ pulses. (A) Input pulse and simulated compressed output pulse. (B) Input spectrum and simulated broadened spectrum.

$R = 300$ m and folding mirrors of 35 cm × 35 cm, a folding ratio of $\Gamma = 39$ is achievable, assuming a clear aperture of five times the beam radius w_m (see Appendix A Section A.2). In this case an effective length of the setup of 2.5 m can be reached. The calculated fluence on the mirrors is kept at roughly of 0.5 J/cm^2, including nonlinear self-focusing effects and nonlinear mode-matching taking into account Kerr lensing in the cell [38]. The peak power is kept at $P/P_c < 0.6$, where we still measure $V_{avg} > 90\%$ [Fig. 8(A)], in order to avoid strong spatio-spectral inhomogeneities and prospectively still achieve a good beam quality.

In conclusion, we introduce a novel multi-pass cell scheme enabling post-compression of high-energy laser pulses in a compact setup. The CMPC enables tuning and down-scaling of the setup size via beam folding using additional planar mirrors, using weakly focused cell modes. Instead of increasing the length of the setup, the folding ratio Γ acts as the energy scaling parameter. We demonstrate post-compression in air from 1.1 ps down to 51 fs in a CMPC with an effective length of 45 cm and a folding ratio $\Gamma = 25$, while keeping the fluence comparable to a standard MPC supporting the same pulse energy but requiring around 2 m cell length. Further up-scaling options promise post-compression of pulses with an energy of 100 mJ and beyond in a table-top setup.

APPENDIX A

1. Nonlinear Pulse Propagation Model

The pulse propagation model used for simulations in this work is presented here. We use single-atom gases as well as ambient air, which mainly consists of molecular gases (N_2 and O_2), as the nonlinear media. In order to conduct simulations, we thus need to take into account time-dependent nonlinear third-order effects, which stem from coupling of the electric field to the rotational states of the gas molecules [39,40]. The full equation for the propagation model used in this work can be written in the frequency and spatial frequency domains as

$$\frac{\mathrm{d}E(k_x,k_y,\omega)}{\mathrm{d}z} = ik_z E(k_x,k_y,\omega) + P^{\mathrm{NL}}(k_x,k_y,\omega), \tag{A1}$$

where $k_z = \sqrt{k^2(\omega) - k_x^2 - k_y^2}$, $k(\omega) = n(\omega)\omega/c_0$ with ω denoting the radial frequency, k_x and k_y the spatial wavenumbers, c_0 the speed of light in vacuum, and $n(\omega)$ the refractive index. The second term P^{NL} in Eq. (A1) contains all the nonlinear effects used in the model. Here we include the Kerr effect via the nonlinear refractive index n_2 up to its first-order derivative, as well as the single damped-oscillator model for the molecular response as described in Refs. [40,41]. The gas-specific single damped-oscillator model is described by the damping time Γ, the frequency Λ, the Raman-Kerr nonlinear refractive index n_2^{R}, and the Raman-Kerr fraction f_{R}. In space and time domains, the nonlinear polarization P^{NL} can be written as

$$\begin{aligned} P^{\mathrm{NL}}(x,y,t) = \frac{\pi\varepsilon_0 c_0 n(\lambda)}{\lambda}\Bigg(\Bigg(n_2|E|^2 - i\left(\frac{\lambda}{2\pi}\frac{n_2}{c_0} + \frac{\mathrm{d}n_2}{\mathrm{d}\omega}\right) \\ \times\left(2E^*\frac{\mathrm{d}E}{\mathrm{d}t} + E\frac{\mathrm{d}E^*}{\mathrm{d}t}\right)\Bigg)(1-f_{\mathrm{R}}) \\ + f_{\mathrm{R}}\, n_2^{\mathrm{R}}\,\frac{\Gamma^2/4+\Lambda^2}{\Lambda}\mathrm{Im}\Bigg(\mathrm{e}^{-(\Gamma/2-i\Lambda)t} \\ \times\int_{-\infty}^{\infty}\mathrm{e}^{(\Gamma/2-i\Lambda)t'}|E(t')|^2\mathrm{d}t'\Bigg)\Bigg)E, \end{aligned} \tag{A2}$$

where $E = E(x,y,t)$ is the electric field of the pulse, E^* the complex conjugate of E, ε_0 the dielectric constant, $n(\lambda)$ the refractive index, and n_2 the nonlinear refractive index. The first derivative $\mathrm{d}n_2/\mathrm{d}\omega$ is determined using the scaling formula described in Ref. [42] [Eq. (A7)]. Equation (A2) describes the delayed molecular response of the medium. For the case of 1 bar of air, we use $\Lambda = 12$ THz, $\Gamma = 10$ THz, $f_{\mathrm{R}} = 0.6$, which we extract from Ref. [40], as well as the Raman-Kerr nonlinear refractive index $n_2^{\mathrm{R}} = 42 \times 10^{-24}$ m^2/W [43]. We further use $n_2 = 8 \times 10^{-24}$ m^2/W [44] for air and $n_2 = 24 \times 10^{-24}$ m^2/W for Krypton [45]. We solve Eq. (A1) using a radially symmetric (2 + 1)D split-step approach with $E = E(r,t)$ and the spatial coordinate $r = \sqrt{(x^2+y^2)}$, where in the spatial domain, the Fourier-transforms are replaced by Hankel-transforms. (In the simulations we use the "pyhank" package by GitHub user etfrogers for Hankel-transforms.)

2. Calculation of CMPC Mirror Dimensions

We here provide some useful equations describing the required minimum mirror dimensions for the CMPC. We consider a pulse energy E, a threshold fluence F_{th}, as well as the CMPC configuration with k and N. We determine the focusing mirror radius-of-curvature R, the diameter of the focusing mirrors D (which is the same as the height of the planar mirrors), and the width of the planar folding mirrors W. The corresponding dimensions are shown in Fig. 10. In order to

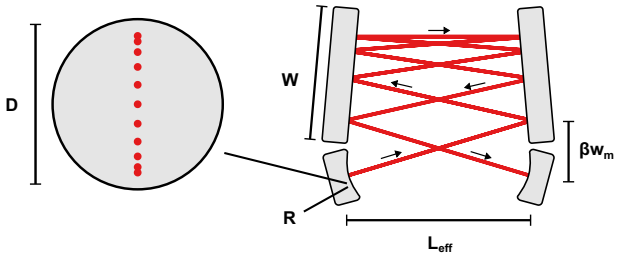


Fig. 10. CMPC geometry.

calculate R, we use the equation for the fluence in the focus $F_0 = 4E/(\lambda R \sin(\pi k/N))$ [32], set $F_0 \leq F_{\text{th}}$, and re-arrange such that

$$R \geq \frac{4E}{\lambda F_{\text{th}}} \frac{1}{\sin(\pi k/N)}. \tag{A3}$$

To find out the width of the planar folding mirrors W, we need to ensure that the beam at any reflection has a sufficient free aperture. For this, we define a factor β, where βw_{m} is the distance between the spot on the focusing mirror and the first reflection on the folding mirror (Fig. 10), and $w_{\text{m}} = ((R\lambda/\pi) \cdot \tan(\pi k/2N))^{1/2}$ [32] is the $1/e^2$ beam radius on the focusing mirror. With some basic geometric considerations, we arrive at

$$W \geq \frac{\Gamma}{4} \beta \sqrt{\frac{4E}{\pi F_{\text{th}}} \frac{\tan(\pi k/2N)}{\sin(\pi k/N)}}, \tag{A4}$$

defining the minimum width of the planar folding mirrors. Here, Γ is the folding ratio. We typically choose a value $\beta = 5$ for our size estimations. The height of the mirrors, or equivalently, the minimal diameter of the focusing mirrors D, can be calculated via

$$D \geq \frac{(2N+1)\beta}{\pi^{3/2}} \sqrt{R\lambda \tan(\pi k/2N)}. \tag{A5}$$

3. Spectral Homogeneity Calculation and Experimental Data

The spatio-spectral homogeneity, expressed as the x- and y-dependent spectral overlap $V(x,y)$ as it is used in Ref. [29], is calculated using the overlap integral

$$V(x,y) = \frac{(\int I_0(\lambda) I(\lambda,x,y) \mathrm{d}\lambda)^2}{\int I_0^2(\lambda)\mathrm{d}\lambda \int I^2(\lambda,x,y)\mathrm{d}\lambda} \times 100, \tag{A6}$$

where λ is the wavelength, I the spectral intensity, and I_0 the spectral intensity at $(x,y) = (0,0)$. The averaged spectral homogeneity is then calculated using the average of $V(x,y)$ weighted with the wavelength-integrated intensity $F(x,y) = \int I(\lambda,x,y)\mathrm{d}\lambda$, yielding

$$V_{\text{avg}} = \frac{\int_{-w}^{w} V(x,y) F(x,y) \mathrm{d}x\mathrm{d}y}{\int_{-w}^{w} F(x,y)\mathrm{d}x\mathrm{d}y}, \tag{A7}$$

where w is the $1/e^2$ beam radius in x- and y-directions, respectively.

In Figs. 11–13 we display $V(x,y)$ for the measurements in Krypton and air in the CMPC, as well as the comparison

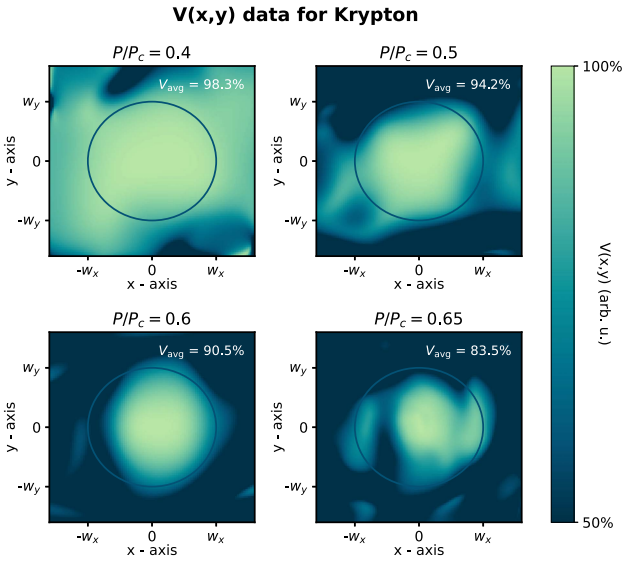


Fig. 11. Spectral homogeneity $V(x,y)$ [Eq. (A6)] for each V_{avg} data point shown in Fig. 8 in the main text. The circles indicate the area of integration for the calculation of V_{avg} [Eq. (A7)].

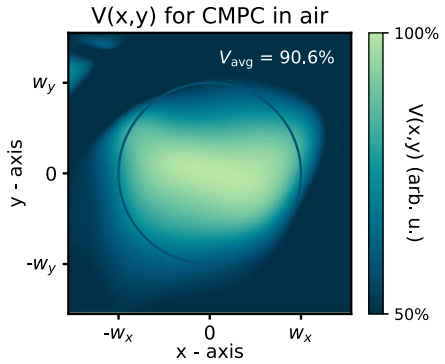


Fig. 12. Spectral homogeneity $V(x,y)$ [Eq. (A6)] for spectral broadening in air at 8 mJ. The circle indicates the area of integration for the calculation of V_{avg} [Eq. (A7)].

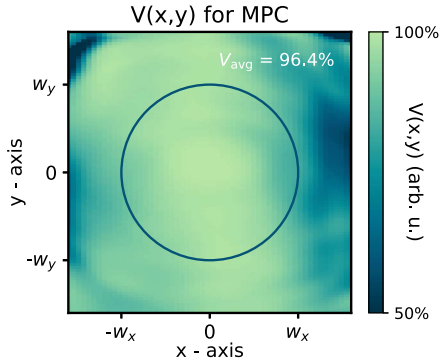


Fig. 13. Spectral homogeneity $V(x,y)$ [Eq. (A6)] for the MPC comparison measurement shown in Fig. 8(C) in the main text. The circle indicates the area of integration for the calculation of V_{avg} [Eq. (A7)].

measurement conducted in a standard MPC. Figure 11 shows $V(x, y)$ for each measurement point, which is displayed in Fig. 8(A) in the main article. In Fig. 12, the spectral homogeneity is shown for the air measurements, carried out at the same parameters as the main spectral broadening and post-compression measurements shown in Fig. 5 in the main text with 1 bar air and 8 mJ pulse energy. Finally, Fig. 13 shows $V(x, y)$ for the comparison measurement in a standard MPC.

Funding. Helmholtz-Lund International Graduate School (HIRS-0018); Vetenskapsrådet/Swedish Research Council (2022-03519).

Acknowledgment. We acknowledge Deutsches Elektronen-Synchrotron DESY (Hamburg, Germany), the Helmholtz Institute Jena (Jena, Germany), and members of the Helmholtz Association HGF for support and/or the provision of experimental facilities.

Disclosures. The authors declare no conflicts of interest.

Data Availability. Data underlying the results presented in this paper are not publicly available at this time but may be obtained from the authors upon reasonable request.

REFERENCES

1. P. Agostini and L. F. DiMauro, "The physics of attosecond light pulses," Rep. Prog. Phys. **67**, 813–855 (2004).
2. P. B. Corkum and F. Krausz, "Attosecond science," Nat. Phys. **3**, 381–387 (2007).
3. F. Krausz and M. Ivanov, "Attosecond physics," Rev. Mod. Phys. **81**, 163–234 (2009).
4. C. M. Heyl, J. Güdde, A. L'Huillier, *et al.*, "High-order harmonic generation with μJ laser pulses at high repetition rates," J. Phys. B **45**, 074020 (2012).
5. E. Esarey, C. B. Schroeder, and W. P. Leemans, "Physics of laser-driven plasma-based electron accelerators," Rev. Mod. Phys. **81**, 1229–1285 (2009).
6. F. Albert, M. E. Couprie, A. Debus, *et al.*, "2020 roadmap on plasma accelerators," New J. Phys. **23**, 031101 (2021).
7. H. Abu-Shawareb, R. Acree, P. Adams, *et al.*, "Lawson criterion for ignition exceeded in an inertial fusion experiment," Phys. Rev. Lett. **129**, 075001 (2022).
8. D. E. Spence, P. N. Kean, and W. Sibbett, "60-fsec pulse generation from a self-mode-locked Ti:sapphire laser," Opt. Lett. **16**, 42–44 (1991).
9. S. Backus, C. G. Durfee, G. Mourou, *et al.*, "0.2-TW laser system at 1 kHz," Opt. Lett. **22**, 1256–1258 (1997).
10. H. Fattahi, H. G. Barros, M. Gorjan, *et al.*, "Third-generation femtosecond technology," Optica **1**, 45–63 (2014).
11. J.-H. Wolter, M. Abdou Ahmed, and T. Graf, "Thin-disk laser operation of Ti:sapphire," Opt. Lett. **42**, 1624–1627 (2017).
12. S. Witte and K. S. E. Eikema, "Ultrafast optical parametric chirped-pulse amplification," IEEE J. Sel. Top. Quantum Electron. **18**, 296–307 (2012).
13. Y. Yin, J. Li, X. Ren, *et al.*, "High-efficiency optical parametric chirped-pulse amplifier in BiB_3O_6 for generation of 3 mJ, two-cycle, carrier-envelope-phase-stable pulses at 17 μm," Opt. Lett. **41**, 1142–1145 (2016).
14. M. Müller, C. Aleshire, A. Klenke, *et al.*, "10.4 kW coherently combined ultrafast fiber laser," Opt. Lett. **45**, 3083–3086 (2020).
15. A.-L. Viotti, M. Seidel, E. Escoto, *et al.*, "Multi-pass cells for post-compression of ultrashort laser pulses," Optica **9**, 197–216 (2022).
16. T. Nagy, S. Hädrich, P. Simon, *et al.*, "Generation of three-cycle multi-millijoule laser pulses at 318 W average power," Optica **6**, 1423–1424 (2019).
17. J. C. Travers, T. F. Grigorova, C. Brahms, *et al.*, "High-energy pulse self-compression and ultraviolet generation through soliton dynamics in hollow capillary fibres," Nat. Photonics **13**, 547–554 (2019).
18. J. C. Travers, "Optical solitons in hollow-core fibres," Opt. Commun. **555**, 130191 (2024).
19. M.-S. Tsai, A.-Y. Liang, C.-L. Tsai, *et al.*, "Nonlinear compression toward high-energy single-cycle pulses by cascaded focus and compression," Sci. Adv. **8**, eabo1945 (2022).
20. E. Schulz, T. Binhammer, D. S. Steingrube, *et al.*, "Intense few-cycle laser pulses from self-compression in a self-guiding filament," Appl. Phys. B **95**, 269–272 (2009).
21. J. Schulte, T. Sartorius, J. Weitenberg, *et al.*, "Nonlinear pulse compression in a multi-pass cell," Opt. Lett. **41**, 4511–4514 (2016).
22. J. Weitenberg, T. Saule, J. Schulte, *et al.*, "Nonlinear pulse compression to sub-40 fs at 4.5 μJ pulse energy by multi-pass-cell spectral broadening," IEEE J. Quantum Electron. **53**, 8600204 (2017).
23. P. Balla, A. B. Wahid, I. Sytcevich, *et al.*, "Postcompression of picosecond pulses into the few-cycle regime," Opt. Lett. **45**, 2572–2575 (2020).
24. G. Fan, P. A. Carpeggiani, Z. Tao, *et al.*, "70 mJ nonlinear compression and scaling route for an Yb amplifier using large-core hollow fibers," Opt. Lett. **46**, 896–899 (2021).
25. G. Mourou, S. Mironov, E. Khazanov, *et al.*, "Single cycle thin film compressor opening the door to zeptosecond-exawatt physics," Eur. Phys. J. Spec. Top. **223**, 1181–1188 (2014).
26. P.-G. Bleotu, J. Wheeler, D. Papadopoulos, *et al.*, "Spectral broadening for multi-joule pulse compression in the APOLLON long focal area facility," High Power Laser Sci. Eng. **10**, e9 (2022).
27. M. Müller, J. Buldt, H. Stark, *et al.*, "Multipass cell for high-power few-cycle compression," Opt. Lett. **46**, 2678–2681 (2021).
28. C. M. Heyl, H. Coudert-Alteirac, M. Miranda, *et al.*, "Scale-invariant nonlinear optics in gases," Optica **3**, 75–81 (2016).
29. Y. Pfaff, G. Barbiero, M. Rampp, *et al.*, "Nonlinear pulse compression of a 200 mJ and 1 kW ultrafast thin-disk amplifier," Opt. Express **31**, 22740–22756 (2023).
30. A. Omar, T. Vogel, M. Hoffmann, *et al.*, "Spectral broadening of 2-mJ femtosecond pulses in a compact air-filled convex–concave multipass cell," Opt. Lett. **48**, 1458–1461 (2023).
31. V. Hariton, K. Fritsch, K. Schwarz, *et al.*, "Spectral broadening in convex-concave multipass cells," Opt. Express **31**, 19554–19568 (2023).
32. C. M. Heyl, M. Seidel, E. Escoto, *et al.*, "High-energy bow tie multipass cells for nonlinear spectral broadening applications," J. Phys.: Photonics **4**, 014002 (2022).
33. H. Stark, C. Grebing, J. Buldt, *et al.*, "Divided-pulse nonlinear compression in a multipass cell," J. Phys.: Photonics **4**, 035001 (2022).
34. H. Schygulla, N. Jimenez, Y. Jiang, *et al.*, "Divided-pulse bulk multipass cell for generating sub-50 fs multi-GW peak power pulses," EPJ Web Conf. **307**, 04066 (2024).
35. M. Kaumanns, D. Kormin, T. Nubbemeyer, *et al.*, "Spectral broadening of 112 mJ, 1.3 ps pulses at 5 kHz in a LG_{10} multipass cell with compressibility to 37 fs," Opt. Lett. **46**, 929–932 (2021).
36. M. Miranda, M. Kotur, P. Rudawski, *et al.*, "Spatiotemporal characterization of ultrashort laser pulses using spatially resolved Fourier transform spectrometry," Opt. Lett. **39**, 5142–5145 (2014).
37. M. A. Arain and G. Mueller, "Design of the advanced LIGO recycling cavities," Opt. Express **16**, 10018–10032 (2008).
38. M. Hanna, L. Daniault, F. Guichard, *et al.*, "Nonlinear beam matching to gas-filled multipass cells," OSA Contin. **4**, 732–738 (2021).
39. C. H. Lin, J. P. Heritage, T. K. Gustafson, *et al.*, "Birefringence arising from the reorientation of the polarizability anisotropy of molecules in collisionless gases," Phys. Rev. A **13**, 813–829 (1976).
40. D. Langevin, J. M. Brown, M. B. Gaarde, *et al.*, "Determination of molecular contributions to the nonlinear refractive index of air for mid-infrared femtosecond laser-pulse excitation," Phys. Rev. A **99**, 063418 (2019).

41. A. Couairon, E. Brambilla, T. Corti, *et al.*, "Practitioner's guide to laser pulse propagation models and simulation: numerical implementation and practical usage of modern pulse propagation models," Eur. Phys. J. Spec. Top. **199**, 5–76 (2011).
42. C. Bree, A. Demircan, and G. Steinmeyer, "Method for computing the nonlinear refractive index via Keldysh theory," IEEE J. Quantum Electron. **46**, 433–437 (2010).
43. E. T. J. Nibbering, G. Grillon, M. A. Franco, *et al.*, "Determination of the inertial contribution to the nonlinear refractive index of air, N_2, and O_2 by use of unfocused high-intensity femtosecond laser pulses," J. Opt. Soc. Am. B **14**, 650–660 (1997).
44. S. Zahedpour, J. K. Wahlstrand, and H. M. Milchberg, "Measurement of the nonlinear refractive index of air constituents at mid-infrared wavelengths," Opt. Lett. **40**, 5794–5797 (2015).
45. J. K. Wahlstrand, Y.-H. Cheng, and H. M. Milchberg, "High field optical nonlinearity and the Kramers-Kronig relations," Phys. Rev. Lett. **109**, 113904 (2012).

B Appendix: Post-Compression of a Q-Switched Laser in a Glass-Rod Multi-Pass Cell

Journal of Physics: Photonics

Check for updates

OPEN ACCESS

RECEIVED
22 September 2025

REVISED
6 November 2025

ACCEPTED FOR PUBLICATION
14 November 2025

PUBLISHED
25 November 2025

Original Content from this work may be used under the terms of the Creative Commons Attribution 4.0 licence.

Any further distribution of this work must maintain attribution to the author(s) and the title of the work, journal citation and DOI.

PAPER

Post-compression of a Q-switched laser in a glass-rod multi-pass cell

Peer Biesterfeld[1,9], Arthur Schönberg[2,9], Marc Seitz[3,9], Nayla Jimenez[2,4,5], Tino Lang[2], Marcus Seidel[2,4,5], Prannay Balla[2], Lutz Winkelmann[2], Jyothish K Sunny[1], Sven Fröhlich[1], Philip Mosel[1], Ingmar Hartl[2], Francesca Calegari[3,6,7], Uwe Morgner[1,8], Milutin Kovacev[1,8], Christoph M Heyl[2,4,5,9] and Andrea Trabattoni[1,3,8,9,*]

[1] Leibniz University Hannover, Institute of Quantum Optics, Welfengarten 1, 30167 Hannover, Germany
[2] Deutsches Elektronen-Synchrotron DESY, Notkestraße 85, 22607 Hamburg, Germany
[3] Center for Free-Electron Laser Science CFEL, Deutsches Elektronen-Synchrotron DESY, Notkestraße 85, 22607 Hamburg, Germany
[4] Helmholtz-Institute Jena, Fröbelstieg 3, 07743 Jena, Germany
[5] GSI Helmholtzzentrum für Schwerionenforschung GmbH, Planckstraße 1, 64291 Darmstadt, Germany
[6] Department of Physics, Universität Hamburg, 22761 Hamburg, Germany
[7] The Hamburg Centre for Ultrafast Imaging, Universität Hamburg, 22607 Hamburg, Germany
[8] Cluster of Excellence PhoenixD (Photonics, Optics, and Engineering-Innovation Across Disciplines), 30167 Hannover, Germany
[9] These authors contributed equally to this work
[*] Author to whom any correspondence should be addressed.

E-mail: andrea.trabattoni@desy.de

Keywords: post-compression, nonlinear optics, ultrafast lasers, ultrafast optics, multi-pass cells

Supplementary material for this article is available online

Abstract

Q-switched lasers are compact, cost-effective, and highly pulse energy-scalable sources for nanosecond-scale laser pulses. The technology has been developed for many decades and is widely used in scientific, industrial and medical applications. However, their inherently narrow bandwidth imposes a lower limit on pulse duration—typically in the few-hundred-picosecond range—limiting the applicability of Q-switched technology in fields that require ultrafast laser pulses in the few-picosecond or femtosecond regime. In contrast, mode-locked lasers can produce broadband, ultrafast (<1 ps) pulses, but are complex, expensive, and typically require a large footprint. To bridge the parameter gap between these two laser platforms—in terms of pulse duration and achievable peak power—we here propose a Herriott-type multi-pass cell (MPC) based post-compression scheme for shortening the pulse durations of Q-switched lasers down to the ultrafast, picosecond regime. We experimentally demonstrate post-compression of 0.5 ns, 1 mJ pulses from a Q-switched laser to 24 ps using a compact glass-rod MPC for spectral broadening. We verify this result numerically and show that compression down to a few picoseconds is possible using the nanosecond MPC (nMPC). Through spectral filtering approaches, the nMPC suppresses detrimental nonlinear processes such as stimulated Raman scattering, which have set severe limitations for fiber-based post-compression of Q-switched lasers until today. Our results pave the way to cost-efficient and compact ultrafast laser platforms based on Q-switched laser technology.

1. Introduction

The continuous development of lasers has had a profound impact on our society. In particular, laser pulses with durations in the nano- ($1\text{ns} = 10^{-9}\text{s}$) to femtosecond ($1\text{fs} = 10^{-15}\text{s}$) range are routinely employed for microsurgery [1, 2] optical gas sensing [3], high-precision surface and volume material processing [4], or imaging of biological samples [5, 6]. Moreover, short-pulsed lasers are playing an indispensable role in fundamental research with applications ranging from the ultrafast spectroscopy of photo-induced electron dynamics in matter [7] via the manipulation of transient states in materials [8]

© 2025 The Author(s). Published by IOP Publishing Ltd

to recent breakthroughs in nuclear spectroscopy [9, 10]. Depending on the laser parameters, in particular the required peak power and pulse duration, different pulsed laser technologies are used, employing predominantly Q-switching or mode-locking schemes.

On the one hand, nanosecond pulses are typically generated using Q-switching methods [11–15]. Q-switched lasers can support high pulse energy (millijoule to joule), they are cost-efficient and can be built as robust and compact modules. Their peak power, however, is limited, hindering their effectiveness, for example, in material machining, dermatological treatment, or as driving light sources for nonlinear optical processes. On the other hand, shorter durations (pico- to femtoseconds) are the realm of mode-locked lasers [14, 16–18]. Such light sources provide pulses that enable the analysis of ultrafast phenomena at femtosecond time scales and furthermore support ultrahigh peak powers, which make them ideal for machining applications, at the expense, however, of high complexity, large footprints and much higher costs. In this context, the idea of compressing the duration of nano- to picosecond or sub-picosecond laser pulses is particularly appealing, as it offers a route to bridge the gap—at least in terms of pulse duration and achievable peak power—between Q-switching and mode-locking laser technologies.

In the last four decades, post-compression methods, i.e. technologies employing nonlinear optical processes to spectrally broaden and temporally compress the laser pulse, have tackled this challenge. Self-phase modulation (SPM) in hollow-core capillaries/fibers [19–21], photonic crystal fibers [22–24], or multi-pass cells (MPCs) [25–28] is used to compress mode-locked lasers even down to the few-femtosecond range. However, the compression of Q-switched lasers has proven more challenging. Compression methods exploiting stimulated Brillouin scattering (SBS) in bulk or liquid media or by propagation in long (>100 m) optical fibers, enabled to compress nanosecond lasers into the picosecond regime [29–33]. However, these efforts were limited in performance by phonon lifetime constraints or competing nonlinear effects—for instance, stimulated Raman scattering (SRS) - as well as in energy scalability, especially for the fiber based approaches. As a result, post-compressing Q-switched lasers to the parameter space of mode-locked lasers at millijoule-class pulse energies has not been achieved until now. Figure 1(a) illustrates this discussion, showing a representative set of post-compressed Q-switched and mode-locked lasers. The figure visualizes the input laser parameters (larger shapes) and the post-compressed output (smaller shapes), connected with dashed lines. The distribution of the displayed data points underlines a major parameter gap between the two laser technologies.

Here, we introduce a novel technology based on a bulk-rod Herriot-type MPC, that opens a route to compress lasers with few MW or sub-MW peak power into the pico- to femtosecond regime, approaching GW power levels. We experimentally demonstrate the technique by compressing a 0.5 ns pulse to 24 ps using a 10 cm-long fused silica (FS) rod as MPC nonlinear medium. Our simulations demonstrate that the method can scale to compression factors exceeding 100. Spectral filtering thereby prevents the rise of detrimental nonlinear processes including SRS and quasi-phase-matched four-wave-mixing (QPM-FWM). Our approach opens a perspective towards low-cost, compact, high-peak-power laser systems for novel implementations in science and industry. This includes, for example, the generation of high-flux extreme-ultraviolet (EUV) light, high-precision laser-driven material machining, or damage-free tissue treatment in dermatology.

2. Concept

Compressing the temporal duration of laser pulses relies on the concept of spectral broadening. Nonlinear optical processes such as SPM are employed for this purpose, being implemented in a variety of post-compression schemes [27]. Typically, a suitable regime of SPM implies the propagation of laser pulses at high peak power (usually ranging from 10 s of MW to the GW level) in nonlinear media such as gases or thin solid-state plates. To the best of our knowledge, pulses with a peak power down to about 8.7 MW have been post-compressed through SPM with an MPC [27]. In this framework, the post-compression of Q-switched pulses with nanosecond duration presents a main challenge: a typical Q-switched laser with a pulse energy of 1 mJ and a duration of 1 ns provides a peak power of only 1 MW, which prevents the post compression in conventional gas-filled or solid-state MPC designs. Long propagation in solid-core fibers with high optical nonlinearity may appear as a good mitigation strategy and has been employed to successfully post-compress nanosecond pulses in the nanojoule-energy regime [32, 42]. A different method involves using compression along with amplification in a fiber-based system. In this approach the compression, of short Q-switched laser pulses (100 ps) with an amplified energy of 0.1 mJ, to 2.7 ps has been demonstrated in a two stage setup [43, 44]. However, Raman and/or Brillouin scattering typically deteriorate the spectral broadening process, limiting energy-scalability especially for nanosecond pulses.

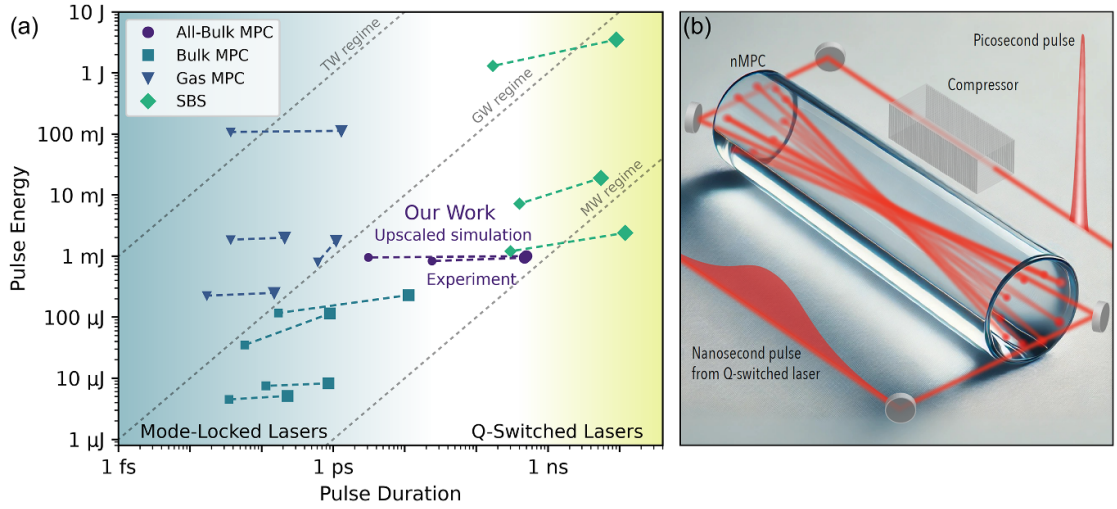


Figure 1. Post compression methods covering the parameter space from nanoseconds to femtoseconds. (a) Parameter overview of representative laser pulse post-compression works. Q-switched laser systems (green) have been post-compressed via SBS (diamonds), while gas-filled (triangles) or bulk (squares) MPCs are widely used for compressing mode-locked laser systems (blue) [26, 29, 30, 34–41]. Our work (purple) bridges the gap between these two laser regimes via post-compression of Q-switched lasers in a Herriott-type, bulk-rod MPC. The experimental output data point takes into account the output pulse duration measured at reduced energy, scaled to the full energy transmitted through the MPC. (b) Illustration of the proposed nanosecond MPC concept.

In order to overcome the above-mentioned limitations, we introduce a new type of MPC made completely out of glass such as FS. The monolithic MPC is equipped with high-reflectivity coated, curved surfaces acting as cavity mirrors (figure 1(b)). This type of MPC, dubbed nanosecond MPC (nMPC), presents unique advantages for long (nanosecond to hundreds of picoseconds) driving pulses. First, it provides both large nonlinear coefficients as well as long nonlinear interaction lengths while keeping the overall footprint of the setup compact. Second, while input pulses with pico- or femtosecond duration would suffer from the high dispersion in the bulk material, nanosecond pulses are insensitive to dispersion due to their narrow bandwidth. Third, the laser-induced damage threshold (LIDT) of the optical coating of the curved surfaces is much higher for nanosecond lasers than for shorter pulses, with values in the range of 10 s of J cm^{-2} [45, 46]. Consequently, MPC configurations with small beam sizes on the mirrors can be realized, thus allowing for many round trips and large spectral broadening factors. Fourth, the optical coatings can act as a spectral filter at each round trip, suppressing competing nonlinear optical processes such as Raman scattering and four-wave mixing that otherwise would strongly limit the pulse compressibility (further details in the discussion).

Based on this concept, simulations with an input pulse energy of 1 mJ, an input pulse duration of 0.5 ns of a Gaussian laser pulse and 150 round-trips ($N = 150, k = 91$), are carried out to demonstrate the potential of the nMPC. The simulation is performed using a symmetric split-step Fourier algorithm to solve the Unidirectional Pulse Propagation equation in (2+1) dimensions, assuming radial symmetry [47]. We consider a FS glass block with curved surfaces of $R = 10$ cm, length $L = 25.43$ cm and an MPC configuration parameter $k = 91$ [27]. The in/out coupling can be achieved through a small uncoated spot in one cell surface. By using a diameter of 3 inch (7.62 cm) for the curved surfaces, the necessary 150 reflections can be fit onto the curved surfaces. As an alternative route, a more dense round-trip pattern can be employed, overcoming geometric limitations of a simple circular pattern [48]. Figure 2 shows the results of the simulation. The spectral bandwidth of the input $\Delta\lambda_{10\mathrm{dB}} = 6$ pm increases by a factor of 220 to $\Delta\lambda_{10\mathrm{dB}} = 1.32$ nm, supporting a pulse duration of 2.2 ps (figure 2(a)). Following second-order phase compensation (103 ps^{-1}), a compressed pulse with a duration of 3.1 ps is obtained, showing very good compressibility. This results in a temporal compression by a factor of 161 and a final peak power of 82 MW (figure 2(b)). We note that large compression factors typically lead to the emergence of pedestals and limit the energy content in the main pulse, as shown in figure 2(b). However, strategies exist to mitigate this effect and optimize the pulse contrast, see the discussion section for more details.

Due to the inherent property of input-to-output beam imaging in MPCs [27], fluctuations in the input beam pointing are not amplified inside the nMPC, even for a large number of round trips (here $N = 150$) and the resulting long propagation distances. MPCs have been demonstrated to exhibit high stability even with a large number of reflections and long propagation distances [49]. Additionally, the

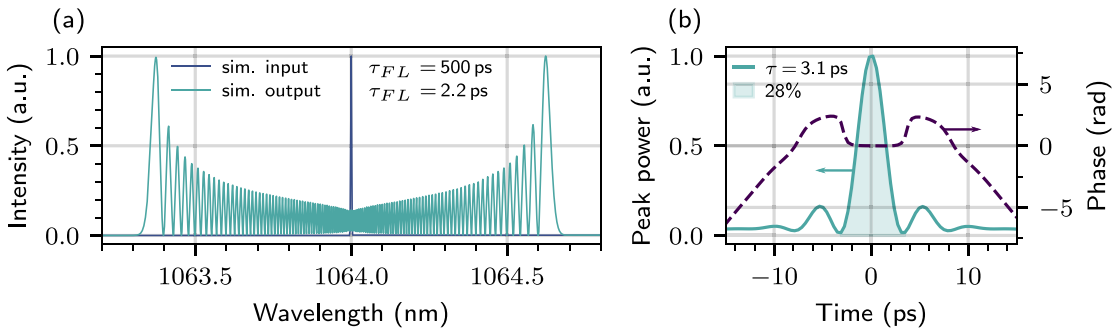


Figure 2. Simulated post-compression using the nMPC concept. (a) Input and output spectra demonstrating a high compression rate in the proposed full-bulk nMPC. (b) Corresponding compressed pulse, where the phase is compensated using GDD only.

all-bulk geometry mitigates the effects of ambient airflow as well as mechanical instability of the optical mounts, further increasing the stability of the system.

In the all-bulk scheme, the main sources of loss are the coated end facets of the bulk material and the absorption in the medium. With modern manufacturing methods, these losses can be kept very low, allowing the realization of such an MPC with an efficiency >90 %. Considering commercially available transmission gratings with efficiencies of >98% the total transmission of the setup can be in the order of 90 %. Alternatively, slightly less efficient but very compact compression can be achieved using a dispersive volume Bragg grating. The efficiency in the required parameter regime is >90% [50]. This allows for a total post-compression efficiency of >80% while maintaining a very small footprint.

The nMPC can potentially be further scaled to higher pulse energies and longer pulses, within limitations imposed mainly by SBS and the critical power of the material. While SBS imposes limits on the pulse duration and intensity, critical self-focusing can lead to beam collapse when the critical power of the material is exceeded. In the current nMPC configuration, the input pulse energy can be scaled up to 10 mJ when using a 4 ns long pulse, where the peak power is roughly half the critical power of FS ($P_{\mathrm{crit,FS}} \approx 5MW$) and the SBS limit is still not exceeded (see figure S4).

3. Experimental demonstration

We experimentally demonstrate the nMPC concept using a simplified setup which is schematically depicted in figure 3(a)). We employ a commercial Q-switched diode-pumped Nd:YAG laser (MPL2310, QS Lasers), emitting at 1064 nm. The passive Q-switching is achieved by a Cr:YAG crystal, resulting in the generation of pulses with a duration full-width at half maximum (FWHM) of 0.4 ns. With an ultracompact footprint (10 × 17 cm), the laser features a pulse energy of 2 mJ at a repetition rate of 100 Hz. The laser cavity is operated in single-mode emission upon thermal stabilization, yielding only (<0.1%) of energy in adjacent longitudinal modes. The single-mode contrast is further enhanced by using an Etalon filter with a free spectral range of 230 pm and a finesse of 41, resulting in an additional reduction of 24 dB for the adjacent modes, leading to a mode contrast of < 0.001%. The effect of multi-mode operation on the performance of the nMPC is discussed in detail in the supplemental (section S2).

For the sake of simplicity of this first test setup, we decomposed the monolithic bulk-rod nMPC into a set of two cavity mirrors, a large glass block, and an in-coupling scraper mirror. We use a 10 cm long block of anti-reflection coated, UV-FS as nonlinear medium, placed in the center between two concave mirrors with a radius of curvature of 0.1 m (figure 3(b)). The input beam is mode-matched to the MPC by a 3-lens telescope and is coupled into the cell by the scraper mirror with a width of 4 mm. The laser pulse undergoes 62 passes in the nMPC. Specifically, the MPC is configured with $N = 31$ and $k = 24$, where N defines the number of round trips and k specifies the chosen configuration which fulfills the re-entrance condition [27]. In this configuration, the linearly mode-matched MPC mode corresponds to a fluence of 0.3 J cm^{-2} on the cell mirrors and a peak intensity of $1{\cdot}10^{10}$W cm^{-2} at the focus. LIDT measurements have been conducted on the glass block, showing laser-induced damage inside the bulk for a driving peak intensity of $2{\cdot}10^{10}$W cm^{-2}. The in-coupled pulses have an energy of 0.94 mJ and a duration of 0.47 ns (FWHM), measured with an in-house developed second-order autocorrelator. The MPC transmission efficiency is measured to be 83%. This value is in good agreement with the calculated efficiency of 86%, considering the reflectivity of the cell mirrors and the FS bulk surfaces as specified by the manufacturer. The beam spatial quality is measured before and after the nMPC, showing a slight degradation of the mean M-square from 1.31 to 1.45 (see figure S1).

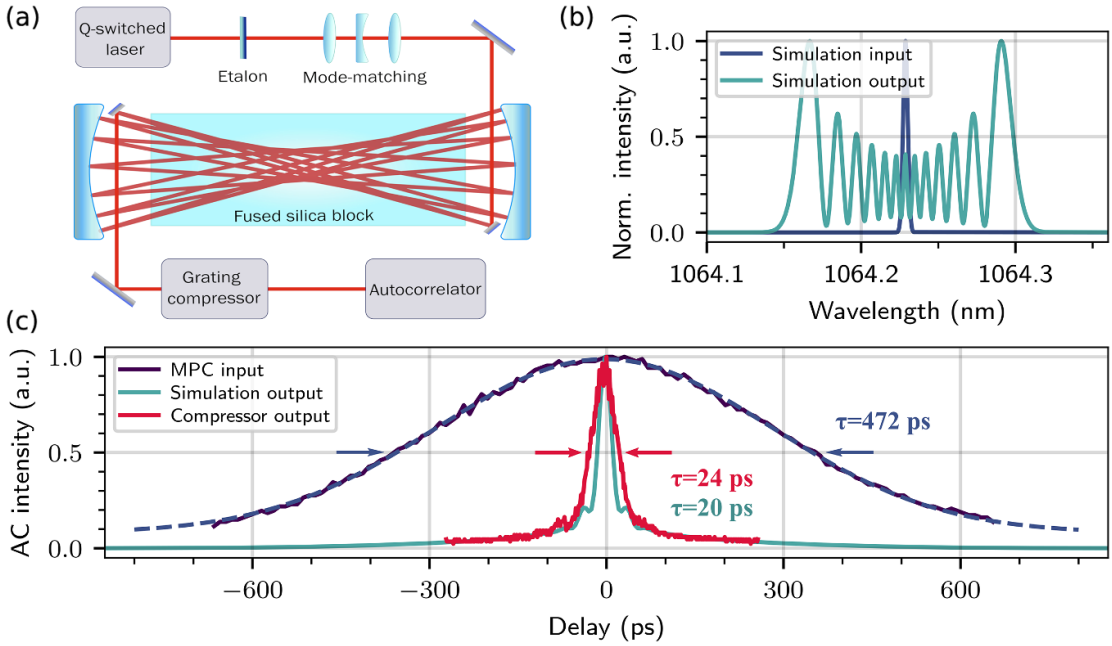


Figure 3. Experimental setup and results. (a) Schematic experimental setup including in particular an MPC using a 10 cm FS rod as a nonlinear medium. (b) Spectral broadening characteristics obtained via numerical (2+1)D simulation mimicking the experimental conditions. (c) Autocorrelation (AC) of the MPC input and compressor output pulse, along with the AC of the GDD-compensated simulated output. The pulse durations τ are obtained by fitting a Gaussian (input) and a Lorentzian (output) to the experimental data, taking the corresponding deconvolution factors into account.

Figure 3(b) shows the simulated SPM-driven spectral broadening occurring in the nMPC for the current experimental parameters. Starting from an input bandwidth of around 6 pm, an output bandwidth of 155 pm is obtained through SPM, corresponding to a transform-limited duration of 20 ps (FWHM). The spectral phase of the simulation output is compensated via GDD compensation ($-1370\,\mathrm{ps}^{-2}$), resulting in a pulse duration close to the Fourier-limited value and an energy content of 60% in the main pulse. Experimentally, spectral broadening is monitored using an Echelle spectrometer with a resolution of 35 pm at 1064 nm. Although this instrument is sufficient to show a signature of SPM, it is not able to resolve the broadened spectrum. For this reason, only the simulated spectra are reported in figure 3(b), while the experimental characterization of the input and output pulses was performed in the time domain. Following spectral broadening in the nMPC, the output beam is collimated and sent to a transmission-grating compressor, where the pulse is compressed in the time domain [27]. The compressor consists of two gratings with a line density of $1740\,\mathrm{l\,mm}^{-1}$, resulting in a total chirp of approx. $-1100\,\mathrm{ps}^{-2}$ and a limited efficiency of $\eta = 12\%$). We note that this compressor was used simply for availability reasons to demonstrate compressibility, disregarding efficiency. The used gratings can easily be replaced by tailored transmission gratings or by a chirped volume Bragg grating (CVBG). A CVBG can provide the required chirp while offering high efficiency ~90%, supporting high pulse energies and average powers exceeding 1 mJ and 250 W in a single compact optical element measuring a few centimeters in length [50].

The duration of the compressed pulses is measured to be 24 ps (FWHM), which is close to the simulated transform limit of 20 ps (figure 3(c)). The compression ratio, based on the measured input duration of 0.47 ns (FWHM), is approximately 20. This result demonstrates the effective compressibility of single-mode q-switched lasers in SPM-driven MPCs.

4. Discussion

Our proof-of-principle experiment demonstrates the nMPC concept and shows the first MPC-based compression of nanosecond-class laser pulses. The compressed pulses which can be obtained in our experiment using an improved compressor setup match the driving peak power range of post-compression setups already demonstrated in literature [26]. In addition, compression factor up-scaling to reach shorter output pulses in a single stage using our scheme appears feasible (see figure 2). Combining an nMPC with a conventional compression method thus holds promise to fully bridge the gap between nanosecond and femtosecond pulse durations, opening up a new class of femtosecond lasers.

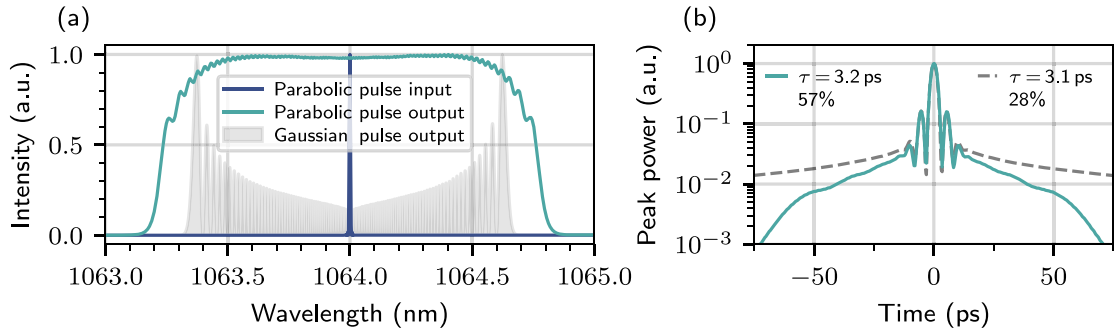


Figure 4. Simulated nMPC post-compression using a parabolic temporal pulse shape. (a) Spectral broadening of a temporally parabolic shaped pulse in comparison to a Gaussian pulse (identical to the data displayed in figure 2). (b) Corresponding GDD-compensated pulses, along with the energy fraction contained in the main pulse.

Taking into account future parameter scaling approaches, it is important to discuss the accessible parameter space supported by an nMPC. In this context, it is critical to consider that multiple detrimental processes can be triggered upon extreme spectral broadening in bulk media, and their contribution depends on the bandwidth of the input pulse. In this framework, we identify five major phenomena: temporal quality of post-compressed pulses, longitudinal mode beating of Q-switched lasers [51], SBS [52–54], SRS [54], and degenerate QPM-FWM [55]. We discuss the impact of these processes for post-compression in an nMPC along with suitable mitigation strategies.

The degradation of the temporal quality for high post compression factors in a single stage is a well-known challenge [56]. This effect is also seen in our simulations: it leads to a low energy content in the main pulse of only 28% for a compression factor of 161 by considering a Gaussian input pulse shape (figure 2). This effect results from the strongly modulated spectral shape and phase of an SPM broadened Gaussian pulse [57]. However, the temporal characteristics for large compression factors can be improved by separation into multiple stages, enhanced frequency chirping or nonlinear polarization ellipse rotation [57–59].

Another option is shaping the temporal intensity profile of the input pulse into a parabolic shape, which can lead to a high-contrast SPM-post-compressed pulse [60]. In the femtosecond regime, this is commonly realized by means of a spatial mask in the Fourier plane [61, 62]. In contrast, operating in the nanosecond regime makes it possible to employ direct temporal pulse-form shaping technology, which is readily available at sub-ns levels with ps resolution [63, 64].

Figure 4 shows this approach in a (2+1)D simulation with an input pulse energy of $E_\mathrm{p} = 0.5$ mJ, 225 round trips through the MPC and a B-integral per pass of $B_\mathrm{pass} = 0.2\pi$. The number of round trips N has been chosen to match the Fourier transform limit of the broadened spectrum displayed in figure 2 for direct comparison. All parameters not specified above are kept as in figure 2. The parabolic input pulse generates a much smoother output spectrum, increasing the energy content of the main pulse by a factor of 2. Our simulations indicate that a further improved energy content in the main pulse can be achieved for decreasing B_pass, compensated by an increased N.

The next challenge for Q-switched laser pulse compression is longitudinal mode beating, which can occur due to additional longitudinal modes emitted from the laser itself, a typical phenomenon for Q-switched lasers [65]. The resulting modulation of the temporal profile of the pulse occurring due to temporal mode interference can distort the phase of the SPM-broadened spectrum, degrading the compressibility of the pulse, as observed in our experiments (see section S2). Our numerical simulations reveal that an additional mode with an energy fraction of only 10^{-4} of the main pulse can already have severe effects on the output spectrum. Thus, mode cleaning before coupling into the nMPC becomes necessary.

Another challenge is SBS, which arises from the nonlinear interaction of an incoming light wave (pump) with the acoustic modes of the medium via electrostriction, generating a periodic modulation of the material density. For pulse energies exceeding a material-dependent threshold intensity, the laser pulse releases energy into a backward-propagating Stokes wave, which is frequency-shifted by a few GHz relative to the incoming wave [52–54]. SBS thus represents a potential loss channel for an nMPC. The SBS frequency shift is a material-dependent property. For FS this shift is equivalent to 16.3 GHz [66]. Following the formalism of transient Brillouin scattering ($\tau < 100$ ns) in fibers [67], it can be shown that the effective intensity for the nMPC example reported above is two orders of magnitude lower than the threshold intensity required for SBS, i,e. $I^\mathrm{eff}_\mathrm{nMPC}/I^\mathrm{th}_\mathrm{SBS} = 0.013$ (see figure S4). For the same intensity, the SBS threshold is instead surpassed when the input pulse duration is increased to $\tau \approx 5$ ns. In

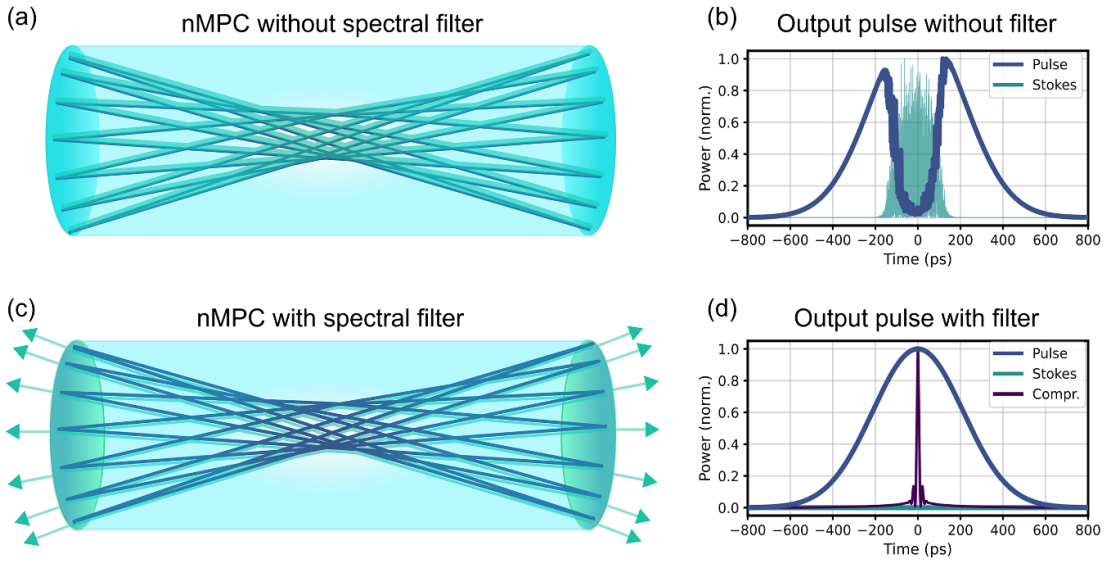


Figure 5. Impact and suppression of SRS in nMPC post-compression. (a) and (c) Illustration of the nMPC with (c) and without (a) spectral SRS filter. The transmitted Stokes components are pictorially indicated with arrows. (b) and (d) Corresponding simulated temporal pulse shapes following spectral broadening in the nMPC. Without filter, the pulse transfers energy to the Stokes field, leading to a distorted temporal pulse shape (b). This effect can be suppressed (d) using a suitable MPC mirror design, acting as spectral filter suppressing the Stokes pulse.

this case, SBS can be suppressed by reducing the peak power at the expense of the single-pass spectral broadening.

In addition to SBS, SRS can severely limit spectral broadening. SRS is an inelastic, stimulated scattering process in which photons are downshifted in energy by an amount determined by the vibrational modes of the medium [54]. In FS, the Stokes wave is frequency-down-shifted by about 13.6 THz [68]. Similar to SBS, the magnitude of SRS becomes important after exceeding a certain intensity threshold. Due to the large frequency shift, dispersion between the original pump pulse and the Stokes pulse can influence the dynamics of SRS [54]. SRS has been the major limiting factor of spectral broadening in fibers [69]. Although large broadening factors up to 80 have been demonstrated in fibers [32, 42], SRS limits the possible pulse energies to far below 1 μJ. While in our proof-of-principle experiment we did not observe any significant SRS onset, in the case of the upscaled simulation reported in figure 2, SRS becomes prominent (see equation (S6) in section S5). However, within the nMPC scheme the SRS contribution can be suppressed by using suitable MPC mirror coatings, acting as spectral filters for the Stokes pulse at each reflection.

Using FS as nonlinear material, the Stokes pulse of a laser pulse centered at 1064 nm appears at around 1112 nm and thus far outside the spectral range covered by the SPM-broadened spectrum, making spectral filtering possible. Figure 5 shows two simulated spectral broadening scenarios in an nMPC using 500 ps, 1 mJ pulses. Attenuating the Stokes field by only 30% per mirror reflection completely suppresses SRS and results in clean, compressible pulses (figures 5(c) and (d)).

Another limiting nonlinear effect is QPM-FWM, which can occur in MPCs with large broadening factors [55]. Similar to SRS, this effect can severely limit spectral broadening due to the generation of spectral side-bands, introducing strong modulations on the pulse in the temporal domain. We analyze this effect numerically and estimate its impact for nMPC post-compression (section S5), identifying a simple mitigation strategy. The location of the spectral side-bands depends on the dispersion properties of the nMPC, including the nonlinear medium and the mirrors, as well as on the MPC configuration. For the considered example case with the laser pulse centered at 1064 nm, the first QPM-FWM peaks appear at 1047 nm and 1082 nm. Similar to SRS, suitable optical coatings can be used to filter out both QPM-FWM induced spectral side-bands at each reflection and fully suppress their effect (see figure S7).

In the presented experiment, the moderate broadening factor of 20 resulted in the absence of the majority of the aforementioned detrimental effects, including SRS and QPM-FWM. However, our simulations reveal the importance of SRS and QPM-FWM suppression via spectral filtering for large spectral broadening factors (figures S5 and S7), indicating the importance of suitable mitigation strategies. We note that the (2+1)D simulation results presented in figures 2 and 4 do not include the effect of SRS and QFM-FWM for computational reasons. However, we also performed (1+1)D simulations with

the same parameters, while also considering SRS and QFM-FWM (see figure S7). In particular, we show that the use of suitable optical coatings effectively filters out and suppresses the contribution of SRS and QFM-FWM even for large compression factors, while maintaining a very high reflectivity (>99.98%) around the center wavelength of the laser.

5. Conclusion and outlook

We introduced a novel approach to compress Q-switched laser pulses using an nMPC, which uses a long glass rod as the nonlinear medium, as well as spectral filtering concepts to suppress detrimental nonlinear effects. Our approach enables efficient spectral broadening of low peak-power sources and extremely high compression factors, while also overcoming key limitations observed in fiber-based spectral broadening, such as SRS. Our proof-of-concept experiment demonstrates the compression of a 0.5 ns long pulse to a duration of 24 ps, with numerically validated scalability down to 3 ps. When combined with a second post-compression stage, the nMPC provides a bridge between nanosecond Q-switched lasers and femtosecond pulses. Our results open perspectives towards low-cost, high-peak-power ultrafast sources. Ultimately, the nMPC technology is promising to support a range of advanced applications, including the generation of high-flux EUV light for material characterization and ultrafast laser spectroscopy research, high-precision laser-driven material machining for industrial manufacturing, and damage-free tissue treatment in dermatology.

Data availability statement

All data that support the findings of this study are included within the article (and any supplementary files).

Supplementary data available at https://doi.org/10.1088/2515-7647/ae1fc4/data1.

Acknowledgments

Views and opinions expressed are however those of the author(s) only and do not necessarily reflect those of the European Union or the European Research Council Executive Agency. Neither the European Union nor the granting authority can be held responsible for them.

Funding

Cluster of Excellence PhoenixD (DFG EXC 2181); Cluster of Excellence 'CUI: Advanced Imaging of Matter' (EXC 2056, 390 715 994); European Innovation Council Pathfinder Project 'NanoXCAN' (101 047 223); Helmholtz Young Investigator Group (VH-NG-1603); Deutsche Forschungsgemeinschaft (545 612 524); Helmholtz-Lund International Graduate School (HELIOS) (HIRS-0018); European Research Council 'SoftMeter' (101 076 500); Bundesministerium für Forschung, Technologie und Raumfahrt (BMFTR) (13N16678); Gottfried Wilhelm Leibniz Universität Hannover; Deutsches Elektronen-Synchrotron DESY; Helmholtz-Institute Jena; Helmholtz Association.

Author contributors

CH and AT conceived the initial idea and supervised the project. PBi, AS, MS, NJ, TL, JKS, SF, PM performed the experiment. PBi and AS carried out the data analysis, as well as the (1+1)D and the (2+1)D simulations supporting the concept and the experiment. PBi, AS, MS, CH, and AT drafted to writing the manuscript. All authors discussed the results and contributed to the manuscript.

ORCID iDs

Peer Biesterfeld 0009-0003-3125-3051
Arthur Schönberg 0009-0001-4189-9978
Marc Seitz 0009-0004-2251-1298
Nayla Jimenez 0000-0002-8317-3585
Christoph M Heyl 0000-0003-2133-5224
Andrea Trabattoni 0000-0002-0187-9075

References

[1] Linz N, Freidank S, Liang X-X and Vogel A 2023 *Ultrafast Laser Nanostructuring: The Pursuit of Extreme Scales* (Springer) pp 1217–45
[2] Skorczakowski M *et al* 2010 Mid-infrared Q-switched Er:YAG laser for medical applications *Laser Phys. Lett.* **7** 498
[3] Hodgkinson J and Tatam R P 2012 Optical gas sensing: a review *Meas. Sci. Technol.* **24** 012004
[4] Sugioka K and Cheng Y 2014 Ultrafast lasers - reliable tool for advanced material processing *Light Sci. Appl.* **3** e149–149
[5] Fan S, Wang S, Yang C, Wise F and Kong L 2023 Advances of mode-locking fiber lasers in neural imaging *Adv. Opt. Mater.* **11** 2202945
[6] Lefort C 2017 A review of biomedical multiphoton microscopy and its laser sources *J. Phys. D: Appl. Phys.* **50** 423001
[7] Cederbaum L and Zobeley J 1999 Ultrafast charge migration by electron correlation *Chem. Phys. Lett.* **307** 205–10
[8] Nicoletti D, Casandruc E, Laplace Y, Khanna V, Hunt C R, Kaiser S, Dhesi S S, Gu G D, Hill J P and Cavalleri A 2014 Optically induced superconductivity in striped $La_{2-x}Ba_xCuO_4$ by polarization-selective excitation in the near infrared *Phys. Rev. B* **90** 100503
[9] Tiedau J *et al* 2024 Laser excitation of the Th-229 nucleus *Phys. Rev. Lett.* **132** 182501
[10] Elwell R, Schneider C, Jeet J, Terhune J E S, Morgan H W T, Alexandrova A N, Tan H B T, Derevianko A and Hudson E R 2024 Laser excitation of the ^{229}Th nuclear isomeric transition in a solid-state host *Phys. Rev. Lett.* **133** 013201
[11] Wang Y and Xu C-Q 2007 Actively Q-switched fiber lasers: switching dynamics and nonlinear processes *Prog. Quantum Electron.* **31** 131–216
[12] Chen X, Wang N, He C and Lin X 2023 Development of all-fiber nanosecond oscillator using actively Q-switched technologies and modulators *Opt. Laser Technol.* **157** 108709
[13] Al-Hiti A S, Yasin M and Harun S W 2022 Nanosecond Q-switched laser with PEDOT: PSS saturable absorber *Appl. Opt.* **61** 1292–9
[14] Paschotta R 2008 *Field Guide to Laser Pulse Generation* (SPIE Press)
[15] Zhou Y, Li X, Xu H, Yan R, Jiang Y, Fan R and Chen D 2021 High-pulse-energy passively Q-switched sub-nanosecond MOPA laser system operating at kHz level *Opt. Express* **29** 17201–14
[16] Kues M, Reimer C, Wetzel B, Roztocki P, Little B E, Chu S T, Hansson T, Viktorov E A, Moss D J and Morandotti R 2017 Passively mode-locked laser with an ultra-narrow spectral width *Nat. Photon.* **11** 159–62
[17] Kim J and Song Y 2016 Ultralow-noise mode-locked fiber lasers and frequency combs: principles, status and applications *Adv. Opt. Photon.* **8** 465
[18] Han Y, Guo Y, Gao B, Ma C, Zhang R and Zhang H 2020 Generation, optimization and application of ultrashort femtosecond pulse in mode-locked fiber lasers *Prog. Quantum Electron.* **71** 100264
[19] Nagy T, Simon P and Veisz L 2020 High-energy few-cycle pulses: post-compression techniques *Adv. Phys. X* **6** 1845795
[20] Frosz M H, Bradley T D, Habib M S, Markos C, Travers J and Wang Y 2024 Editorial: advances and applications of hollow-core fibers *IEEE J. Sel. Top. Quantum Electron.* **30** 1001003
[21] Nisoli M, De Silvestri S and Svelto O 1996 Generation of high energy 10 fs pulses by a new pulse compression technique *Appl. Phys. Lett.* **68** 2793–5
[22] Gebhardt M, Gaida C, Hädrich S, Stutzki F, Jauregui C, Limpert J and Tünnermann A 2015 Nonlinear compression of an ultrashort-pulse thulium-based fiber laser to sub-70 fs in Kagome photonic crystal fiber *Opt. Lett.* **40** 2770–3
[23] Heidt A M, Rothhardt J, Hartung A, Bartelt H, Rohwer E G, Limpert J and Tünnermann A 2011 High quality sub-two cycle pulses from compression of supercontinuum generated in all-normal dispersion photonic crystal fiber *Opt. Express* **19** 13873–9
[24] Mak K F, Travers J C, Joly N Y, Abdolvand A and Russell P S J 2013 Two techniques for temporal pulse compression in gas-filled hollow-core kagomé photonic crystal fiber *Opt. Lett.* **38** 3592–5
[25] Schulte J, Sartorius T, Weitenberg J, Vernaleken A and Russbueldt P 2016 Nonlinear pulse compression in a multi-pass cell *Opt. Lett.* **41** 4511–4
[26] Weitenberg J, Vernaleken A, Schulte J, Ozawa A, Sartorius T, Pervak V, Hoffmann H-D, Udem T, Russbüldt P and Hänsch T W 2017 Multi-pass-cell-based nonlinear pulse compression to 115 fs at 7.5 μJ pulse energy and 300 W average power *Opt. Express* **25** 20502–10
[27] Viotti A-L, Seidel M, Escoto E, Rajhans S, Leemans W P, Hartl I and Heyl C M 2022 Multi-pass cells for post-compression of ultrashort laser pulses *Optica* **9** 197–216
[28] Hanna M, Délen X, Lavenu L, Guichard F, Zaouter Y, Druon F and Georges P 2017 Nonlinear temporal compression in multipass cells: theory *J. Opt. Soc. Am. B* **34** 1340–7
[29] Tarasov A A and Chu H 2017 Subnanosecond Nd:YAG laser with multipass cell for SBS pulse compression *Solid State Lasers Xxvi: Technology and Devices* Ed W A Clarkson and R K Shori (*Proc. SPIE*) **10082** 100820Q
[30] Feng C, Xu X and Diels J-C 2017 High-energy sub-phonon lifetime pulse compression by stimulated Brillouin scattering in liquids *Opt. Express* **25** 12421–34
[31] Maier M, Kaiser W and Giordmaine J A 1966 Intense Light Bursts in the Stimulated Raman Effect *Phys. Rev. Lett.* **17** 26
[32] Johnson A M, Stolen R H and Simpson W M 1984 80× single-stage compression of frequency doubled Nd:yttrium aluminum garnet laser pulses *Appl. Phys. Lett.* **44** 729–31
[33] Mollenauer L F, Stolen R H, Gordon J P and Tomlinson W J 1983 Extreme picosecond pulse narrowing by means of soliton effect in single-mode optical fibers *Opt. Lett.* **8** 289–91
[34] Weitenberg J, Saule T, Schulte J and Rubbuldt P 2017 Nonlinear pulse compression to sub-40 fs at 4.5 μJ pulse energy by multi-pass-cell spectral broadening *IEEE J. Quantum Electron.* **53** 8600204
[35] Song J, Wang Z, Renchong L, Xianzhi W, Teng H, Zhu J and Wei Z 2021 Generation of 172 fs pulse from a Nd:YVO4 picosecond laser by using multi-pass-cell technique *Appl. Phys. B* **127** 50
[36] Seidel M *et al* 2022 Ultrafast MHz-rate burst-mode pump-probe laser for the FLASH FEL facility based on nonlinear compression of ps-level pulses from an yb-amplifier chain *Laser Photon. Rev.* **16** 2100268
[37] Silletti L *et al* 2023 Dispersion-engineered multi-pass cell for single-stage post-compression of an ytterbium laser *Opt. Lett.* **48** 1842–5
[38] Ueffing M, Reiger S, Kaumanns M, Pervak V, Trubetskov M, Nubbemeyer T and Krausz F 2018 Nonlinear pulse compression in a gas-filled multipass cell *Opt. Lett.* **43** 2070–3
[39] Viotti A L, Alisauskas S, Wahid A B, Balla P, Schirmel N, Manschwetus B, Hartl I and Heyl C M 2021 60 fs, 1030 nm FEL pump-probe laser based on a multi-pass post-compressed Yb:YAG source *J. Synchrotron Radiat.* **28** 36–43

[40] Kaumanns M, Kormin D, Nubbemeyer T, Pervak V and Karsch S 2021 Spectral broadening of 112 mJ, 1.3 ps pulses at 5 kHz in a LG10 multipass cell with compressibility to 37 fs *Opt. Lett.* **46** 929–32
[41] Feng C, Xu X and Diels J-C 2014 Generation of 300 ps laser pulse with 1.2 J energy by stimulated Brillouin scattering in water at 532 nm *CLEO: 2014* SM2F.7 (https://doi.org/10.1364/CLEO_SI.2014.SM2F.7)
[42] Kafka J D, Kolner B H, Baer T and Bloom D M 1984 Compression of pulses from a continuous-wave mode-locked Nd:YAG laser *Opt. Lett.* **9** 505
[43] Steinmetz A, Eidam T, Nodop D, Limpert J and Tünnermann A 2011 Nonlinear compression of Q-Switched laser pulses to the realm of ultrashort durations *Opt. Express* **19** 3758–64
[44] Steinmetz A, Jansen F, Stutzki F, Lehneis R, Limpert J and Tünnermann A 2012 Sub-5-ps, multimegawatt peak-power pulses from a fiber-amplified and optically compressed passively Q-switched microchip laser *Opt. Lett.* **37** 2550–2
[45] Niemz M H 1995 Threshold dependence of laser-induced optical breakdown on pulse duration *Appl. Phys. Lett.* **66** 1181–3
[46] Atkočaitis E, Smalakys L and Melninkaitis A 2022 Pulse temporal scaling of lidt for anti-reflective coatings deposited on lithium triborate crystals *Opt. Express* **30** 28401
[47] Couairon A, Brambilla E, Corti T, Majus D, Ramirez-Gongora O and Kolesik M 2011 Practitioner's guide to laser pulse propagation models and simulation *Eur. Phys. J. Spec. Top.* **199** 5–76
[48] Robert C 2007 Simple, stable and compact multiple-reflection optical cell for very long optical paths *Appl. Opt.* **46** 5408–18
[49] Schönberg A *et al* 2025 Compact, folded multi-pass cells for energy scaling of post-compression *Photon. Res.* **13** 761
[50] Glebov L, Smirnov V, Rotari E, Cohanoschi I, Glebova L, Smolski O, Lumeau J, Lantigua C and Glebov A 2014 Volume-chirped bragg gratings: monolithic components for stretching and compression of ultrashort laser pulses *Opt. Eng., Bellingham* **53** 051514
[51] Corless J D, West J A, Bromage J and Stroud C R 1997 Pulsed single-mode dye laser for coherent control experiments *Rev. Sci. Instrum.* **68** 2259–64
[52] Chiao R Y, Townes C H and Stoicheff B P 1964 Stimulated Brillouin Scattering and Coherent Generation of Intense Hypersonic Waves *Phys. Rev. Lett.* **12** 592–5
[53] Armandillo E and Proch D 1983 Highly efficient, high-quality phase-conjugate reflection at 308 nm using stimulated Brillouin scattering *Opt. Lett.* **8** 523–5
[54] Agrawal G P 2013 *Nonlinear fiber optics Engineering Professional Collection* 5th edn (Academic)
[55] Hanna M, Daher N, Guichard F, Délen X and Georges P 2020 Hybrid pulse propagation model and quasi-phase-matched four-wave mixing in multipass cells *J. Opt. Soc. Am. B* **37** 2982–8
[56] Escoto E, Viotti A-L, Alisauskas S, Tünnermann H, Hartl I and Heyl C M 2022 Temporal quality of post-compressed pulses at large compression factors *J. Opt. Soc. Am. B* **39** 1694–702
[57] Escoto E, Pressacco F, Jiang Y, Rajhans S, Khodakovskiy N, Hartl I, Seidel M, Heyl C M and Tünnermann H 2024 Improved temporal characteristics for post-compressed pulses via application-tailored nonlinear polarization ellipse rotation *Opt. Lett.* **49** 6841–4
[58] Pfaff Y. et al 2022 Nonlinear pulse compression of a thin-disk amplifier and contrast enhancement via nonlinear ellipse rotation *Opt. Express* **30** 10981–90
[59] Benner M, Karst M, Mendez C A, Stark H and Limpert J 2023 Concept of enhanced frequency chirping for multi-pass cells to improve the pulse contrast *J. Opt. Soc. Am. B* **40** 301–5
[60] Nguyen D, Piracha M U, Mandridis D and Delfyett P J 2011 Dynamic parabolic pulse generation using temporal shaping of wavelength to time mapped pulses *Opt. Express* **19** 12305–11
[61] Monmayrant A, Weber S and Chatel B 2010 A newcomer's guide to ultrashort pulse shaping and characterization *J. Phys. B: At. Mol. Opt. Phys.* **43** 103001
[62] Lefort C, Kalashyan M, Ducourthial G, Mansuryan T, O'Connor R P and Louradour F 2014 Sub-30-fs pulse compression and pulse shaping at the output of a 2-m-long optical fiber in the near-infrared range *J. Opt. Soc. Am. B* **31** 2317–24
[63] Rogers C E and Gould P L 2016 Nanosecond pulse shaping at 780 nm with fiber-based electro-optical modulators and a double-pass tapered amplifier *Opt. Express* **24** 2596–606
[64] Meijer R A, Stodolna A S, Eikema K S E and Witte S 2017 High-energy Nd:YAG laser system with arbitrary sub-nanosecond pulse shaping capability *Opt. Lett.* **42** 2758–61
[65] Sooy W R 1965 The natural selection of modes in a passive Q-switched laser *Appl. Phys. Lett.* **7** 36–37
[66] Bai Z, Yuan H, Liu Z, Xu P, Gao Q, Williams R J, Kitzler O, Mildren R P, Wang Y and Lu Z 2018 Stimulated Brillouin scattering materials, experimental design and applications: A review *Opt. Mater.* **75** 626–45
[67] Keaton G L, Leonardo M J, Byer M W and Richard D J 2014 Stimulated Brillouin scattering of pulses in optical fibers *Opt. Express* **22** 13351–65
[68] Stolen R H, Tomlinson W J, Haus H A and Gordon J P 1989 Raman response function of silica-core fibers *J. Opt. Soc. Am. B* **6** 1159
[69] Nakashima T, Nakazawa M, Nishi K and Kubota H 1987 Effect of stimulated Raman scattering on pulse-compression characteristics *Opt. Lett.* **12** 404–6

Journal of Physics: Photonics

SUPPLEMENT

Supplementary material for Post-compression of a Q-switched laser in a glass-rod multi-pass cell

Peer Biesterfeld[1,†], Arthur Schönberg[2,†], Marc Seitz[3,†], Nayla Jimenez[2,4,5], Tino Lang[2], Marcus Seidel[2,4,5], Prannay Balla[2], Lutz Winkelmann[2], Jyothish K. Sunny[1], Sven Fröhlich[1], Philip Mosel[1], Ingmar Hartl[2], Francesca Calegari[3,6,7], Uwe Morgner[1,8], Milutin Kovacev[1,8], Christoph M. Heyl[2,4,5,‡] and Andrea Trabattoni[1,3,8,‡,*]

[1] Leibniz University Hannover, Institute of Quantum Optics, Welfengarten 1, 30167 Hannover, Germany
[2] Deutsches Elektronen-Synchrotron DESY, Notkestraße 85, 22607 Hamburg, Germany
[3] Center for Free-Electron Laser Science CFEL, Deutsches Elektronen-Synchrotron DESY, Notkestraße 85, 22607 Hamburg, Germany
[4] Helmholtz-Institute Jena, Fröbelstieg 3, 07743 Jena, Germany
[5] GSI Helmholtzzentrum für Schwerionenforschung GmbH, Planckstraße 1, 64291 Darmstadt, Germany
[6] Department of Physics, Universität Hamburg, 22761 Hamburg, Germany
[7] The Hamburg Centre for Ultrafast Imaging, Universität Hamburg, 22607 Hamburg, Germany
[8] Cluster of Excellence PhoenixD (Photonics, Optics, and Engineering-Innovation Across Disciplines), 30167 Hannover, Germany

[†]These authors contributed equally to this work.
[‡]These authors contributed equally to this work.
[*]Author to whom any correspondence should be addressed.

E-mail: andrea.trabattoni@desy.de

Keywords: Post-compression, Nonlinear optics, Ultrafast lasers, Ultrafast optics, Multi-pass cells

S1 Characterising the beam quality

Maintaining the beam quality is an important characteristic of an MPC. In our experiment, the beam quality is measured before and after the nMPC, showing a slight degradation of the mean M^2 from 1.31 to 1.45 (Fig. S1). This is potentially caused by the beam passing through the surface of the FS bulk with an angle at each pass. This problem could potentially be mitigated by the proposed all-bulk MPC, which would eliminate the need for surface passes. We observed an improving output beam quality with increasing power.

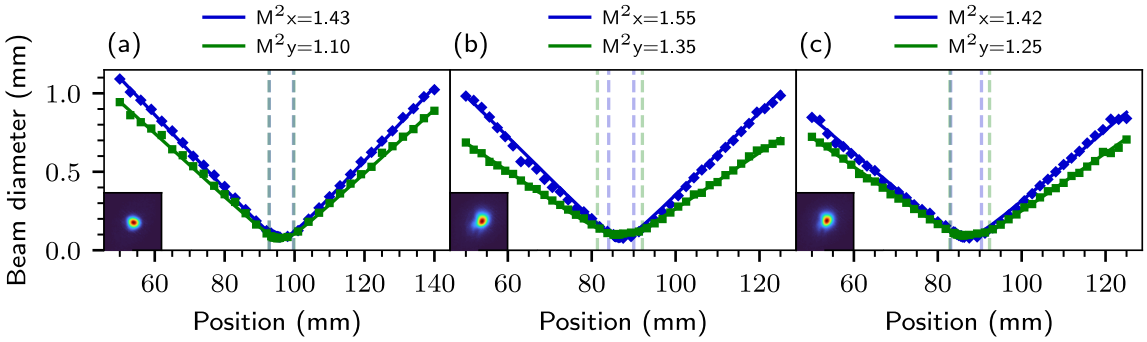


Figure S1: **Spatial beam quality characterization.** Beam quality measurement of MPC input (a), output (b) and output without Etalon at 1.35 mJ input energy (c). The panels include the corresponding beam profiles at the focus position (insets).

S2 Influence of additional longitudinal laser modes in post-compression schemes

Unlike mode-locked lasers, Q-switched lasers typically emit non-phase-locked secondary longitudinal modes (LM). These modes can distort the SPM process as secondary modes cause distortions of the temporal pulse envelope. This can be critical even if only a very small fraction of the energy is emitted in weak additional modes. For the passively Q-switched laser used in our experiment, the manufacturer specifies the single LM operation as having an energy part of less than 0.1% in different

LMs. In our simulation, we observed good agreement with the experimental results for a single second mode that contained 0.01% of the pulse energy.

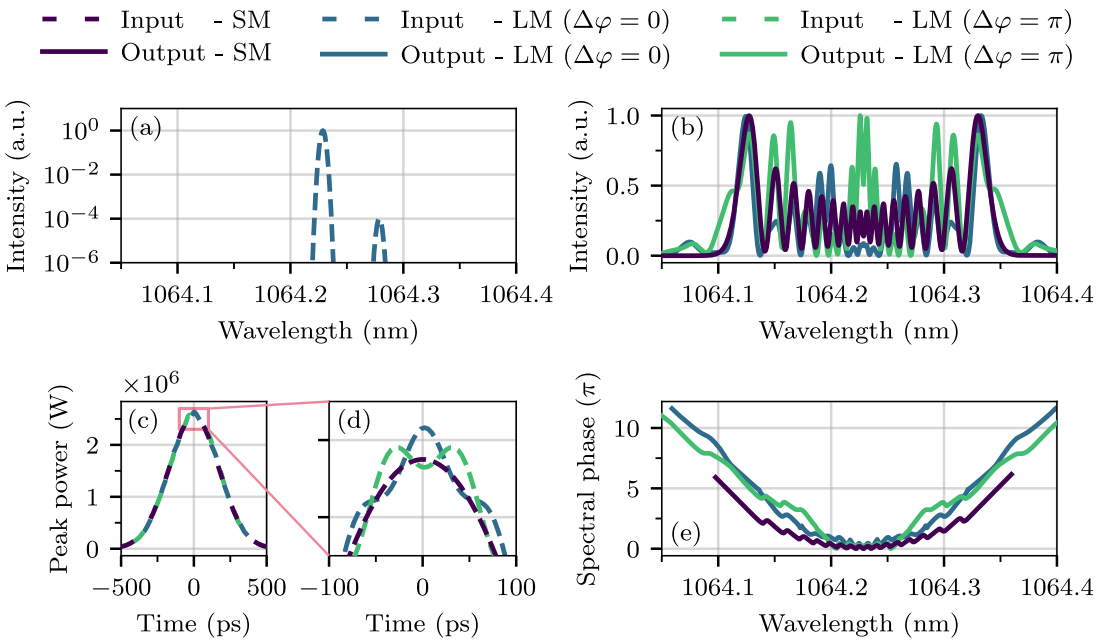


Figure S2: **Simulation results visualizing the influence of a secondary longitudinal mode on the compressibility of the MPC output.** (a) Input spectrum with a secondary longitudinal mode (LM) with 0.01% of the energy (b) Spectral broadening performance for single longitudinal mode operation (SM) and for secondary LM operation. The broadening is shown for two different relative phases $\Delta\varphi$ between the LMs. (c,d) Temporal Intensity profile, with oscillations caused by interference with the second LM. (e) From SPM generated spectral phase, which has to be compensated for compression.

Figure S2(a) shows an example of a single secondary LM separated by 50 pm. Although the interference modulates the temporal pulse envelope by only a few percent (Fig. S2(c, d)), our simulations reveal that the broadened spectra are distorted with a strong dependence on the respective inter-mode phase (Fig. S2(b)), compared to the single-mode case. Figure S2(d) displays the spectral phase of the three cases, where only the single-mode operation indicates a spectral phase that fits a parabola closely, thus enabling compression by GDD compensation.

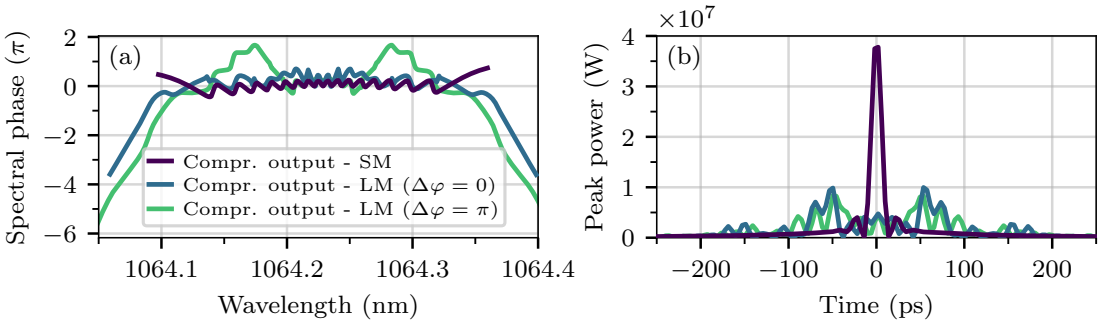


Figure S3: **Influence of secondary LM's on compressibility of the MPC output.** (a) Remaining spectral phase after GDD compensation. (b) Corresponding compressed output pulses.

Figure S3(a) shows the spectral phase after GDD compensation. It is evident that the outer spectral components, in particular, hinder successful pulse compression. The corresponding compressed pulses are displayed in Figure S3(b), where temporal break-up is observed in cases where a weak second mode is present. This demonstrates that, to achieve high compression factors and a well-defined output pulse, the system must operate in a single mode. In this work, single-mode operation is ensured by using a Fabry-Pérot etalon. In our experiment, the effect discussed here was

observed, and it prevented compression close to the Fourier transform limit (FTL) in the absence of the etalon.

S3 Estimation of Stimulated Brillouin Scattering (SBS)

While SBS can be used as the main nonlinear process for pulse compression of long pulses - typically 10 ns or longer down to below 1 ns [1, 2] - it is detrimental for spectral broadening through SPM. For pulses that are longer than the phonon lifetime of the material $\tau \gg T_B$ (for fused silica $T_B \simeq 5\,\mathrm{ns}$), the SBS threshold peak intensity I_{th} can be calculated using the steady-state SBS gain coefficient g_B and the threshold parameter Θ [3]. This material-dependent quantities and the interaction length L define the single-pass peak intensity threshold as [4]:

$$I_{\mathrm{th}} = \frac{\Theta}{g_B \cdot L} \approx \frac{\Theta}{g_B \cdot z_R}, \quad \tau \gg 2z_R/v_{\mathrm{g}}, \tag{S1}$$

Here $L \approx z_{\mathrm{R}}$ denotes the interaction length, z_{R} the Rayleigh length and v_{g} the group velocity of the pulse. For the transient Brillouin scattering regime, i.e., when the pulse duration is shorter than the phonon lifetime, the temporal interaction decreases, thus increasing the threshold intensity. In this regime, SBS can be modeled using numerical methods that have been developed for optical fibers. Here, the threshold peak intensity scales with pulse duration as [4]:

$$I_{\mathrm{th}} = \frac{2\Theta}{g_B v_{\mathrm{g}} \tau} \left(\frac{T_B \Theta}{\tau} + 1 \right), \quad \tau \leq 2L/v_{\mathrm{g}}. \tag{S2}$$

In order to quantify this intensity threshold for the nMPC, we define an effective intensity I_{eff} of a single pass through the nMPC, that would produce the same nonlinearity, i.e., the same B-integral, as propagation in a fiber with the corresponding constant mode size:

$$B_{\mathrm{pass}} = \frac{2\pi}{\lambda} n_2 L_{\mathrm{MPC}} I_{\mathrm{eff}} \tag{S3}$$

Considering the basic geometry of an MPC filled with a nonlinear medium, the B-integral can be written as [5]:

$$B_{\mathrm{pass}} = 4\pi^2 \frac{n_2 P}{\lambda^2} \frac{k}{N} \tag{S4}$$

Using equations S3 and S4, we obtain the effective intensity:

$$I_{\mathrm{eff}} = \frac{\pi P\, n}{\lambda\, L_{\mathrm{MPC}}} \frac{k}{N} \tag{S5}$$

Here, P denotes the pulse peak power and n the refractive index. The MPC configuration is defined by the cell length L_{MPC}, the number of round trips N, and by the re-entrance condition defined by the integer k. For a given set of material parameters, the SBS threshold intensity can be calculated in terms of interaction length (eq. S1) and pulse duration (eq. S2). This threshold can then be compared to the effective Intensity in the MPC using equation S5.

Figure S4 shows the impact of SBS in a fused silica nMPC for input pulse durations from 0.1 ns to 100 ns. For parameters that lay under the curves in Figure S4, the contribution of SBS is negligible, as in the case of our experimental demonstration. For the same MPC configuration as used in the experiment, a sufficient single-pass B-integral of at least $\geq 0.1\pi$ could be achieved with an input laser pulse duration of up to 6 ns. For longer pulse durations, a large number of passes would be needed to compensate for the low single-pass B-integral. Alternatively, the SBS component needs to be attenuated after each pass.

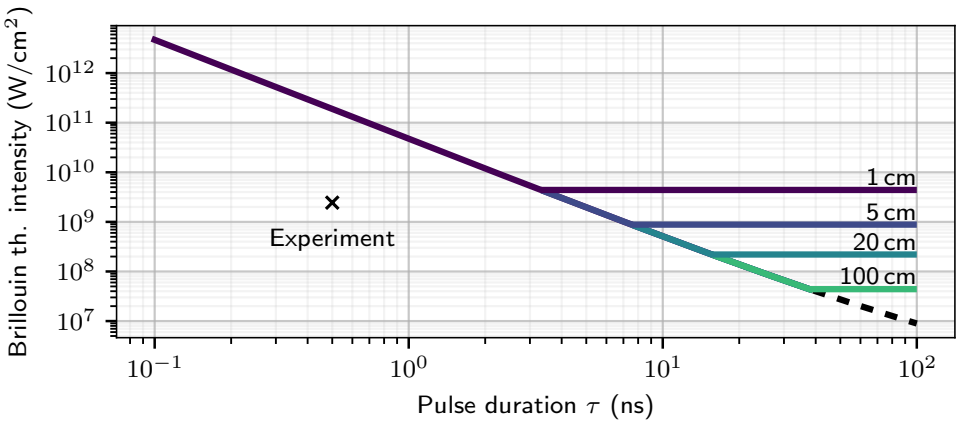


Figure S4: **SBS threshold in an nMPC**. The dependence of the Brillouin threshold intensity is plotted as a function of the input pulse duration (eq. S2). For long pulses, the threshold is dominated by the interaction length (eq. S1). Our experimental parameters are far below the SBS threshold (eq. S5). The following parameters were used: $g_B = 5\,\mathrm{cm/GW}$, $T_B = 5\,\mathrm{ns}$, $n_{\mathrm{FS}} = 1.45$, $\Theta = 22$ and $n_2 = 2.19 \cdot 10^{-16}\,\mathrm{cm^2/W}$ [4, 6–8].

S4 Simulation of Stimulated Raman scattering (SRS)

The threshold intensity above which SRS becomes significant depends on the pulse duration and material-dependent parameters. It can be heuristically defined as [6]:

$$I_{\mathrm{th}}^{\mathrm{SRS}} = \frac{32}{L_{\mathrm{W}}\, g_{\mathrm{R}}}\,. \tag{S6}$$

Here, g_{R} is the Raman gain parameter, which is approximately $g_{\mathrm{R}} = 1 \cdot 10^{-13}\,\mathrm{m/W}$ for 1 µm wavelength in fused silica [6]. $L_{\mathrm{W}} = \tau/|v_{\mathrm{gp}}^{-1} - v_{\mathrm{gs}}^{-1}|$ is the so-called walk-off length, after which the pump and Stokes pulses temporally walk off, thus limiting further Raman gain with v_{gp}, v_{gs} defining the group velocities of the pump and the generated Stokes pulse, respectively. In the case of nanosecond pulses, L_{W} is long and $I_{\mathrm{th}}^{\mathrm{SRS}}$ small, thus defining a severe constraint for the achievable SPM spectral broadening. However, as shown in the main manuscript and in Fig. S5, suitably nMPC mirrors can act as a spectral filter introducing a loss for the Stokes wave. A moderate SRS attenuation of 30% per pass is already sufficient to fully suppress the overall SRS contribution. Considering the THz-level frequency shift of the SRS Stoke wave, the production of such optical coatings is fully feasible [9].

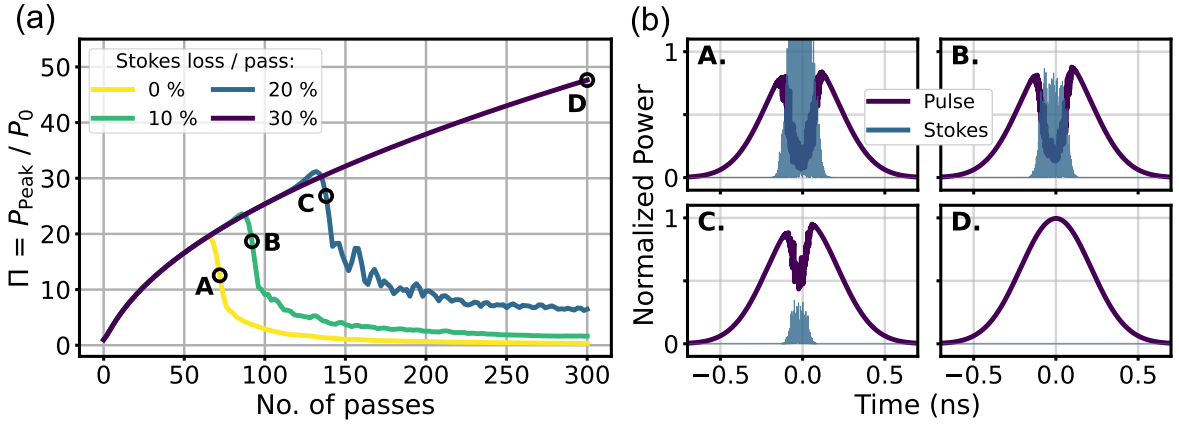


Figure S5: **Impact of SRS in an nMPC for different Stokes losses**. (a) Simulated peak power enhancement $\Pi = P_{\mathrm{peak}}\,/\,P_0$ after spectral broadening of 1 mJ, 0.5 ns pulses in an all-bulk fused silica nMPC with $N = 150$, $k = 91$, $R = 0.1\,\mathrm{m}$. P_{peak} is calculated by applying the optimized GDD to the output pulses. P_0 denotes the input peak power. The figure displays Π for different values of loss applied per pass to the stokes pulse. (b) Uncompressed pulses and Stokes fields for different Stokes losses corresponding to the data displayed in (a). The displayed data correspond to different number of passes in the nMPC, as indicated with circles in (a).

Below, we describe the numerical model used for the SRS simulation. For computational cost reasons, we use a (1+1)D model that takes temporal effects into account, while the spatial dimension is modeled using the ray-transfer matrix formalism. For the nonlinear propagation including SRS, we follow the same approach as described in ref. [10] (eqs. (10) and (11)), defining the two coupled equations for pump and Stokes fields. We modify the equations slightly, omitting the last term in both equations, which describes spontaneous Raman scattering. Further, we include the full linear dispersion. The two coupled equations read as:

$$\begin{aligned}\frac{\partial u_p}{\partial z} + iDu_p = i\gamma_p(1-f_R)u_p\left(|u_p|^2+2|u_s|^2\right) + \\ + \; i\gamma_p f_R u_p \int_{-\infty}^{\infty} h_R(t-t')\left[|u_p(t')|^2+|u_s(t')|^2\right]dt' \\ + \; i\gamma_p f_R u_s \int_{-\infty}^{\infty} h_R(t-t')u_p(t')u_s^*(t')\exp[i\Omega_R(t-t')]dt'\end{aligned}$$

$$\begin{aligned}\frac{\partial u_s}{\partial z} + iDu_s = i\gamma_s(1-f_R)u_s\left(|u_s|^2+2|u_p|^2\right) + \\ + \; i\gamma_s f_R u_s \int_{-\infty}^{\infty} h_R(t-t')\left[|u_s(t')|^2+|u_p(t')|^2\right]dt' \\ + \; i\gamma_s f_R u_p \int_{-\infty}^{\infty} h_R(t-t')u_s(t')u_p^*(t')\exp[-i\Omega_R(t-t')]dt' \;,\end{aligned}$$

where u_i, $i = p, s$ (pump and Stokes, respectively) are the fields in the temporal domain, normalized such that the power $P_i(t) = |u_i|^2$. The dispersion operator D includes all dispersion orders, incorporated by solving the left-hand side of the equations in the frequency domain and using refractive index data of fused silica [11]. Further, γ_i is the nonlinear coupling parameter which is proportional to the nonlinear refractive index n_2, defined in ref. [10]. We use $n_2 = 2.19 \cdot 10^{-20}\,\mathrm{m^2/W}$ [12] for the nonlinear refractive index of fused silica. Finally, $f_\mathrm{R} = 0.18$ is the Raman fraction of fused silica [10], and $h_\mathrm{R}(t)$ is the delayed response function of the SRS interaction in the temporal domain.

To determine $h_\mathrm{R}(t)$, we use the data for the response function in the frequency domain $\hat{h}_R(\omega)$ provided in ref. [10, 13] and fit a simplified model $f_h(\omega) = a \cdot \omega \cdot \exp\left[-(b\cdot\omega)^8\right]$ with the fitting parameters a, b to the imaginary part. We calculate the real part using the Kramers-Kronig relationship, while ensuring normalization $\int_{-\infty}^{-\infty} f_h(t)\,dt = 1$ [10]. Figure S6 shows the response functions in the temporal and frequency domains.

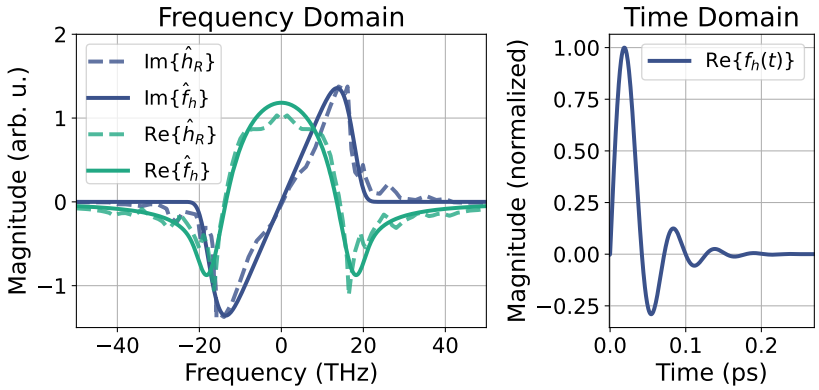


Figure S6: **Raman gain of fused silica**. The data for the delayed response function of the SRS interaction in frequency domain $\hat{h}_R(\omega)$ are taken from ref. [10]. The fitted functions $\hat{f}_h(\omega)$ in the frequency domain and $f_h(t)$ in the time domain are used in the simulations.

The Stokes field is initialized with a random noise following a Gaussian distribution using the one-photon-per-mode method [6]. We solve the model using a coupled Runge-Kutta-4 split-step algorithm on a $2^{18} = 262144$ temporal/spectral grid with a temporal window of $[-1.27, 1.27]$ ns and a step size $dz = 0.00246$ m.

S5 Quasi-Phase-Matched Four-Wave-Mixing (QPM-FWM) simulations

Quasi-Phase-Matched Four-Wave-Mixing (QPM-FWM) can occur at large spectral broadening factors in MPCs, as discussed in ref. [14]. Following ref. [14], we performed (1+1)D simulations to quantify the possible contribution of QPM-FWM in a nMPC. A 0.5 ns, 1 mJ pulse is propagated in a full-bulk fused silica nMPC, with $R = 10\,\text{cm}$, $N = 150$, $k = 91$, resulting in $2N = 300$ passes. Figure S7(a)-(c) shows the impact of QPM-FWM on the broadened spectrum after 1, 100, and 270 passes through the nMPC. Spectral side bands appear at specific wavelengths, which are determined by the dispersion landscape of the nMPC. More specifically, QPM-FWM occurs at wavelengths for which the phase-matching condition $\Delta\phi = (2k_1 - k_2 - k_3)L_{\text{MPC}} = n2\pi$ (n integer) applies after one pass, where $k(\omega_i) \equiv k_i$ is the wave-number, $i = 1$ denotes the fundamental wavelength and $i = 2, 3$ the FWM components [14].

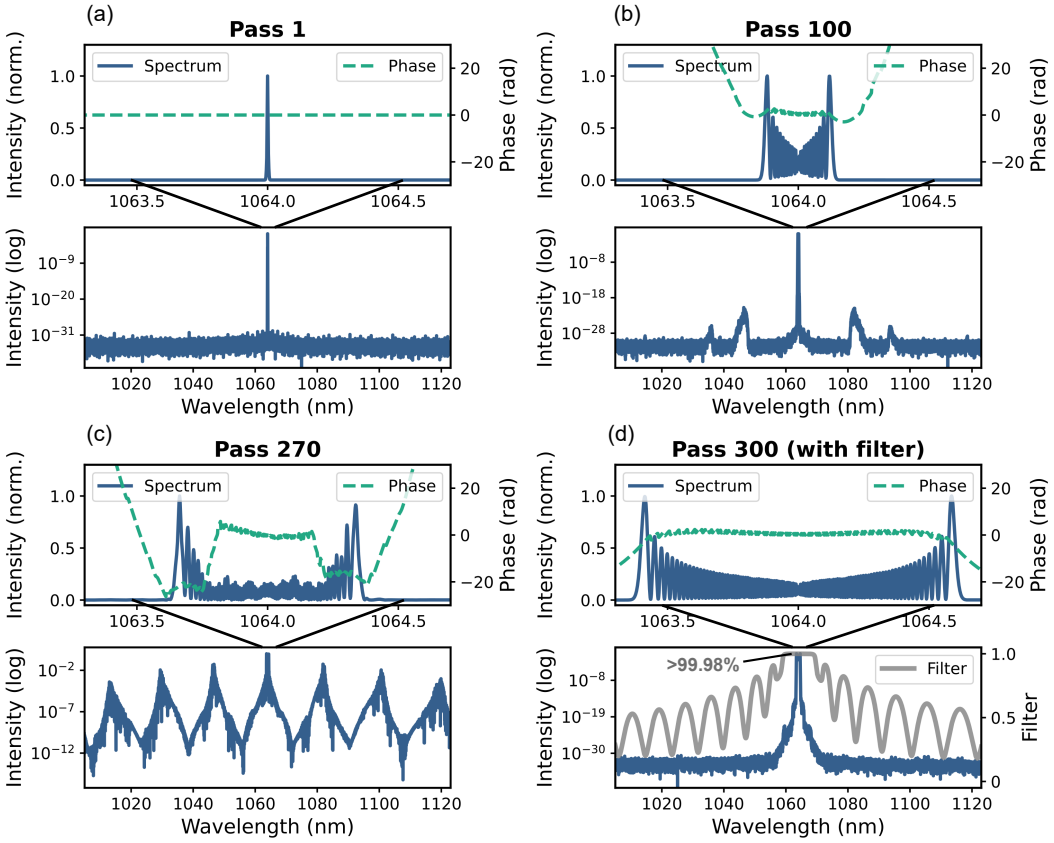


Figure S7: **Impact of QPM-FWM in an nMPC**. The QPM-FWM contribution is simulated after (a) 1, (b) 100, and (c) 270 passes without using a spectral filter. (d) Plot of the broadened spectrum applying a spectral filter after each pass. In each of the Figures (a)-(d), the spectrum is plotted in linear scale (upper plot) and logarithmic scale (lower plot, zoomed view of upper plot).The spectral phase is plotted after subtracting the GDD, optimized for the highest peak power. The gray line in (d), lower panel visualizes the spectral filter.

Figure S7(c) clearly shows a large energy transfer to the FWM spectral components and a distortion of the main spectrum. Furthermore, the phase exhibits discontinuities which cannot be compensated via simple removal of group-delay-dispersion (GDD), resulting in an incompressible pulse in the time domain. To suppress both SRS and QPM-FWM, we apply a spectral filter at each reflection at the nMPC mirror in the simulation. Figure S7(d) shows that the contributions of QPM-FWM and SRS are fully suppressed by the spectral filter, resulting in a clean and compressible SPM-broadened spectrum. The spectral filter consists of two dielectric multi-layer mirror coatings, one with a central wavelength offset to the longer and one to the shorter side of the spectrum. The effective filter per round-trip in the nMPC is shown in Fig. S7(d). After GDD removal, the phase is smooth without discontinuities.

References

1. Feng, C., Xu, X. & Diels, J.-C. Generation of 300 ps laser pulse with 1.2 J energy by stimulated Brillouin scattering in water at 532 nm. *CLEO: 2014,* SM2F.7. https://opg.optica.org/abstract.cfm?URI=CLEO_SI-2014-SM2F.7 (2014).
2. Feng, C., Xu, X. & Diels, J.-C. High-energy sub-phonon lifetime pulse compression by stimulated Brillouin scattering in liquids. *Opt. Express* **25,** 12421–12434. https://opg.optica.org/oe/abstract.cfm?URI=oe-25-11-12421 (2017).
3. Chen, B. *et al.* Gain characteristics of stimulated Brillouin scattering in fused silica. *Opt. Express* **31,** 5699–5707. https://opg.optica.org/oe/abstract.cfm?URI=oe-31-4-5699 (2023).
4. Keaton, G. L., Leonardo, M. J., Byer, M. W. & Richard, D. J. Stimulated Brillouin scattering of pulses in optical fibers. *Opt. Express* **22,** 13351–13365. https://opg.optica.org/oe/abstract.cfm?URI=oe-22-11-13351 (2014).
5. Viotti, A.-L. *et al.* Multi-pass cells for post-compression of ultrashort laser pulses. *Optica* **9,** 197–216. https://opg.optica.org/optica/abstract.cfm?URI=optica-9-2-197 (2022).
6. Agrawal, G. P. *Nonlinear fiber optics* 5th ed. Includes bibliographical references and index. 629 pp. ISBN: 9780123970237 (Academic Press, Oxford, 2013).
7. Boyd, R. W. *Nonlinear optics* Fourth edition. 1609 pp. ISBN: 9780128110034 (Elsevier, AP Academic Press, London, 2020).
8. Kabaciński, P., Kardaś, T. M., Stepanenko, Y. & Radzewicz, C. Nonlinear refractive index measurement by SPM-induced phase regression. *Opt. Express* **27,** 11018–11028. https://opg.optica.org/oe/abstract.cfm?URI=oe-27-8-11018 (2019).
9. Paschotta, R. *Dielectric Mirrors* RP Photonics Encyclopedia. 2005. https://www.rp-photonics.com/dielectric_mirrors.html (2025).
10. Headley, C. & Agrawal, G. P. Unified description of ultrafast stimulated Raman scattering in optical fibers. *Journal of the Optical Society of America B* **13,** 2170. ISSN: 1520-8540 (1996).
11. Malitson, I. H. Interspecimen Comparison of the Refractive Index of Fused Silica*,†. *Journal of the Optical Society of America* **55,** 1205. ISSN: 0030-3941 (1965).
12. Kabaciński, P., Kardaś, T. M., Stepanenko, Y. & Radzewicz, C. Nonlinear refractive index measurement by SPM-induced phase regression. *Opt. Express* **27,** 11018–11028. https://opg.optica.org/oe/abstract.cfm?URI=oe-27-8-11018 (2019).
13. Stolen, R. H., Tomlinson, W. J., Haus, H. A. & Gordon, J. P. Raman response function of silica-core fibers. *Journal of the Optical Society of America B* **6,** 1159. ISSN: 1520-8540 (1989).
14. Hanna, M., Daher, N., Guichard, F., Délen, X. & Georges, P. Hybrid pulse propagation model and quasi-phase-matched four-wave mixing in multipass cells. *J. Opt. Soc. Am. B* **37,** 2982–2988. https://opg.optica.org/josab/abstract.cfm?URI=josab-37-10-2982 (2020).

C Appendix: Efficient Broadband Second-Harmonic Generation in a Multi-Pass Cell

arXiv:2607.03192v1 [physics.optics] 3 Jul 2026

Efficient broadband second-harmonic generation in a multi-pass cell

Arthur Schönberg[1,*], Nikolas Rupp[1], Ana Oliveira e Silva[1,2], Lorenzo Pratolli[1,2], Yujiao Jiang[1], Vincent Wanie[2,3], Terence Mullins[2,3], Francesca Calegari[1,2,3], and Christoph M. Heyl[1,4,5]

[1] *Deutsches Elektronen-Synchrotron DESY, Notkestr. 85, 22607 Hamburg, Germany*
[2] *Center for Free-Electron Laser Science CFEL, Deutsches Elektronen-Synchrotron DESY, Notkestr. 85, 22607 Hamburg, Germany*
[3] *The Hamburg Centre for Ultrafast Imaging, Universität Hamburg, Luruper Chaussee 149, 22761 Hamburg, Germany*
[4] *Helmholtz-Institut Jena, Fröbelstieg 3, 07743 Jena, Germany*
[5] *GSI Helmholtzzentrum für Schwerionenforschung GmbH, Planckstraße 1, 64291 Darmstadt, Germany*
[*] *arthur.schoenberg@desy.de*

July 7, 2026

Abstract

Second-harmonic generation (SHG) is a widely used nonlinear optical process which has been optimized for high frequency conversion efficiency, broad bandwidths as well as optimum spatial and temporal quality of the generated light. However, limitations of the generation efficiency arise due to temporal dispersion and pulse walk-off effects introduced by the nonlinear crystal. To circumvent these limitations, quasi-waveguide schemes, in particular multi-pass cells (MPCs), can be employed, providing flexible phase-tuning capabilities. In this work, we demonstrate for the first time broadband and efficient SHG in an MPC. SHG efficiencies of 72 % (for 63 fs, 50 µJ pulses) and 47 % (for 15 fs, 20 µJ pulses) are obtained by simultaneously matching the relative phase and group-delay between the fundamental and second-harmonic fields over multiple passes through the MPC. Our work sets a new record for efficient Gaussian-beam, ultra-short pulse SHG and provides a general route to address efficiency-bandwidth limitations of nonlinear optical processes.

1 Introduction

Second-harmonic generation (SHG) was first observed in 1961 [1], shortly after the invention of the laser [2], and has since become a cornerstone of nonlinear optics. Today, SHG is indispensable for producing tunable mid-infrared, visible and ultraviolet radiation [3–13], for ultrafast pulse characterization [14, 15], and for a variety of imaging and frequency-comb applications [16–19]. Efficient $\chi^{(2)}$ conversion hinges on (i) a strong second-order nonlinearity—typically provided by non-centrosymmetric crystals—and (ii) fulfillment of the phase-matching condition [20, 21]. While many $\chi^{(2)}$ processes (SFG, DFG, optical rectification, OPA) share these requirements [22, 23], achieving simultaneous phase and group-delay (GD) matching in broadband, few-cycle regimes remains challenging. Phase-matching can be achieved by various techniques, including type I, type II, noncritical birefringent phase-matching as well as quasi-phase-matching (QPM) [22]. Free-space QPM has also been demonstrated using multi-pass cells [24–26]. However, in the above examples, phase-matching can typically only be achieved for a certain spectral bandwidth, typically determined by the crystal length. This leads to efficiency and bandwidth limits of the frequency-converted pulse [22]. To overcome this challenge, in particular for SHG, methods such as adiabatic frequency conversion [27, 28] and prism-based phase-and group delay matching [29, 30] have been developed. More recent works propose micro-structured fiberbased phase-and GD matching [31]. While constituting promising approaches for efficient SHG, these methods either rely on single- or few-pass free-space geometries or wave-guides, where tunability of the relative phase between SHG and

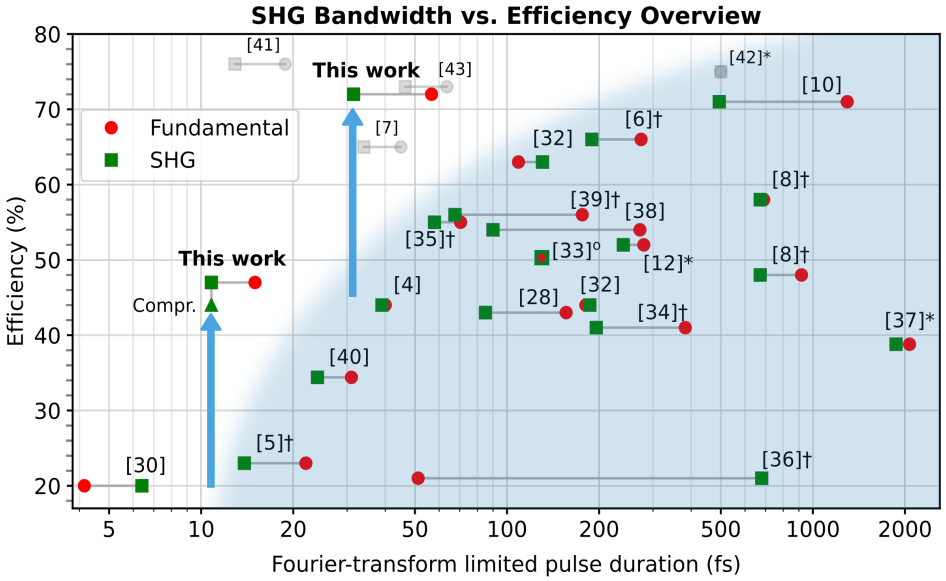


Figure 1: Overview of various works on second-harmonic generation (SHG), relating efficiency to the fundamental (red dots) input and SHG output (green squares) bandwidths, here expressed as the full-width half-maximum (FWHM) of the Fourier-transform limited (FTL) pulses. The green triangle indicates the efficiency after compression of the SH pulse. The gray markers indicate flat-top or non-Gaussian beam systems. The blue arrows indicate the estimated efficiency improvement over the state of the art. †The FTL was calculated using the spectral bandwidth provided in the reference. *The pulse duration was assumed as the FTL, since the reference did not provide the FTL or bandwidth. °No FTL, bandwidth or pulse duration of the SH pulse provided.

fundamental fields remains constrained, leaving the challenge to compromise between efficiency and bandwidth.

Here, we address this challenge by implementing SHG inside a Herriott-type multi-pass cell (MPC), enabling phase and group-delay compensation. A $\chi^{(2)}$ nonlinear crystal is placed in the center of our second-harmonic multi-pass cell (SHG-MPC), enabling SHG for every pass through the MPC. The SHG-MPC operates in a pressure-tunable gas cell filled with air or krypton. Group-delay (GD) compensating mirrors provide $-15\,\mathrm{fs}$ relative GD per reflection between the fundamental and second-harmonic field. Fine tuning of phase and group delay is achieved by adjusting the gas pressure and crystal angle (θ), enabling efficient, broadband SHG, ultimately limited by higher-order dispersion.

To demonstrate the SHG-MPC concept, we investigate two experimental regimes. Using 1030 nm, 63 fs, 50 µJ fundamental pulses and a 78 µm β-BaB_2O_4 (BBO) crystal, we achieve an SHG efficiency of 72%. With shorter 1030 nm, 15 fs, 20 µJ driving pulses and a 95 µm BBO crystal, we obtain 47% SHG efficiency, with 44% retained after compression. In both cases, the generated second-harmonic output exhibits excellent pulse and beam quality. Our results demonstrate that MPCs are versatile tools for efficiently driving and tailoring SHG and potentially other second-order nonlinear processes.

Figure 1 provides an overview over selected SHG works, comparing the bandwidth of the input and output pulses with the achieved conversion efficiencies. For most works, a single-pass generation scheme is used. The trade-off between bandwidth and efficiency is clearly visible, highlighted by the blue background to guide the eye. Compared with the works in Fig. 1, the SHG-MPC results obtained in this work show a notable increase in efficiency. For the two experimental regimes investigated here, the achieved efficiencies exceed the current state of the art by estimated factors of 1.6 and 2.2, respectively.

2 Concept: Second-harmonic-generation in multi-pass cells

The SHG-MPC is characterized by its flexible phase- and amplitude tuning capabilities. This flexibility

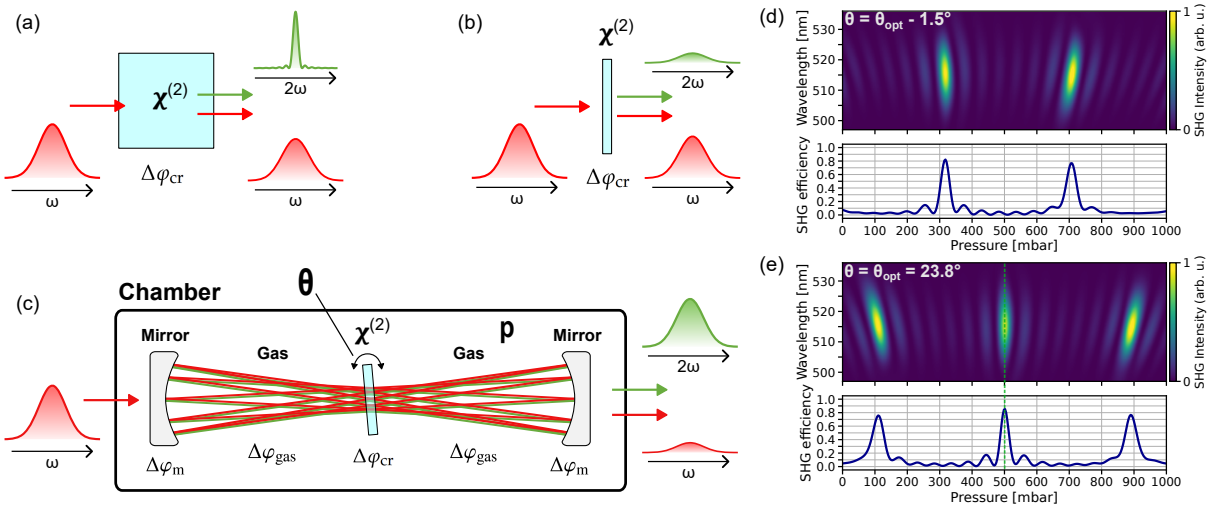


Figure 2: Illustration of the SHG-MPC concept and simulated spectrograms. (a) In a thick crystal, SHG can achieve high conversion efficiency, but the spectral bandwidth is limited by the narrow phase-matching bandwidth. (b) A thin crystal provides a much broader phase-matching bandwidth, but the reduced interaction length lowers the conversion efficiency. (c) Top view of the SHG-MPC, which combines high efficiency and broad bandwidth by appropriately compensating the phase and group-delay (GD) mismatch after each pass through a thin crystal. (d,e) Simulated idealized spectrograms of the spectrally resolved SH pulse as a function of gas pressure for two crystal angles. (d) Relative GD uncompensated. (e) Relative GD compensated. The simulation parameters match the experiment, except that ideal Gaussian beams are used as the fundamental input. The input pulse has a wavelength of 1030 nm, a duration of 30 fs, and an energy of 25 µJ. The MPC parameters are $R = 1\,\mathrm{m}$ (radius of curvature), $N = 4$ round trips ($2N = 8$ passes) through a 100 µm-thick BBO crystal, and a cavity length of $L = 29.5\,\mathrm{cm}$. A relative GD of $-15\,\mathrm{fs}$ is compensated at each mirror reflection, delaying the fundamental pulse. The simulations are performed using the model described in Supplementary Section S1. The optimal phase-matching angle is $\theta_{\mathrm{opt}} = 23.8°$.

stems from the fact that the MPC acts as a quasi-waveguide in which the properties of the pulses can be adjusted at each pass though the cell using appropriate optical elements. In particular, the cavity mirrors can be used to tune the phase and to compensate for the dispersion accumulated in the nonlinear crystal. In addition, two extra tuning parameters are introduced to precisely control the relative phase between the second-harmonic (SH) field and the fundamental field. These parameters are (i) the gas pressure p in the vacuum chamber in which the SHG-MPC is set up and the critical angle θ relative to the optical axis of the (uniaxial) crystal. Figure 2 illustrates the SHG-MPC concept in comparison to single-pass SHG approaches. In Fig. 2(a), a long crystal is used, which narrows the spectral bandwidth of the SHG output but enables highly efficient SHG. In contrast, Fig. 2(b) shows that a thin crystal can convert the full bandwidth, but typically yields low conversion efficiencies due to the reduced interaction length. Fig. 2(c) illustrates the SHG-MPC in which both broad bandwidths and high conversion efficiencies can be achieved by tuning the the relative phases between the SH and fundamental fields.

In the SHG-MPC concept, we focus on the precise tuning of the relative phase (phase-matching) and the relative group-delay (GD-matching) between the SH and the fundamental fields. In a nonlinear, birefringent crystal exhibiting a $\chi^{(2)}$-nonlinearity, phase-matching is typically achieved by propagating the fields in different axes with different dispersion relations $k_i(\omega)$. Here, fundamental and second harmonic fields and the corresponding crystal axes are denoted with $i = 1, 2$, respectively. We define the define the "zeroth"-order wavenumber-mismatch as

$$\Delta k^{(0)} = 2k_1^{(0)}(\bar{\omega}_1) - k_2^{(0)}(\bar{\omega}_2) = \\ = \frac{\bar{\omega}_2}{c_0}\left(n_1(\bar{\omega}_1) - n_2(\bar{\omega}_2)\right), \qquad (1)$$

where $\bar{\omega}_i$ is the central frequency of the respective field, n_i the refractive index and c_0 the speed of light in vacuum. For a given material length L, the

zeroth-order phase-mismatch is $\Delta\phi^{(0)} = \Delta k^{(0)} \cdot L$. In SHG, phase-matching is usually referred to the case when $\Delta k^{(0)} = 0$. In this work, we focus on type I phase-matching, where the fundamental field $i = 1$ is polarized orthogonally to the second-harmonic field $i = 2$. When phase matching is achieved, high conversion efficiencies are typically obtained for relatively narrowband pulses. However, for ultrashort pulses, higher order phase-mismatch terms can become relevant, with the next order being the group-delay (GD) mismatch. The GD wavenumber-mismatch between the fundamental and second-harmonic field can be written as

$$\Delta k^{(1)} = k_1^{(1)}(\bar{\omega}_1) - k_2^{(1)}(\bar{\omega}_2) \ , \tag{2}$$

where the accumulated GD in the medium is $\Delta\varphi^{(1)} = \Delta k^{(1)} \cdot L$. In general, when $\Delta k^{(0)} = 0$, typically $\Delta k^{(1)} \neq 0$, i.e. when the phase is matched, the GD is not necessarily matched simultaneously. In the temporal domain, a GD mismatch results in a temporal walk-off of the fundamental and second-harmonic pulses. In the frequency domain, a GD mismatch appears as a linearly varying spectral phase mismatch, causing different frequency components of the pulses to walk off temporally during propagation. This leads to a narrowing of the acceptance bandwidth of the conversion process for long crystals. Multi-pass cells provide the possibility of tuning the relative phase $\Delta\varphi$ of the two fields after each pass through the crystal, including the zeroth-order phase and the GD, overcoming the acceptance bandwidth limit compared to a single-pass generation scheme. Assuming that the crystal is positioned in the center and both sides of the MPC are symmetric, the relative accumulated phase per pass amounts to

$$\begin{aligned}\Delta\varphi_{\text{pass}}(\omega;\theta,p) &= \\ &= \underbrace{\Delta\varphi_{\text{cr}}(\omega;\theta)}_{\text{Crystal}} + \underbrace{\Delta\varphi_{\text{gas}}(\omega;p)}_{\text{Gas}} + \underbrace{\Delta\varphi_{\text{m}}(\omega)}_{\text{Mirror}}\end{aligned} \tag{3}$$

where we indicate the dependencies of each term on the two tuning parameters in the experiment, which are gas pressure p and the "critical" crystal angle θ relative to the optical axis of the (uniaxial) crystal, as shown in Fig. 2(c). The term $\Delta\varphi_{\text{cr}}(\omega;\theta)$ denotes the relative dispersion induced by propagation through the crystal depending on the angle θ of the wavevector $\vec{k}$ to the optical axis, $\Delta\varphi_{\text{gas}}(\omega;p)$ is the dispersion of the ambient gas depending on pressure p and $\Delta\varphi_{\text{m}}(\omega)$ the phase induced by the mirror. Note that we do not include the relative Gouy-phase contribution, as this is typically negligibly small within the interaction length in the crystal [44].

Equation (3) contains all contributions to the phase-mismatch between fundamental and second-harmonic field. If we consider the zeroth and first order only, Eq. (3) can be expressed as the sum of the phase-mismatch $\Delta\varphi^{(0)} = 2\varphi_1^{(0)} - \varphi_2^{(0)}$ and the GD-mismatch $\Delta\varphi^{(1)} = \varphi_1^{(1)} - \varphi_2^{(1)}$ of each dispersive element in the SHG-MPC. The phase- and group-delay terms of the gas and crystal are obtained from their respective Sellmeier equations, while the contributions from the optics are taken from the coating specifications of the mirrors (see Supplement Fig. S6). Phase-matching occurs when the following condition is fulfilled:

$$\begin{aligned}&\Delta\varphi_{\text{pass}}^{(0)}(\theta,p) = \\ &= \Delta\varphi_{\text{cr}}^{(0)}(\theta) + \Delta\varphi_{\text{gas}}^{(0)}(p) + \Delta\varphi_m^{(0)} \overset{!}{=} 2\pi n \ ,\end{aligned} \tag{4}$$

where n is an integer. At the same time, for the first-order phase terms, the condition

$$\begin{aligned}&\Delta\varphi_{\text{pass}}^{(1)}(\theta,p) = \\ &= \Delta\varphi_{\text{cr}}^{(1)}(\theta) + \Delta\varphi_{\text{gas}}^{(1)}(p) + \Delta\varphi_m^{(1)} \overset{!}{=} 0\end{aligned} \tag{5}$$

needs to be fulfilled to ensure GD matching. The amount of GD that is then required to be compensated by the mirrors can be determined by

$$\Delta\varphi_{\text{m}}^{(1)} = -\left(\Delta\varphi_{\text{cr}}^{(1)}(\theta_{\text{pm}}) + \Delta\varphi_{\text{gas}}^{(1)}(p_{\text{ref}})\right) \ , \tag{6}$$

where θ_{pm} is the phase-matching angle (23.4° for BBO) and p_{ref} the reference pressure of the gas that can be arbitrarily set. In our experiments, we choose $p_{\text{ref}} = 500\,\text{mbar}$ of air, in order to enable a large phase tuning range above and below the GD matching point within the gas pressure tuning range supported by the setup of 0-1 bar. A high conversion efficiency is then achieved by passing through the crystal multiple times.

Figures 2(d,e) show simulated spectrograms and conversion efficiencies of the generated SH signal in a thin BBO crystal as a function of pressure p. In this example, the mirror phase is chosen such that the phase and GD conditions in Eqs. (4) and (5) are simultaneously fulfilled at $p_{\text{opt}} = 500\,\text{mbar}$ and $\theta_{\text{opt}} = 23.8°$. Several main maxima of the SHG signal occur at pressures, where zeroth-order phase-matching condition defined in Eq. (4) is fulfilled. However, phase matching alone is not sufficient for efficient broadband SHG: the relative GD between the fundamental and SH pulses must also be compensated. If the crystal angle θ is not chosen appropriately, as illustrated in Fig. 2(d), the GD condition of

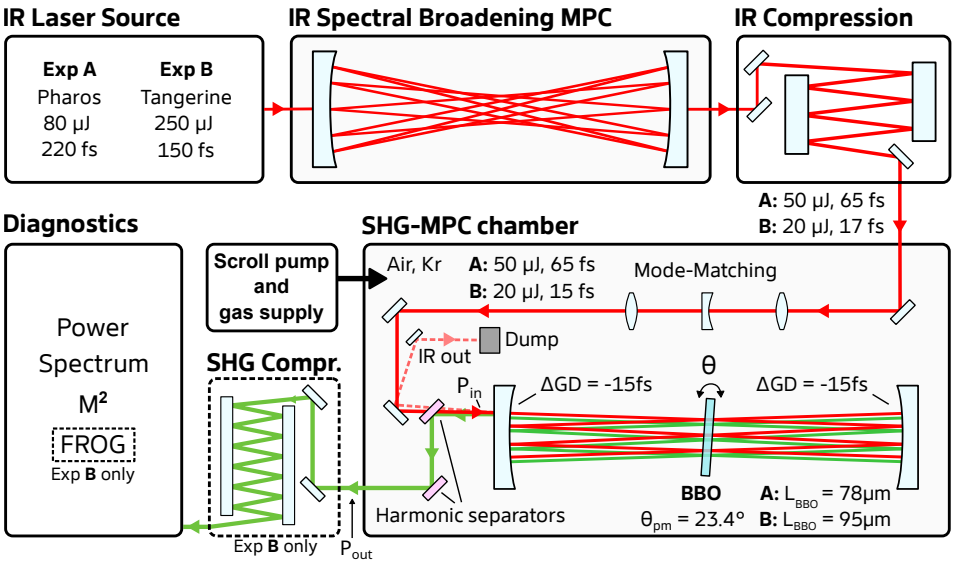


Figure 3: Experimental setup for both the long pulse (Exp A) and the short pulse (Exp B) experiments. Two different laser systems with similar parameters are used. After spectral broadening and post-compression, the pulses are sent into the chamber, where mode-matching and SHG in the SHG-MPC is carried out. Two harmonic separators are used to fully filter out the remaining fundamental light. In Exp B, the SH pulses are compressed using a chirped mirror compressor. The spectrum, M^2 and power is analyzed subsequently. Frequency-resolved optical gating (FROG) measurements are additionally carried out in Exp B.

Eq. (5) is not fulfilled at the phase-matching pressure. In this case, pressure tuning can maximize the phase matching, but the fundamental and SH pulses remain temporally mismatched, limiting the bandwidth and conversion efficiency. By adjusting the crystal angle to θ_{opt}, the GD condition is shifted to coincide with the phase-matching condition at $p_{\mathrm{opt=500\,mbar}}$, as shown in Fig. 2(e). At this point, both phase and GD matching are achieved simultaneously, resulting in broadband and efficient SHG.

Figures 2(d) and (e) furthermore illustrate the dispersion behavior of the SHG-MPC. The three dominant maxima in Fig. 2(e) are separated by approximately 390 mbar, corresponding to a relative phase shift of 2π between the 1030 nm fundamental and the 515 nm SHG field over an MPC length of about 29.5 cm in air. Below 500 mbar, the spectra are tilted toward shorter wavelengths, indicating anomalous dispersion, whereas above this pressure the tilt reverses, corresponding to normal dispersion. Around 500 mbar, where the group velocities are matched, both the conversion efficiency and the generated bandwidth reach their maximum values, indicating simultaneous phase and group-delay matching. Additional weaker maxima and minima arise between the main peaks. The number of these minor peaks is determined by the number of passes through the MPC. A more detailed analytical treatment is provided in reference [44].

3 Experiment and Results

For the experimental demonstration of the broadband SHG-MPC we conduct two experiments with two different pulse durations and bandwidths at 1030 nm wavelength. In the first experiment (referred to as experiment A), we perform SHG of 50 µJ, 63 fs pulses with a Fourier-transform limit (FTL) of about 56 fs. Here we reach a conversion efficiency of 72%. In the second experiment (referred to as experiment B), we perform SHG using 15.4 fs pulses, yielding an FTL of 10 fs with an efficiency of 47%. In experiment B we additionally compress the pulses using chirped mirrors down to 13.8 fs. In both experiments, the fundamental pulses are first post-compressed using a self-phase modulation (SPM) - based MPC post-compression system. In experiment B, the post-compressed laser system developed in reference [45] is used. For the experimental validation of broadband SHG-MPC we investigate two distinct parameter sets at a wavelength of 1030 nm. Experiment A employs 50 µJ, 63 fs fundamental pulses (Fourier-transform limit 56 fs) as the input to the SHG-MPC. Experiment B uses 20 µJ, 15.4 fs funda-

mental pulses (Fourier-transform limit 14.5 fs), with the generated second-harmonic light subsequently compressed. In both configurations the fundamental pulses are first post-compressed in a conventional self-phase-modulation (SPM) multi-pass cell (MPC) [45].

Figure 3 displays the common experimental layout for both configurations. After spectral broadening and compression, the fundamental pulses are directed into the SHG-MPC chamber, that can be filled with the selected gas at pressures ranging from 0 to 1 bar. Inside this chamber, the beam is mode-matched and guided to the SHG-MPC. Before coupling into the SHG-MPC, the beam passes through a first harmonic separator (HS). The SHG-MPC consists of two concave mirrors with a radius-of-curvature (ROC) of $R = 1\,\mathrm{m}$ and is configured to $N = 4$ round-trips (8 passes) with a configuration parameter of $k = 1$ [46]. This corresponds to an MPC length of about $L = 29.5\,\mathrm{cm}$. The mirror coatings are specifically designed to compensate a group-delay (GD) of about $-15\,\mathrm{fs}$ between 1030 nm and 515 nm, which is the relative GD accumulated over a single pass through the MPC including dispersion in the SHG crystal at a reference pressure of 500 mbar of air. As nonlinear crystals two Beta-Barium Borate (β-BaB_2O_4, BBO) crystals with thicknesses of $L_{\mathrm{cr}} = 78\,\mu\mathrm{m}$ and $L_{\mathrm{cr}} = 95\,\mu\mathrm{m}$ are used, both cut to the type I phase-matching angle of $\theta_{\mathrm{pm}} = 23.4°$ used without substrate. The thinner BBO crystal is employed in experiment A, whereas the thicker crystal is used in experiment B, as this configuration experimentally yielded the optimum results. The crystal is placed in the center of the SHG-MPC. In this MPC configuration, the beam is weakly focused and the $1/e^2$ beam sizes are rather small with 385 µm beam radius at the MPC mirrors and 340 µm waist radius in the focus. The BBO crystal is mounted such that the incidence angle θ can be adjusted, i.e. $\theta = \theta_{\mathrm{pm}} + \Delta\theta$, where $\Delta\theta$ is the detuning from the phase-matching angle. After 8 passes through the SHG-MPC and the crystal, both fundamental and SHG beams are coupled out. The fundamental field is filtered using two harmonic separators in order to obtain a pure SHG beam.

We conduct measurements using both air (Experiment A and B) and Krypton (A). In order to record spectrograms as, for example, in Fig. 2(e), we scan the gas pressure of the chamber from about 50 mbar to 1 bar. In these spectrograms, the SHG signal appears as multiple spectrally dependent maxima. While a signal maximum at a fixed wavelength reveals phase-matching between fundamental and SHG fields, the spectral tilt of these maxima is a direct indicator for GD matching. By tuning the crystal angle θ such that the spectrum in one of the maxima appears vertical, GD matching can be achieved. In order to match both phase- and GD, we tune the pressure to the vertical maximum. Afterwards, the SHG beam is characterized using various beam and pulse diagnostics. In experiment B, we further compress the SHG pulse using a pair of chirped mirrors with an average group-delay dispersion (GDD) of $-40\,\mathrm{fs}^2$ per reflection.

A. Long Pulse Conversion

In Experiment A we use post-compressed pulses with 63 fs pulse duration and an FTL of 56 fs. We attenuate the pulse energy to 50 µJ. The repetition rate is set to 4 kHz. Here, we use the short BBO with $L_{\mathrm{cr}} = 78\,\mu\mathrm{m}$ thickness. By recording the spectrum and the output power simultaneously and scanning the pressure in the chamber, we obtain similar spectrograms as shown in Fig. 2(e). We use both air and Krypton as gas media in the SHG-MPC chamber. While air is a more practical gas to use, Krypton provides larger dispersion, resulting in four phase-matching maxima within our fixed pressure tuning range.

Figure 4 shows the experimental results for Krypton. In Fig. 4(a), the spectrogram is shown together with the corresponding measured SHG efficiency. In Fig. 4(b-c) the fundamental and SH pulses at the largest efficiency are plotted in temporal and spectral domain. Since the SH pulses are not compressed here, the FTL pulse is plotted along with the measured input fundamental pulse. The bandwidth of the resulting SH pulses around 515 nm support an FTL of 31.5 fs. We measure a maximum conversion efficiency of 72% at a pressure of $p = 315\,\mathrm{mbar}$ in krypton. The efficiency $\eta = P_{\mathrm{in}}/P_{\mathrm{out}}$ is determined using the input power P_{in} at the position right before coupling into the SHG-MPC and the output power P_{out} right after the vacuum chamber, both indicated in Fig. 3. We measure the beam quality of the SH beam using a commercial M^2 device (DataRay WinCamD-IR-BB) after out-coupling of the vacuum chamber revealing an excellent beam quality of $M^2 < 1.1$ of the output SH beam. The simulated spectrum in Fig. 4, as well as the simulated spectrograms (Fig. S1 in the supplement) are in excellent agreement. Here we use the measured fundamental input pulses as the input and simulate the experimental conditions, using the (3+1)D nonlinear pulse propagation model described in the supplement section S1. The resulting FTL of the simulated pulse is 31.5 fs in agreement with the experimentally obtained spectrum. We further simulate the same experiment excluding effects

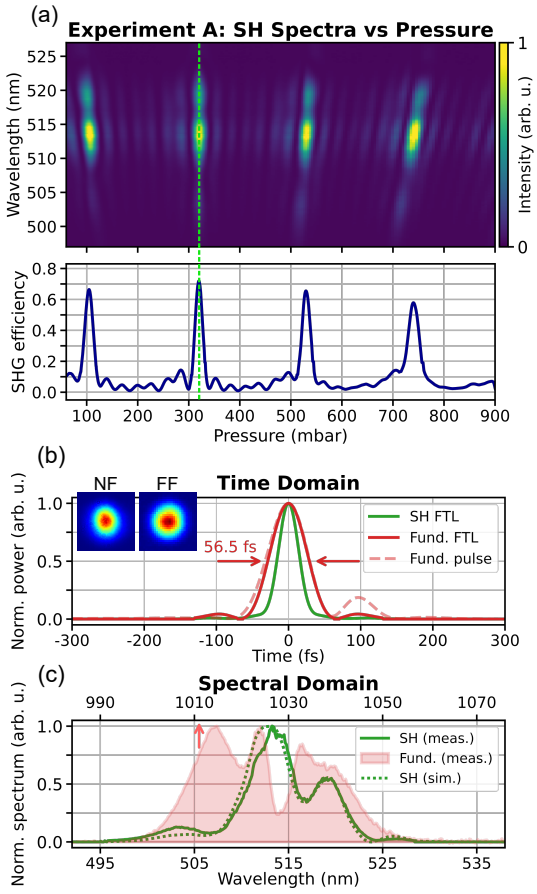


Figure 4: Experimental results of experiment A. (a) Spectrograms containing the spectrally-resolved SHG signal recorded as a function of gas pressure (here: Krypton) and the corresponding measured efficiencies displayed in the line-out plot. The green dashed line indicates the highest efficiency reached after GD matching at around 315 mbar. (b) Measured input and output pulses in the temporal domain. In this experiment the SH pulses are not compressed, thus the FTL pulses are shown. The insets show the beam profile of the SH beam in the near-field (NF) and far-field (FF). (c) Input and output spectrum. The simulated spectrum is in very good agreement with the measurement.

of SPM in order to investigate its influence on the generation process. Here, the simulations show that the maximum efficiency does not change, while the output FTL duration increases to 37 fs. We therefore conclude that the nonlinear dynamics in this experiment are dominated by SHG, whereas SPM has a secondary influence, decreasing the Fourier-transform-limited pulse duration by about 15%.

B. Short Pulse Conversion

In Experiment B we use post-compressed pulses with 15.4 fs pulse duration, an FTL of 14.5 fs and a pulse energy of 20 µJ. The post-compressed laser system was described earlier by Siletti et al. [45]. The repetition rate of the system is set to 5 kHz. Here, we use air as the dispersive medium in the SHG-MPC, resulting in fewer phase-matched maxima due to the lower dispersion of air compared to Krypton. We further change the crystal to the longer one with $L_{\mathrm{cr}} = 95\,\mu\mathrm{m}$. The experimental results are shown in Fig. 5. In the recorded spectrograms (Fig. 5(a)), we observe a global maximum at around 490 mbar. The signal maxima appear curved, effectively reducing the bandwidth and efficiency of the SHG process at a fixed gas pressure. The curvature results from higher-order relative phase terms between fundamental and SH fields, with the main contribution arising from a relative group-delay dispersion (GDD). The GDD (and higher phase orders) result from both, the phase characteristics of the mirror coatings and the dispersion of the materials in the MPC, where the latter is responsible for the major part of the GDD mismatch. While the MPC mirrors are designed for GD matching, higher order phase terms are not compensated. The spectra in Fig. 5 exhibit modulations that can be attributed to both the modulation of the post-compressed input spectrum as well as the phase introduced by the mirrors. The efficiency maxima exhibit a double-peak structure, which we are able to reproduce in our simulations by implementing the angle variation of the critical θ angle, introduced by the MPC beam geometry (supplement Fig. S3). According to our simulations, this effects does not significantly reduce the SHG conversion efficiency, but can introduce a second peak as seen in the experimental spectrograms as seen in Fig. 5(a). In section 4, we discuss how to eliminate the angular variation of the critical angle θ in the SHG-MPC. After setting the gas pressure to the efficiency maximum (indicated in Fig. 5(a)), we compress the pulse using a pair of chirped mirrors with an average GDD of $-40\,\mathrm{fs}^2$ per reflection and a total of 12 reflections, yielding about $-480\,\mathrm{fs}^2$ of compensated GDD. We characterize the SH pulses using frequency-resolved optical gating (FROG) device, where we retrieve a pulse duration of 13.8 fs and a conversion efficiency of 47 %. This efficiency is measured before the chirped mirror compressor. The total compressor transmission amounts to 93.4% , which can still be optimized by employing higher reflectivity chirped mirrors. The bandwidth measured with a spectrometer supports a pulse duration of 10 fs, while the retrieved spec-

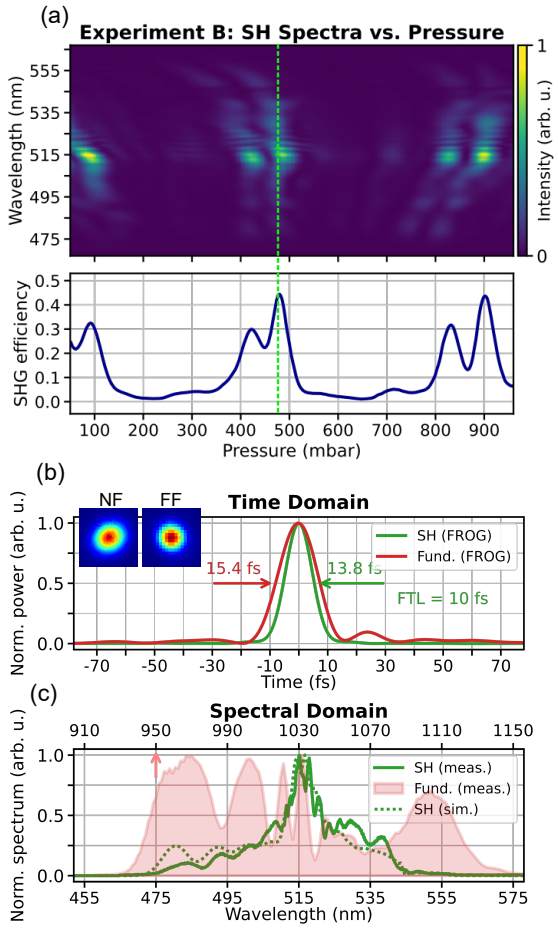


Figure 5: Experimental results of experiment B. (a) Spectrograms recorded as a function of gas pressure (here: air) and the corresponding measured efficiencies. The green dashed line indicates the highest efficiency at around 490 mbar. (b) Measured input and output pulses in the temporal domain. The insets show the beam profile of the SH beam in the near-field (NF) and far-field (FF). (c) Measured input and SH output spectra, as well as the simulated SH spectrum. The simulated spectrum is in excellent agreement with the experiment.

trum from the FROG measurement reveals an FTL of 12.6 fs. We attribute this discrepancy to the limited phase-matching bandwidth of the SHG crystal in the FROG setup. The simulated FTL duration of 10 fs, in agreement with the spectrometer-based estimate, further supports this interpretation. When SPM is suppressed in the simulations, the resulting FTL duration increases to 11.5 fs, showing again that SPM only plays a minor role in the SHG MPC. We measure a very good beam quality of $M^2 = 1.18 \pm 0.12$ for the SH output, compared to about $M^2 = 1.16$ for the fundamental input beam.

4 Discussion and Outlook

The SHG-MPC enables efficient nonlinear frequency-doubling of broadband pulses by exploiting the phase-tuning capabilities of MPCs. Instead of passing through a relatively thick nonlinear medium once, the propagation is split into many passes, where in-between each pass, the free propagation of the pulses and reflection at the MPC mirror is used to compensate the accumulated phase in the nonlinear crystal. In this way, the SHG-MPC enables to overcome the efficiency-bandwidth limit of single-pass SHG schemes.

A challenge that may arise is due to the typically round beam pattern geometry of the MPC, which can lead to considerable angles variations at the SHG crystal, changing the propagation axis of the beams and thus the dispersion relations in a non-isotropic crystal. This issue, however, can be circumvented by two measures. First, the beam geometry can be changed to a linear pattern, as shown in Fig. 6(a)-(c). Second, uniaxial crystals – for example BBO – can be used, with the beam pattern aligned such that the angles vary only along the ϕ-axis, while the θ-axis, along which the extraordinary SH field propagates, remains constant for each pass. The angle θ again refers to the angle of the $\vec{k}$-vector to the optical axis z of the crystal and ϕ is the angle relative to the xz plane [47,48]. In this way, extraordinary propagation of the SH field takes place at a defined θ-angle, leading to unchanged dispersion properties in the crystal at each pass. In the experiments, the MPC configuration is chosen such that the angular variation is small ($< \pm 0.5°$) by making the beam pattern on the mirrors as compact as possible, while still maintaining efficient in/out-coupling. While a double-peak in the efficiency (Fig. 5) appears – due to the remaining angle variations in the θ-direction – the efficiency does not significantly reduce. However, for different configurations, where the angles can be large, e.g. in tight-focusing geometries, the linear pattern approach should be implemented.

Another interesting aspect to discuss is mode-matching of the second harmonic in the SHG-MPC. In general, the input beam sent into an MPC needs to be matched to the transversal mode defined by the cell. In the context of the SHG-MPC, the question arises whether the generated SH field satisfies the mode-matching conditions as well. In our (3+1)D simulations, taking into account all relevant spatio-

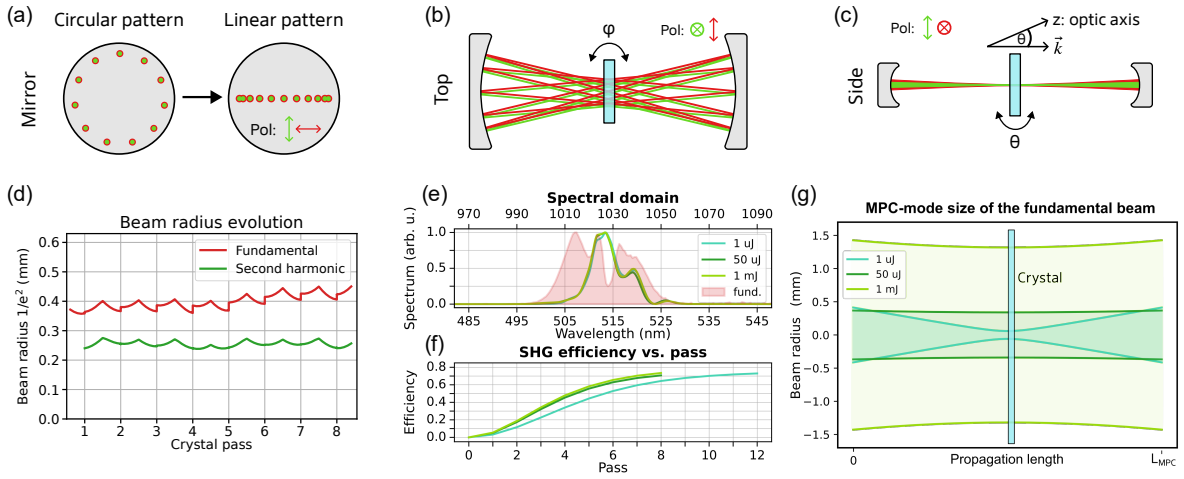


Figure 6: Optimized geometry and corresponding beam properties for an SHG-MPC employing a uniaxial crystal (e.g., BBO). The polarizations of the fundamental (red) and SH (green) beams are indicated by arrows, with the SH polarized along the extraordinary axis. Crosses denote polarization vectors pointing into the plane of the figure. (a) Comparison of a conventional round beam pattern, typically used in standard MPC configurations, with the proposed linear pattern. (b) Top view of the MPC with the linear pattern. From this perspective, the linear and round patterns appear identical. (c) Side view of the MPC, where the linear pattern appears like a single beam at a fixed angle θ. (d) Simulated beam-radius evolution of the fundamental and SH beams throughout the SHG-MPC using the parameters of Experiment A. (e–g) Simulations of energy-scaled SHG-MPCs using the measured fundamental spectrum from Fig. 3 as the simulation input. (e) Simulated MPC output spectra for three input pulse energies (1 µJ, 50 µJ, and 1 mJ), together with the input spectrum. (f) Corresponding evolution of the SHG conversion efficiency per pass. (g) Comparison of the fundamental (1030 nm) MPC beam radii for the three pulse energies. The MPC geometries are chosen such that the maximum peak intensity in the crystal is approximately 600 GW cm^{-2}, while the crystal thickness is fixed at 100 µm in all cases.

temporal pulse propagation effects (see supplementary section S1), we show that the SH automatically fulfills the mode-matching condition, if the fundamental beam is mode-matched to the MPC. Figure 6(d) shows the simulated beam radius over all eight passes in the SHG-MPC. Here we simulate the scenario of experiment A (section 3A) and show that the SH mode follows the fundamental mode and is very well mode-matched. As expected for SHG in the low conversion limit, the mode radius of the SH beam is reduced by a factor $\sqrt{2}$ relative to the fundamental mode, enabling to satisfy mode-matching for the SHG field in the nearly linear regime, where Kerr lensing is negligible [46]. The abrupt increases of the radius of the fundamental beam observed in Fig. 6(d) arise from the conversion process. As SHG depletes the central portion of the fundamental beam, the remaining intensity distribution broadens, resulting in an increased effective beam radius. Another relevant aspect to explore is energy-scaling of the SHG-MPC. In our experiments, we use pulses with moderate pulse energies of a few 10s of µJ. However, the pulse energy is not limited to this range, but can be scaled to either lower or higher pulse energies. For lower (higher) pulse energies, the MPC can be configured to tighter (looser) focusing geometries in order to reach suitable intensities inside the crystal. Energy up-scaling can be done in a compact way by using convex-concave (cx-cv) MPCs [49] or by scaling up the radius-of-curvature (ROC) and the MPC length, where the mode-size scales as a square-root with the ROC [50], optionally combined with beam path folding in order to decrease the MPC length [51]. The important parameter for scaling is the peak intensity of the fundamental field in the nonlinear crystal, which we try to keep around 600 GW/cm^2. Fig. 6(e) displays simulated MPC output spectra for low (1 µJ), moderate (50 µJ) and high energy (1 mJ), revealing very similar characteristics. For the 50 µJ case, we consider the same SHG-MPC configuration and input pulse as used in experiment A. The high energy case uses an up-scaled version of this configuration by increasing the mirror ROC to $R = 4.5$ m and an MPC length to about 1.3 m, where we keep the num-

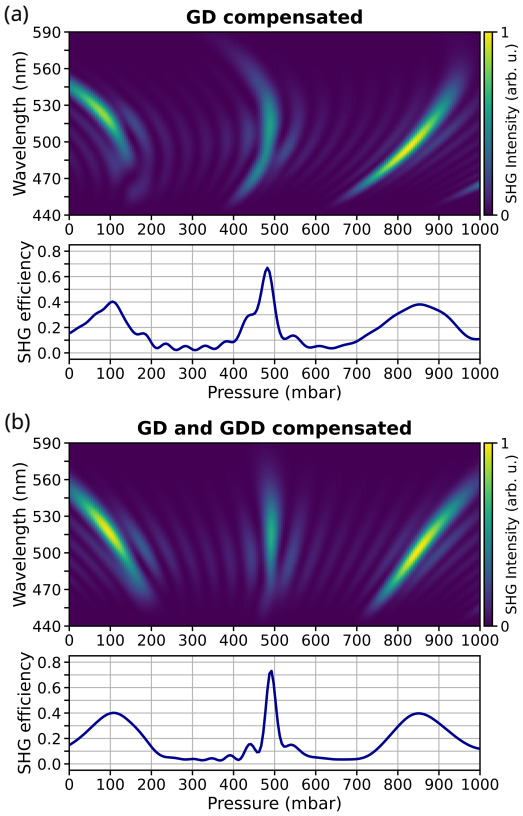


Figure 7: Simulated spectrogram traces and efficiencies for a 7 fs Gaussian pulse input using a 100 µm BBO crystal and air as dispersive gas. (a) GD compensated with remaining GDD. (b) Both GD and GDD compensated using formulas Eq. (6) and Eq. (7).

ber of round-trips at $N = 4$ and $k = 1$. In the low energy case, we consider $R = 50\,\text{mm}$, $N = 6$ round-trips and $k = 5$, resulting in an MPC length of about 10 cm and strongly focusing geometry. Figure 6(f) shows the efficiency per pass. The number of passes is chosen to reach saturation of the efficiency. Figure 6(g) displays the eigenmode structure of each MPC in the focal region. We calculate efficiencies of ¿ 70% for all three configurations, using the same experimentally measured input temporal profiles as in our experiment (experiment A, section 3) with 63 fs input pulse duration and an FTL of 56 fs.

In addition to energy up-scaling, an interesting development direction for the SHG-MPC is pulse duration down-scaling. The main challenge arises from higher-order phase-mismatch introduced by the dispersion of the crystal, gas and the MPC mirrors. For very short pulses, higher order relative phases terms such as the second-order phase (group-delay-dispersion, GDD) and third order (third-order-dispersion, TOD) can limit the bandwidth and the SHG conversion efficiency. Similar to GD, the GDD can be matched approximately by setting the second-order mirror dispersion to

$$\Delta\varphi_{\text{m}}^{(2)} \approx -\left(\Delta\varphi_{\text{cr}}^{(2)}(\theta_{\text{pm}}) + \Delta\varphi_{\text{gas}}^{(2)}(p_{\text{ref}})\right), \quad (7)$$

where $\Delta\varphi_{\text{cr}}^{(2)}(\theta_{\text{pm}})$ and $\Delta\varphi_{\text{gas}}^{(2)}(p_{\text{ref}})$ is the accumulated GDD in the crystal and the gas respectively, at phase-matching angle θ_{pm} and reference pressure p_{ref}. Figure 7 shows simulated spectrograms for a two-cycle, 7 fs input pulse centered at 1030 nm wavelength. In this simulation, the MPC configuration and dispersion properties are similar to experiment B, however, here we use an idealized mirror dispersion, which compensates the relative GD by −15 fs (Fig. 7(a) and (b)) and in addition the relative GDD by about $-12\,\text{fs}^2$ in 7(b). In Fig. 7(a) the higher-order phase-mismatch can be identified by the curvature of the signal maxima in the spectrograms. Although the GD is matched, the full bandwidth cannot be supported, resulting in a reduced bandwidth and efficiency. In contrast, the spectrogram in Fig. 7(b) the case with matched GDD is shown. Under ideal conditions, even for a 7 fs input pulse, the resulting efficiency can reach up to 80% with a resulting bandwidth of the SHG pulse of 5.7 fs FTL. The capabilities of matching first- and second order phases while supporting the necessary bandwidth depend on the available mirror coatings.

5 Conclusion

In this work we experimentally demonstrate efficient second-harmonic generation of broadband pulses in a multi-pass cell. We show that by using the phase-tuning capabilities of MPCs, the SHG-MPC can increase the efficiency of the SHG process for broadband pulses. In the experiment, we use a thin free-standing BBO crystal placed in the center of a symmetric MPC consisting of two mirrors with GD-compensating optical coatings inside a vacuum chamber. By optimizing two key parameters, the pressure of the gas in the chamber and the critical angle θ of the crystal, we demonstrated conversion of 50 µJ, 1030 nm, 63 fs (56 fs FTL) to the SH with 31.5 fs FTL with an efficiency of 72%, exhibiting excellent beam quality. In a second experiment, we demonstrate SHG for shorter pulses, where we use 20 µJ, 1030 nm, 15.4 fs (14.6 fs FTL) fundamental pulses, converting them into 10 fs FTL pulses with an efficiency of 47%

(44% after compression), which we compress down to 13.8 fs at an $M^2 = 1.18$. Comparing the bandwidth and resulting efficiency to existing works, we show in Fig. 1 that our results outperform common SHG techniques, pushing current efficiency-bandwidth records. The efficiency and bandwidth limits of our method are mainly defined by the achievable mirror dispersion characteristics. This combination of high conversion efficiency and broad bandwidth is particularly relevant for applications requiring energetic few-cycle visible or near-visible pulses, such as attosecond science, where efficient second-harmonic generation can help access shorter driving wavelengths and thereby increase the efficiency of high-harmonic generation [52]. Our results further indicate that MPCs open new degrees of freedom to tailor second-order nonlinear processes, including not only SHG but also, for example, sum-frequency generation and optical-parametric amplification [53,54], enabling new routes to push the parameter limits of these processes.

Funding & Acknowledgments

We acknowledge DESY (Hamburg, Germany), a member of the Helmholtz Association HGF, for support and the provision of experimental facilities. We further acknowledge support from the Helmholtz-Lund International Graduate School (HELIOS) (HIRS-0018) as well as from the Deutsche Forschungsgemeinschaft (DFG, German Research Foundation) – Project 545612524. V.W. acknowledges funding from the German Research Foundation (DFG) - project ID 545611997. We thank Robin Mevert and Prof. Dr. Uwe Morgner, both members of Leibniz Universität Hannover (LUH) for providing critical optical components for the experiments.

Disclosures

The authors declare no conflicts of interest.

Data Availability Statement

Data underlying the results presented in this paper are not publicly available but may be obtained from the authors upon reasonable request. Except where otherwise noted, all figures and images in this document are the original work of the authors and are licensed under a CC-BY 4.0 License.

Supplementary Material

S1 SHG-MPC simulation model

S1.1 (3+1)D model

The simulation model used in this work is based on the Unidirectional Pulse Propagation Equation (UPPE) [55]

$$\partial_z E(k_x,k_y,\omega,z) = iK_z(k_x,k_y,\omega)\,E(k_x,k_y,\omega,z) + iQ(k_x,k_y,\omega)\frac{P(k_x,k_y,\omega,z)}{2\varepsilon_0}\ , \tag{S1}$$

where $K_z(k_x,k_y,\omega) = \sqrt{k^2(k_x,k_y,\omega)-k_x^2-k_y^2}$ and $k(k_x,k_y,\omega) = \frac{\omega}{c_0}n(k_x,k_y,\omega)$, with the spatial frequencies k_x and k_y, the frequency ω and the permittivity of free space $\varepsilon_0 \approx 8.854{,}187{,}819\cdot 10^{-12}\,\mathrm{F/m}$. The propagation equation is solved in a non-field resolved manner, where the rapidly oscillating center frequency terms $\bar{\omega}$ are multiplied out by $\tilde{E}(\bar{\omega}+\omega) = E(\omega)\mathrm{e}^{i\bar{\omega}t}$. The wavenumber-dependent refractive index is calculated self-consistently according to reference [56], giving rise to spatial propagation effects in non-isotropic media, for example and most notably the spatial walk-off of the second harmonic in the crystal [56]. The nonlinear propagation coupling is defined as $Q(k_x,k_y,\omega) = \frac{\omega^2}{c^2 K_z(k_x,k_y,\omega)}$, where we make an isotropic approximation $K_z(k_x,k_y,\omega)\approx k(\omega)$ in the nonlinear part only. The nonlinear polarization $P_{\mathrm{o/e}}(x,y,t,z)$ for ordinary (o) and extraordinary (e) field is solved in the time-domain and takes into account second-order $\chi^{(2)}$ effects as well as self-phase modulation (SPM). The nonlinear polarization for the second- and third-order nonlinearities is defined as [56]:

$$P_{\mathrm{o/e}}(x,y,t,z) = P^{(2)}_{\mathrm{o/e}}(x,y,t,z) + P^{(3)}_{\mathrm{o/e}}(x,y,t,z) \tag{S2}$$

$$P^{(2)}_{\mathrm{o}} = \frac{\kappa_o}{4}\Big(\overbrace{2E_eE_o^*}^{\text{SHG process}} + E_eE_e + E_eE_e^* + E_oE_e^* + E_eE_o\Big) \tag{S3}$$

$$P^{(2)}_{\mathrm{e}} = \frac{\kappa_e}{4}\Big(\overbrace{E_oE_o}^{\text{SHG process}} + 2E_oE_e^* + E_eE_o^* + E_eE_o + E_oE_o^*\Big)\ , \tag{S4}$$

where we indicate the nonlinear processes that are responsible for the SHG generation in BBO with type I phase-matching. The pre-factors (coupling parameters) are $\kappa_{o/e} = 2\varepsilon_0\frac{\omega d_{\mathrm{eff}}}{n_{o/e}(\omega)}$, with the d_{eff} as the medium and its orientation dependent second-order response [56]. The additional factor of $1/4$ in the above equations arises from the convention used to calculate the intensity from the electric field $I = \frac{1}{2}nc_0\varepsilon_0|E|^2$, as opposed to $I = 2nc_0\varepsilon_0|E|^2$ used in reference [56] and by other authors [22]. For an explanation of these convention differences, we refer to the preface of reference [57].
Finally, the third-order polarization (SPM) is defined as

$$P^{(3)}_{\mathrm{o/e}}(x,y,t,z) = \gamma_{o/e}\,|E_{o/e}(x,y,t,z)|^2\,E_{o/e}(x,y,t,z)\ , \tag{S5}$$

with $\gamma_{o/e} = \frac{1}{2}\varepsilon_0^2 c_0 n_{o/e}^2 n_{2,o/e}$.

We use an in-house developed code for the numerical evaluation of Equation (S1), which is solved using a Fourier split-step method. The linear part is solved in reciprocal space and frequency domain and the nonlinear part is solved in real space and time domain using the Runge-Kutta 4 (RK4) method.

S1.2 (1+1)D model

In addition to the (3+1)D model including all spatio-temporal effects, we use a (1+1)D model, where the spatial domain is modeled using the Gaussian ABCD matrix formalism, additionally taking into account Kerr lensing [58]. This hybrid approach enables fast numerical calculations of MPC post-compresison as well as the SHG-MPC by summarizing the two spatial variables x and y into a simple ABCD-matrix based

calculation, while capturing the same nonlinear effects of the temporal and spatial domain as the (3+1)D model. The temporal and spatial domain is modeled by equation S1, but without the spatial coordinates

$$\partial_z E(\omega, z) = ik_z(\omega)\, E(\omega, z) + iQ(\omega)\frac{P(\omega, z)}{2\varepsilon_0} \,, \tag{S6}$$

where $k_z = \frac{\omega}{c_0} n(\omega)$ and $Q(\omega) = \frac{\omega^2}{c_0^2 k_z}$. Again, nonlinear polarization $P_{\mathrm{o/e}}(t, z)$ for ordinary (o) and extraordinary (e) field is as usually solved in the time-domain and takes into account second-order $\chi^{(2)}$ effects as well as self-phase modulation (SPM). The nonlinear polarization for the second- and third-order nonlinearities is defined as [56]:

$$P_{\mathrm{o/e}}(t, z) = P^{(2)}_{\mathrm{o/e}}(t, z) + P^{(3)}_{\mathrm{o/e}}(t, z) \tag{S7}$$

$$P^{(2)}_{\mathrm{o}} = \frac{\kappa_o}{4}\Big(\overbrace{2E_e E_o^*}^{\text{SHG process}} + E_e E_e + E_e E_e^* + E_o E_e^* + E_e E_o \Big) \tag{S8}$$

$$P^{(2)}_{\mathrm{e}} = \frac{\kappa_e}{4}\Big(\overbrace{E_o E_o}^{\text{SHG process}} + 2E_o E_e^* + E_e E_o^* + E_e E_o + E_o E_o^* \Big) \,, \tag{S9}$$

where we indicate the nonlinear processes that are responsible for the SHG generation in BBO with type I phase-matching. The pre-factors (coupling parameters) are again $\kappa_{o/e} = 2\varepsilon_0 \frac{\omega d_{\mathrm{eff}}}{n_{o/e}(\omega)}$, with the d_{eff} as the medium and its orientation dependent second-order response [56]. SPM is modeled using

$$P^{(3)}_{\mathrm{o/e}}(t, z) = \gamma_{o/e}\, |E_{o/e}(t, z)|^2\, E_{o/e}(t, z) \,, \tag{S10}$$

with $\gamma_{o/e} = \frac{1}{2}\varepsilon_0^2 c_0 n_{o/e}^2 n_{2,o/e}$.

Finally, the spatial effects are modeled using the ABCD transfer matrices for translation $M_L = \left(\begin{smallmatrix} 1 & L/n \\ 0 & 1 \end{smallmatrix}\right)$ and focusing $M_f = \left(\begin{smallmatrix} 1 & 0 \\ -1/f & 1 \end{smallmatrix}\right)$. Kerr lensing is accounted for by calculating the Kerr-focal length f_{Kerr} as [58]:

$$f_{\mathrm{Kerr}} = 0.47 \frac{\pi w^4}{P_{\mathrm{peak}} n_2 dz} \,, \tag{S11}$$

where P_{peak} is the peak power. Kerr lensing is then incorporated by modeling one propagation step of a distance $\mathrm{d}z$ as

$$M_{dz} = M_{dz/2} \cdot M_{f_{\mathrm{Kerr}}} \cdot M_{dz/2} \,. \tag{S12}$$

S2 Simulation of experiments

In this section, we show a collection of numerical results modeling our experimental results. All simulations use the same MPC geometry, consisting of two mirrors with a radius of curvature (ROC) of $R = 1\,\mathrm{m}$, $N = 4$ round-trips, and a configuration parameter $k = 1$, resulting in an MPC length of $L_{\mathrm{MPC}} = 29.5\,\mathrm{cm}$. For the simulations, we use the (3+1)D model described in section S1.

Figures S1 and S2 present a comparison between experiment and simulation for experiment A considering a BBO crystal with a thickness of 78 µm. In both datasets, the input pulses have a central wavelength of 1030 nm, a duration of 63 fs, and an energy of 50 µJ. These pulses correspond to retrieved pulse profiles obtained from FROG measurements (Fig. S4), which are used as input for the simulations. The simulations additionally include the wavelength-dependent phase and reflectivity characteristics of the mirrors, as provided by LAYERTECH GmbH (Fig. S6). The BBO crystal angle relative to the optical axis is set to $\theta = 24°$, and the gas pressure is varied between approximately 60 mbar and 900 mbar. In both cases, excellent agreement between simulation and experiment is observed in the spectrograms as well as in the

spectra. Furthermore, the measured second-harmonic (SH) spectrum supports a Fourier transform-limited (FTL) pulse duration of 31.5 fs, which is in exact agreement with the value obtained from the simulated SH spectrum. We furthermore incorporate an estimated anti-reflective (AR) coating loss of 1% for each field, fundamental and SH, which yields a maximum efficiency of 71% for both gases, which is very close to the measured maximum efficiency of 72%.

Figure S3 shows the experimental and simulated spectrograms for experiment B (see Section 3B of the main manuscript), using air as the ambient gas medium and fundamental input pulses at 1030 nm with a duration of 15.4 fs and an energy of 20 µJ. These input pulses were characterized using FROG measurements (Fig. S5) and used as input for the simulations. In this simulation, the BBO crystal thickness was increased to 95 µm and the θ angle is set to 23.2°. Furthermore, the measured and simulated SH spectra show good agreement, with both supporting a FTL pulse duration of 10 fs. The secondary maxima are reproduced as well, when the angular variation in the critical θ direction resulting from the MPC geometry is accounted for. As discussed in the main manuscript, the spectra retrieved from the FROG measurements exhibit a reduced bandwidth. This narrowing can be attributed to the limited phase-matching bandwidth of the BBO crystal used in the FROG setup (Fig. S5). In this simulation we apply an estimated AR-coating loss of 2% for each field, which results in a maximum conversion efficiency of about 53%, which is reasonably close to the measured efficiency of 47%.

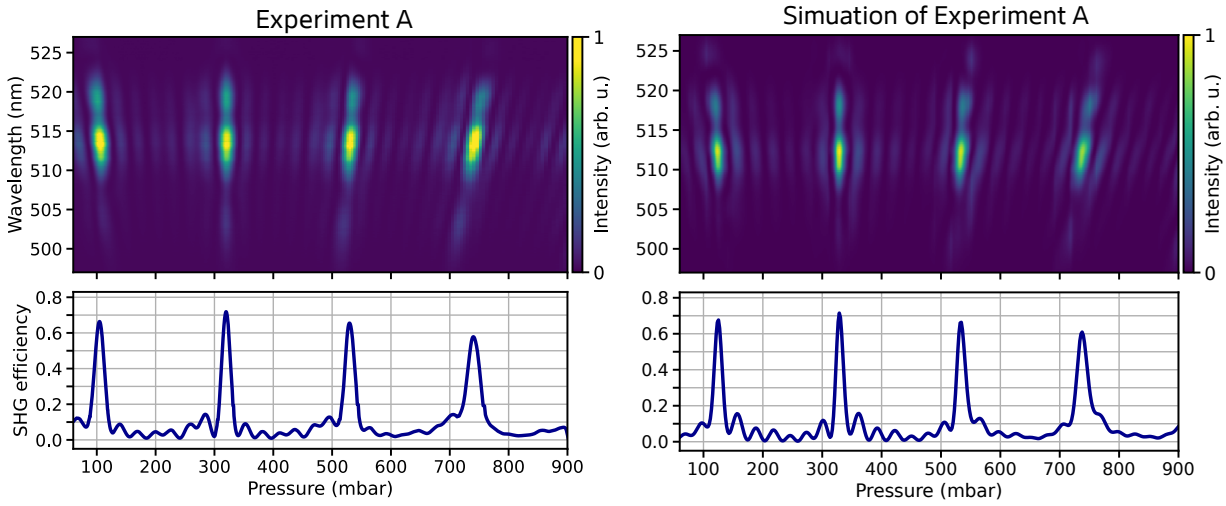


Figure S1: Experimental (left) and simulated (right) spectrograms for experiment A (section 3A in the main manuscript) using Krypton as the ambient gas for 63 fs, 50 µJ fundamental pulses. The data for the input pulse is retrieved from FROG measurements.

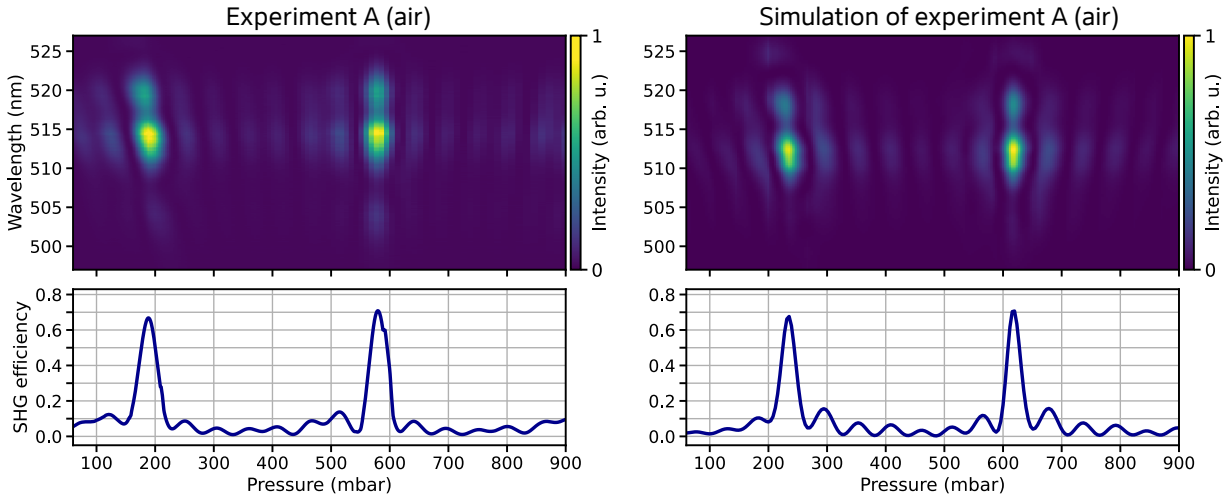


Figure S2: Experimental (left) and simulated (right) spectrograms for experiment A, but with air as the ambient gas (not shown in the main manuscript) for 63 fs, 50 µJ fundamental pulses as the input. The data for the input pulse is retrieved from FROG measurements.

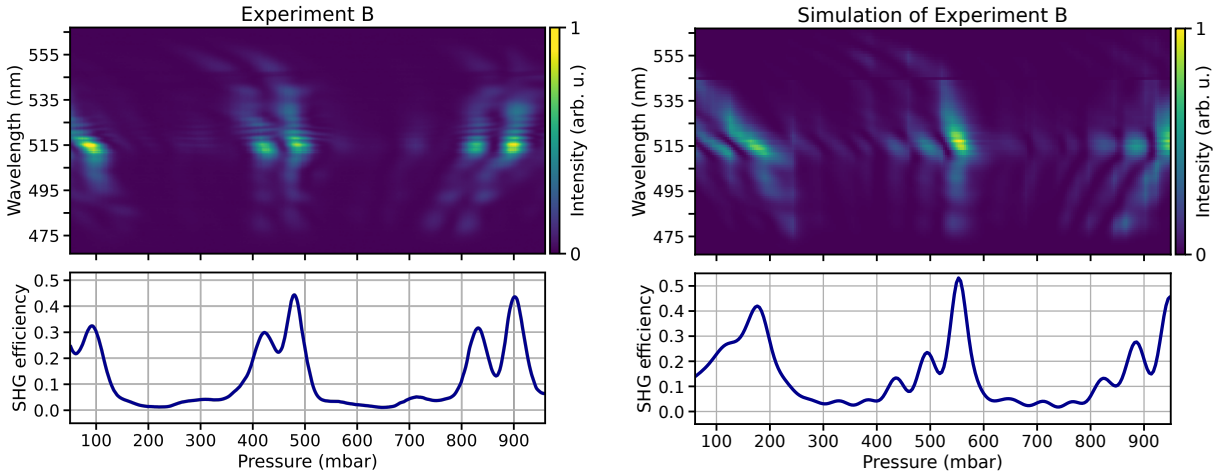


Figure S3: Experimental (left) and simulated (right) spectrograms for experiment B using air as the ambient gas for 15.4 fs, 20 µJ input fundamental pulses. The data for the input pulse is retrieved from FROG measurements.

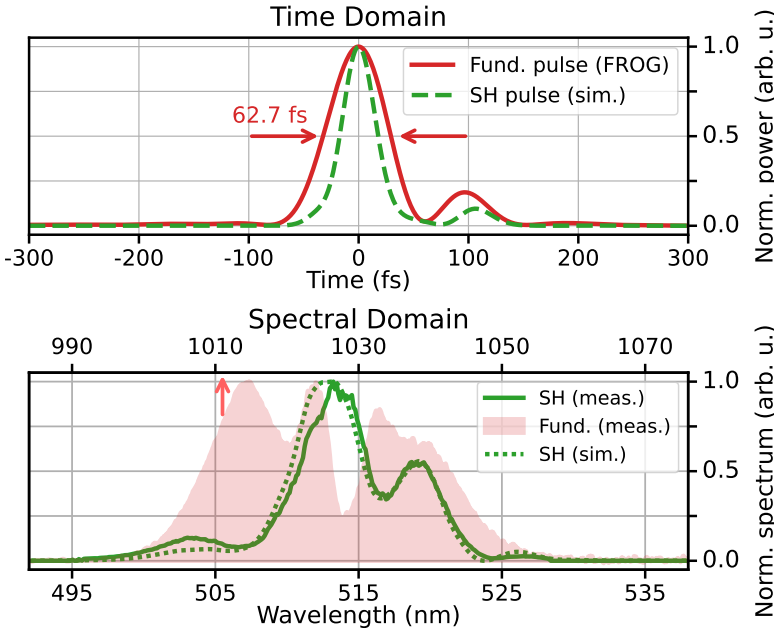


Figure S4: Fundamental and SH pulses from experiment and simulation (Experiment A). The upper plot shows the time domain pulses, the measured fundamental pulse and the compressed simulated SH pulse. In this experiment we did not compress the SH pulses, thus we do not show a compressed measured SH pulse. The lower plot shows the measured input spectrum (red), the measured SH spectrum (green) and the simulated SH spectrum (green, dotted).

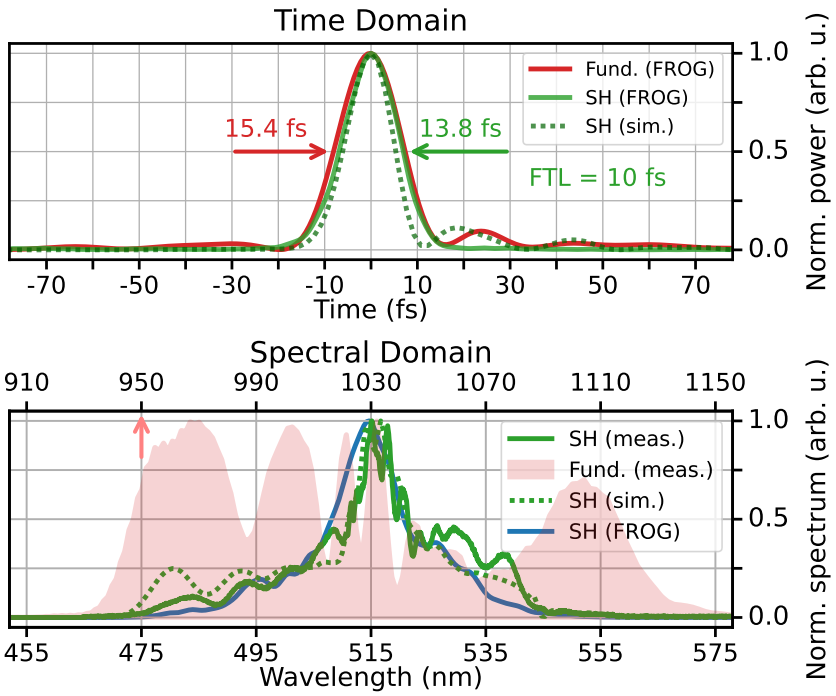


Figure S5: Fundamental and SH pulses from experiment and simulation (Experiment B). The upper plot shows the time domain pulses with the measured fundamental pulse (red), the measured SH pulse (green) and the compressed simulated SH pulse (green, dotted). The lower plot shows the measured input spectrum (red), the measured SH spectrum (green) and the simulated SH spectrum (green, dotted).

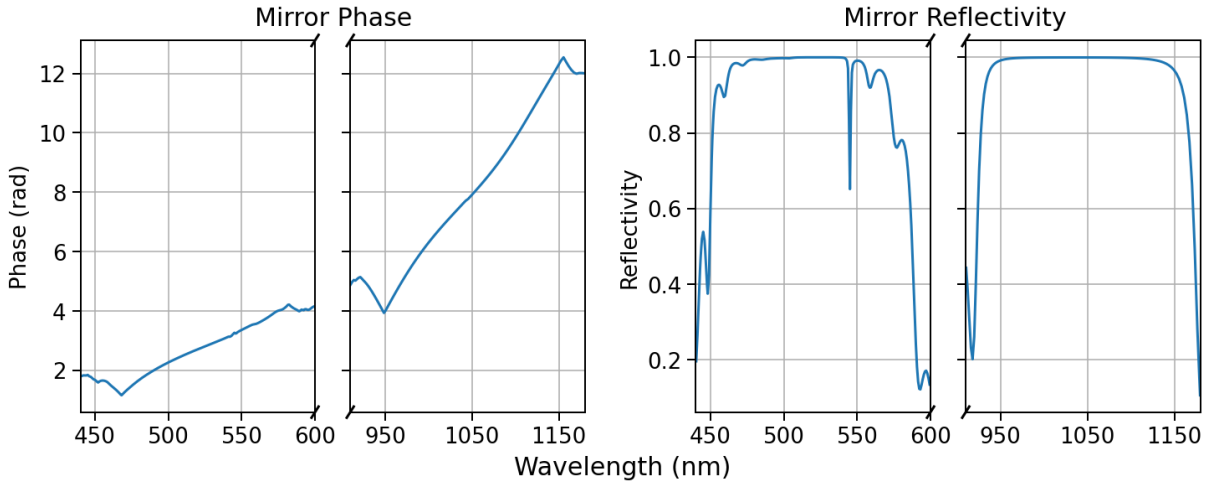


Figure S6: Mirror data for the mirrors used in the experiments and simulations, as provided by the manufacturer LAYERTEC GmbH.

S3 Second-harmonic beam quality measurements

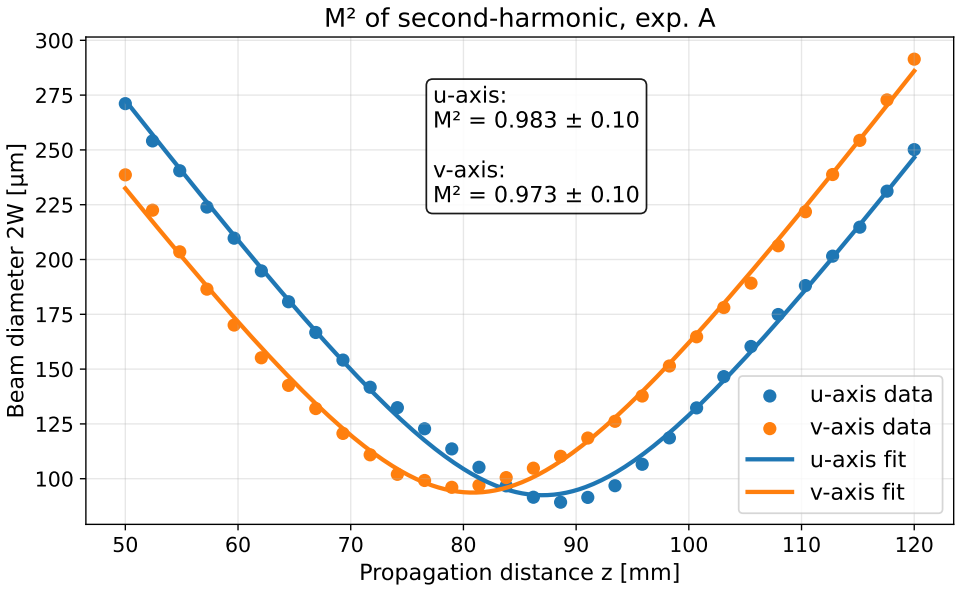


Figure S7: M^2 measurement of the output Ssecond-harmonic beam in experiment A (long pulse).

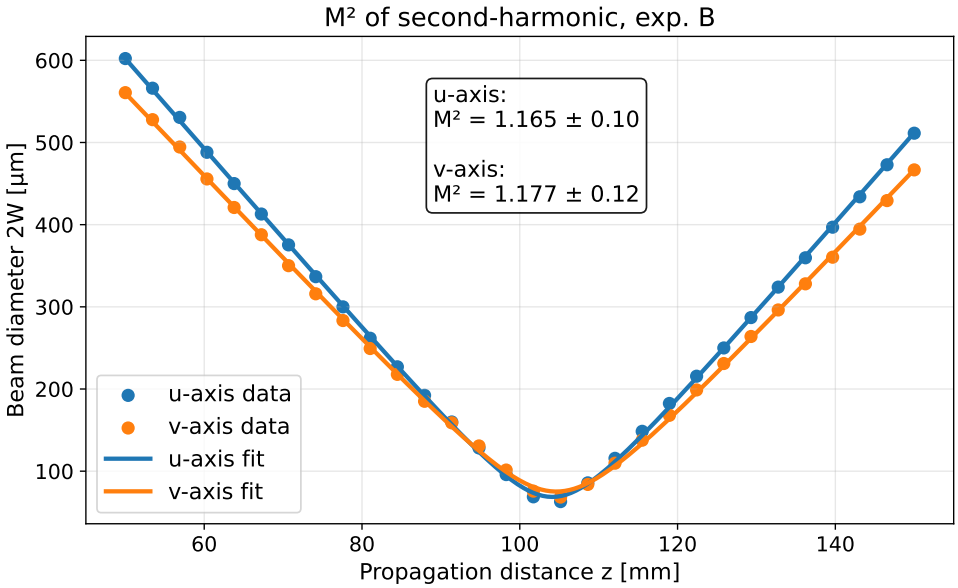


Figure S8: M^2 measurements of the output second-harmonic beam in experiment B (short pulse).

References

[1] P. A. Franken, A. E. Hill, C. W. Peters, and G. Weinreich, "Generation of optical harmonics," *Physical Review Letters*, vol. 7, no. 4, pp. 118–119, Aug. 1961.

[2] T. H. Maiman, "Stimulated optical radiation in ruby," *Nature*, vol. 187, no. 4736, pp. 493–494, Aug. 1960.

[3] P. Mason, D. Jackson, and E. Gorton, "CO_2 laser frequency doubling in $ZnGeP_2$," *Optics Communications*, vol. 110, no. 1–2, pp. 163–166, Aug. 1994.

[4] X. Liu, L. Qian, and F. W. Wise, "Efficient generation of 50-fs red pulses by frequency doubling in LiB_3O_5," *Optics Communications*, vol. 144, no. 4-6, pp. 265–268, Dec. 1997.

[5] T. Kanai, X. Zhou, T. Sekikawa, S. Watanabe, and T. Togashi, "Generation of subterawatt, sub-10-fs blue pulses at 1-5 kHz by broadband frequency doubling," *Optics Letters*, vol. 28, no. 16, p. 1484, Aug. 2003.

[6] J. Rothhardt, T. Eidam, S. Hadrich, F. Jansen, F. Stutzki, T. Gottschall, T. V. Andersen, J. Limpert, and A. Tunnermann, "135 W average-power femtosecond pulses at 520 nm from a frequency-doubled fiber laser system," *Optics Letters*, vol. 36, no. 3, p. 316, Jan. 2011.

[7] O. Gobert, G. Mennerat, R. Maksimenka, N. Fedorov, M. Perdrix, D. Guillaumet, C. Ramond, J. Habib, C. Prigent, D. Vernhet, T. Oksenhendler, and M. Comte, "Efficient broadband 400 nm noncollinear second-harmonic generation of chirped femtosecond laser pulses in BBO and LBO," *Applied Optics*, vol. 53, no. 12, p. 2646, Apr. 2014.

[8] B. Gronloh, P. Russbueldt, B. Jungbluth, and H.-D. Hoffmann, "Ultrafast green laser exceeding 400 W of average power," in *Laser Sources and Applications II*, J. I. Mackenzie, H. Jelinkova, T. Taira, and M. A. Ahmed, Eds., vol. 9135. SPIE, May 2014, p. 91350C.

[9] N. Ma, M. Chen, C. Yang, S. Lu, X. Zhang, and X. Du, "High-efficiency 50 W burst-mode hundred-picosecond green laser," *High Power Laser Science and Engineering*, vol. 8, 2020.

[10] C. Röcker, A. Loescher, F. Bienert, P. Villeval, D. Lupinski, D. Bauer, A. Killi, T. Graf, and M. Abdou Ahmed, "Ultrafast green thin-disk laser exceeding 1.4 kW of average power," *Optics Letters*, vol. 45, no. 19, p. 5522, Sep. 2020.

[11] L. Zhang, Y. Long, M. Zhang, C. Li, Y. Wang, S. Pan, X. Zhang, and X. Zhang, "Femtosecond green and ultraviolet lasers generated using second-harmonic generation based on $K_3B_6O_{10}Br$ nonlinear optical crystals," *Optical Engineering*, vol. 59, no. 5, p. 1, May 2020.

[12] M. Karst, P. Pfaller, R. Klas, Z. Wang, P. Gierschke, J. Rothhardt, and J. Limpert, "22-W average power high pulse energy multipass-cell-based post-compression in the green spectral range," *Optics Letters*, vol. 48, no. 5, p. 1300, Feb. 2023.

[13] S. Xu, Y. Gao, X. Liu, Z. Ou, F. Javed, X. He, H. Lu, J. Chen, C. Guo, C. Zhou, Q. Lue, and S. Ruan, "Extremely efficient, high beam quality second harmonic generation using a thin-disk regenerative amplifier," *Optics and Laser Technology*, vol. 181, p. 111963, Feb. 2025.

[14] J.-C. M. Diels, J. J. Fontaine, I. C. McMichael, and F. Simoni, "Control and measurement of ultrashort pulse shapes (in amplitude and phase) with femtosecond accuracy," *Applied Optics*, vol. 24, no. 9, p. 1270, May 1985.

[15] K. Naganuma, K. Mogi, and H. Yamada, "General method for ultrashort light pulse chirp measurement," *IEEE Journal of Quantum Electronics*, vol. 25, no. 6, pp. 1225–1233, Jun. 1989.

[16] V. K. Valev, "Characterization of nanostructured plasmonic surfaces with second harmonic generation," *Langmuir*, vol. 28, no. 44, pp. 15 454–15 471, Aug. 2012.

[17] M. Nuriya, S. Fukushima, A. Momotake, T. Shinotsuka, M. Yasui, and T. Arai, "Multimodal two-photon imaging using a second harmonic generation–specific dye," *Nature Communications*, vol. 7, no. 1, p. 11557, May 2016.

[18] T. Fortier and E. Baumann, "20 years of developments in optical frequency comb technology and applications," *Communications Physics*, vol. 2, no. 1, Dec. 2019.

[19] Y. Ma, S. H. Salman, C. Li, C. Mahnke, Y. Hua, S. Droste, J. Fellinger, A. S. Mayer, O. H. Heckl, C. M. Heyl, and I. Hartl, "Compact, All-PM Fiber Integrated and Alignment-Free Ultrafast Yb:Fiber NALM Laser With Sub-Femtosecond Timing Jitter," *J. Lightwave Technol.*, vol. 39, no. 13, pp. 4431–4438, Jul. 2021. [Online]. Available: https://opg.optica.org/jlt/abstract.cfm?URI=jlt-39-13-4431

[20] J. A. Giordmaine, "Mixing of light beams in crystals," *Physical Review Letters*, vol. 8, no. 1, pp. 19–20, Jan. 1962.

[21] P. D. Maker, R. W. Terhune, M. Nisenoff, and C. M. Savage, "Effects of dispersion and focusing on the production of optical harmonics," *Physical Review Letters*, vol. 8, no. 1, pp. 21–22, Jan. 1962.

[22] R. W. Boyd, *Nonlinear Optics*, 4th ed. London: Elsevier, AP Academic Press, 2020.

[23] S. A. Akhmanov and R. V. Khokhlov, "Parametric Amplifiers and Generators of Light," *Soviet Physics Uspekhi*, vol. 9, no. 2, pp. 210–222, Feb. 1966.

[24] N. Kovalenko, V. Hariton, K. Fritsch, and O. Pronin, "Free-space quasi-phase matching," *Optics Letters*, vol. 48, no. 23, p. 6220, Nov. 2023.

[25] O. Pronin, K. Fritsch, V. Hariton, and N. Kovalenko, "Device and method for nonlinear optical frequency-conversion," US Patent Application US20 240 402 567A1, Dec. 5, 2024, patent application publication US20240402567A1. [Online]. Available: https://patents.google.com/patent/US20240402567A1/en

[26] N. Kovalenko, A. Pai, and O. Pronin, "Free-space quasi-phase matched second harmonic generation in crystalline quartz," 2026.

[27] A. Leshem, G. Meshulam, G. Porat, and A. Arie, "Adiabatic second-harmonic generation," *Optics Letters*, vol. 41, no. 6, p. 1229, Mar. 2016.

[28] A. Dahan, A. Levanon, M. Katz, and H. Suchowski, "Ultrafast adiabatic second harmonic generation," *Journal of Physics: Condensed Matter*, vol. 29, no. 8, p. 084004, Jan. 2017.

[29] T. R. Zhang, H. R. Choo, and M. C. Downer, "Phase and group velocity matching for second harmonic generation of femtosecond pulses," *Applied Optics*, vol. 29, no. 27, p. 3927, Sep. 1990.

[30] P. Baum, S. Lochbrunner, and E. Riedle, "Tunable sub-10-fs ultraviolet pulses generated by achromatic frequency doubling," *Optics Letters*, vol. 29, no. 14, p. 1686, Jul. 2004.

[31] A. Tishchenko, T. Geernaert, N. Vermeulen, F. Berghmans, and T. Baghdasaryan, "Simultaneous modal phase and group velocity matching in microstructured optical fibers for second harmonic generation with ultrashort pulses," *Optics Express*, vol. 30, no. 7, p. 12026, Mar. 2022.

[32] M. Galletti, H. Pires, V. Hariton, C. P. João, S. Künzel, M. Galimberti, and G. Figueira, "High efficiency second harmonic generation of nanojoule-level femtosecond pulses in the visible based on BiBO," *High Power Laser Science and Engineering*, vol. 7, 2019.

[33] M. Ghotbi, M. Ebrahim-Zadeh, A. Majchrowski, E. Michalski, and I. V. Kityk, "High-average-power femtosecond pulse generation in the blue using BiB_3O_6," *Optics Letters*, vol. 29, no. 21, p. 2530, Nov. 2004.

[34] A. Major, D. Sandkuijl, and V. Barzda, "Efficient frequency doubling of a femtosecond Yb:KGW laser in a BiB_3O_6 crystal," *Optics Express*, vol. 17, no. 14, p. 12039, Jul. 2009.

[35] H. Zhu, T. Wang, W. Zheng, P. Yuan, L. Qian, and D. Fan, "Efficient second harmonic generation of femtosecond laser at 1 μm," *Optics Express*, vol. 12, no. 10, p. 2150, 2004.

[36] H. Liu, H.-Y. Lin, Z.-C. Huang, J.-J. Ruan, and D. Sun, "Second harmonic generation at 544 nm of a femtosecond laser," *Optik*, vol. 208, p. 164537, Apr. 2020.

[37] Y. Zhang, J. Liu, Z. Qin, and X. Su, "Double-pass second-harmonic generation of picosecond pulses with custom-poled KTP crystal," *Optics Continuum*, vol. 3, no. 3, p. 461, Mar. 2024.

[38] C. Röcker, A. Loescher, J.-P. Negel, M. Delaigue, F. Morin, C. Honninger, E. Mottay, P. Villeval, A. Holvoet, D. Lupinski, T. Graf, and M. Abdou Ahmed, "Direct amplification of sub-300 fs pulses in a versatile thin-disk multipass amplifier," *Optics Communications*, vol. 460, p. 125159, Apr. 2020.

[39] X. Zhao, Z. Wang, X. Wang, F. Yu, and X. Xu, "Broadband second-harmonic-generation in GdCOB crystals," *Optics Express*, vol. 30, no. 5, p. 6546, Feb. 2022.

[40] D. Wang, Q. Liu, Z. Li, X. Yuan, H. Wu, Z. Liu, W. Liu, and G. Chang, "Generation of 1-MHz, 64-W, 26-fs green pulses via second-harmonic generation of nonlinearly compressed pulses at 1.03 μm," *High Power Laser Science and Engineering*, vol. 13, 2025.

[41] C. Aparajit, K. Jana, A. D. Lad, Y. M. Ved, A. Couairon, and G. R. Kumar, "Efficient second-harmonic generation of a high-energy, femtosecond laser pulse in a lithium triborate crystal," *Optics Letters*, vol. 46, no. 15, p. 3540, Jul. 2021.

[42] D. Hillier, C. Danson, S. Duffield, D. Egan, S. Elsmere, M. Girling, E. Harvey, N. Hopps, M. Norman, S. Parker, P. Treadwell, D. Winter, and T. Bett, "Ultrahigh contrast from a frequency-doubled chirped-pulse-amplification beamline," *Applied Optics*, vol. 52, no. 18, p. 4258, Jun. 2013.

[43] S. Y. Mironov, V. N. Ginzburg, V. V. Lozhkarev, G. A. Luchinin, A. V. Kirsanov, I. V. Yakovlev, E. A. Khazanov, and A. A. Shaykin, "Highly efficient second-harmonic generation of intense femtosecond pulses with a significant effect of cubic nonlinearity," *Quantum Electronics*, vol. 41, no. 11, pp. 963–967, Nov. 2011.

[44] A. Schönberg, "Development of Ultrafast Laser Sources using Multi-Pass Cells," Ph.D. dissertation, Deutsches Elektronen-Synchrotron (DESY), 2026, to be submitted.

[45] L. Silletti, A. bin Wahid, E. Escoto, P. Balla, S. Rajhans, K. Horn, L. Winkelmann, V. Wanie, A. Trabattoni, C. M. Heyl, and F. Calegari, "Dispersion-engineered multi-pass cell for single-stage post-compression of an ytterbium laser," *Optics Letters*, vol. 48, no. 7, p. 1842, Mar. 2023.

[46] A.-L. Viotti, M. Seidel, E. Escoto, S. Rajhans, W. P. Leemans, I. Hartl, and C. M. Heyl, "Multi-pass cells for post-compression of ultrashort laser pulses," *Optica*, vol. 9, no. 2, p. 197, Feb. 2022.

[47] B. E. A. Saleh and M. C. Teich, *Fundamentals of photonics*, 3rd ed. Hoboken, NJ: John Wiley & Sons, 2019.

[48] T. A. Maldonado and T. K. Gaylord, "Light propagation characteristics for arbitrary wavevector directions in biaxial media by a coordinate-free approach," *Applied Optics*, vol. 30, no. 18, p. 2465, Jun. 1991.

[49] V. Hariton, K. Fritsch, K. Schwarz, N. Kovalenko, G. Figueira, G. Arisholm, and O. Pronin, "Spectral broadening in convex-concave multipass cells," *Optics Express*, vol. 31, no. 12, p. 19554, May 2023.

[50] C. M. Heyl, M. Seidel, E. Escoto, A. Schönberg, S. Carlström, G. Arisholm, T. Lang, and I. Hartl, "High-energy bow-tie multi-pass cells for nonlinear spectral broadening applications," *Journal of Physics: Photonics*, vol. 4, no. 1, p. 014002, Jan. 2022.

[51] A. Schönberg, S. Rajhans, E. Escoto, N. Khodakovskiy, V. Hariton, B. Farace, K. Põder, A.-K. Raab, S. Westerberg, M. Merdanov, A.-L. Viotti, C. L. Arnold, W. P. Leemans, I. Hartl, and C. M. Heyl, "Compact, folded multi-pass cells for energy scaling of post-compression," *Photonics Research*, vol. 13, no. 3, p. 761, Feb. 2025.

[52] A. Comby, E. Bloch, S. Beauvarlet, D. Rajak, S. Beaulieu, D. Descamps, A. Gonzalez, F. Guichard, S. Petit, Y. Zaouter, V. Blanchet, and Y. Mairesse, "Bright, polarization-tunable high repetition rate extreme ultraviolet beamline for coincidence electron–ion imaging," *Journal of Physics B: Atomic, Molecular and Optical Physics*, vol. 53, no. 23, p. 234003, Nov. 2020.

[53] J. H. Nägele, T. Steinle, J. Thannheimer, P. Flad, and H. Giessen, "Dispersion-engineered multipass optical parametric amplification," *Nature*, vol. 647, no. 8088, pp. 74–79, Nov. 2025.

[54] S. Rajhans, N. Rupp, E. Escoto, A. Schönberg, D. Laumer, M. Sumfleth, I. Abdallah, B. Manschwetus, C. Juliano, N. Javid, C. Arnold, T. GORKHOVER, M. Drescher, R. Riedel, I. Hartl, C. Heyl, and T. Lang, "Optical parametric multi-pass cell amplifier," *Optica*, Jun. 2026.

[55] A. Couairon, E. Brambilla, T. Corti, D. Majus, O. de J. Ramírez-Góngora, and M. Kolesik, "Practitioner's guide to laser pulse propagation models and simulation: Numerical implementation and practical usage of modern pulse propagation models," *The European Physical Journal Special Topics*, vol. 199, no. 1, pp. 5–76, Nov. 2011.

[56] T. Lang, A. Harth, J. Matyschok, T. Binhammer, M. Schultze, and U. Morgner, "Impact of temporal, spatial and cascaded effects on the pulse formation in ultra-broadband parametric amplifiers," *Optics Express*, vol. 21, no. 1, p. 949, Jan. 2013.

[57] R. L. Sutherland, *Handbook of Nonlinear Optics*, 2nd ed. New York: Marcel Dekker, 2003.

[58] M. Hanna, N. Daher, F. Guichard, X. Délen, and P. Georges, "Hybrid pulse propagation model and quasi-phase-matched four-wave mixing in multipass cells," *Journal of the Optical Society of America B*, vol. 37, no. 10, p. 2982, Sep. 2020.

Acknowledgements

First and foremost, I would like to thank my long-time supervisor Christoph M. Heyl. Not only is he an outstanding scientist, but also the best supervisor I can personally imagine. It has been a great pleasure to work with Christoph and hopefully I will continue to do so in the future.
I furthermore would like to thank all my colleagues who supported me on this pretty long journey. In particular, I would like to thank Sarper Salman, Chrstoph Mahnke, Victor Hariton, Nayla Jimenez, Tino Lang, Yannick Schrödel, Ayhan Tajalli, Supriya Rajhans, Esmerando Escoto and Nikita Khodakovskiy for not only helping me with my work, but also being amazing friends along the way. I would like to mention Victor Hariton in particular, with whom we had so many discussions came up with an unimaginable number of great research ideas (most of them didn't work). However, once in a while, some ideas do and did work, and I hope that we will come up with crazy new things in the future as well.
I would also like to thank the Helmholtz-Lund International Graduate School (HELIOS) for accepting (even) me as a PhD student and supporting me over the course of the dissertation.
Finally, I cannot thank my family enough, especially my mother Swetlana Schönberg and my son Radomir Schönberg for always supporting me, not just throughout the PhD, but also before and beyond that.

Eidesstattliche Erklärung / Affadavit

Hiermit versichere ich an Eides statt, die vorliegende Dissertationsschrift selbst verfasst und keine anderen als die angegebenen Hilfsmittel und Quellen benutzt zu haben. Sofern im Zuge der Erstellung der vorliegenden Dissertationsschrift generative Künstliche Intelligenz (gKI) basierte elektronische Hilfsmittel verwendet wurden, versichere ich, dass meine eigene Leistung im Vordergrund stand und dass eine vollständige Dokumentation aller verwendeten Hilfsmittel gemäß der Guten wissenschaftlichen Praxis vorliegt. Ich trage die Verantwortung für eventuell durch die gKI generierte fehlerhafte oder verzerrte Inhalte, fehlerhafte Referenzen, Verstöße gegen das Datenschutz- und Urheberrecht oder Plagiate.

I hereby declare and affirm that this doctoral dissertation is my own work and that I have not used any aids and sources other than those indicated. If electronic resources based on generative artificial intelligence (gAI) were used in the course of writing this dissertation, I confirm that my own work was the main and value-adding contribution and that complete documentation of all resources used is available in accordance with good scientific practice. I am responsible for any erroneous or distorted content, incorrect references, violations of data protection and copyright law or plagiarism that may have been generated by the gAI.



Hamburg, 07.07.2026 Unterschrift